polymers

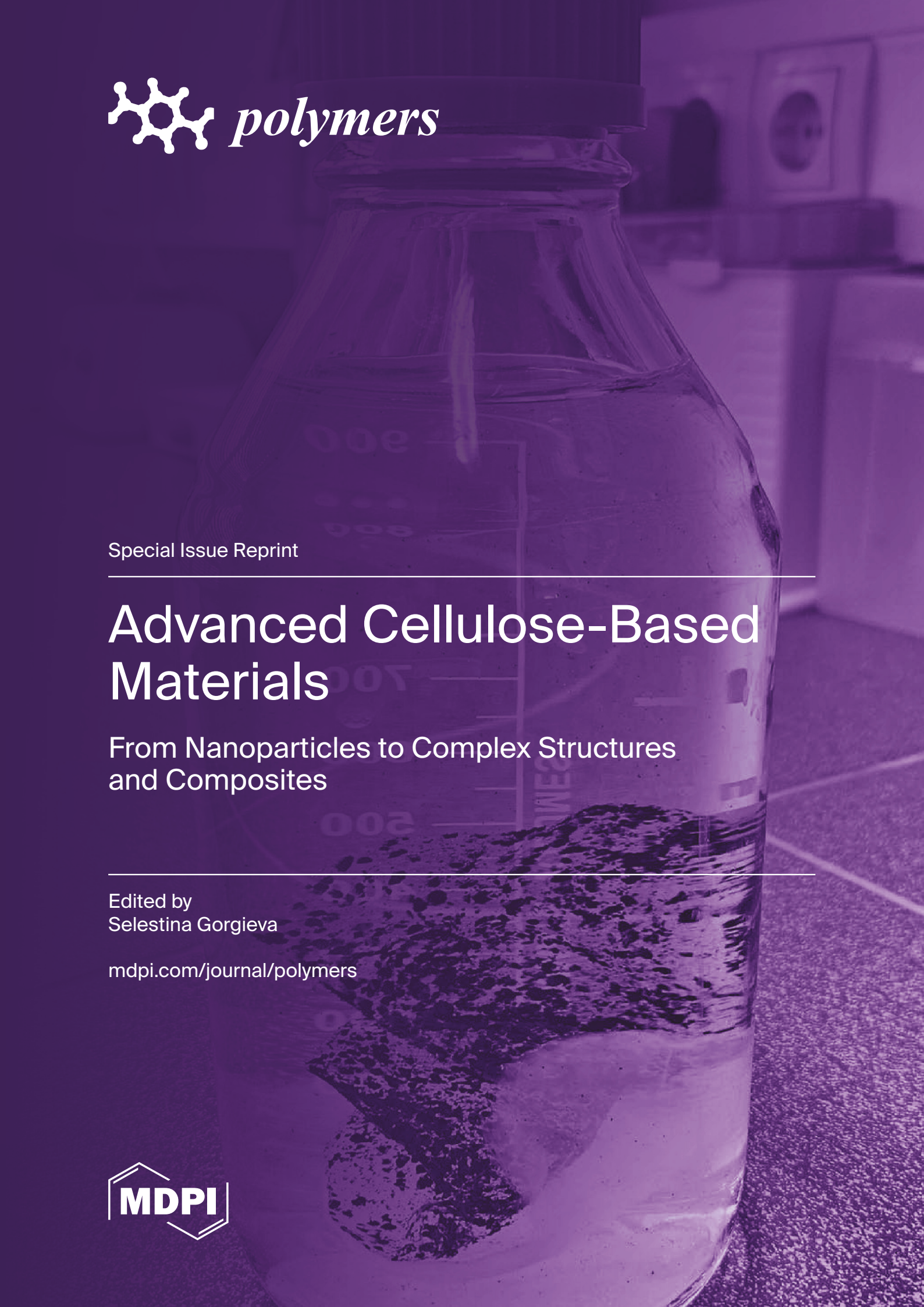

Special Issue Reprint

Advanced Cellulose-Based Materials

From Nanoparticles to Complex Structures and Composites

Edited by
Selestina Gorgieva

mdpi.com/journal/polymers

MDPI

Advanced Cellulose-Based Materials: From Nanoparticles to Complex Structures and Composites

Advanced Cellulose-Based Materials: From Nanoparticles to Complex Structures and Composites

Guest Editor

Selestina Gorgieva

MDPI

Basel • Beijing • Wuhan • Barcelona • Belgrade • Novi Sad • Cluj • Manchester

Guest Editor
Selestina Gorgieva
Faculty of Mechanical
Engineering
University of Maribor
Maribor
Slovenia

Editorial Office
MDPI AG
Grosspeteranlage 5
4052 Basel, Switzerland

This is a reprint of the Special Issue, published open access by the journal *Polymers* (ISSN 2073-4360), freely accessible at: https://www.mdpi.com/journal/polymers/special_issues/86DNJ5P4F1.

For citation purposes, cite each article independently as indicated on the article page online and as indicated below:

Lastname, A.A.; Lastname, B.B. Article Title. *Journal Name* **Year**, *Volume Number*, Page Range.

ISBN 978-3-7258-7310-4 (Hbk)
ISBN 978-3-7258-7311-1 (PDF)
https://doi.org/10.3390/books978-3-7258-7311-1

Cover image courtesy of Selestina Gorgieva

Contents

About the Editor

Selestina Gorgieva

Selestina Gorgieva is a Scientific Counsellor in Materials Science at the University of Maribor with over 15 years of research experience in the field of biopolymers. After completing her PhD in 2014 in the field of biopolymer scaffolding materials, she has led and participated in numerous national and international projects focused on nanocellulose composites, sustainable feedstocks, and advanced biopolymer membranes for energy and biomedical applications. Her research interests encompass bio-nanomaterials design, processing, and characterization, with a strong emphasis on sustainable and functional materials, such as bacterial nanocellulose.

polymers

MDPI

Editorial

Advanced Cellulose-Based Materials: From Nanoparticles to Complex Structures and Composites

Selestina Gorgieva

Faculty of Mechanical Engineering, University of Maribor, Smetanova Ulica 17, 2000 Maribor, Slovenia; selestina.gorgieva@um.si

Cellulose has long been recognised as the fundamental structural component of plant cell walls and is currently established as a highly adaptable molecular scaffold for next-generation sustainable materials. Its abundance, renewability, and intrinsic physicochemical properties position cellulose at the centre of the emerging bio-based and circular materials economy. With parallel advances in nanotechnology, biotechnology, and materials processing, cellulose can now be transformed into nanoscale building blocks, namely cellulose nanocrystals (CNCs) and cellulose nanofibrils (CNFs), that exhibit high tensile strength, low density, large specific surface areas, and high aspect ratios, being exceptionally attractive for applications in high-performance composites, biomedical engineering, energy-storage and energy-conversion devices, optical materials, and sustainable alternatives to conventional plastics and leather.

Despite this rapid progress, several scientific and technological challenges continue to limit broader industrial deployment of cellulose-derived materials. One of the most significant obstacles is the scalable and energy-efficient top-down disintegration of biomass into nanoscale form. Established isolation methods, such as high-pressure homogenisation, micro grinding, and chemical pretreatments remain energy-intensive or rely on environmentally demanding reagents. Conversely, bottom-up biosynthetic routes, particularly bacterial cellulose production, offer advantages in structural purity, crystallinity, and nanoscale uniformity but require further optimisation to achieve economically viable large-scale output. Interfacial incompatibility between hydrophilic nanocellulose and hydrophobic polymer matrices presents another major challenge, limiting dispersion, reinforcing efficiency, and mechanical performance in composite systems. Addressing this issue requires advanced surface-functionalisation strategies that enhance interfacial adhesion while preserving nanocellulose integrity. A further challenge is translating nanoscale material properties into predictable macroscopic performance, which demands precise control over hierarchical assembly from the nanometre to the bulk scale. To address these challenges and to highlight emerging strategies in this rapidly evolving field, this Special Issue entitled "Advanced Cellulose-Based Materials: From Nanoparticles to Complex Structures and Composites" was organised. The collected contributions demonstrate the breadth of ongoing research, ranging from nanocellulose processing and functionalisation to the development of porous materials, bio-based composites, and engineered nano-macro, 3D and 4D architectures.

A relevant research direction highlighted in this Special Issue concerns cellulose-based porous materials for acoustic insulation applications. Seciureanu et al. (contribution 1) investigated foam-formed porous materials derived from cellulose fibers, demonstrating their potential as sustainable alternatives to conventional synthetic acoustic insulation materials. Their results revealed that the internal pore structure and distribution significantly influence sound absorption and transmission loss, emphasising the importance

of controlling the porous architecture in the design of cellulose-based acoustic materials. Building upon this concept, Nastac et al. (contribution 2) explored the modification of cellulose foams using hemicellulose-derived xylan derivatives to enhance structural integrity and surface properties. Their study demonstrated that introducing xylan-based surface modifiers significantly reduces the wettability of cellulose foams while improving mechanical stability, without compromising acoustic performance. This work highlights the potential of integrating various plant-derived polysaccharides to develop multifunctional, fully bio-based material systems. Another prominent theme concerns the development of nanocellulose-reinforced composite materials. Hwang et al. (contribution 3) investigated the enzymatic pretreatment of cellulose nanofibrils followed by spray drying to produce nanofibril powders suitable for composite processing. Their findings demonstrate that enzyme-assisted processing can significantly reduce energy consumption during nanofibril production while maintaining the reinforcing capabilities of the resulting nanocellulose in polypropylene composites. Such approaches represent an important step toward more sustainable and scalable nanocellulose manufacturing technologies. Advances in cellulose-based materials for energy-related applications are represented in work of Hren et al. (contribution 4) reporting the development of fully polysaccharide-based anion exchange membranes composed of chitosan reinforced with neat or quaternized cellulose nanofibrils. These membranes exhibited significantly improved mechanical properties, ionic conductivity, and power density when tested in direct ethanol fuel cells, demonstrating the potential of cellulose nanomaterials as structural and functional components in electrochemical energy systems. In addition to nanocomposites and membranes, several contributions explore the engineering of hierarchical cellulose architectures. Wang et al. (contribution 5) reported the fabrication of compressible and elastic cellulose wood structures using deep eutectic solvents combined with alkaline treatment. Selective removal of lignin and hemicellulose produced a honeycomb-like cellular architecture capable of reversible compression and high elasticity. Such structures may enable new applications in sensing technologies, filtration systems, and biomedical scaffolds.

The application of nanotechnology to traditional cellulose-based industries is addressed in work of Maślana et al. (contribution 6). In this paper, the strategies to enhance the retention of inorganic fillers during papermaking by using nanoparticle additives, including silica nanospheres, titanium dioxide nanoparticles, and boron nitride nanoflakes were investigated. Their study demonstrated that silica nanoparticles significantly enhance calcium carbonate retention, offering new opportunities to improve paper performance and production efficiency. The versatility of cellulose-based materials is further illustrated by the work of Bautista-Morenilla et al. (contribution 7), who investigated microblasting with powdered cellulose as a dry-cleaning technique for paper-based artworks. This approach proved effective for removing contaminants from printed materials without causing morphological damage to the paper substrate, providing a sustainable and compatible method for cultural heritage conservation. In a comprehensive review Potočnik et al. (contribution 8) summarise recent progress in the biosynthesis and modification of bacterial cellulose using synthetic biology approaches. The authors highlight advances in the genetic and metabolic engineering of cellulose-producing bacteria and discuss the potential to design microbial systems capable of producing cellulose with tailored structural and functional properties. Beyond the studies presented in here, the bacterial cellulose has emerged as a particularly promising platform for the development of advanced materials, from applications in wound dressings, drug delivery systems, and tissue engineering scaffolds [1–4]. Furthermore, the incorporation of conductive polymers or nanoparticles into bacterial cellulose matrices has enabled the development of flexible electronic devices, biosensors, and energy storage systems [5–7].

https://doi.org/10.3390/polym18060701

Collectively, the research contributions in this Special Issue demonstrate substantial progress in the development of cellulose-based materials. Nevertheless, several challenges and emerging opportunities will shape the field's future trajectory. Sustainable and scalable nanocellulose production remains central, with greener processing routes integrating enzymatic pretreatment, mechanical fibrillation, and solvent-based fractionation gaining attention for reducing energy consumption and chemical waste. Advanced surface-functionalisation strategies, including click chemistry, bioinspired coatings, and enzymatic grafting, will broaden the functional spectrum and improve compatibility with diverse material systems. At the structural level, mastering supramolecular interactions and hierarchical organisation remains crucial for connecting nanoscale attributes with macroscopic properties. Emerging fabrication methods such as directed self-assembly, templating, and additive manufacturing are expected to provide new levels of structural control.

Future cellulose-based systems will increasingly integrate multifunctionality, combining mechanical strength with electrical conductivity, catalytic activity, or environmental responsiveness. Finally, although cellulose is inherently renewable and biodegradable, the environmental impacts of specific processing routes must be carefully evaluated. Integrating life-cycle assessment, green-chemistry principles, and recyclable process design will be essential to ensure that cellulose-based materials meaningfully contribute to global sustainability goals. With rapid progress in nanocellulose engineering, hierarchical structuring, and synthetic-biology-driven biofabrication, cellulose is poised to remain a foundation for advanced sustainable materials.

Funding: This work was developed within the scope of the project N2-0388 and program P2-0118 financed by Slovenian Agency for Research and Innovation (ARIS) and project FABULOSE funded by European Union (grant agreement No 101214009).

Acknowledgments: The Guest Editor wishes to thank the authors for their contributions to this Special Issue, the reviewers for their diligent efforts in evaluating the submitted manuscripts, and the Polymers editorial team for their outstanding support.

Conflicts of Interest: The author declares no conflicts of interest.

List of Contributions:

1. Seciureanu, M.; Nastac, S.-M.; Guiman, M.-V.; Nechita, P. Cellulose Fibers-Based Porous Lightweight Foams for Noise Insulation. *Polymers* **2023**, *15*, 3796. https://doi.org/10.3390/polym15183796.
2. Nastac, S.M.; Nechita, P.; Guiman, M.V.; Roman, M.; Rosca, I.C. Applications of Xylan Derivatives to Improve the Functional Properties of Cellulose Foams for Noise Insulation. *Polymers* **2023**, *15*, 4648. https://doi.org/10.3390/polym15244648.
3. Hwang, S.; Walker, C.C.; Johnson, D.; Han, Y.; Gardner, D.J. Spray Drying Enzyme-Treated Cellulose Nanofibrils. *Polymers* **2023**, *15*, 4086. https://doi.org/10.3390/polym15204086.
4. Hren, M.; Makuc, D.; Plavec, J.; Roschger, M.; Hacker, V.; Genorio, B.; Božič, M.; Gorgieva, S. Efficiency of Neat and Quaternized-Cellulose Nanofibril Fillers in Chitosan Membranes for Direct Ethanol Fuel Cells. *Polymers* **2023**, *15*, 1146. https://doi.org/10.3390/polym15051146.
5. Wang, W.; Chen, M.; Wu, Y. Compressible Cellulose Wood Prepared with Deep Eutectic Solvents and Its Improved Technology. *Polymers* **2023**, *15*, 1593. https://doi.org/10.3390/polym15071593.
6. Maślana, K.; Sielicki, K.; Wenelska, K.; Kędzierski, T.; Janusz, J.; Mariańczyk, G.; Gorgon-Kuza, A.; Bogdan, W.; Zielińska, B.; Mijowska, E. Facile Strategy for Boosting of Inorganic Fillers Retention in Paper. *Polymers* **2024**, *16*, 110. https://doi.org/10.3390/polym16010110.
7. Bautista-Morenilla, I.; Ruiz-Recasens, C.; Campo-Francés, G. Powdered Cellulose Microblasting for Dry Cleaning Printed Works on Paper. *Polymers* **2024**, *16*, 176. https://doi.org/10.3390/polym16020176.

8. Potočnik, V.; Gorgieva, S.; Trček, J. From Nature to Lab: Sustainable Bacterial Cellulose Production and Modification with Synthetic Biology. *Polymers* **2023**, *15*, 3466. https://doi.org/10.3390/polym15163466.

References

1. Jančič, U.; Nacu, I.; Verestiuc, L.; Rancan, F.; Gorgieva, S. Bioactive bacterial nanocellulose membranes for non-surgical debridement and infection prevention in burn wound healing. *Carbohydr. Polym. Technol. Appl.* **2025**, *10*, 100762. [CrossRef]
2. Gorgieva, S.; Trček, J. Bacterial Cellulose: Production, Modification and Perspectives in Biomedical Applications. *Nanomaterials* **2019**, *9*, 1352. [CrossRef] [PubMed]
3. Jančič, U.; Trček, J.; Verestiuc, L.; Vukomanović, M.; Gorgieva, S. Bacterial nanocellulose loaded with bromelain and nisin as a promising bioactive material for wound debridement. *Int. J. Biol. Macromol.* **2024**, *266*, 131329. [CrossRef] [PubMed]
4. Trpeska, L.L.; Petrushevska, M.; Geskovski, N.; Crcarevska, M.S.; Djurdjic, B.; Vuksanovich, V.; Jančič, U.; Gorgieva, S. Bacterial Nanocellulose Wound Dressings with Gentamicin-Loaded Chitosan Nanoparticles for Surgical Site Infection Management. *Polymers* **2026**, *18*, 510. [CrossRef] [PubMed]
5. Shah, N.; Ul-Islam, M.; Khattak, W.A.; Park, J.K. Overview of bacterial cellulose composites: A multipurpose advanced material. *Carbohydr. Polym.* **2013**, *98*, 1585–1598. [CrossRef] [PubMed]
6. Iguchi, M.; Yamanaka, S.; Budhiono, A. Bacterial cellulose—A masterpiece of nature's arts. *J. Mater. Sci.* **2000**, *35*, 261–270. [CrossRef]
7. Lin, N.; Durfresne, A. Nanocellulose in biomedicine: Current status and future prospect. *Eur. Polym. J.* **2014**, *59*, 302–325. [CrossRef]

polymers

MDPI

Article

Efficiency of Neat and Quaternized-Cellulose Nanofibril Fillers in Chitosan Membranes for Direct Ethanol Fuel Cells

Maša Hren [1], Damjan Makuc [2], Janez Plavec [2,3,4], Michaela Roschger [5], Viktor Hacker [5], Boštjan Genorio [4], Mojca Božič [6] and Selestina Gorgieva [1,*]

[1] Faculty of Mechanical Engineering, University of Maribor, Smetanova 17, 2000 Maribor, Slovenia
[2] Slovenian NMR Centre, National Institute of Chemistry, Hajdrihova 19, 1000 Ljubljana, Slovenia
[3] EN-FIST Centre of Excellence, Trg Osvobodilne fronte 13, 1000 Ljubljana, Slovenia
[4] Faculty of Chemistry and Chemical Technology, University of Ljubljana, Večna pot 113, 1000 Ljubljana, Slovenia
[5] Institute of Chemical Engineering and Environmental Technology, Graz University of Technology, Inffeldgasse 25/C, 8010 Graz, Austria
[6] Dravske Elektrarne Maribor d.o.o., Obrežna ulica 170, 2000 Maribor, Slovenia
* Correspondence: selestina.gorgieva@um.si

Abstract: In this work, fully polysaccharide based membranes were presented as self-standing, solid polyelectrolytes for application in anion exchange membrane fuel cells (AEMFCs). For this purpose, cellulose nanofibrils (CNFs) were modified successfully with an organosilane reagent, resulting in quaternized CNFs (CNF (D)), as shown by Fourier Transform Infrared Spectroscopy (FTIR), Carbon-13 (C13) nuclear magnetic resonance (^{13}C NMR), Thermogravimetric Analysis (TGA)/Differential Scanning Calorimetry (DSC), and ζ-potential measurements. Both the neat (CNF) and CNF(D) particles were incorporated in situ into the chitosan (CS) membrane during the solvent casting process, resulting in composite membranes that were studied extensively for morphology, potassium hydroxide (KOH) uptake and swelling ratio, ethanol (EtOH) permeability, mechanical properties, ionic conductivity, and cell performance. The results showed higher Young's modulus (119%), tensile strength (91%), ion exchange capacity (177%), and ionic conductivity (33%) of the CS-based membranes compared to the commercial Fumatech membrane. The addition of CNF filler improved the thermal stability of the CS membranes and reduced the overall mass loss. The CNF (D) filler provided the lowest (4.23×10^{-5} cm^2 s^{-1}) EtOH permeability of the respective membrane, which is in the same range as that of the commercial membrane (3.47×10^{-5} cm^2 s^{-1}). The most significant improvement (~78%) in power density at 80 °C was observed for the CS membrane with neat CNF compared to the commercial Fumatech membrane (62.4 mW cm^{-2} vs. 35.1 mW cm^{-2}). Fuel cell tests showed that all CS-based anion exchange membranes (AEMs) exhibited higher maximum power densities than the commercial AEMs at 25 °C and 60 °C with humidified or non-humidified oxygen, demonstrating their potential for low-temperature direct ethanol fuel cell (DEFC) applications.

Keywords: chitosan; cellulose nanofibrils; anion exchange membrane; direct alkaline alcohol fuel cell

1. Introduction

Fuel cells are an advantageous, clean, and efficient technology for power generation. The alkaline medium of anion exchange membrane fuel cells (AEMFCs) offers advantages in cost, stability, and durability, due primarily to the use of non-precious metal catalysts, as well as ease of handling, storage, and transportation of liquid fuels, which can facilitate mature commercialization compared to gaseous hydrogen. One of the device-level challenges in alkaline fuel cells is membrane selection. Membranes in the form of solid polymer electrolytes are a crucial segment of AEMFCs. They consist of a hydrophobic polymer backbone with positive hydrophilic groups that function according to the Donnan exclusion principle [1] and serve as a barrier between the anode and cathode while conducting

ions and suppressing the passage of electrons [2,3]. The first anion exchange membrane (AEM), developed by the Tokuyama Corporation (Japan) consists of polychloroprene as a polymer backbone crosslinked with divinylbenzene and containing quaternary ammonium functional groups such as tri-ethylamine [4]. Since then, various types of AEMs have been developed, such as poly(vinyl alcohol) (PVA) [5], poly(ether ketone) [6], poly(ether ether ketone) (PEEK) [7], poly(ether sulfone) (PES) [8], poly(vinylidene fluoride) (PVDF) [9], and polyetherimide (PEI) [10]. As can be seen, the field of AEMs is covered commercially entirely by the fully synthetic membrane types. In contrast, biopolymer-based materials intended for such use have yet to be developed to meet the stringent requirements for commercial use.

Chitosan (CS) has been introduced into fuel cell research as an environmentally friendly, abundant biopolymer. This amino polysaccharide, which consists of randomly arranged units of glucosamine and N-acetylglucosamine linked by a β-1,4 bond, is derived from the biopolymer chitin by a deacetylation process. As a polysaccharide, it provides an abundance of hydroxyl (OH) groups with excellent ability to H-bond during the drying process, allowing the formation of microspheres, fibers, films, and membranes. CS is weakly alkaline due to the glucosamine monomer containing a primary NH_2 group with a pKa of about 6.5 [11], which is protonated at low pH values, promoting solubility and film formation of CS in acidic solutions and stability at neutral to high pH values. The latter makes it highly resistant in alkali-rich media, such as those found in AEMFCs. However, its brittleness requires blending with another polymer or doping with fillers to reduce cracking and improve handling. The ionic conductivity, fuel permeability, and ion exchange capacity, as well as the mechanical and thermal properties of AEMs, can be improved by modifying biopolymers, or by introducing fillers and forming composites [12]. To improve the properties of biopolymer membranes, various fillers have been incorporated into the chitosan matrix, including multi-walled carbon nanotubes [13], functionalized MXene [14], N-doped graphene oxide [14,15], and a composite of quaternized cellulose nanocrystals and quaternized PPO [16].

In our previous work [15,17,18], we demonstrated the ability of CS membranes with modified graphene oxide (GO) as inorganic fillers to improve the cell performance of AEMFCs. In this article, we use the organosilane reagent to modify cellulose nanofibrils (CNFs), and use them as quaternary ammonium-bearing fillers, which is the novelty of this work. We hypothesize that the combination of CS with (modified) CNF fillers will bring numerous advantages to CS membranes in terms of mechanical and thermal enhancement, ionic conduction, and, ultimately, an increase in power density while preventing EtOH crossover. With extensive physicochemical and morphological characterization, we seek to elucidate the effects of the CNF filler and its modified counterpart on composite properties and overall performance in a laboratory-scale fuel cell assembly.

2. Materials and Methods

2.1. Materials

Chitosan (CS, degree of deacetylation: 90%, molecular weight: 50–100 kDa, particle size < 200 μm) was purchased from Biolog Heppe GmbH, Landsberg, Germany. Nanofibrillated cellulose (CNF, ~3 wt.% water dispersion) was purchased from the University of Maine, Orono, ME, USA. Dimethyloctadecyl[3-(trimethoxysilyl)propyl]ammonium chloride (DMAOP, 42 wt.% solution in methanol), magnesium hydroxide $Mg(OH)_2$ nanopowder (<100 nm particle size (laser PSA), 99.8% trace metals basis), sodium hydroxide (NaOH), hydrochloric acid (HCl), ethanol (EtOH), and potassium hydroxide (KOH) were purchased from and manufactured by Sigma Aldrich, Darmstadt, Germany, and used without further purification. All the reagents and solvents were analytical grade and used as received. The Fumasep Fumatech FAA-3-50 membrane was obtained from Fumatech BWT GmbH, Bietigheim-Bissingen, Germany.

2.2. CNF Quaternization

Modification of CNF by the DMAOP reagent was performed according to the following procedure: component A (10 g 3 wt.% CNF in 40 mL methanol, 30 min mixing, room temperature) was mixed with component B (25 mL DMAOP reagent was added to 100 mL Milli-Q water, 2 h mixing, room temperature, pH adjusted to 2, 4, 6, 8, or 10). The resulting mixtures were stirred additionally for 24 h, and the final dispersion was centrifuged (9000 min^{-1}, 10 min), and the precipitate was washed thoroughly with Milli-Q water by centrifugation at 9000 min^{-1}, freeze dried, and, finally, heated in an oven at 110, 130, or 150 °C for 1, 2, or 3 h. The resulting modified CNF was used as the final product and designated CNF(D).

2.3. Characterization of CNF

The attenuated total reflectance-Fourier transform infrared spectroscopy (ATR-FTIR) spectra were recorded using a Perkin-Elmer Spectrum One FTIR spectrometer (Waltham, MA, USA) with a Golden Gate ATR attachment and a diamond crystal. The transmission spectra were recorded in the range 4000 to 650 cm^{-1}. Each spectrum obtained is the average of 16 spectra recorded at a resolution of 4 cm^{-1}. The Nuclear Magnetic Resonance (NMR) spectra were recorded using the NMR recording technique on solid samples on a Bruker AVANCE NEO 400 MHz NMR spectrometer (Bruker, Billerica, MA, USA) with a 4 mm CP-MAS probe and TopSpin 4.0.9 software. The Larmor frequencies of the 13C and 29Si nuclei were 100.63 and 79.49 MHz, respectively. The chemical shifts of the 13C and 29Si NMR nuclei are given relative to the TMS Standard (δ 0.0 ppm). The samples were rotated at 15,000 Hz for all measurements. The zeta potential (ζ) was determined by the dynamic light scattering (DLS) method at 25 °C at a 90° angle with a Zetasizer Nano ZS90 (Malvern Panalytical Ltd., Worcestershire, United Kingdom) system using capillary cells. The combined TGA-DSC analysis was performed using a Mettler Toledo Thermogravimetric Analyser/Differential Scanning Calorimeter (TGA/DSC1) (Mettler-Toledo International Inc., Greifensee, Switzerland) thermal analyzer. The test temperature range was between 30 and 700 °C with a heating step of 10 K/min under an N_2 atmosphere. The morphology of the CNF was imaged by Field Emission Scanning Electron Microscopy (FE-SEM) on a Carl Zeiss FE-SEM SUPRA 35 VP electron microscope (Carl Zeiss, Yena, Germany) at a 1 kV accelerating voltage and a working distance of about 4.5 mm. The samples were mounted on an aluminum support and sputtered with a 10 nm thick palladium layer.

2.4. Membrane Preparation

The neat CS membranes were prepared as described previously [17,19]. Briefly, the CS was dissolved in Milli-Q water, while the pH was adjusted to 2 (with 1 M HCl), and a 1% wt.% aqueous $Mg(OH)_2$ dispersion was added until a pH of 6 was reached. The obtained dispersion was diluted to the final amount of 1 wt.% CS and 12.6 mM $Mg(OH)_2$, and 25 mL was poured into a Petri dish with a diameter of 8.5 cm. After drying in an oven at 60 °C for 24 h, the membrane was neutralized in 1 M NaOH with shaking for 30 min at room temperature, then washed with Milli-Q water and air dried. For the preparation of the CS-CNF composite membranes, the selected amounts of CNF or CNF(D) fillers were added to a CS-Mg $(OH)_2$ dispersion. The names of the membranes prepared with the corresponding ingredients are listed below in Table 1.

Table 1. Membrane sample names and corresponding filler content.

Sample	m_{CNF} (g)	$m_{CNF(D)}$ (g)
CS	0	0
CS-CNF	0.375	0
CS-CNF(D)	0	0.125
CS-CNF-CNF(D)	0.375	0.125
CS-CNF-$CNF(D)_H$	0.375	0.375

2.5. Membrane Characterization

The ATR-FTIR spectra were recorded in the same manner as for the CNF fillers. The XRD spectra of the membranes were recorded using a Bruker Siemens D5005 X-ray diffractometer (Bruker, Billerica, MA, USA). The reflections at 2θ were observed in the range of 2° to 70°, with an increment of 0.04° when using Cu-Kα radiation at a voltage of 40 kV and a current of 40 mA. The relative degree of crystallinity of the polymer phase was determined from the ratio between the integrated area of the crystal peaks and the total integrated area of the diffraction spectrum [20]. SEM imaging was performed using an FEI Sirion 400 NC (Sirion 400 NC, FEI, Hillsboro, OR, USA) with an INCA 350 EDS electron microscope with 9 kV accelerating voltage from a working distance of about 5–6.9 mm. Prior to analysis, the samples were sputtered with a 10 nm thick gold layer. The thermal stability of the membranes was determined by TGA analysis using a Perkin-Elmer TGA 8000 thermogravimetric analyzer (Waltham, MA, USA). The temperature range of the test was between 30 °C and 700 °C, with a heating step of 10 K/min in a N_2 atmosphere. The mechanical properties of the membranes were determined by tensile testing using the Shimadzu Europa GmbH AG-X plus 10 kN instrument (Düsseldorf, Germany). The membrane samples were cut into a rectangular shape of 1 × 2 cm, the distance between the clamps was 20 mm, and the tension speed was set to 1 mm/min. The passage of EtOH through the CS membranes was measured in temperature-controlled diffusion cells at 25 ± 1 °C [17,18]. The diffusion cells consisted of two glass chambers (a chamber with a solution source—chamber A and a receiving chamber—chamber B). Each of the chambers holds 25 mL of solution, and between the chambers is a membrane in a plastic holder separating the chambers. Before each experiment, the membrane was soaked in distilled water for 24 h to avoid the influence of base release from the membrane to the solution. Compartment A was filled with 25 mL of 2 M EtOH in a 6 M KOH solution. Compartment B was filled with 25 mL of 6 M KOH solution. The membrane sample had an effective surface area of 7.03 cm^2. The concentration of EtOH flowing through was determined by conductivity measurements taken with a conductometer in chamber B at different time intervals. The EtOH transfer, P (cm^2 s^{-1}), was calculated according to Equation (1):

$$P\left(\frac{cm^2}{s}\right) = \frac{(C_B - C_{B0})}{(t - t_0)} \cdot \frac{V_B \cdot l}{A \cdot C_{A0}} \quad (1)$$

where C_{A0} is the initial concentration of EtOH in the solution source compartment (compartment A), and V_B is the KOH volume in the receiving compartment (compartment B), A is the area of the membrane sample, and l is the thickness of the membrane sample. The KOH uptake and swelling ratio tests of the CS membranes were performed in 6 M KOH at 60 °C. The dry membranes were cut to a size of 1 cm × 1 cm and weighed, and their mass (W_{dry}), surface area (A_{dry}), and thickness (T_{dry}) were recorded. The membranes were then immersed in an alkaline medium, 6 M KOH, at 60 °C. After immersion, the excess alkali solution on the surface of the membranes was removed with a paper towel and weighed ($Wwet$), and their dimension-based surface area (A_{wet}) and thickness (T_{wet}) were measured at room temperature. The alkali uptake (AU) and through-plane (SR_{Tp}) and in-plane (SR_{Ip}) swelling ratios were determined after 24 h using the following equations:

$$AU = \frac{W_{wet} - W_{dry}}{W_{dry}} \cdot 100\ \% \quad (2)$$

$$SR_{Through-plane} = \frac{T_{wet} - T_{dry}}{T_{dry}} \cdot 100\ \% \quad (3)$$

$$SR_{In-plane} = \frac{A_{wet} - A_{dry}}{A_{dry}} \cdot 100\ \% \quad (4)$$

The ion exchange capacity (*IEC*) values were determined by potentiometric titration. The anion exchange membranes in OH^- form (pre-dipped in 1 M NaOH) were then immersed in 40 mL of 0.01 M HCl for 24 h. These solutions were then titrated with a standard solution of 0.1 M KOH. Before immersing the membrane and performing the titration, we first cut and weighed about 0.02 g of membrane sample and noted its exact mass. After titration, the IEC parameter was calculated, and expressed as the milliequivalent (meq) of OH^- ions per gram of dry membrane using the following Equation (5):

$$IEC\left(\frac{meq}{g}\right) = \frac{(V_{blank} - V_{membrane}) \cdot c_{HCl}}{m_{dry\ membrane}} \quad (5)$$

where V_{blank} and $V_{membrane}$ represent the volumes (mL) of 0.1 M KOH solution consumed for the blank and sample membranes, respectively. c_{HCl} represents the molar concentration (mol/L) of the HCl solution and $m_{dry\ membrane}$ represents the mass of the dry membrane samples (g). The ionic conductivity of the membranes was measured in Milli-Q water in the frequency range from 125 Hz to 10^6 Hz using two-electrode AC impedance spectroscopy, which was used to analyze the impedance response of the membrane sample and to determine the resistance. Prior to the measurement, the membrane sample was cut to a size of 1×3 cm^2 and soaked in Milli-Q water for 24 h. The ionic conductivity of the membranes was calculated using Equation (6):

$$\sigma\left(\frac{mS}{cm}\right) = \frac{L}{R \cdot S} \quad (6)$$

where L (cm) is the distance between the two electrodes, and S (cm^2) is the area (28.28 mm^2) of the sample subjected to measurements. The resistance of the membrane is expressed by R (Ω).

2.6. Cell Performance Test

The cell performance test for the obtained membranes and the reference membrane Fumatech FAA-3-50 was performed in an optimized test setup [21] as follows. The membranes were first immersed in 1 M KOH for 24 h and then washed thoroughly with ultrapure water to remove the excess KOH. The electrodes were prepared by depositing the ink from the anode/cathode catalysts in 2-propanol (99.9%) and ultrapure water (7:3) and a commercial ionomer onto the GDL using a Sono-Tek ultrasonic spray coater. The cathode was prepared by spraying a commercial PtRu/C catalyst (platinum 40%, ruthenium 20% on carbon black, HiSPEC® 10000) on carbon paper (Sigracet 29 BC, fuel cell store, 0.235 mm thick), and the PdNiBi/C catalyst ink [22] was applied on carbon cloth (ELAT-hydrophobic plain cloth, fuel cell store, 0.406 mm thick), which constituted the anode. Electrodes with a cathode metal loading of 0.5 mg cm^{-2} and an anode metal loading of 0.75 mg cm^{-2} were obtained with this preparation. The MEA consisted of the mentioned electrodes and the membrane, a sample of CS and (un)modified CNF or the commercial membrane, and was used in a self-designed alkaline direct ethanol fuel cell [21]. The operating temperature and concentration of the supplied fuel were varied. Pure oxygen was fed to the fuel cell at a constant flow of 25 mL min^{-1} at the cathode, and a mixture of 1 M ethanol and 1 M KOH or a mixture of 3 M EtOH and 5 M KOH with a constant flow of 5 mL min^{-1} at the anode. The measurements were performed at room temperature, 60 °C and 80 °C. The polarization curves (I-V diagram) were obtained using a Zahner IM6ex potentiostat. The results were plotted as an I-V diagram with additional representation of the power density.

3. Results and Discussion

3.1. CNF Quaternization

The first step of the reaction between CNF and the silane reagent DMAOP in the presence of water consists of the hydrolysis of the alkoxy groups of the latter to form silanols (Figure 1a). The acid-catalyzed hydrolysis of silanes allows the formation of silanol groups,

reduces self-condensation reactions between the silanol groups, and keeps the hydrolyzed intermediates stable. In contrast, under basic conditions, the condensation reaction begins as soon as the hydrolysis reaction of silanes starts, leading to rapid consumption of silanol groups by the self-condensation reaction, and the formation of three-dimensional structures with high M_w [23].

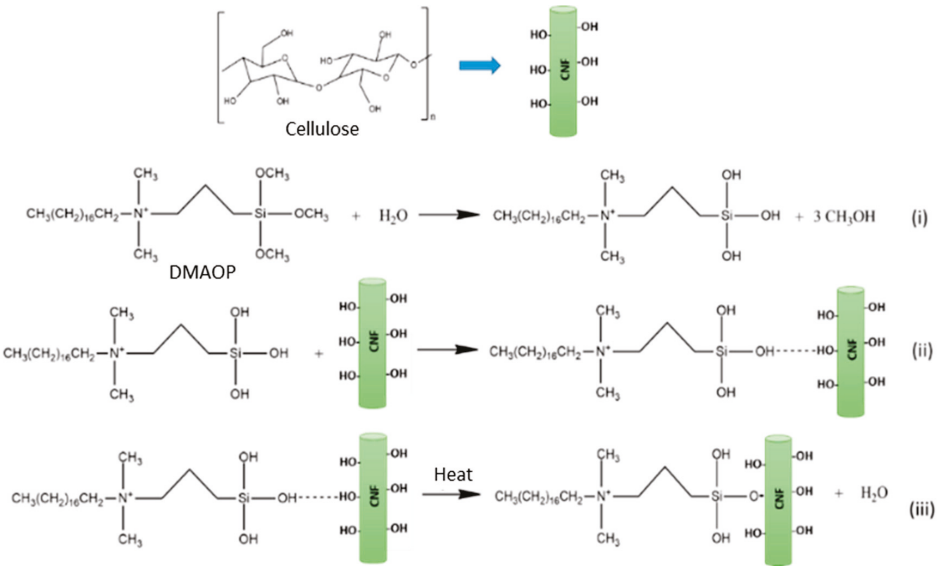

(**a**)

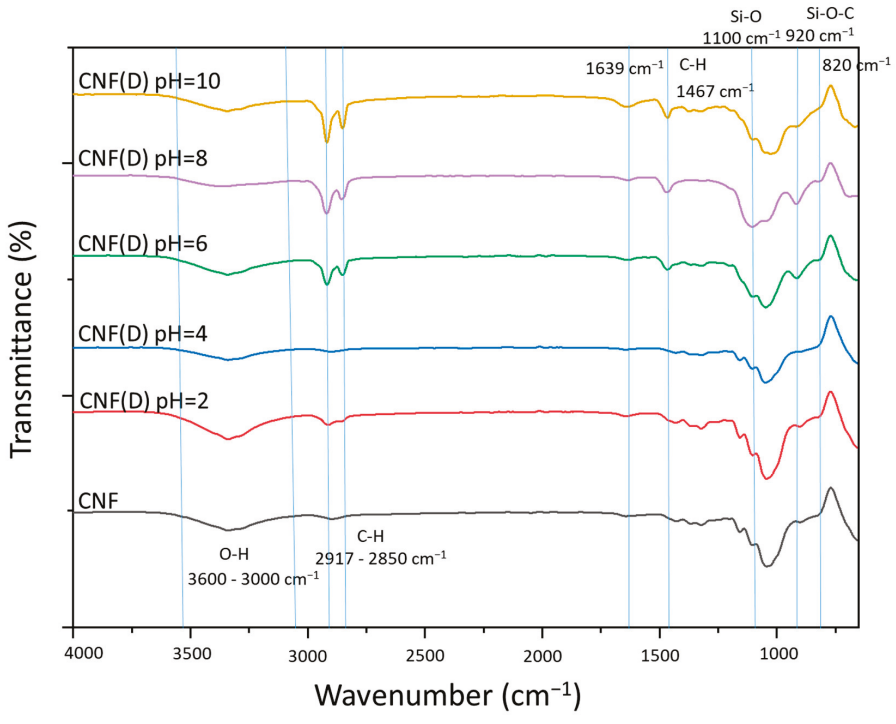

(**b**)

Figure 1. (**a**) Tentative representation of the reaction between cellulose nanofibrils (CNF) and the Dimethyloctadecyl[3-(trimethoxysilyl)propyl]ammonium chloride (DMAOP) reagent and (**b**) Attenuated total reflectance-Fourier transform infrared spectroscopy (ATR-FTIR) spectral lines for the reference (CNF) and modified quaternized CNFs (CNF(D)) at the pH 2–10.

To demonstrate the pH dependence of the modification process, the ATR-FTIR spectral lines (Figure 1b) for neat and modified CNF were examined at different pH values. The spectral line for the reference CNF shows a broad band at 3600–3000 cm^{-1} (O-H stretching) and ~2900 cm^{-1} (symmetric and asymmetric C-H stretching), 1000–1070 cm^{-1} is the region of primary (~1030 cm^{-1}) and secondary (~1055 cm^{-1}) alcohols, and the small band ~900 cm^{-1} was assigned to ether (C-O-C stretching) [24]. The pronounced band at ~2850 cm^{-1} appeared in the samples after the reaction with DMAOP and is associated with the presence of a long nonpolar alkyl chain on the reagent. The weak peak at 1639 cm^{-1} illustrates the vibrations of the remaining absorbed water [25]. The increased intensity of this peak, especially at high pH, is consistent with the Si-OH form of the DMAOP reagent, and suggests its interaction with the OH groups on cellulose via H-bonds [26]. The peak at a wavelength of about 1467 cm^{-1} is associated with the quaternary ammonium group in the DMAOP molecule, and can also be assigned to the C-H bond, illustrating the bending of the alkyl groups attached to the quaternary ammonium [25,27–29]. The characteristic peaks for Si-O alkoxysilanes can be observed at about 1090 cm^{-1} [30], and the peaks at about 1100 and 820 cm^{-1} show the vibrations of symmetric and asymmetric Si-O-Si stretching [31]. The band at 1820 cm^{-1} is observed in the products at reactions pH = 6 and pH = 8, indicating that the DMAOP reagent has self-polymerized and formed Si-O-Si bonds. The peaks in the 950–700 cm^{-1} range consisted of Si-C, C-O, and Si-O bonds, and, in combination, these peaks represent the Si-O-C bond [32]. The peak at about 920 cm^{-1} is most prominent in the samples obtained at pH = 6 and pH = 8, indicating the formation of Si-O-C bonds between the CNF and DMAOP.

The ^{13}C NMR data of reference CNF (Figure 2) show a resonance signal between 62 and 104 ppm, which can be attributed to the different forms of C atoms in the cellulose monomer unit (C1-C6).

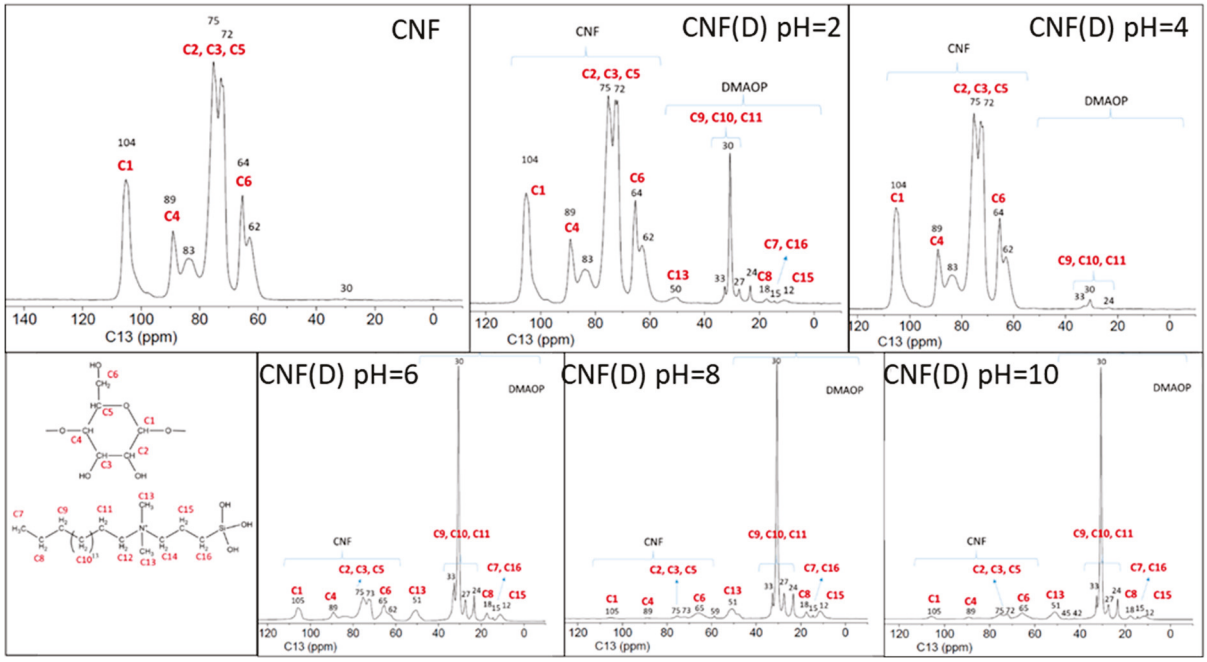

Figure 2. Carbon-13 (C13) nuclear magnetic resonance (^{13}C NMR) spectra of reference CNF and CNF(D) at different pH reaction conditions (2, 4, 6, 8 and 10).

The spectra of the modified (CNF(D)) samples obtained at different pH conditions show additional resonance signals in the range of 12 to 33 ppm, which can be attributed to C atoms in the DMAOP reagent (C7-C16). It should be emphasized that the analysis was performed after intensive repeated washing of the reaction products with water by centrifugation, which presumably prevents the presence of the DMAOP reagent in free

form. Moreover, the peaks characteristic of the C atoms in the DMAOP reagent are more pronounced for the product at reactions pH = 6, pH = 8, and pH = 10, while the peaks for the product obtained under acidic conditions are less pronounced, especially at pH = 4, where only a fleeting signal is observed for the three carbon atoms present in the DMAOP. Based on the NMR results, we could not determine the type of binding (electrostatic/covalent) of DMAOP to CNF. Next, we performed additional washing with ethanol, and again recorded the ^{13}C NMR spectra of the samples prepared at pH = 4 and pH = 8 (Figure 3), as they differed the most. Therefore, we were interested in whether the CNF(D) sample was stable after washing with ethanol, which is present in ethanol fuel cells, thus providing a modified CNF that is stable under fuel cell operating conditions. The detected carbon signals in the DMAOP reagent between 12 ppm and 52 ppm on the CNF product (reaction pH = 8) [33] indicated persistent binding between the CNF and DMAOP at this pH.

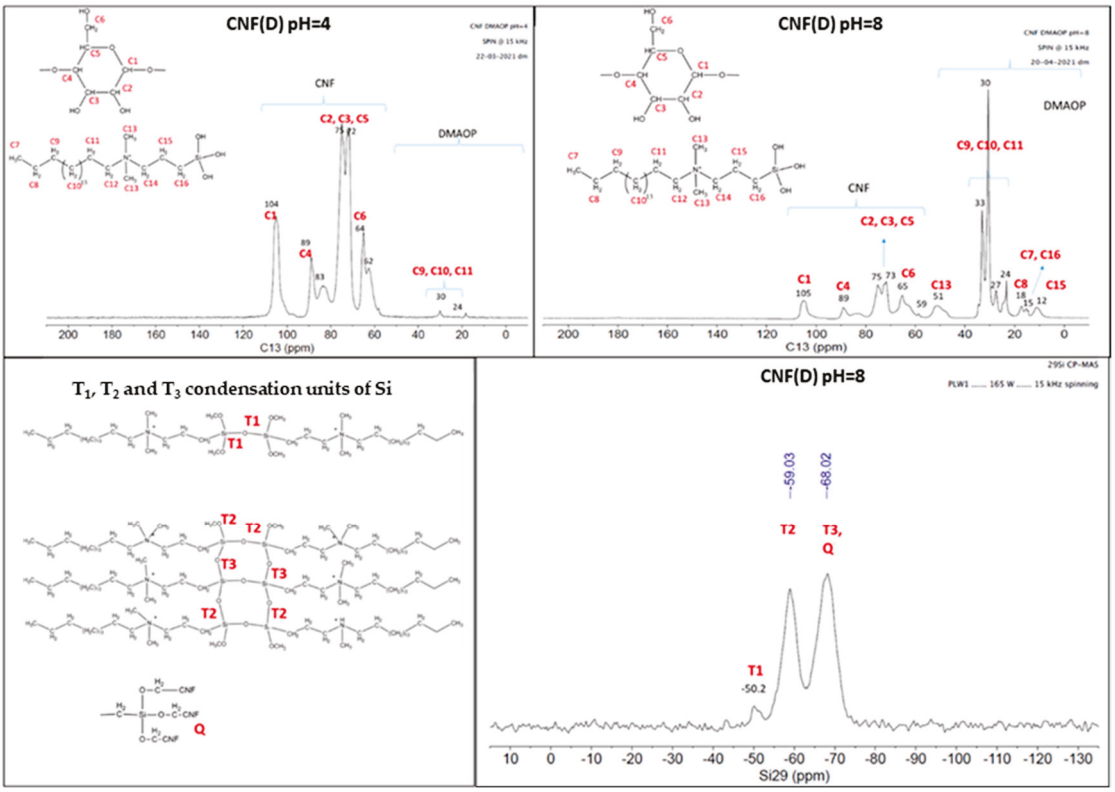

Figure 3. ^{13}C NMR and ^{29}Si NMR spectra of CNF(D) samples at pH = 4 and pH = 8 reaction conditions.

Examination of the ^{13}C NMR spectra for the sample after the reaction between the CNF and DMAOP at reaction conditions of pH = 4 and pH = 8 after extensive washing of the product with ethanol and water revealed that the reagent DMAOP was absent in the product obtained in the reaction of pH = 4, while it was readily detectable in the product obtained at the reaction of pH = 8. The ^{29}Si NMR spectrum (Figure 3) for the sample CNF(D) pH = 8 gives us information about the bonding of the Si atoms in the product, and we observed three different resonance signals between −50 ppm and −68 ppm due to different Si units formed during the condensation of the reagent.

The presence of a positive charge on the modified CNF was investigated further based on the ζ-potential measured in the pH range of 2–12 (Figure 4). CNF itself has an isoelectric point at a low pH (~4), with negative ζ-potential values at a pH of >4 due to deprotonation of the carboxyl group of the remaining hemicellulose residue from CNF processing [34,35]. The positive charge of the CNF(D) samples was caused by the quaternary ammonium group of the DMAOP reagent, as this group carries a permanent positive charge. Thus,

the results confirmed the presence of a permanent positive charge in the reaction product obtained at pH = 6 to pH = 10, as evidenced by the ATR-FTIR and NMR data.

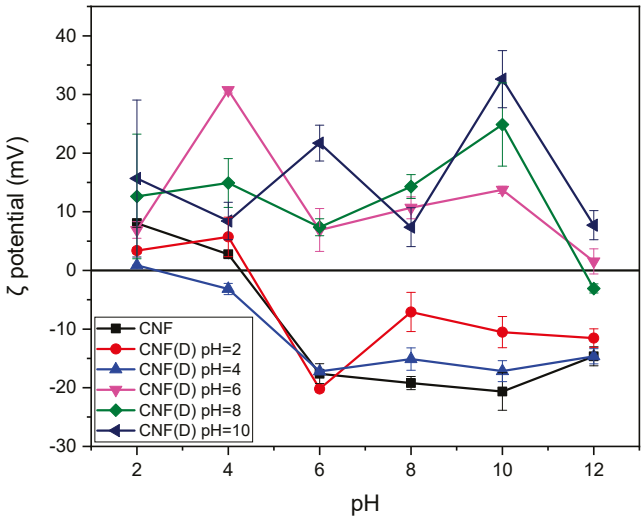

Figure 4. ζ potential values (mV) for CNF and CNF(D) at different pH reaction conditions (2, 4, 6, 8, and 10).

The temperature stability of the CNF(D) products was evaluated by TGA and DSC analysis (Figure 5, Table 2). For all the samples tested, the observed mass loss in the temperature range from 30 to 180 °C was due to evaporation of the absorbed water. The degradation of CNF typically occurred in a single step in the range of 245–380 °C with a mass loss of about 75% [36], while the degradation of the DMAOP reagent occurred in two steps, namely, in the range of 205–265 °C with a mass loss of 14% associated with the decomposition of the quaternary ammonium groups, and in the range of 370–525 °C with a mass loss of 37% when pyrolysis occurred of the long, nonpolar alkyl chain [37]. For the CNF(D) pH = 4 sample, one-step degradation was observed in the range of 255–370 °C with a mass loss of 71%, which is consistent with the CNF sample, and indicates unsuccessful modification. The CNF(D) pH = 8 sample showed three mass loss zones, representing a one-step degradation of the CNF component in the 330–420 °C range, with 37% mass loss and a two-step degradation of the DMAOP component in the 205–245 °C range with 11% mass loss, and in the 430–510 °C range with 12% mass loss. Moreover, the CNF(D) sample obtained at pH = 8 degraded at a higher temperature than the pure CNF reference sample, which is a clear indication of improved stability after modification. In the DSC thermogram of the neat CNF sample, an endothermic peak can be seen at about 350 °C, which can be attributed to the degradation of CNF due to the breaking of glycosidic bonds, leading to the depolymerization of the cellulose. In comparison, the CNF(D) pH = 8 sample showed an additional endothermic peak at about 230 °C, which was also observed for the DMAOP pH = 4 and DMAOP pH = 8 samples and belongs to the DMAOP reagent, representing the decomposition of the silane [38] and disintegration of the DMAOP polymer network (breaking of the Si-O-Si and S-O-C bonds). The indicated transition was not observed in the CNF(D) pH = 4 and CNF reference samples, confirming the previous findings for unsuccessful modification.

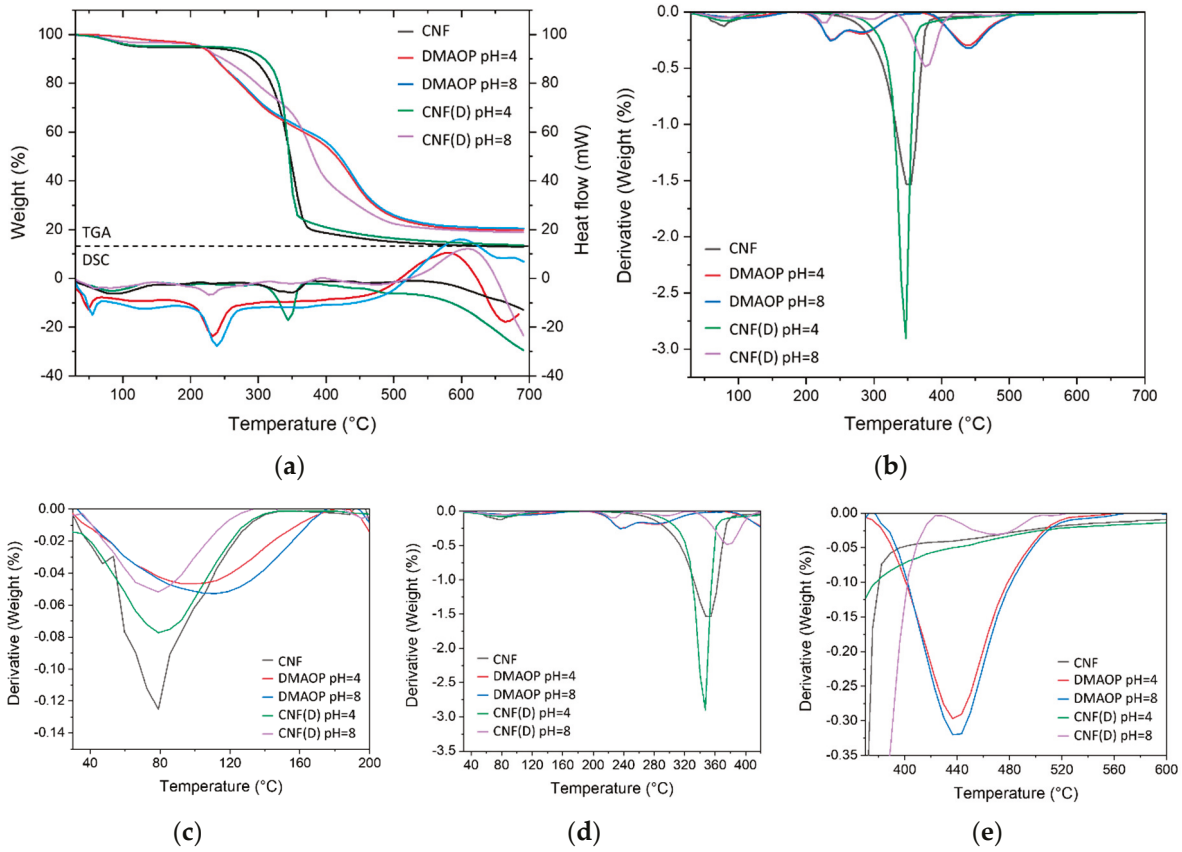

Figure 5. (**a**) Thermogravimetric Analysis (TGA) and Differential Scanning Calorimetry (DSC) curves, (**b**) derivation of the TGA curve with approximate areas (**c**–**e**), for samples of the reference CNF, the hydrolyzed reagent DMAOP at pH = 4 and pH = 8, and the product CNF(D) at pH = 4 and pH = 8.

Table 2. Temperature areas and percentages of mass loss obtained by TGA analysis for samples of the reference CNF, the hydrolyzed reagent DMAOP at pH = 4 and pH = 8, and the product CNF(D) at pH = 4 and pH = 8.

Sample	T1 (°C)			T2 (°C)			T3 (°C)			Δy1 (%)	Δy2 (%)	Δy3 (%)	Δy (%)
	$T1_s$	$T1_p$	$T1_e$	$T2_s$	$T2_p$	$T2_e$	$T3_s$	$T3_p$	$T3_e$				
CNF	30	80	145	245	350	380	/	/	/	5.2	74.7	/	87.2
DMAOP pH = 4	30	105	175	205	235	265	370	440	525	3.0	14.4	36.6	80.3
DMAOP pH = 8	30	110	175	205	235	265	370	440	525	2.9	14.2	37.0	79.3
CNF(D) pH = 4	30	80	145	255	345	370	/	/	/	4.6	71.2	/	86.2
CNF(D) pH = 8	30	80	180	205 330	230 375	245 420	430	470	510	3.1	10.9 37.2	12.0	80.8

The effect of DMAOP modification on CNF morphology was examined using FE-SEM imaging (Figure 6). A large heterogeneity of the CNF sample was observed, as well as the presence of aggregates formed by intense hydrogen bonding during the drying process, grouping CNF fibrils with a fiber diameter of ~50 nm and a length of 100 µm into larger clusters. In the image of the CNF(D) pH = 8 product, particles of about 10 µm can be seen that are absent in the CNF(D) pH = 4 product, and we assumed that these are aggregates of the DMAOP reagent. As mentioned earlier, the hydrolysis of the DMAOP reagent is slower under acidic conditions than under alkaline conditions. This is why, at pH = 8, the DMAOP reagent not only reacts with cellulose but also polymerizes with itself to form aggregates of the polymerized DMAOP reagent, which explains their detection on the SEM images. Since

the manufacturing process of the CNF(D) product involves a drying step, redispersion is required when this product is incorporated into membranes. Redispersion is somewhat limited, due to the H-bonds formed between the CNF(D) product. In the SEM images of redispersed CNF(D) pH = 8, particles can still be seen that are presumably polymerized clumps of the DMAOP reagent.

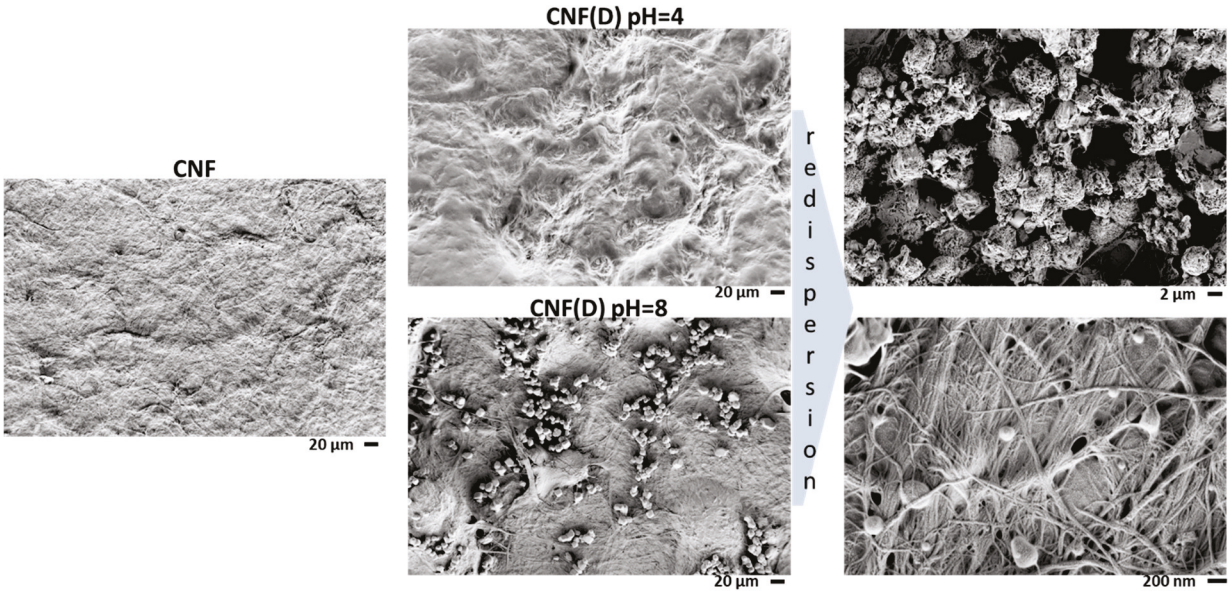

Figure 6. Field Emission Scanning Electron Microscopy (FE-SEM) images of CNF and CNF(D) at pH = 4 and pH = 8 reaction conditions before and after redispersion in Milli-Q water.

Based on the results, the efficient modification of CNF by the DMAOP reagent was confirmed for the pH = 8 reaction condition, so we selected the CNF(D) pH = 8 sample as the optimal product and included it in further CS membranes.

3.2. Characterization of CS Membranes: Effect of Fillers on Membrane Properties

Figure 7a shows the collected ATR-FTIR spectra of CS membranes with CNF and CNF(D) fillers. In addition to the peaks attributed to CNF and CNF(D) fillers, as described in Section 3.1 CNF Quaternization, observed peaks were attributed to the CS polymer: a broad peak from 3650–3250 cm^{-1} attributed to O-H stretching vibrations, with three well-defined peaks attributed to free OH groups (3450 cm^{-1}), N-H stretching (3370 cm^{-1}), and H-bonded O-H stretching (3300 cm^{-1}); the peak at ~2900 cm^{-1} was attributed to C-H stretching, that at 1647 cm^{-1} to C=O vibrations in the amide group, that at 1590 cm^{-1} to N-H vibrations, that at 1144 cm^{-1} to asymmetric stretching of the C-O-C bridge, and that at 1150 cm^{-1} to the skeletal vibration involving C-O stretching [19].

In the case of the neat CS, as well as the CS-CNF membrane, the peak at 2900 cm^{-1} is single, and attributed to the C-H stretching of the atoms in the polysaccharide matrix, and in the case of the presence of CNF(D) in the CS composite membrane, a double sharp peak occurred, which was attributed to the long nonpolar tail of the DMAOP molecule, confirming the presence of modified CNF in the CS membranes.

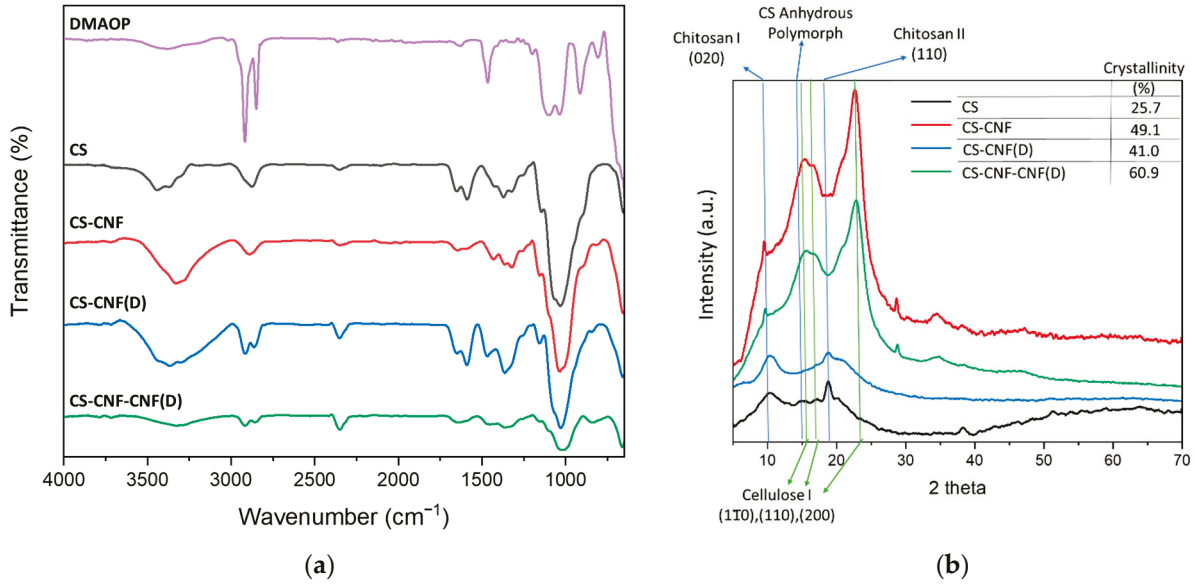

Figure 7. (**a**) ATR-FTIR spectral lines of CS membranes, including CNF(D) and corresponding reference membranes, and (**b**) X-ray diffractograms (XRD) of CS membranes containing CNF and CNF(D) fillers.

Figure 7b shows the XRD diffractograms of the neat CS and the membranes with (modified) CNF as a filler. Since all the membranes contained CS, sharp peaks were observed in all the samples at about 2θ = 10° (020) and 2θ = 19° (110), which are characteristic of the crystal structure of the hydrated crystal of CS I and the anhydrous CS II, respectively. The broad peak between 2θ = 13° and 19° was due to the amorphous structure of the CS membrane. The calculated crystallinity index of the neat CS membrane was 25.7%. By adding fillers, we were able to increase the crystallinity index of the CS membranes. Zhang et al. [39] reported an increase in the crystallinity of CS membranes with increasing the filler content of the modified TEMPO-CNF from 22% for CS membranes to 87%. We observed an approximately twofold increase in the crystallinity of CS membranes when CNF fillers were added, and an additional increase (up to 60.9%) when a mixture of CNF and CNF(D) fillers was added, indicating a compatibilization of the fillers with the CS matrix, due mainly to H-bonds between the two polysaccharide components. For all CS membranes containing CNF, the XRD pattern of crystalline cellulose polymorph I is observed with diffraction peaks at 2θ at about 15°, 17°, and 23.5°, belonging to the (110), (110), and (200) planes, respectively (Gong et al. 2017). For the CS-CNF (D) sample, which contained only the modified CNF(D) in addition to CS, we did not observe the diffraction peaks characteristic of cellulose I, but a broad amorphous peak between 15° and 25°, assuming that the DMAOP treatment affects the crystallinity of the CNF itself.

Figure 8 shows an SEM image of the homogeneous and smooth CS membrane with no visible pores, whereas the CS-CNF membrane contains both agglomerates of CNF fibers and individual intertwined fibers, and also has desiccation cracks on the top surface that allow a view into the depth and reveal a network of intertwined CNF fibers. The membrane CS-CNF (D) shows a strong agglomeration and non-uniform distribution of the CNF(D) filler in the CS matrix of the membrane, as well as clusters (< μm in size) on the fibers, which are presumably the polymerized reagent DMAOP, as also observed by SEM analysis of the CNF(D) fillers themselves (Figure 6).

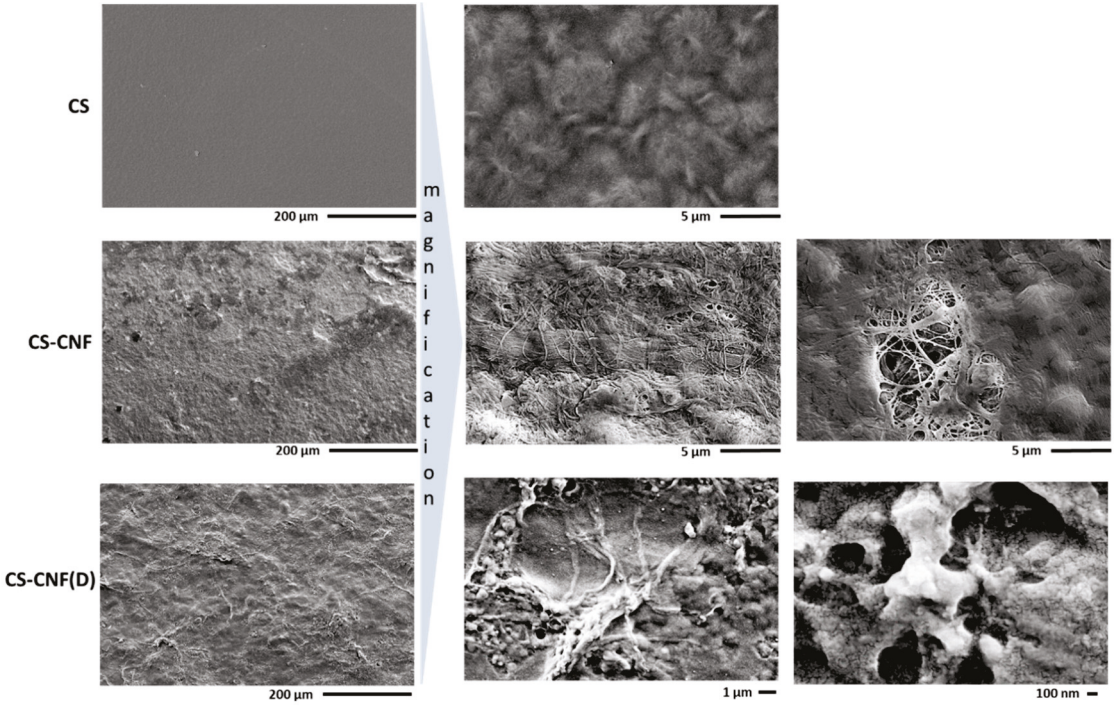

Figure 8. FE-SEM images of CS membranes with CNF and CNF(D) fillers.

3.3. Thermal Stability of the Membranes

Examining the thermographs (Figure 9, Table 3) of CS membranes with CNF and CNF(D) fillers, we can see three ranges of mass loss, namely, 30–135 °C (T1) due to water evaporation; 180–400 °C (T2) due to the degradation of the polymer network in CS, CNF, and modified CNF(D) components, including the degradation of glycosidic bonds and glucopyranose units [40]; and 360–520 °C (T3), due to the degradation of the CNF(D) filler. The addition of fillers to the CS membrane leads to a change in the initial temperature of degradation (T_s) and the peak temperature of degradation (T_p), as well as a change in mass loss. The addition of neat CNF into the CS membrane resulted in a 15% lower mass loss over the entire temperature range from 30 to 700 °C (Δy) compared to the reference CS membrane. The addition of the CNF filler improved the thermal stability of the CS membranes, as we found that the membranes with this filler reached the peak of thermal decomposition at a higher temperature (300–305 °C) than the reference CS membrane (283 °C). Compared to the CS membrane, the total mass loss of the membranes with this filler also decreased (from 85.7% in CS to 72.6% in CS-CNF). The addition of the CNF(D) filler led to a 4% increase in mass loss, which can be attributed to the instability of the quaternary ammonium groups of the modified filler. As with the CNF(D) filler itself (Figure 5), we also observed an additional range of mass loss at $T3_p$ around 430 °C for CS membranes with CNF(D) filler, which represents the degradation of the CNF(D) filler. The thermal stability of polymers is related to their degree of crystallinity, and usually a higher degree of crystallinity leads to better thermal stability. The CS-CNF and CS-CNF-CNF (D) membranes were found to have higher crystallinity compared to the reference CS membrane, which explains the higher degradation temperature peaks for these membranes.

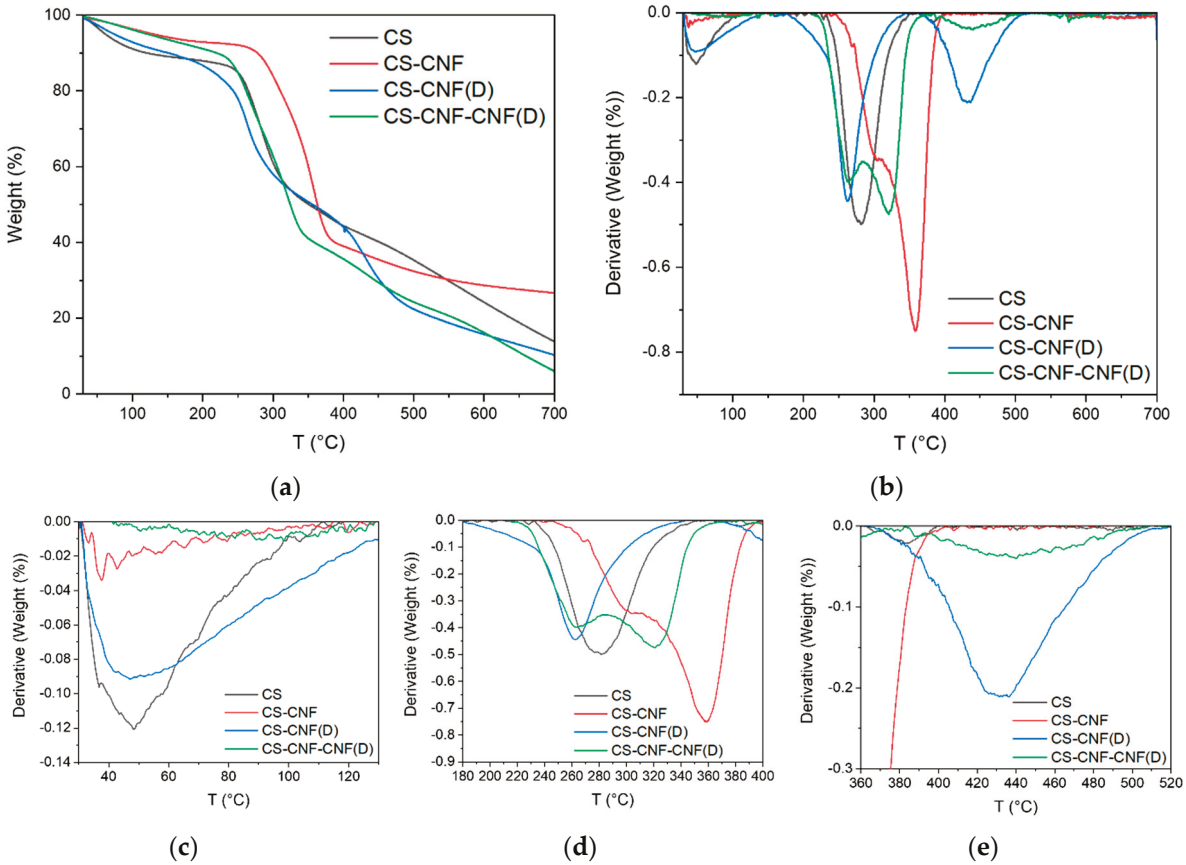

Figure 9. (**a**) TGA curves, (**b**) the first derivative of TGA curve, (**c**) display of the first mass loss area, (**d**) display of the second mass loss area, and (**e**) display of the third mass loss area for CS membranes with CNF and CNF(D) fillers.

Table 3. Temperature areas of mass loss and percentage of mass loss for CS membranes with CNF and CNF(D) fillers determined by TGA analysis.

Sample	T1 (°C)			T2 (°C)			T3 (°C)			Δy1 (%)	Δy2 (%)	Δy3 (%)	Δy (%)
	$T1_s$	$T1_p$	$T1_e$	$T2_s$	$T2_p$	$T2_e$	$T3_s$	$T3_p$	$T3_e$				
CS	30	49	110	235	283	345	/	/	/	9.1	35.9	/	85.7
CS-CNF	30	40	105	250	361	400	/	/	/	3.1	53.1	/	72.6
CS-CNF(D)	30	49	135	180	262	340	360	430	520	8.7	36.4	28.8	89.2
CS-CNF-CNF(D)	30	90	120	220	305	367	385	440	500	4.7	50.9	13.0	93.7

3.4. Mechanical Properties, Swelling Ratio, Alkaline Uptake, Ethanol Permeability, IEC and Ion Conductivity of the CS Composite Membranes

Figure 10a shows that the mechanical properties of the CS-based AEMs are comparable to, or even better than, those of the commercial Fumatech FAA-3-50 membrane. We observed excellent mechanical properties of the CS-CNF (D) membrane with a Young's modulus of 2.26 GPa and a tensile strength of 61.9 MPa. Compared to the reference CS membrane, a strong improvement in Young's modulus was observed for all membranes with functionalized CNF filler (359% for CS-CNF (D), 520% for CS-CNF-CNF (D), 431% for CS-CNF-CNF (D)H), indicating the increased degree of crystallinity of these membranes compared to the reference CS membrane. Compared to the reference CS membrane, there was a 12% improvement in tensile strength for the CS-CNF (D) membrane.

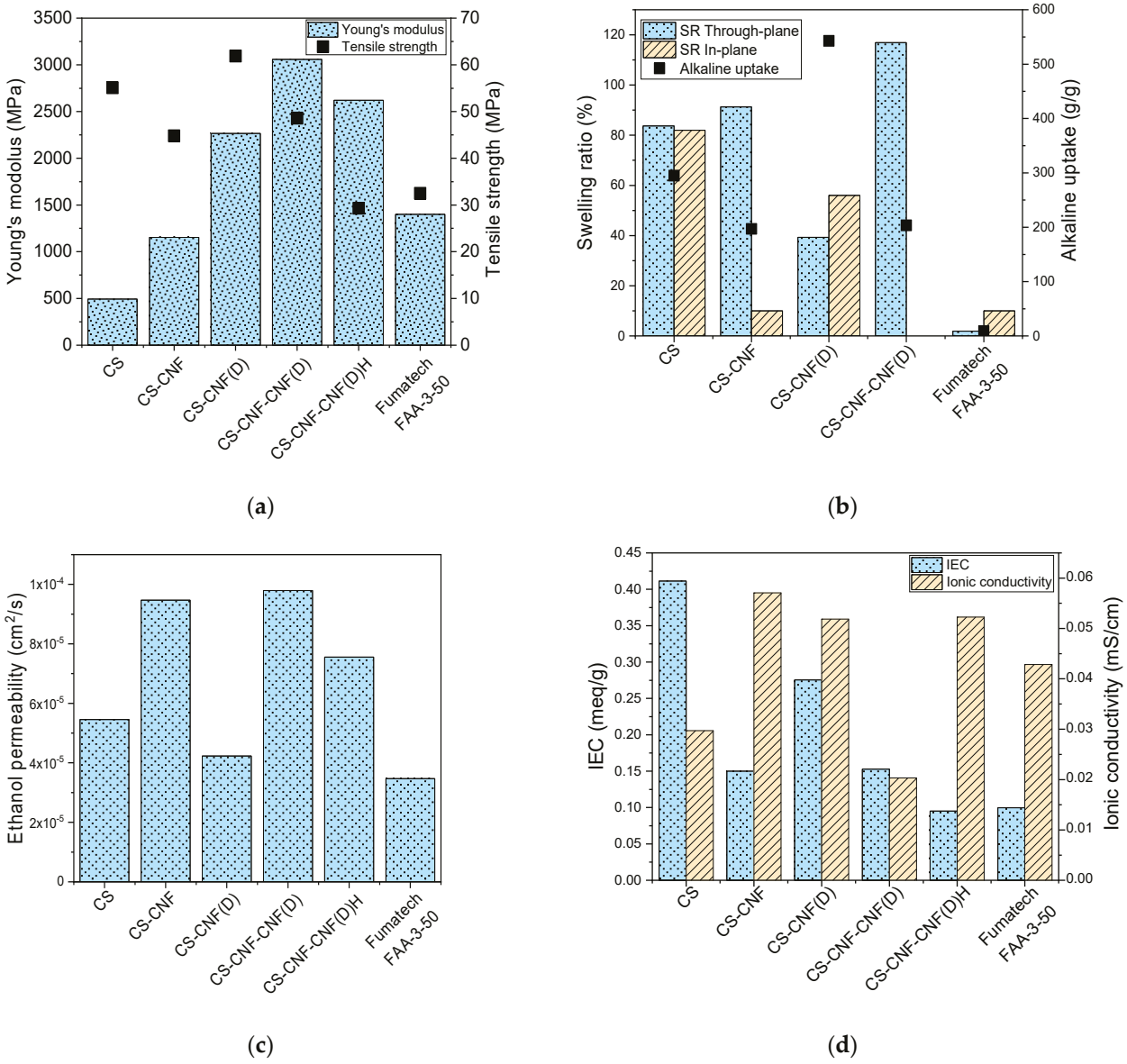

Figure 10. Comparison of the membrane's (**a**) mechanical properties, (**b**) swelling ratio and alkaline uptake, (**c**) ethanol (EtOH) permeability, (**d**) ion exchange capacity and ionic conductivity for the CS-based AEMs and the commercial Fumatech FAA-3-50 AEM.

Membrane swelling and alkali uptake are shown in Figure 10b. A significant increase in through-plane swelling and alkali uptake was observed for the CS-based membranes with CNF fillers compared to the Fumatech FAA-3-50. There was a correlation between the higher alkali uptake and higher ionic conductivity [16], and we also observed an increase in the alkali uptake of the CS-based membranes compared to the Fumatech FAA-3-50, as well as increased ionic conductivity for some of the CS-based membranes compared to the Fumatech FAA-3-50. Through-plane swelling can strengthen the contact between the current collectors and the membrane electrode assembly in the AAEMFC, which has a positive effect on the operation of the fuel cell. Conversely, in-plane swelling can loosen the contact between the AEM and the catalysts, and increase the resistance of the membrane electrode assembly. [41] For this reason, it is desirable that in-plane swelling be as low as possible, as this is the only way to ensure that the dimensional stability of the membrane is constant during fuel cell operation. Following these findings, we observed the highest power density for the membrane (CS-CNF) that also had the largest through-plane and low in-plane swelling. Accordingly, the CS-CNF-CNF (D) membrane with the highest

through-plane swelling ratio and the lowest in-plane swelling provided the highest power density of the CS–based membranes with CNF(D) fillers.

For AEMFC applications, the fuel permeability of the membrane should be kept as low as possible, because high fuel transfer leads to reduced fuel cell efficiency. Figure 10c shows that the CNF(D)-containing membrane had the lowest ethanol permeability (4.23×10^{-5} cm^2 s^{-1}) of the CS-based AEMs compared to all the manufactured CS-based membranes, while the value for the commercial Fumatech FAA-3-50 membrane was in the same range (3.47×10^{-5} cm^2 s^{-1}).

Figure 10d shows the IEC and ionic conductivity properties of the AEMs. For all CS-based membranes with fillers, except CS-CNF (D), an improvement in ionic conductivity was observed compared to the commercial membrane, while the reference CS membrane had a lower ionic conductivity than the commercial membrane. The reason for the improvement in the ionic conductivity of the membranes with fillers, but not in that of the reference CS membrane, is that the presence of functionalized CNF fillers introduces a positive charge into the membrane. In addition, the presence of CNF-based fillers allows for a more diverse three-dimensional structure of the membranes, and can lead to the formation of a network of intertwined fibers with gaps present, which contributes to the transfer of OH-ions through the membrane, since ionic conduction by the diffusion mechanism occurs only when free volume is available within the polymer chains. The reference CS membrane exhibited the highest IEC (0.41 meq/g), followed by the CS-CNF (D) membrane (0.28 meq/g), which had a higher IEC compared to the CS-CNF membrane with unmodified filler (0.15 meq/g), due to the presence of quaternary ammonium groups on CNF(D).

3.5. Direct Ethanol Alkaline Fuel Cell (DEAFCs) Performance

The prepared CS membranes with CNF and CNF(D) fillers were tested in an ethanol fuel cell under different operating conditions, and compared with the commercial Fumatech FAA-3-50 membrane (Figure 11a–e). The presence of humidified oxygen instead of non-humidified oxygen had almost no effect on the commercial Fumatech FAA-3-50 membrane; on the contrary, for all CS membranes, the presence of humidified oxygen at the same temperature (60 °C) resulted in a decrease in P_{max} compared to the fuel cell in which non-humidified oxygen was fed at the cathode. We attributed this to the highly hydrophilic nature of the CS-based membranes, which resulted in higher water uptake, which, if too high, leads to reduced fuel cell efficiency. For fuel cells operating at room temperature with non-humidified oxygen, we found that, compared to the reference CS membrane (22.2 mW cm^{-2}), the CS-CNF (D) membrane had a lower power density at all operating conditions of the fuel cell (15–70% reduction compared to the CS membrane). This was consistent with the ionic conductivity results, which showed that the introduction of CNF(D) filler does not significantly affect the ionic conductivity of the CS membranes (Figure 10d). The increased temperature of 80 °C with humidified oxygen compared to 60 °C with humidified oxygen resulted in an increase in power density for all CS-based and commercial AEMs embedded in the fuel cells, which was expected, since we associated the moderately higher AAEMFC operating temperature with increased P_{max}. We found that the fuel cells achieved the maximum P_{max} values with each of the membranes at 80 °C, humidified oxygen, and a fuel mixture of 5 M KOH and 3 M EtOH, as both the increased temperature and higher fuel concentration have a positive effect on fuel cell operation. A significant improvement in power density at 80 °C was observed for the CS membrane with unmodified CNF filler compared to the commercial membrane (62.4 vs. 35.1 mW cm^{-2}), which was not detectable for the CS membrane with CNF(D) at these operating conditions. This behavior can be explained by the morphological features observed by the SEM analysis (Figure 8) of the CS-CNF (D) membrane, which showed a strong agglomeration and non-uniform distribution of the CNF(D) filler on the CS base of the membrane, with a poor interweaving of the fibers over the whole surface. At the same conditions of 80 °C and humidified oxygen, as expected, a significant decrease in P_{max} was observed for the less concentrated fuel mixture of 1 M KOH and 1 M EtOH compared to the more concentrated

mixture of 3 M KOH and 3 M EtOH for all CS membranes (67–84% lower P_{max}) and for the commercial membrane (57% lower P_{max}). Based on the membrane tests in a single fuel cell, we found that the most promising CS membrane was the CS membrane with CNF filler.

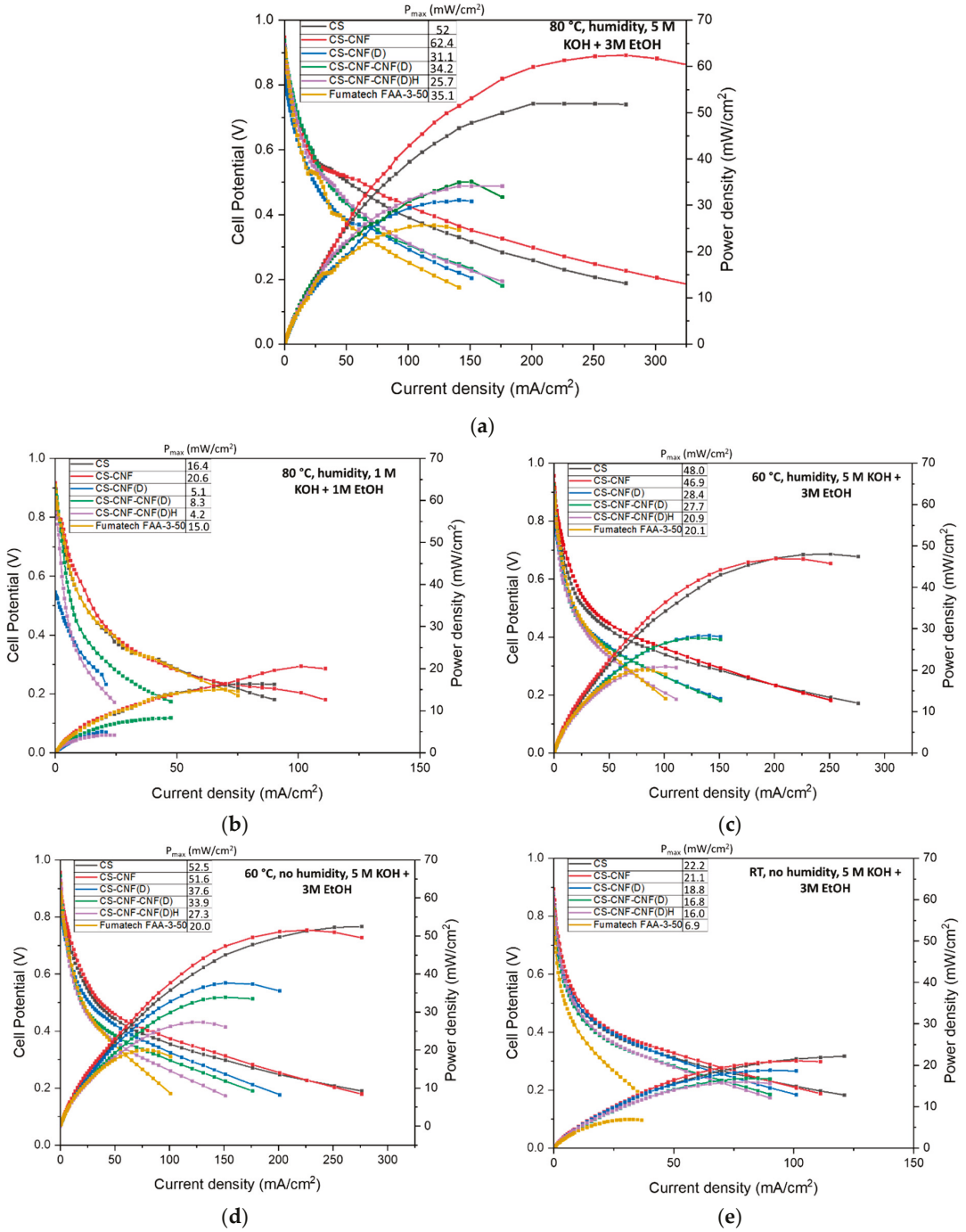

Figure 11. The results of membrane testing in the alkaline anion exchange membrane fuel cells (AAEMFC) under different operating conditions. Cell voltage and power density versus current density plots using CS membranes with or without CNF and CNF(D) fillers and a commercial Fumatech FAA-3-50 under different operating conditions: (**a**) 80 °C, humidified oxygen, and a fuel mixture of 5 M KOH and 3 M EtOH, (**b**) 80 °C, humidified oxygen, and a fuel mixture of 1 M KOH and 1 M EtOH, (**c**) 60 °C, humidified oxygen, and a fuel mixture of 5 M KOH and 3 M EtOH, (**d**) 60 °C, without oxygen humidification, and a fuel mixture of 5 M KOH and 3 M EtOH, (**e**) RT, without oxygen humidification, and a fuel mixture of 5 M KOH and 3 M EtOH.

The fuel cell tests showed that all CS-based AEMs had higher maximum power densities than the commercial Fumatech AEM at 25 °C and 60 °C with humidified oxygen and without oxygen humidification, indicating that all newly prepared CS-based membranes are suitable for DEFC applications at low temperatures. At 80 °C with humidified oxygen and without oxygen humidification, the CS membranes with CNF(D) filler underperformed in comparison to the commercial Fumatech AEM, implying that the CS-based membranes with CNF(D) fillers are not suitable for DEFCs operating at higher temperatures. At the highest temperature, 80 °C, and under both fuel concentrations, the CS-CNF membrane was the best performing membrane, with a P_{max} of 62.4 mW cm^{-2} at 80 °C, humidified oxygen, and a fuel mixture of 5 M KOH and 3 M EtOH, and a P_{max} of 20.6 mW cm^{-2} at 80 °C, humidified oxygen, and a fuel mixture of 1 M KOH and 1 M EtOH. Under all other conditions, the reference CS membrane proved to be the best performing and the CS-CNF membrane the second best. At the higher operating temperature, the CS-CNF membrane achieved the highest maximum power density in this study. The CS and CS-CNF membranes outperformed all the CS-based membranes with CNF(D) fillers. However, the CS-based AEMs with CNF(D) fillers exhibited better mechanical properties, with higher Young's modulus and tensile strength, except for the CS-CNF-CNF (D)H membrane. The CS-CNF (D) membrane also had significantly lower ethanol permeability than the CS and CS-CNF membranes, which was also comparable to the fuel permeability of the commercial membrane. Although the CS-CNF (D) had the highest IEC among all the CS-based membranes with fillers, it did not produce a higher P_{max} than the CS or CS-CNF membranes when embedded in a fuel cell. For all CS-based membranes with fillers, except CS-CNF (D), we observed an improvement in ionic conductivity compared to the commercial Fumatech AEM, while the reference CS membrane had a lower ionic conductivity than the commercial membrane.

4. Conclusions

The trade-off between sustainability, durability, performance, and cost is necessary for the development of new materials that are expected to have far-reaching effects in the long term. In this direction, a series of CS-based composite membranes with (modified) CNF as filler were prepared, and characterized with respect to their potential application in alkaline fuel cells. The CNF was modified efficiently with a DMAOP reagent, which allowed enrichment with quaternary amino groups as hydroxide conductors. The resulting fully bio-based composites were superior to the commercial Fumatech membranes in terms of Young's modulus, tensile strength, ion exchange capacity, and ionic conductivity, while the CS membrane with modified CNF filler achieved up to the same values in terms of EtOH crossover limitation. In terms of performance in a laboratory fuel cell assembly, an improvement of up to 78% in power density at 80 °C was observed for the CS membrane with neat CNF compared to the commercial Fumatech membrane (62.4 vs. 35.1 mW cm^{-2}), as well as a higher maximum power density, even in the experiment at RT. These results demonstrate their potential as sustainable membrane materials for DEFC applications at low temperatures.

Author Contributions: Study conception and design: M.B., M.H. and S.G.; data collection: M.H., M.R., D.M. and J.P.; analysis and interpretation of results: M.H., S.G. and M.R.; draft manuscript preparation: M.H. and S.G. Acquisition of funding: M.B., V.H. and B.G. All authors have read and agreed to the published version of the manuscript.

Funding: This work was supported by funding from Slovenian Research Agency (ARRS) Young Researcher Programme, Textile Chemistry Programme (P2-0118/0795), P1-242 Programme, and project "GO DEFC" (Grant number N2-0087) and the Austrian Science Fund (FWF), (Grant number I 3871-N37).

Institutional Review Board Statement: Not applicable.

Informed Consent Statement: All authors reviewed and approved final submission.

Data Availability Statement: Data available on request from the authors.

Acknowledgments: The authors would like to thank Silvo Hribernik (Faculty of Electrical Engineering and Computer Science, University of Maribor) for performing the SEM microscopy in Figure 6.

Conflicts of Interest: The authors declare no conflict of interest.

References

1. Xu, T. Ion exchange membranes: State of their development and perspective. *J. Memb. Sci.* **2005**, *263*, 1–29. [CrossRef]
2. Cermenek, B.; Ranninger, J.; Hacker, V. *Alkaline Direct Ethanol Fuel Cell*; Elsevier Inc.: Amsterdam, The Netherlands, 2018; Volume 1904, ISBN 9780128114582.
3. Zhao, T.S.; Li, Y.S.; Shen, S.Y. Anion-exchange membrane direct ethanol fuel cells: Status and perspective. *Front. Energy Power Eng. China* **2010**, *4*, 443–458. [CrossRef]
4. Couture, G.; Alaaeddine, A.; Boschet, F.; Ameduri, B. Polymeric materials as anion-exchange membranes for alkaline fuel cells. *Prog. Polym. Sci.* **2011**, *36*, 1521–1557. [CrossRef]
5. Choudhury, R.R.; Gohil, J.M.; Dutta, K. Poly(vinyl alcohol)-based membranes for fuel cell and water treatment applications: A review on recent advancements. *Polym. Adv. Technol.* **2021**, *32*, 4175–4203. [CrossRef]
6. Oroujzadeh, M.; Etesami, M.; Mehdipour-Ataei, S. Poly(ether ketone) composite membranes by electrospinning for fuel cell applications. *J. Power Sources* **2019**, *434*, 226733. [CrossRef]
7. Son, T.Y.; Kim, D.J.; Vijayakumar, V.; Kim, K.; Kim, D.S.; Nam, S.Y. Anion exchange membrane using poly(ether ether ketone) containing imidazolium for anion exchange membrane fuel cell (AEMFC). *J. Ind. Eng. Chem.* **2020**, *89*, 175–182. [CrossRef]
8. Elakkiya, S.; Arthanareeswaran, G.; Venkatesh, K.; Kweon, J. Enhancement of fuel cell properties in polyethersulfone and sulfonated poly (ether ether ketone) membranes using metal oxide nanoparticles for proton exchange membrane fuel cell. *Int. J. Hydrogen Energy* **2018**, *43*, 21750–21759. [CrossRef]
9. Pal, S.; Mondal, R.; Chatterjee, U. Sulfonated polyvinylidene fluoride and functional copolymer based blend proton exchange membrane for fuel cell application and studies on methanol crossover. *Renew. Energy* **2021**, *170*, 974–984. [CrossRef]
10. Lee, C.; Na, H.; Jeon, Y.; Jung Hwang, H.; Kim, H.J.; Mochida, I.; Yoon, S.H.; Park, J.I.; Shul, Y.G. Poly(ether imide) nanofibrous web composite membrane with SiO_2/heteropolyacid ionomer for durable and high-temperature polymer electrolyte membrane (PEM) fuel cells. *J. Ind. Eng. Chem.* **2019**, *74*, 7–13. [CrossRef]
11. Gorgieva, S.; Kokol, V. Preparation, characterization, and in vitro enzymatic degradation of chitosan-gelatine hydrogel scaffolds as potential biomaterials. *J. Biomed. Mater. Res. Part A* **2012**, *100*, 1655–1667. [CrossRef]
12. Muhmed, S.A.; Nor, N.A.M.; Jaafar, J.; Ismail, A.F.; Othman, M.H.D.; Rahman, M.A.; Aziz, F.; Yusof, N. Emerging chitosan and cellulose green materials for ion exchange membrane fuel cell: A review. *Energy Ecol. Environ.* **2019**, *5*, 85–107. [CrossRef]
13. Zhou, T.; He, X.; Lu, Z. Studies on a novel anion-exchange membrane based on chitosan and ionized organic compounds with multiwalled carbon nanotubes for alkaline fuel cells. *J. Appl. Polym. Sci.* **2018**, *135*, 46323. [CrossRef]
14. Wang, L.; Shi, B. Hydroxide Conduction Enhancement of Chitosan Membranes by Functionalized MXene. *Materials* **2018**, *11*, 2335. [CrossRef] [PubMed]
15. Gorgieva, S.; Osmić, A.; Hribernik, S.; Božič, M.; Svete, J.; Hacker, V.; Wolf, S.; Genorio, B. Efficient chitosan/nitrogen-doped reduced graphene oxide composite membranes for direct alkaline ethanol fuel cells. *Int. J. Mol. Sci.* **2021**, *22*, 1740. [CrossRef]
16. Cheng, X.; Wang, J.; Liao, Y.; Li, C.; Wei, Z. Enhanced Conductivity of Anion-Exchange Membrane by Incorporation of Quaternized Cellulose Nanocrystal. *ACS Appl. Mater. Interfaces* **2018**, *10*, 23774–23782. [CrossRef] [PubMed]
17. Hren, M.; Hribernik, S.; Gorgieva, S.; Motealleh, A.; Eqtesadi, S.; Wendellbo, R.; Lue, S.J.; Božič, M. Chitosan-$Mg(OH)_2$ based composite membrane containing nitrogen doped GO for direct ethanol fuel cell. *Cellulose* **2021**, *28*, 1599–1616. [CrossRef]
18. Kaker, B.; Hribernik, S.; Mohan, T.; Kargl, R.; Stana Kleinschek, K.; Pavlica, E.; Kreta, A.; Bratina, G.; Lue, S.J.; Božič, M. Novel Chitosan–$Mg(OH)_2$ Based Nanocomposite Membranes for Direct Alkaline Ethanol Fuel Cells. *ACS Sustain. Chem. Eng.* **2019**, *7*, 19356–19368. [CrossRef]
19. Jančič, U.; Božič, M.; Hribernik, S.; Mohan, T.; Kargl, R.; Kleinschek, K.S.; Gorgieva, S. High oxygen barrier chitosan films neutralized by alkaline nanoparticles. *Cellulose* **2021**, *28*, 10457–10475. [CrossRef]
20. Abdou, E.S.; Nagy, K.S.A.; Elsabee, M.Z. Extraction and characterization of chitin and chitosan from local sources. *Bioresour. Technol.* **2008**, *99*, 1359–1367. [CrossRef]
21. Roschger, M.; Wolf, S.; Mayer, K.; Singer, M.; Hacker, V. Alkaline Direct Ethanol Fuel Cell: Effect of the Anode Flow Field Design and the Setup Parameters on Performance. *Energies* **2022**, *15*, 7234. [CrossRef]
22. Cermenek, B.; Genorio, B.; Winter, T.; Wolf, S.; Connell, J.G.; Roschger, M.; Letofsky-Papst, I.; Kienzl, N.; Bitschnau, B.; Hacker, V. Alkaline Ethanol Oxidation Reaction on Carbon Supported Ternary PdNiBi Nanocatalyst using Modified Instant Reduction Synthesis Method. *Electrocatalysis* **2020**, *11*, 203–214. [CrossRef] [PubMed]
23. Bel-Hassen, R.; Boufi, S.; Salon, M.C.B.; Abdelmouleh, M. Adsorption of Silane onto Cellulose Fibers. II. The Effect of pH on Silane Hydrolysis, Condensation, and Adsorption Behavior. *J. Appl. Polym. Sci.* **2008**, *108*, 1958–1968. [CrossRef]
24. Gorgieva, S.; Vogrinčič, R.; Kokol, V. The Effect of Membrane Structure Prepared from Carboxymethyl Cellulose and Cellulose Nanofibrils for Cationic Dye Removal. *J. Polym. Environ.* **2018**, *27*, 318–332. [CrossRef]

25. Jankauskaite, V.; Balčiunaitiene, A.; Alexandrova, R.; Buškuviene, N.; Žukiene, K. Effect of cellulose microfiber silylation procedures on the properties and antibacterial activity of polydimethylsiloxane. *Coatings* **2020**, *10*, 567. [CrossRef]
26. Jiang, C.; Zhang, Y.; Wang, Q.; Wang, T. Superhydrophobic polyurethane and silica nanoparticles coating with high transparency and fluorescence. *J. Appl. Polym. Sci.* **2013**, *129*, 2959–2965. [CrossRef]
27. Tan, W.; Li, Q.; Dong, F.; Chen, Q.; Guo, Z. Preparation and characterization of novel cationic chitosan derivatives bearing quaternary ammonium and phosphonium salts and assessment of their antifungal properties. *Molecules* **2017**, *22*, 1438. [CrossRef] [PubMed]
28. Patrulea, V.; Hirt-Burri, N.; Jeannerat, A.; Applegate, L.A.; Ostafe, V.; Jordan, O.; Borchard, G. Peptide-decorated chitosan derivatives enhance fibroblast adhesion and proliferation in wound healing. *Carbohydr. Polym.* **2016**, *142*, 114–123. [CrossRef] [PubMed]
29. Badawy, M.E.I.; Rabea, E.I.; Taktak, N.E.M. Antimicrobial and inhibitory enzyme activity of N-(benzyl) and quaternary N-(benzyl) chitosan derivatives on plant pathogens. *Carbohydr. Polym.* **2014**, *111*, 670–682. [CrossRef]
30. Li, H.; Bao, H.; Bok, K.X.; Lee, C.Y.; Li, B.; Zin, M.T.; Kang, L. High durability and low toxicity antimicrobial coatings fabricated by quaternary ammonium silane copolymers. *Biomater. Sci.* **2016**, *4*, 299–309. [CrossRef]
31. Riaz, S.; Ashraf, M.; Hussain, T.; Hussain, M.T. Modification of silica nanoparticles to develop highly durable superhydrophobic and antibacterial cotton fabrics. *Cellulose* **2019**, *26*, 5159–5175. [CrossRef]
32. Teresa, O.H.; Choi, C.K. Comparison between SiOC thin films fabricated by using plasma enhance chemical vapor deposition and SiO2 thin films by using fourier transform infrared spectroscopy. *J. Korean Phys. Soc.* **2010**, *56*, 1150–1155. [CrossRef]
33. Mathew, R.T.; Cooney, R.P.; Zujovic, Z.; Doyle, C.; Wheelwright, W.; De Silva, K. A Sustained Release Anchored Biocide System Utilizing the Honeycomb Cellular Structure of Expanded Perlite. *ACS Appl. Bio Mater.* **2018**, *1*, 1959–1971. [CrossRef]
34. Gorgieva, S.; Vogrinčič, R.; Kokol, V. Polydispersity and assembling phenomena of native and reactive dye-labelled nanocellulose. *Cellulose* **2015**, *22*, 3541–3558. [CrossRef]
35. Sim, K.; Lee, J.; Lee, H.; Youn, H.J. Flocculation behavior of cellulose nanofibrils under different salt conditions and its impact on network strength and dewatering ability. *Cellulose* **2015**, *22*, 3689–3700. [CrossRef]
36. Žepič, V.; Fabjan, E.; Kasunič, M.; Korošec, R.C.; Hančič, A.; Oven, P.; Perše, L.S.; Poljanšek, I. Morphological, thermal, and structural aspects of dried and redispersed nanofibrillated cellulose (NFC). *Holzforschung* **2014**, *68*, 657–667. [CrossRef]
37. Wang, X.; Shi, L.; Zhang, J.; Cheng, J.; Wang, X. Self-assembly fabrication, microstructures and antibacterial performance of layer-structured montmorillonite nanocomposites with cationic silica nanoparticles. *RSC Adv.* **2017**, *7*, 31502–31511. [CrossRef]
38. Jeong, J.; Ayyoob, M.; Kim, J.H.; Nam, S.W.; Kim, Y.J. In situ formation of PLA-grafted alkoxysilanes for toughening a biodegradable PLA stereocomplex thin film. *RSC Adv.* **2019**, *9*, 21748–21759. [CrossRef]
39. Zhang, X.; Li, Y.; Guo, M.; Jin, T.Z.; Arabi, S.A.; He, Q.; Ismail, B.B.; Hu, Y.; Liu, D. Antimicrobial and UV Blocking Properties of Composite Chitosan Films with Curcumin Grafted Cellulose Nanofiber. *Food Hydrocoll.* **2021**, *112*, 106337. [CrossRef]
40. Vasilev, A.; Efimov, M.; Bondarenko, G.; Kozlov, V.; Dzidziguri, E.; Karpacheva, G. Thermal behavior of chitosan as a carbon material precursor under IR radiation. *IOP Conf. Ser. Mater. Sci. Eng.* **2019**, *693*, 012002. [CrossRef]
41. Ming Yang, J.; Chih Chiu, H. Preparation and characterization of polyvinyl alcohol/chitosan blended membrane for alkaline direct methanol fuel cells. *J. Memb. Sci.* **2012**, *419–420*, 65–71. [CrossRef]

polymers

MDPI

Article

Powdered Cellulose Microblasting for Dry Cleaning Printed Works on Paper

Iris Bautista-Morenilla *, Cristina Ruiz-Recasens and Gema Campo-Francés

Research Group of Conservation of Cultural Heritage, Art and Conservation Department, Fine Arts Faculty, University of Barcelona, Pau Gargallo, 4, 08028 Barcelona, Spain; cruiz@ub.edu (C.R.-R.); gcampo@ub.edu (G.C.-F.)
* Correspondence: ibautista@ub.edu

Abstract: This study evaluates the practical feasibility of using powdered cellulose microblasting for dry cleaning paper-based printed artworks in a real setting of conservation treatment. The control parameters used for this purpose are the potential morphological changes in the surface, the level of cleanliness achieved, and the amount of residue remaining in the artwork after the treatment. In this study, cleaning of a lithography was conducted entirely with powdered cellulose microblasting. The outcomes were evaluated before and after treatment using optical microscopy, scanning electron microscopy, energy-dispersive X-ray spectroscopy, and spectrophotometry. The results indicate that powdered cellulose microblasting is a feasible and efficient technique for conducting the dry cleaning of printed works on paper without causing morphological changes to their surface. Additionally, it offers significant benefits by enabling precise treatment control, reducing cleaning time, and using materials stable in the long term and compatible with the substrate. Moreover, it mitigates the long-term negative effects caused by synthetic polymer residues from the cleaning materials commonly used in the dry cleaning of paper.

Keywords: cellulose powder; cultural heritage; cleaning methods; microblasting; paper artwork

1. Introduction

Dry cleaning is a conservation treatment often conducted on cultural assets for the removal of unwanted materials such as surface soil, dust, dirt, insect droppings, build-up, or other surface deposits [1]. Depending on the characteristics of the work and the specific circumstances of each case, this treatment may be considered necessary for preventive reasons, due to the conservation risks associated with certain deposits on the surface of the object, or for aesthetic purposes, in order to improve the legibility of the artefact. However, dry cleaning of paper-based works can be a disruptive process that may cause abrasion of the paper surface, forcing foreign materials such as dust or eraser powder into the paper matrix and damaging the media [2]. Indeed, cleaning remains a complex conservation challenge that requires enhanced research and practical efforts to develop and evaluate a range of new or modified options [3,4]. Methods typically used to conduct this treatment on paper-based artworks and documents have been shown to have significant disadvantages for the artefact's characteristics and its long-term stability [5,6].

Vacuum cleaning is commonly used as the initial phase of a dry cleaning procedure and is considered one of the least intrusive methods. Often, it is complemented by the use of a soft brush to optimize results. However, its effectiveness is limited or insignificant when dirt has solidified due to biological, physical, and chemical processes [7–9].

Erasers and sponges are widely used for dry cleaning documents, offering a significant benefit in terms of ease of control. The cleaning process can be halted as needed, enabling the exclusion of fragile areas or regions that do not require cleaning. Both erasers and sponges demonstrate effective removal of visible dirt between fibers. Additionally, these techniques are cost-effective and do not necessitate the use of specialized equipment [10].

However, the literature highlights their main drawbacks [11–15] related to the stability of the media, changes in brightness and/or surface texture [16,17], as well as residues that, to a greater or lesser extent depending on the type of the treated paper, infiltrate the interstices of the paper fibers [18], affecting the absorption properties of the artwork [19,20] and posing a risk to the future conservation of the work due to containing abrasive materials, sulfur, hydrochloric acid, plasticizers, drying oils, etc. [21–24].

Microblasting is another alternative to dry cleaning. Its efficiency, effectiveness, and fundamental processes in the cleaning of historic surfaces have been reported in the literature [6,25]. Microblasting involves projecting abrasive particles propelled by pressurized air to disrupt the adhesion between surface deposits and the substrate, a phenomenon based on the kinetic energy formula ($E_k = \frac{1}{2}m \times v^2$), where m is mass or abrasive, and v is velocity [26]. The scientific literature details various application parameters, with the most influential factors including pressure, distance, angle, time, nozzle, particle flow, and specific abrasive properties. Properly selecting the abrasive and adjusting these key parameters can thereby alter the effects on the surface, where the least aggressive angle for different substrates is close to 75° [25–28].

Although microblasting has been mainly used in architectural preservation [29], previous scientific studies have obtained positive experimental results in paper works [30–32] and canvas paintings [10,33] by replacing hard abrasives traditionally used in inorganic supports with high-purity powdered cellulose microfibers, a VOC/SVOC-free sulfite bleached pulp from nonconiferous wood [33]. A fiber length below 40 μm has been found to produce successful results in previous experimental dry cleaning studies [10,30–32]. Indeed, microblasting of powdered cellulose emerged as an advantageous system due to its higher cleaning efficiency without affecting the morphology of the surfaces, and the low amount of cleaning material residue remaining in the treated samples. These included porous papers, even those in poor condition with low mechanical properties, open fiber structure, and rough surface texture.

However, so far, microblasting with powdered cellulose has been only conducted in selected spots in limited extent. Its applicability to the conservation treatment of an artefact remains uncertain and may present unforeseen challenges inherent to the transfer of an experimental method to the real-world context.

On this basis, the authors hypothesized that microblasting of powdered cellulose could be an alternative to conventional dry cleaning methods, avoiding their proven negative effects and enhancing treatment development. The authors of this study and other authors in the literature [6] consider powdered cellulose to be suitable for cleaning paper-based works due to its compatibility with the support and long-term stability. Compatibility ensures that the cleaning material does not cause any adverse reactions with the original work, including the paper, inks, or other constituent elements. Long-term stability makes it appropriate for use in conservation projects, complying with one of the mandatory principles in the field.

In the view of the above, this research aimed at evaluating the practical feasibility and the effectiveness of powdered cellulose microblasting for dry cleaning paper within the real context of a conservation treatment. The control parameters used for this purpose were the potential morphological changes in the surface, the level of cleanliness achieved, and the amount of residue remaining in the artwork after the treatment. The treatment's performance was evaluated based on factors commonly considered in conservation projects. These include the device's ease of use in cleaning large surfaces, the time required to complete the treatment, the ability to adjust the cleaning intensity in real time based on the treatment needs and specificities, the capacity to stop the cleaning promptly in unexpected circumstances, and the technique's spatial resolution, which enables the treatment of specific areas without affecting their surroundings.

2. Materials and Methods

The methodology involved applying the cleaning system to a paper artwork with surface dirt. Various parameters were measured at different locations before and after treatment using optical microscopy, electron microscopy, and spectrophotometry.

The selected artwork was a sacrificial work, an artist's proof lithograph created approximately 20 years ago on a 220 g/m^2; intaglio paper with a relatively smooth texture, although the surface was quite porous due to low sizing (Figure 1).

Figure 1. Selected lithograph for the study. (**A**) Margin detail: The paper appears to have a porous and loosely packed fiber structure. The large amount of surface dirt is visible to the naked eye. (**B**) Central area detail: The contrast between the surface of inked areas and the support is visible. In the red ink, less penetration of dirt is especially clear due to the smoother texture of the inked areas. The gloss effect created by overlapping of the inks, red and black in this case, is also apparent. (**C**) Optical microscopy fiber analysis with Lofton–Merrit staining test: results indicate that paper is made of sulfite-based bleached chemical pulp with some unbleached fibers. The fibers are in an acceptable condition. The small amount of sizing is apparent from the minimal visible residue between fibers and the ease of separation without prewashing.

The support was a bleached sulfite-based chemical pulp paper with some unbleached fibers. The mechanical strength of the artwork was good, and its fibers were in good condition. However, due to the low degree of sizing, it was mechanically sensitive to abrasion or friction and was rather porous.

Prior to treatment, the primary concern with the paper was the substantial accumulation of dust and surface dirt that had infiltrated the interstices of the surface fibers. The ink exhibited a comparable level of dust, but due to the smoother and more continuous surface of lithographic ink, particles remained more superficial.

The cleaning was carried out using Arbocel® BE600-30PU (Barcelona, Spain) cellulose with a particle size of 30 µm from J. Rettenmaier and Söhne (Figure 2). According to the literature, this fiber size is the least damaging to paper surfaces [6] and acrylic inks [32]. Cellulose fibers were projected using a CTS5/B (CTS Europe, Barcelona, Spain) footswitch-

operated microblaster through a straight tungsten carbide nozzle with a diameter of 0.7 mm. A silenced 1.5 HP compressor and a dehumidifier filter (CTS Europe, Barcelona, Spain) were also employed to reduce the compressed air's humidity, preventing cellulose clumping.

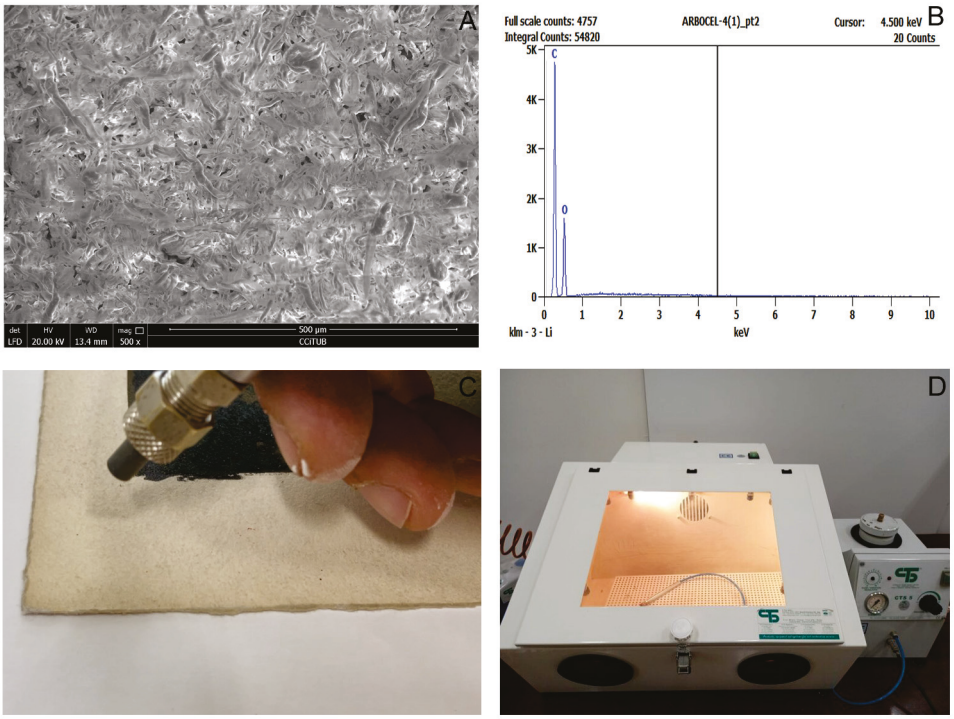

Figure 2. At the top, SEM image of powdered cellulose Arbocel® at 500× magnification (**A**) and the EDX related spectra (**B**). At the bottom, the equipment used for cleaning is observed: picture C shows a straight tungsten carbide nozzle with a diameter of 0.7 mm, and picture (**D**) shows a footswitch-operated microblaster, a CTS5/B, and a Box CTS4 cabinet with an environmental dust collector.

The treatment was developed in a Box CTS4 cabinet (CTS Europe, Barcelona, Spain) with an environmental dust collector. The cleaning process was carried out by drawing circles across the entire surface of the work to ensure homogeneity and prevent unwanted marks, as recommended in the literature [6]. Cleaning parameters were selected based on previous studies and were tested before conducting the cleaning trials to identify any necessary adjustments. The pressure (20 kPa) and angle (70°) were not modified. Distance and time were adjusted and reduced when it was determined that cleaning was complete for each area of the artwork.

In previous research [26,30], 20 kPa has been demonstrated to produced the highest cleaning efficiency with paper substrates without causing mechanical damage to the treated surfaces. Additionally, a working angle of 70° has been shown to minimize the cleaning mechanism via impact, which is inherent to right angles, while enhancing friction or cutting mechanisms. This typically results in milder effects on the surface [26].

Optical microscopy, scanning electron microscopy, and spectrophotometry analyses were conducted before and after the cleaning treatment to verify its feasibility without causing morphological surface changes and to detect any residues of cleaning material on the artefact.

The artwork underwent examination in six representative areas using optical microscopy. Six samples were extracted for analysis through scanning electron microscopy, and six spectrophotometry readings were taken—three in the paper area to assess the level of cleanliness and three in the black ink area to evaluate residues (Figure 3).

Figure 3. Location of the spots examined with each analytical technique: optical microscopy (marked in blue), scanning electron microscopy (market in red), and spectrophotometry (marked in green).

Optical microscopy was performed using a AM4113-FVW Dino-Lite® (AnMo Electronics Corporation, Getafe, Spain) surface microscope at magnifications ranging from 60× to 200× with direct LED. All the images were processed with 2.0 Dino-Capture® software. Analysis of surface morphology allowed the detection of possible texture changes or fiber alterations, accurately determining the effects and effectiveness of the cleaning tests.

Scanning electron microscopy was carried out using an FEI ESEM QUANTA 200 (FEI Company, Barcelona, Spain) instrument in low-vacuum mode. The analyses were conducted in a vacuum chamber at 130 Pa with an acceleration voltage of 20 kV and a working distance between 9.4 and 10.4 mm. Images were captured in backscattered electron mode, and the morphology of the samples was studied at magnifications between 100× and 2000×. Determining the surface morphology before and after cleaning enabled the identification of possible texture changes, any residues remaining on the surface, and a more precise assessment of the effectiveness of the tested cleaning system.

A Konica Minolta CM 2600d spectrophotometer (Konica Minolta, Valencia, Spain) with a range of 400 to 700 nm and a measurement interval of 10 nm was used to assess potential color changes resulting from the cleaning process. Analyses were conducted with a 10° reflection optical geometry and a measurement area of Ø 5 mm. The results are expressed in the CIELAB 1976 system (Konica Minolta, Valencia, Spain) with reference to illuminant D65.

The chromatic values were obtained using CM-S100w 3.20.0002 Spectra Magic software (Konica Minolta, Valencia, Spain) and processed in a spreadsheet to obtain the differences in each of the three coordinates (ΔL*, Δa*, and Δb*) before and after cleaning.

3. Results and Discussion

Surface optical microscopy at 120× magnification indicates that the results meet the feasibility control parameters established at the beginning of the study. The evidence shows that the level of cleanliness achieved was remarkable, even in the spaces between fibers. Additionally, no morphological changes or residues were detected in the artwork after the treatment.

Figure 4 displays six areas that were studied before (left) and after (right) cleaning. The selected spots included both media and noninked paper to test the cleaning results on the support and ink. The results show that the paper became whiter after cleaning, while the intensity of the inks remained unchanged. Additionally, no surface changes were detected in any of the treated areas, and no residues were observed at 120× magnification.

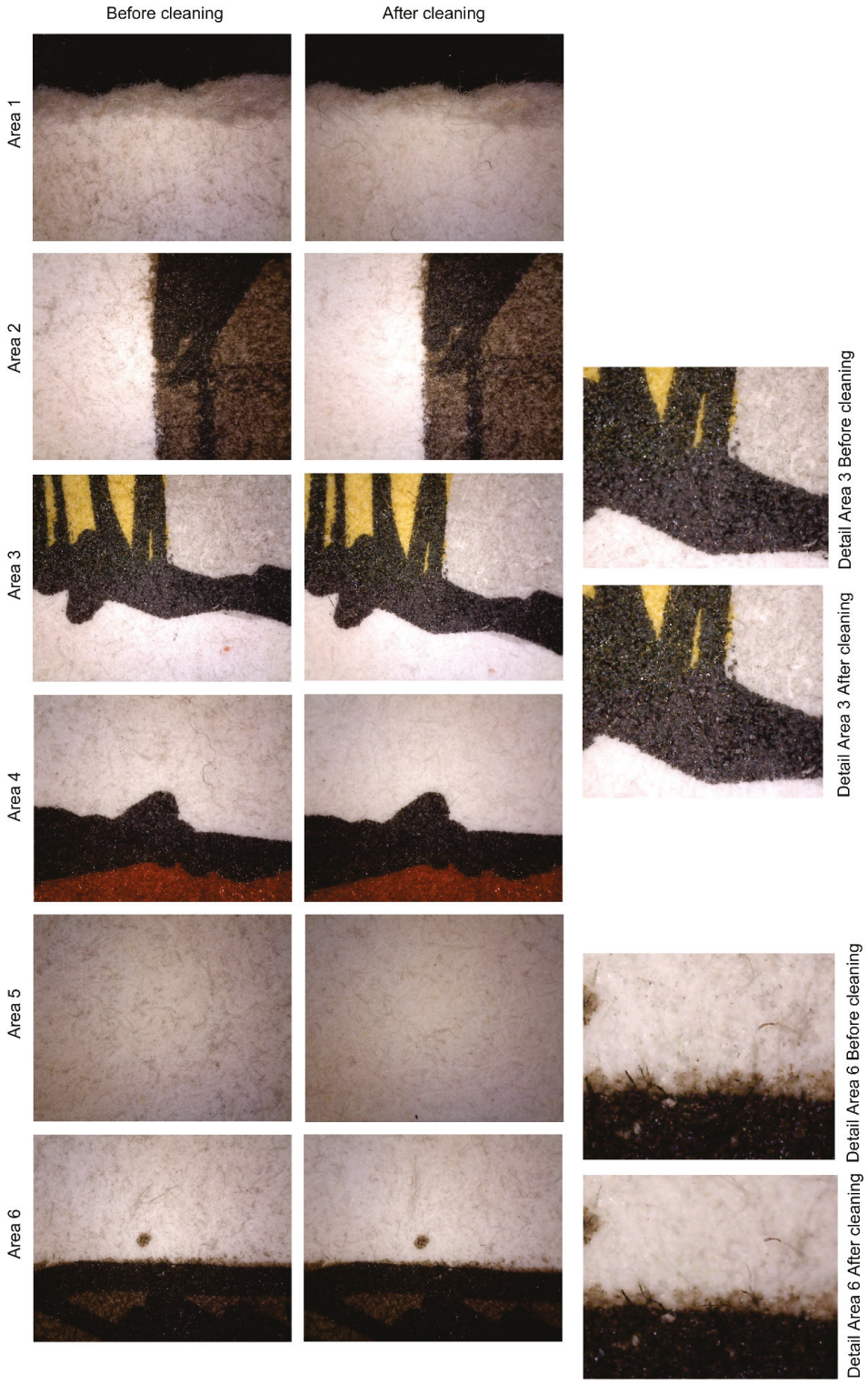

Figure 4. Photographs from optical microscopy taken at 120× magnification before treatment (**left column**) and after cleaning (**right column**). The numbers in each photograph correspond to the area that was examined, as located in Figure 3. Also, areas 3 and 6 are shown in detail on the right.

Prior to treatment, the surfaces showed dirt particles of two different sizes, circular in shape and brown to black in color, especially visible in noninked areas (refer specially to images of areas 1 and 5 in Figure 4). There was also dirt of smaller granulometry that had penetrated the interfiber spaces, visually resulting in a continuous medium grey tone in some areas. After cleaning, nearly all circular particles was removed, and interfiber dirt was reduced. As a result, the paper had a much lighter appearance. In the detailed view of area 6 (Figure 4), it is clear that, after cleaning, the circular particles remaining on the surface were negligible. The grey tone of the interfiber soiling was reduced, and no residues of the powdered cellulose used in the treatment were visible. Additionally, it was evident that the fibers of the paper maintained their position, even those that were free, without ink to consolidate them to the more compacted base of the support. This is consistent with the results previously reported in the literature [6,30], where this technique was found to be effective in removing dirt from paper without damaging the surface.

As previously mentioned, the visual intensity of the inked areas remained the same, indicating that no visual loss of color materials was detected. This is in accordance with what has been reported in the literature, both for etching inks [31] and acrylics [32]. Yellow- and red-colored areas became more vivid after cleaning (refer to areas 3 and 4, Figure 4), and grey ink was perceived lighter (see areas 2 and 3 in Figure 4). Black ink appeared deeper and stronger, creating a greater contrast with the colors and the background. The inks also exhibited the same level of brightness, maintaining the nuances of transparency and changes in reflectance when overlapping (refer to the detail of area 3 in Figure 4).

As for residues, the black ink areas also show no traces of cellulose powder residue, which would appear as visible lumps due to their white color, as reported in previous studies [31].

The electron microscopy confirmed the same observations regarding morphology, cleaning efficiency, and absence of residues. Similar results were obtained, with unnoticeable changes in surface morphology, remarkable removal of soiling, and no residues of the cleaning material detected at 2000× magnification.

Figure 5 shows the studied area before and after cleaning. The upper images display twisted and contoured document fibers, along with numerous white or light grey dirt particles. In contrast, the lower images show the paper after cleaning, with fewer dirt particles and the same fiber morphology as before cleaning. No residues of powdered cellulose were observed, which would be clearly visible at this magnification, as previously reported [10].

The cleaning efficacy previously detected using optical microscopy was confirmed via spectrophotometry, which revealed the effects of cleaning on the color of the artwork. In Figures 6 and 7, we can observe the difference in L* (blue), a* (orange), and b* (grey) at different measured spots before and after cleaning.

Spots 1, 2, and 3 were readings performed on the paper without ink on it (refer to Figure 3 to locate the measured areas). The difference in a* and b* (Figure 6) and the difference in L* (Figure 7) indicate that after cleaning, the paper became less reddish-yellow and whiter, as the removed dust had a warm grey tone. Therefore, its removal resulted in a whiter and cooler color, characteristic of the paper in this artwork. This was also reported in the literature [30].

Spots 4, 5, and 6 represented measurements taken on the black ink. Spots 4 and 6 were locations of completely opaque ink. In contrast, spot 5 was a reading in an area of lower ink intensity, with a more greyish tone.

On the black ink, changes in hue were minimal and negligible (see Figure 6). The major change was observed in luminosity, the L* variable. Areas with a high concentration of black ink appeared darker after cleaning because the grey of the dust was removed, revealing the deep black of the ink. The difference in L* plotted in Figure 8 displays this change for spots 4 and 6, which showed a darkening after cleaning due to the appearance of the black inner ink, which, before cleaning, was under a layer with a brownish-greyish tone. In areas with a lower amount of black ink and, therefore, a more greyish tone in the

engraving (area 5), the behavior was more similar to that obtained on paper, as the dust was darker than the ink. As observed during the microscopy analysis, areas with grey ink and a lower concentration of black ink became lighter. Thus, spot 5 located in Figure 3 shows a positive difference in the L* measurements (refer to Figure 8).

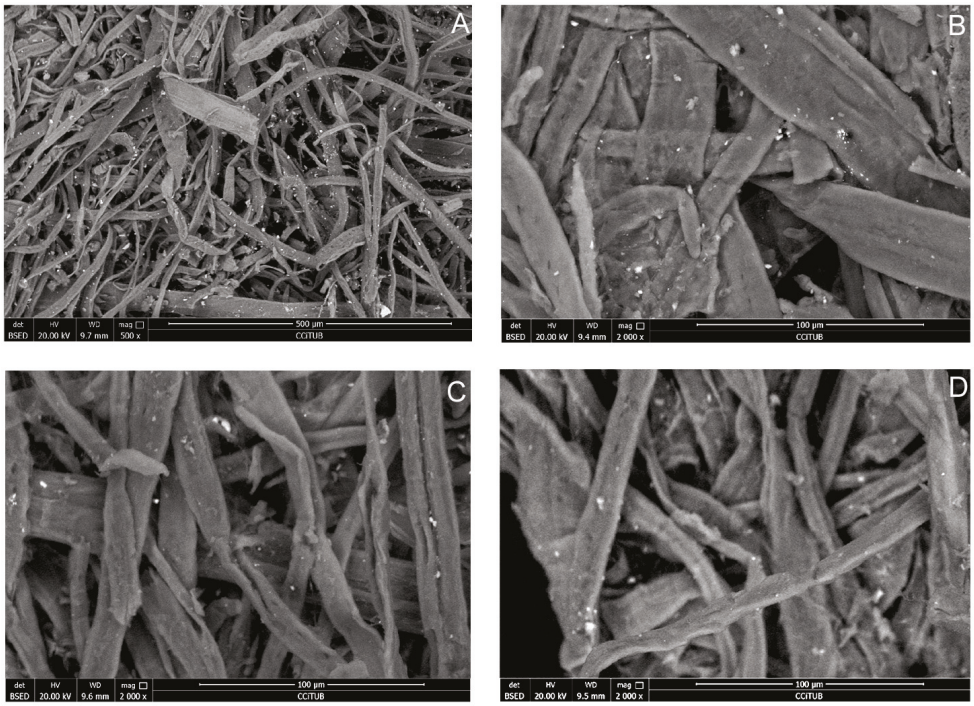

Figure 5. Photographs from electron microscopy taken at 500× (**A**) and at 2000× magnification (**B**–**D**), before treatment (upper image (**A**,**B**)) and after cleaning (lower image (**C**,**D**)). These images show samples taken from the upper left corner of the stamp (spot (**C**), marked in red in Figure 3).

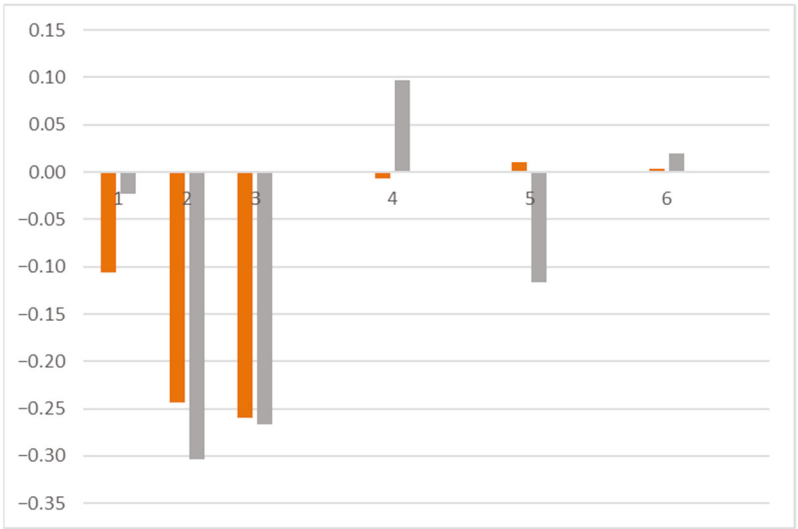

Figure 6. Difference in a* (orange) and b* (grey) at each measured point, before and after cleaning.

In terms of the technique's performance and its practical application in treatment development, there are several factors that should be considered to ensure optimal results. During a cleaning intervention, it is necessary to adjust the cleaning intensity dynamically based on the conservator's decisions during the treatment. This adjustment should consider various factors, such as the composition, structure, and condition of the area being cleaned,

as well as the nature and characteristics of the surface dirt, its interaction with the artefact, and the risk it poses in the short and long term.

A priori, the cleaning intensity can be adjusted by modifying several parameters, including pressure, distance, time, and working angle. However, the effects of cleaning vary depending on these variables.

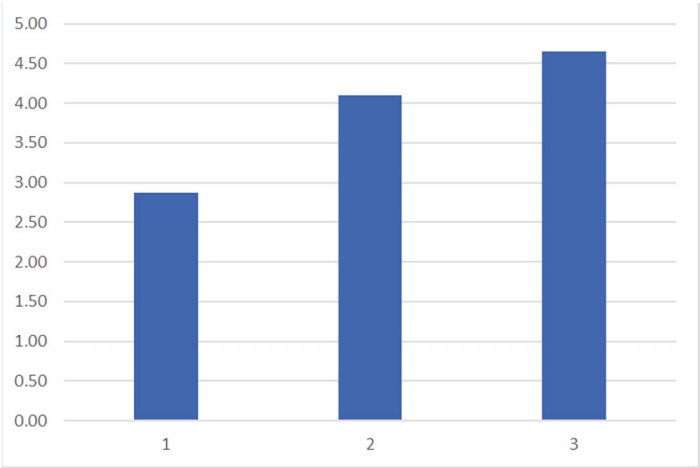

Figure 7. Spots 1, 2, and 3: difference in L* in measurements on the support of the artwork without the presence of supporting elements, before and after cleaning.

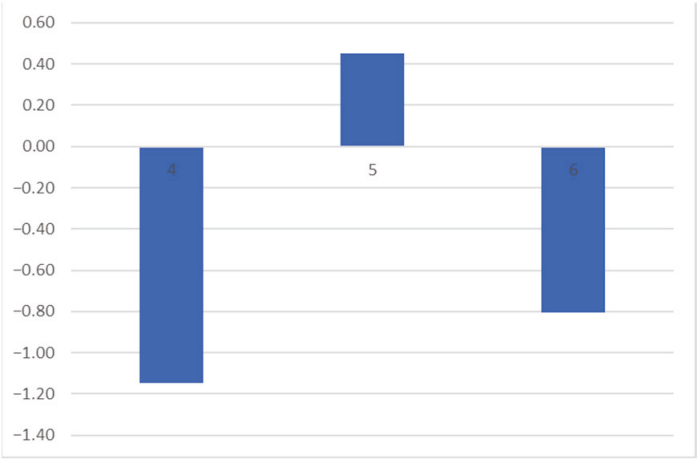

Figure 8. Spots 4, 5, and 6: difference in L* in measurements on black ink, before and after cleaning.

Changing the pressure is difficult to carry out dynamically, especially because the conservator would have to look away from the cleaning zone to the instrument's command, which would enable changes in the pressure but involves the loss of visual control during the operation. On the other hand, adjusting the instrument's regulator to change the pressure can result in significant and sometimes abrupt changes. This can lead to overly aggressive cleaning in certain areas.

As previously stated, altering the working angle affects the cleaning mechanism of the particles upon collision with the surface. Controlling the intensity of the cleaning and the area affected is dependent on the angle of modification. A change in the angle results in an unpredictable variation in cleaning intensity. When the angle of impact is closer to the vertical, the cleaning becomes more aggressive. On the one hand, a sharper working angle results in a more elliptical collision zone for the particles, making it more challenging to control the area being cleaned. On the other hand, a pressure of 20 kPa allows for comfortable cleaning. The energy with which the particles reach the surface is usually sufficient to remove common dirt from paper works, while keeping the hand

comfortably resting on the work surface. Adjustments are made by slightly moving the hand backwards from the work. This movement is almost intuitive and does not distract from the view of the work or the concentration needed during the operation.

To adjust the cleaning intensity, time is another variable that needs to be controlled. Checking the cleaning targets helps with deciding when to stop cleaning each area.

4. Conclusions

The results of this study indicate that powdered cellulose microblasting is a dry-cleaning technique that, when applied with the appropriate parameters, may be highly effective in cleaning printed works on paper.

In this study, the selected artwork was cleaned efficiently according to the control parameters used to make this assessment. On the one hand, it did not cause morphological changes of the surface, as observed from the optical and scanning electron microscope results. Additionally, both microscopic techniques confirmed that powdered cellulose could be easily vacuumed from paper, even when porous and with an open structure, as well as from lithographic inks, as no residues were detected on the artefact after cleaning.

Through optical and electronic microscopy, it was determined that the level of cleanliness achieved was good, as there has been remarkable remove of soiling, both of free particles and soil imbedded within the fibre's spaces. This has had a visual effect, both detectable with optical microscopy and spectrophotometry. Dark and cold colours became darker and cooler after cleaning recovering their own nature. In spectrophotometry this is expressed in a decrease of the L*, a* and b*. Other colours or tones appear more vivid when observed with optical microscopy. For example, spectrophotometry revealed an increase in the L* variable in visually grey tones, even when these were low concentration of black ink. In non-inked areas the paper becomes whiter and less reddish-yellow, as the removed soil has a warm grey tone. This is confirmed by spectrophotometry analyses that reveal an increase in brightness of the non-inked paper, confirming the effectiveness of the cleaning method.

The cleanliness control was easy and effective, significantly reducing the treatment time and using materials with a composition compatible with the substrate. After conducting this study, it was concluded that varying the distance and time during the intervention while keeping the pressure constant at 20 kPa and the working angle at 70° is advisable. Additionally, it was found that the working position for cleaning using this technique and these parameters is comfortable, allowing for a full day of work. Furthermore, the technique reduces treatment time compared to commonly used dry cleaning methods for works on paper.

The high long-term stability of cellulose suggests that there will be no harmful effects over time. This has been the case in previous natural ageing studies. Additionally, the compatibility of cellulose with the treated work and the absence of morphological changes and cleaning material residues on the surface suggest that this method will not result in physical, chemical, or mechanical changes. However, further research could explore this topic in more detail.

On the basis of the above, it was confirmed that the microblasting of cellulose powder can be considered a feasible and efficient technique for the dry cleaning of printed works on paper. However, the conservator is the only one who can decide and assess the suitability of any tool, material, or procedure for any specific situation. Therefore, it is plausible that this method, like any other, may not be appropriate for all graphic document works and in all contexts.

This research suggests that microblasting of powdered cellulose is an advantageous technique in comparison to the methods commonly used in dry cleaning paper-based works. The studied technique mitigates the proven negative effects and foreseeable ones that may be caused by the poor stability of the used cleaning materials and their low compatibility with the original artefacts.

Author Contributions: Conceptualization, C.R.-R., I.B.-M. and G.C.-F.; methodology, I.B.-M. and C.R.-R.; cleaning tests, I.B.-M. and C.R.-R.; analysis, C.R.-R. and I.B.-M.; results and discussion, I.B.-M., C.R.-R. and G.C.-F.; manuscript redaction, C.R.-R., I.B.-M. and G.C.-F. All authors have read and agreed to the published version of the manuscript.

Funding: This research received no external funding.

Institutional Review Board Statement: Not applicable.

Data Availability Statement: Data are contained within the article.

Conflicts of Interest: The authors declare no conflicts of interest.

References

1. BPG Surface Cleaning. 2021. Book and Paper Group Wiki. American Institute for Conservation (AIC). Available online: https://www.conservation-wiki.com/wiki/BPG_Surface_Cleaning (accessed on 22 December 2023).
2. Zervos, S.; Alexopoulou, I. Paper conservation methods: A literature review. *Cellulose* **2015**, *22*, 2859–2897. [CrossRef]
3. Ormsby, B.; Bartoletti, A.; Van den Berg, K.; Stavroudis, C. Cleaning and Conservation. Heritage Science. Special Collection. 2021. Available online: https://link-springer-com.sire.ub.edu/collections/gcecfejheh (accessed on 22 December 2023).
4. Casini, A.; Chelazzi, D.; Baglioni, P. Advanced methodologies for the cleaning of works of art. *Sci. China Technol. Sci.* **2023**, *66*, 2162–2182. [CrossRef]
5. Zidan, Y.; El-Shafei, A.; Noshy, W.; Salim1, E. A comparative study to evaluate conventional and nonconventional cleaning treatments of cellulosic paper supports. *Mediter. Archaeol. Archaeom.* **2017**, *17*, 337–353.
6. Jaček, B. Das "weiche Feinstrahlen". Ein neuer Ansatz zur Trockenreinigung von Papier und Pergament. *Restauro* **2013**, *3*, 44–47.
7. Tarnowski, A.; McNamara, C.; Bearce, K.; Mitchell, R. Sticky microbes and dust on objects in historic houses. In Proceedings of the American Institute for the Conservation of Historic and Artistic Works (AIC) 32nd Annual Meeting, Portland, OR, USA, 9–14 June 2004; pp. 11–28. Available online: http://resources.culturalheritage.org/wp-content/uploads/sites/8/2015/02/osg011-02.pdf (accessed on 22 December 2023).
8. Lithgow, K.; Lloyd, H.; Brimblecombe, P.; Yoon, Y.H.; Thickett, D. Managing dust in historic houses–a visitor/conservator interface. *Our Cult. Past-Your Future* **2005**, *II*, 662–669. Available online: https://www.researchgate.net/publication/267851256_Managing_dust_in_historic_houses_-_a_visitorconservator_interface (accessed on 22 December 2023).
9. Lloyd, H.; Bendix, C.; Brimblecombe, P.; Thickett, D. Dust in historic libraries. *Mus. Microclim.* **2007**, 135–144. Available online: https://www.english-heritage.org.uk/siteassets/home/learn/conservation/collections-advice--guidance/musmicdustpaper.pdf (accessed on 22 December 2023).
10. Bautista-Morenilla, I.; Ruiz-Recasens, C.; Iglesias-Campos M, Á.; Oriola-Folch, M. Powdered cellulose microblasting: A useful technique for dry-cleaning the reverse side of canvas paintings. *Herit. Sci.* **2022**, *10*, 170. [CrossRef]
11. López, A.; Narváez, J.; Tello, N.; Blanc, R.; Espejo, T. Impact of Erasers for Dry-cleaning Surfaces in Graphic Documents. In *Science and Art VII Experimental Sciences and Heritage Conservation*; Ministerio de Cultura y Deporte: Madrid, Spain, 2018; pp. 410–418. Available online: https://es.calameo.com/read/0000753354c1fd0863020 (accessed on 22 December 2023).
12. Cowan, J.; Guild, S. *Dry Methods for Surface Cleaning of Paper*; Canadian Conservation Institute Technical Bulletin; Government of Canada Publications: Dartmouth, NS, Canada, 2005; Volume 11, pp. 1–12. Available online: https://publications.gc.ca/collections/collection_2016/pch/NM95-55-11-2001-eng.pdf (accessed on 22 December 2023).
13. Brokerhof, A.W.; De Groot, S.; Perdesoli, J.L.; Van Keulen, H.; Reissland, B.Y.; Ligterink, F. Dry-cleaning. The effect of new wishabs Spezialschwamm and Spezialpulver on paper. *Pap. Restaur.* **2002**, *3*, 13–19.
14. Noehles, M. Die Kunst des Radierens: Radiermittel im Überblick. *Pap. Restaur.* **2002**, *3*, 22–28.
15. Nitzberg, N.; Duhl, S. *Surface Cleaning, Paper Conservation Catalog*; American Institute for Conservation Book and Paper Group, AIC: Washington, DC, USA, 1988.
16. Pearlstein, E.J.; Cabelli, D.; King, A.; Indictor, N. Effects of Eraser Treatment on Paper. *J. Am. Inst. Conserv.* **1982**, *22*, 1–12. [CrossRef]
17. Sterlini, P. Surface cleaning products and their effects on paper. *Pap. Conserv. News* **1995**, *76*, 3–7.
18. Chércoles Asensio, R.; de la Roja, J.M.; Navarro Manteca, E.; San Andrés Moya, M. *Uso de Gomas de Borrar para Limpieza Mecánica de Obra Gráfica. Valoración de su Eficacia Limpiadora y Efectos Sobre el Papel*; En Conservación de arte contemporáneo: 20ª jornada, febrero 2019; Museo Nacional Centro de Arte Reina Sofía: Madrid, Spain, 2019; pp. 89–102.
19. James, C.; Cohn, M.B. *Old Master Prints and Drawings: A Guide to Preservation and Conservation*; Amsterdam University Press: Amsterdam, The Netherlands, 1997; pp. 237–238.
20. McInnis, K. Two studies in paper conservation practice. Dry cleaning of paper. *ICCM Bull.* **1980**, *6*, 33–52. [CrossRef]
21. Daudin-Schotte, M.; Bisschoff, M.; Joosten, I.; van Keulen, H.; van den Berg, K.J. Dry Cleaning Approaches for Unvarnished Paint Surfaces. In *New Insights into the Cleaning of Paintings, Proceedings from the Cleaning 2010 International Conference*; Universidad Politécnica de Valencia and Museum Conservation Institute: Valencia, Spain; Smithsonian Institute: Washington, DC, USA, 2013; pp. 209–219.
22. Moffatt, E.; Laver, M. Erasers and related dry cleaning materials. *CCI Anal. Rep.* **1981**, *1738*, 2–7.

23. Silverman, R.; Irwin, S. Fire and Ice Revisited: A Comparison of Two Soot Removal Techniques for Book. *Int. Preserv. News* **2009**, *49*, 31–35.
24. Moy, S.A. Groomstick: A study to determine its potential to deposit. In *Objects Specialty Group Postprints Volume 11, 2004*; American Institute for Conservation of Historic & Artistic Works: Washington, DC, USA, 2007; Volume 11, pp. 29–42.
25. Iglesias-Campos M, Á.; Pérez JL, P.; Fortes, S.G. Microblasting cleaning for façade repair and maintenance: Selecting technical parameters for treatment efficiency. *Constr. Build. Mater.* **2015**, *94*, 605–612. [CrossRef]
26. Iglesias-Campos, M.; Prada, J.L.; García, S. Spot analysis to determine technical parameters of microblasting cleaning for building materials maintenance. *Constr. Build. Mater.* **2017**, *132*, 21–32. [CrossRef]
27. Iglesias-Campos, M.A.; García Fortes, S.; Prada Pérez, J.L. Influence of projection angle in sandblasting cleaning on detrictic stone materials in Architectural Heritage. *Mater. De Construcción* **2014**, *64*, e021. [CrossRef]
28. Iglesias-Campos, M.A. Effects of mechanical cleaning by manual brushing and abrasive blasting on lime render coatings on Architectural Heritage. *Mater. De Construcción* **2014**, *64*, e039. [CrossRef]
29. Moropoulou, A.; Delegou, E.T.; Avdelidis, N.P.; Koui, M. Assessment of cleaning conservation interventions on architectural surfaces using an integrated methodology. *MRS Online Proc. Libr. OPL* **2002**, *712*, II2-5. [CrossRef]
30. Iglesias-Campos, M.; Ruiz-Recasens, C.; Díaz-Gonzalez, E. First experiments for the use of microblasting technique with powdered cellulose as a new tool for dry-cleaning artworks on paper. *J. Cult. Herit.* **2014**, *15*, 365–372. [CrossRef]
31. Iglesias-Campos, M.; Ruiz-Recasens, C. Surface cleaning of intaglio prints with microblasting powdered cellulose and erasing: Treatment effects on inks and support texture. *J. Cult. Herit.* **2015**, *16*, 329–337. [CrossRef]
32. Stoveland, L.P.; Frøysaker, T.; Stols-Witlox, M.; Grøntoft, T.; Steindal, C.C.; Madden, O.; Ormsby, B. Evaluation of novel cleaning systems on mock-ups of unvarnished oil paint and chalk-glue ground within the Munch Aula Paintings Project. *Herit. Sci.* **2021**, *9*, 144. [CrossRef]
33. ARBOCEL® BE 600-30 PU.SpecialChem. Available online: https://coatings.specialchem.com/product/a-jrs-rettenmaier-arbocel-be-600-30-pu (accessed on 22 December 2023).

polymers

MDPI

Article

Facile Strategy for Boosting of Inorganic Fillers Retention in Paper

Klaudia Maślana [1,*], Krzysztof Sielicki [1], Karolina Wenelska [1,*], Tomasz Kędzierski [1], Joanna Janusz [2], Grzegorz Mariańczyk [2], Aleksandra Gorgon-Kuza [2], Wojciech Bogdan [2], Beata Zielińska [1] and Ewa Mijowska [1]

[1] Department of Nanomaterials Physicochemistry, Faculty of Chemical Technology and Engineering, West Pomeranian University of Technology in Szczecin, Piastow Ave. 45, 70-311 Szczecin, Poland; krzysztof-sielicki@zut.edu.pl (K.S.); tomasz.kedzierski@zut.edu.pl (T.K.); bzielinska@zut.edu.pl (B.Z.); emijowska@zut.edu.pl (E.M.)

[2] Arctic Paper Kostrzyn SA, ul. Fabryczna 1, 66-470 Kostrzyn nad Odra, Poland; joanna.janusz@arcticpaper.com (J.J.); grzegorz.marianczyk@arcticpaper.com (G.M.); wojciech.bogdan@arcticpaper.com (W.B.)

* Correspondence: klaudia.maslana@zut.edu.pl (K.M.); kwenelska@zut.edu.pl (K.W.)

Abstract: Achieving the desired properties of paper such as strength, durability, and printability remains challenging. Paper mills employ calcium carbonate ($CaCO_3$) as a filler to boost paper's brightness, opacity, and printability. However, weak interaction between cellulose fibers and $CaCO_3$ particles creates different issues in the papermaking industry. Therefore, this study explores the influence of various inorganic additives as crosslinkers such as mesoporous SiO_2 nanospheres, TiO_2 nanoparticles, h-BN nanoflakes, and hydroxylated h-BN nanoflakes (h-BN-OH) on inorganic fillers content in the paper. They were introduced to the paper pulp in the form of a polyethylene glycol (PEG) suspension to enable bonding between the inorganic particles and the paper pulp. Our findings have been revealed based on detailed microscopic and structural analyses, e.g., transmission and scanning electron microscopy, X-ray diffraction, Raman spectroscopy, and N_2 adsorption/desorption isotherms. Finally, the inorganic fillers ($CaCO_3$ and respective inorganic additives) content was evaluated following ISO 1762:2001 guidelines. Conducted evaluations allowed us to identify the most efficient crosslinker (SiO_2 nanoparticles) in terms of inorganic filler retention. Paper sheets modified with SiO_2 enhance the retention of the fillers by ~12.1%. Therefore, we believe these findings offer valuable insights for enhancing the papermaking process toward boosting the quality of the resulting paper.

Keywords: cellulose; crosslinker; fillers; polymer

1. Introduction

The process of papermaking involves converting raw materials, like wood fibers or recycled paper, into a product that meets quality standards and market demands. One of the main challenges in this process is achieving the desired properties in the final product, such as strength, durability, brightness, opacity, and printability, which enhance the strength and stiffness of the paper, avoiding poor folding, tearing, and cracking resistance. To achieve this, paper mills often use fillers such as $CaCO_3$ [1]. However, the weak interaction between cellulose fibers and $CaCO_3$ particles can lead to a range of problems in papermaking [2,3]. This problem is related to the cellulose fibers' structural properties, which have a highly crystalline structure with a low surface-area-to-volume ratio. As a consequence, a limited availability of active sites for hydrogen bonds, both between fibers and with $CaCO_3$ particles, is observed [4,5]. The interaction between cellulose fibers and $CaCO_3$ particles affects paper mass drainage and retention. The presence of fillers can interfere with water flow through the paper machine, leading to longer drying times and increased energy consumption [6].

Various strategies have been developed to overcome these obstacles to enhance the affinity of the paper mass to $CaCO_3$. One of the strategies is the addition of crosslinkers, which can improve the interaction between the cellulose fibers and $CaCO_3$ particles. Crosslinkers are chemical compounds that can form bonds between the cellulose fibers, creating a more stable network that can better resist the disruptive effects of fillers [7,8]. The addition of fillers such as SiO_2 [9], TiO_2 [10], h-BN [11], and h-BN-OH [12] has been shown to be effective in improving the affinity of the paper mass to $CaCO_3$. These compounds can form bonds with both the cellulose fibers and $CaCO_3$ particles, creating a stronger network that improves the strength, stiffness, and printability of the paper. Therefore, using crosslinkers in papermaking is an important strategy for improving the quality and performance of paper products.

Silicon dioxide (SiO_2) can form covalent bonds with both the cellulose fibers and $CaCO_3$ particles. The SiO_2 particles can also serve as a connector between the cellulose fibers and $CaCO_3$ particles, helping to strengthen the inter-fiber bonding and improve the stiffness and strength of the paper. In addition to its role as a crosslinker, SiO_2 can also improve the drainage and retention of the paper mass. The SiO_2 particles are hydrophilic, which means that they can help absorb water and improve the flow of the paper mass through the paper machine. This can lead to faster drying times and increased productivity. SiO_2 can be added to the paper mass in various forms, including colloidal silica, precipitated silica, and silica fume [9,13].

Titanium dioxide (TiO_2) as a crosslinker can also improve the optical properties of paper products. TiO_2 is a white pigment that can reflect and scatter light, leading to a brighter and more opaque paper. This can be particularly beneficial in applications where high brightness and opacity are expected. In addition, TiO_2 can also improve the drainage and retention of the paper mass—similar to SiO_2. This can lead to faster drying times and increased productivity. TiO_2 can be added to the paper mass in various forms, including rutile, anatase, and nano-sized TiO_2 particles. Rutile and anatase are two crystalline forms of TiO_2, with rutile being the most commonly used form in papermaking due to its higher refractive index and opacity. Nano-sized TiO_2 particles have a smaller particle size and can provide additional benefits such as improved printability and ink adhesion [10,14].

Hexagonal boron nitride (h-BN) is a layered material that consists of hexagonally arranged boron and nitrogen atoms. It has a high surface area and unique surface chemistry that make it attractive for various applications. When added to the paper mass, h-BN can form covalent bonds with both the cellulose fibers and $CaCO_3$ particles, improving the interaction between them and creating a more stable network. The h-BN particles can also serve as a connector between the fibers and fillers, enhancing the stiffness and strength of the paper. h-BN-OH is a derivative of h-BN that has been functionalized with hydroxyl groups. The hydroxyl groups increase the surface energy and wettability of the h-BN particles, allowing them to interact with the cellulose fibers and $CaCO_3$ particles more effectively. The hydroxyl groups can also provide additional chemical functionality, allowing for further modifications and improvements in the paper properties [12,15].

In this work, the impact of different inorganic fillers on calcium carbonate content in the paper was investigated. For this reason, mesoporous SiO_2 nanoparticles, TiO_2 nanoparticles, h-BN nanoflakes, and hydroxylated h-BN nanoflakes (h-BN-OH) have been explored as additives. They have been introduced to the paper pulp in the form of a polyethylene glycol (PEG) mixture to induce bonding between the inorganic structures and paper pulp components. Various characterization methods were employed to determine the chemical structure and morphology of prepared samples, including TEM, SEM, XRD, Raman spectroscopy, and TGA. The ash content (residual solid particles after the combustion process) was evaluated according to ISO 1762:2001. It allowed us to select mesoporous silica as the most efficient filler, enhancing the retention of the fillers by 12.1% in respect to unmodified paper sheets.

2. Experimental Part

2.1. Chemicals

Eucalyptus-derived cellulose fibers, wood-derived cellulose fibers, chemical thermomechanical pulp cellulose (CTMP), cationic starch, calcium carbonate, and potassium amyl xanthate (PAX) were derived by Arctic Paper Kostrzyn SA. Polyethylene glycol 2000 (PEG, M = 1800–2200 g/mol) was purchased from Carl Roth, Karlsruhe, Germany. Titanium dioxide was kindly supplied by Grupa Azoty Police (Police, Poland). Tetraethyl orthosilicate (TEOS) and boron nitride (BN, ~1 μm, 98%) were purchased from Sigma Aldrich (Poznań, Poland). Ammonia solution (NH_4·OH, 25%), sulfuric acid (H_2SO_4, 95%), nitric acid (HNO_3, 65%), and potassium permanganate ($KMnO_4$) were delivered from Chempur (Piekary Śląskie, Poland).

2.2. Synthesis of Silicon Dioxide (SiO_2)

SiO_2 nanoparticles were prepared according to a modified Stöber method [16]; 5.8 mL of TEOS and 150 mL of ethanol were initially mixed in a round bottom flask and stirred for 10 min at room temperature (RT). Next, 7.8 mL of ammonia solution was added, and the mixture was further stirred for 12 h. After that, the product was separated by centrifugation, washed a few times with ethanol, and dried.

2.3. Synthesis of Hexagonal Boron Nitride (h-BN)

A total of 0.2 g of bulk boron nitride was placed in a flask, and then, 200 mL of ethanol was added. Afterward, the obtained mixture was sonicated using an ultrasonic homogenizer for 12 h. The final product was washed with distilled water and dried at 80 °C.

2.4. Synthesis of Oxidized Hexagonal Boron Nitride (h-BN-OH)

To prepare h-BN-OH, a modified Hummers method was applied [12]. Briefly, 0.2 g of h-BN powder was placed in a round-bottomed flask, and then, 13.5 mL of H_2SO_4 and 4.4 mL of HNO_3 were added. The mixture was stirred to obtain a homogenous dispersion. After that, 1.2 g of $KMnO_4$ was partially introduced, and finally, the mixture was heated to 90 °C and kept at this temperature for 12 h. Next, the mixture was cooled to RT, filtrated, and washed a few times with distilled water until the pH value approached 7. Finally, the product was dried at 80 °C overnight.

2.5. Preparation of PEG Solution

In the experiments, the different polyethylene glycol (PEG) variants (PEG 2000, PEG 4000, PEG 10000, and PEG 20000) were tested to choose the optimal one. During the preparation of paper sheets using the Rapid-Köthen machine (Lodz, Poland) different performance characteristics of the paper with the tested PEG variants were evaluated. The final selection of PEG 2000 was based on its superior performance during the paper sheet preparation process. PEG 2000 exhibited the best solubility in the chosen solvent and its integration with paper pulp. An appropriate PEG 2000 amount was added to 1 L of distilled water, and with the use of a magnetic stirrer, it was completely dissolved. The amount of PEG 2000 was calculated in 1 ton of dry pulp to obtain a concentration of 1 kg of PEG/ton of dry cellulose (typical commercial procedure).

2.6. Preparation of Paper Sheets

As a reference sample, a sheet of paper without the addition of inorganic fillers was prepared. The reference paper sample contained only standard commercial components used for the production of paper sheets. Paper with a grammage of 80 g/m^2 was created by combining three types of cellulose fibers: short-fiber cellulose pulp (eucalyptus derived), long-fiber cellulose pulp (birch-derived), and chemical thermomechanical pulp cellulose (CTMP) with a mass ratio of 70/20/10, respectively. The cellulosic mass was mixed in a plastic container using a mechanical stirrer for 15 min. Subsequently, PAX and a cationic

starch solution (3.8%) were added to the mixture with 2 and 5 kg per ton of dry cellulose fibers, respectively. Finally, $CaCO_3$ and appropriate crosslinkers (SiO_2, TiO_2, h-BN, and h-BN-OH) dispersed in PEG solution were introduced to the system. To do so, 1 kg of crosslinkers per 1 ton of dry cellulose fibers was first dispersed in 100 mL of PEG solution and sonicated to obtain a homogeneous mixture. The prepared mixture was mechanically stirred with cellulosic mass for 15 min. Paper sheets were formed using a Rapid-Köthen Automatic Sheet-Forming Machine (Lodz, Poland), following the guidelines of PN-ISO 5262–2. This method of producing modified paper sheets using the mentioned equipment replicates the conditions found in large-scale production, facilitating easy scalability of the entire process. The prepared paper sheets were denoted as reference for the sample without any crosslinker, and PEG/SiO_2, PEG/TiO_2, PEG/h-BN, and PEG/h-BN-OH for samples where additional PEG suspension containing SiO_2, TiO_2, h-BN, and h-BN-OH were added, respectively. The reference was prepared by the same procedure but without the addition of PEG/inorganic filler mixture.

2.7. Characterization

High-resolution transmission electron microscopy (HR-TEM) (Washington, DC, USA) imaging was performed with the FEI Tecnai F20 microscope at an accelerating voltage of 200 kV. The images were taken directly on sample-drop-cast Cu grids with carbon film. A scanning electron microscope (SEM) (VEGA3, TESCAN) (Brno, Czech Republic) was used to determine the morphology of the prepared sheets. The chemical bonding of the structures in the paper sheets was examined using Raman spectroscopy (InVia Renishaw, Wotton-under-Edge, UK) equipped with an excitation wavelength of 785 nm. It is an ideal method to study the structural properties of the nanomaterials. The phase composition was determined by X-ray diffraction (XRD) patterns by using an Aeris (Malvern Panalytical, Malvern, UK) diffractometer using Cu Kα radiation. The content of $CaCO_3$ was determined in accordance with the International Organization of Standardization (ISO 1762:2001). The thermogravimetric analysis was conducted using an SDT Q600 Thermogravimeter (TA Instruments, New Castle, DE, USA) under air flow of 100 mL/min. In each case, the samples were heated from room temperature to 600 °C at a linear heating rate of 10 °C/min. The samples were measured in an alumina crucible with a mass of about 5.0 mg. N2 adsorption/desorption isotherms were acquired at liquid nitrogen temperature (77 K) using a Micromeritics ASAP 2460 (Norcross, GA, USA). The Brunauer–Emmett–Teller (BET) and density functional theory (DFT) methods were adopted to calculate the specific surface area and pore size distribution.

3. Results

TEM images of SiO_2, TiO_2, h-BN, and h-BN-OH are presented in Figure 1. SiO_2 and TiO_2 reveal distinct morphologies. SiO_2 (Figure 1A) exhibits particles with spherical morphology, showcasing visible porosity within the silica structure. High porosity directly leads to the high surface area of SiO_2. Similarly, TiO_2 (Figure 1B) nanoparticles display a spherical or quasi-spherical morphology, relative to SiO_2, and exhibit observable porosity with evident pores. For h-BN, the TEM image illustrates a flat and two-dimensional (2D) sheet-like structure. It is a layered material with a hexagonal lattice resembling graphene, showcasing a thin and planar 2D nature. Hydroxylated h-BN (h-BN-OH, Figure 1D) also portrays this 2D planar structure, with the presence of hydroxyl (OH) groups altering surface characteristics but not the fundamental structural morphology.

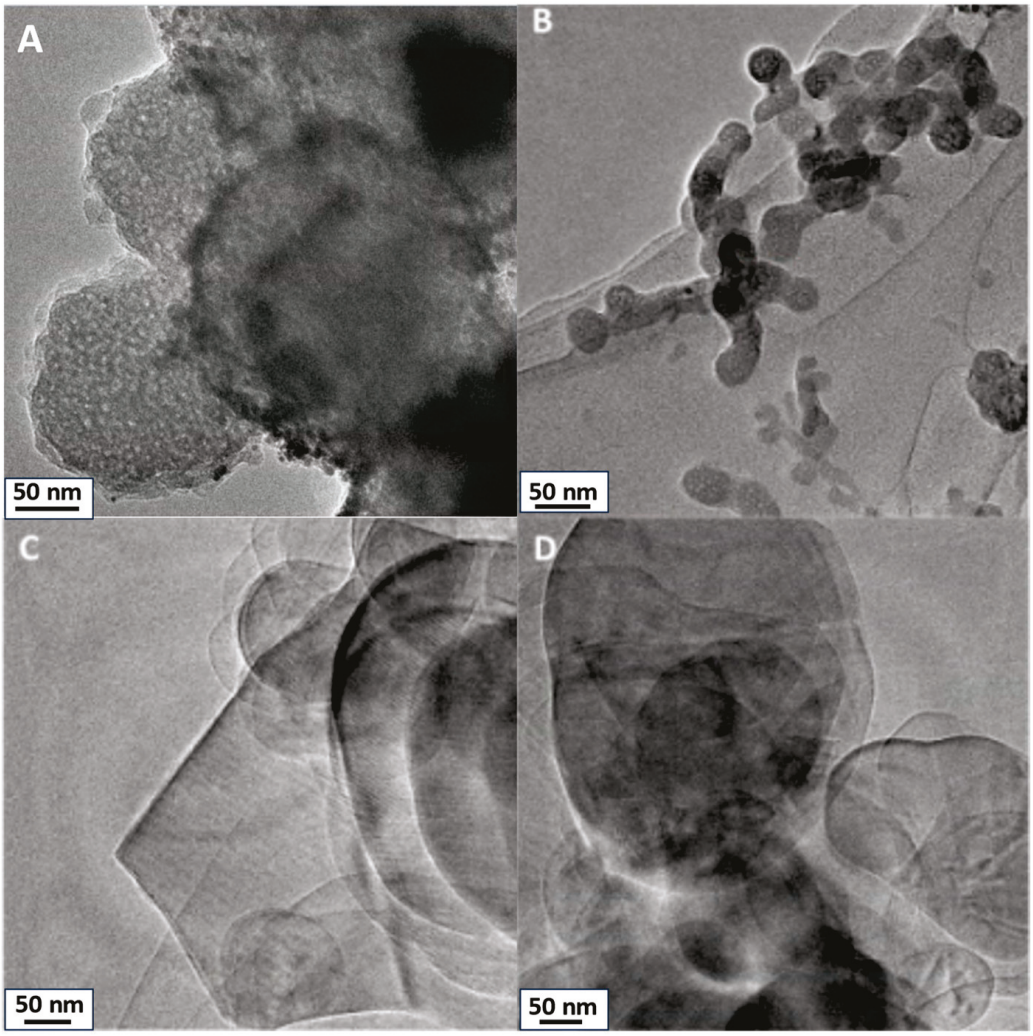

Figure 1. TEM images of crosslinkers: (**A**) SiO_2, (**B**) TiO_2, (**C**) h-BN, and (**D**) h-BN-OH.

XRD patterns of all crosslinkers (SiO_2, TiO_2, h-BN, and h-BN-OH) are shown in Figure 2. Both h-BN and h-BN-OH show reflections corresponding to boron nitride (2θ = ~26.7°, 41.6°, 43.7°, 54.9°, 75.6°; ICDD PDF no. 00-034-0421). For h-BN-OH, a clear shift of peaks toward the higher angles is observed in comparison to h-BN. For example, the signal at ~26.39°, corresponding to the (002) plane of h-BN, is shifted to 26.83°. This is due to the expansion of crystallographic structure by the incorporation of the -OH functional groups into the lattice. SiO_2 exhibits one broad peak centered at around 23°, which can be assigned to the amorphous structure of silica oxide [17,18]. TiO_2 is composed of two crystal phases: anatase (ICDD PDF no. 04-014-8515) and rutile (ICDD PDF no. 00-021-1276). There are ~83.9% of anatase and ~16.1% of rutile in the sample [19].

N_2 adsorption/desorption isotherms acquired at liquid nitrogen temperature are presented in Figure 3. The isotherms for TiO_2, SiO_2, h-BN, and h-BN-OH are type II isotherms, where there is a wide range of pore sizes [20]. From TEM, it is clear that pores are present. The highest content is in SiO_2, which can result in a high surface area. The highest surface area was determined for the SiO_2, which is 275.4 m^2/g. h-BN-OH exhibits a larger specific surface area compared to h-BN, which is 38.7 m^2/g and 19.8 m^2/g, respectively. This is due to the expansion of individual h-BN layers by hydroxyl groups and the creation of a larger surface area that is accessible for N_2 adsorption. The lowest specific surface area from all crosslinkers was measured for the TiO_2 (10.8 m^2/g). A similar dependence can be observed for the total pore volume (Figure 3b). The measured total pore

volumes were 0.248, 0.035, 0.011, and 0.008 cm^3/g for SiO_2, h-BN-OH, h-BN, and TiO_2, respectively. Data collected from the N_2 adsorption/desorption test are collected in Table 1.

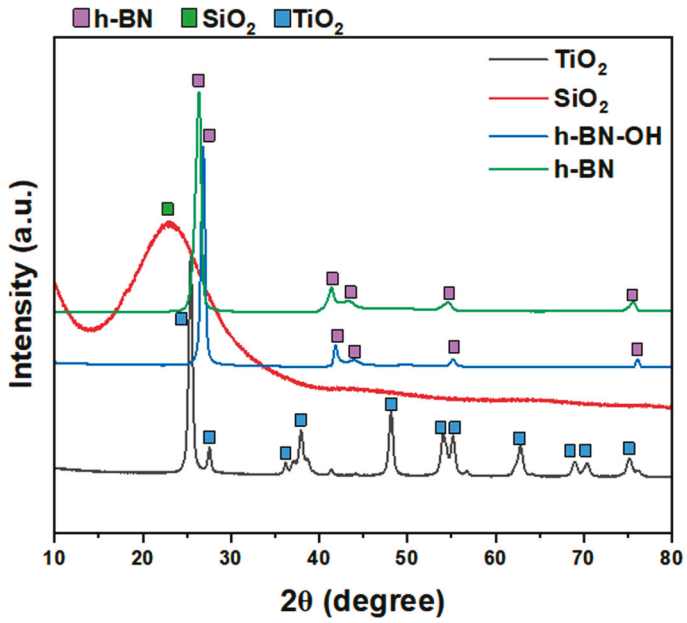

Figure 2. XRD patterns of crosslinkers: TiO_2, SiO_2, h-BN-OH, and h-BN.

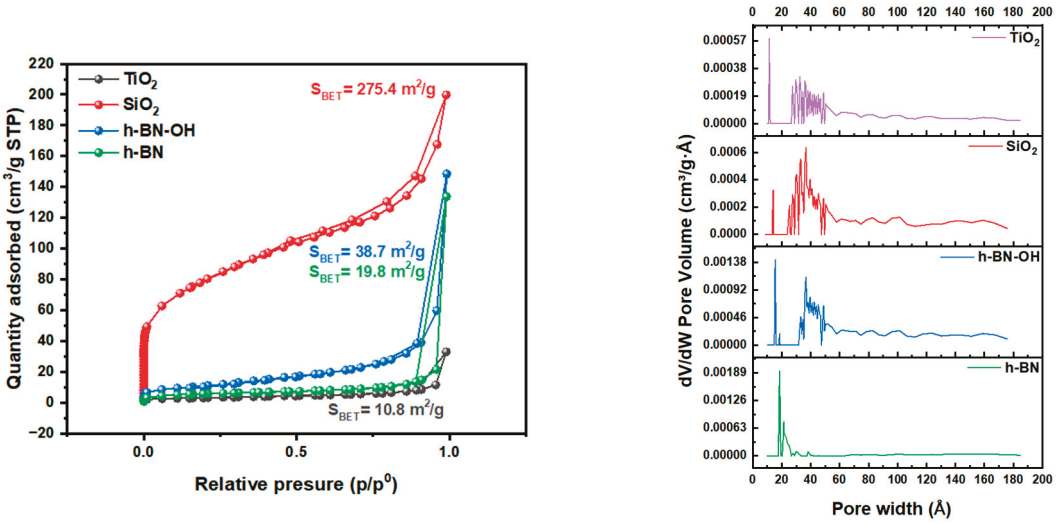

(**a**) (**b**)

Figure 3. (**a**) N_2 adsorption/desorption isotherms of crosslinkers, TiO_2, SiO_2, h-BN, and h-BN-OH, and (**b**) pore size distribution.

Table 1. BET surface area, micropore volume, and median pore width of samples.

	BET Surface Area (m^2/g)	Total Pore Volume (cm^3/g)	Median Pore Width (nm)
TiO_2	10.8	0.00772	0.9509
SiO_2	275.4	0.24762	1.0085
h-BN-OH	38.7	0.03475	1.1414
h-BN	19.8	0.01100	1.2515

Next, the impact of different crosslinkers on the morphology of the prepared paper samples was evaluated via SEM (Figure 4). The reference sample exhibits the presence of $CaCO_3$ between the cellulose fibers with uneven distribution. The PEG/SiO_2 and PEG/TiO_2 paper samples (Figure 4B,C) show a more even distribution of $CaCO_3$ particles along cellulose fibers compared to the reference sample. In the material with PEG/SiO_2, the amount of $CaCO_3$ between the fibers is much higher compared to the reference sample. Paper samples with h-BN and h-BN-OH exhibit agglomerated $CaCO_3$ particles. This may lead to increased permeability of $CaCO_3$ through cellulose fibers, which will result in a reduced content of calcium carbonate in the sample.

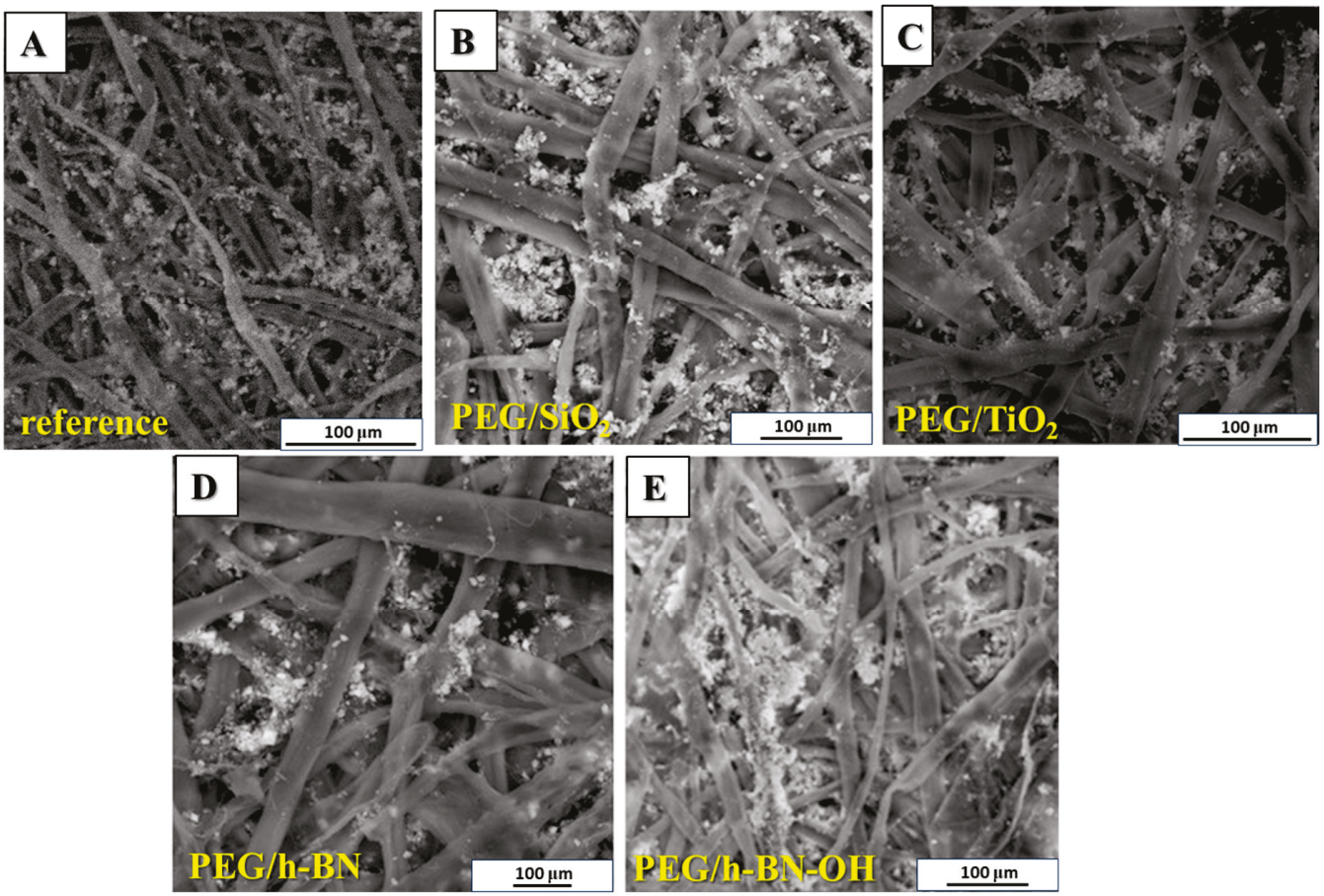

Figure 4. SEM images of (**A**) reference paper and paper containing different crosslinkers: (**B**) PEG/SiO_2, (**C**) PEG/TiO_2, (**D**) PEG/h-BN, and (**E**) PEG/h-BN-OH.

Figure 5 presents the Raman spectra of paper samples (reference, PEG/SiO_2, PEG/TiO_2, PEG/h-BN, and PEG/h-BN-OH). Cellulose is a linear polymer made up of repeating glucose units linked by β-1,4-glycosidic bonds. It exhibits a high degree of crystallinity, with both crystalline and amorphous regions in its structure. Raman spectroscopy is sensitive to various vibrational modes present in cellulose. The main Raman-active modes for cellulose fibers include C-C and C-O bonds. These vibrations are observed around 1095 cm^{-1}, offering valuable information about the molecular bonds within the cellulose structure [21,22]. Next, out-of-plane ring bending (C-C-C and C-O-C), observed in the range of 400 to 600 cm^{-1}, provides insights into the spatial arrangement and flexibility of the cellulose rings. Additionally, Raman peaks associated with deformations in the CH_2 and CH_3 groups are prominent in the range of 1300 to 1470 cm^{-1} [23] (orange zones). Furthermore, Raman spectroscopy studies revealed the distinctive peaks of $CaCO_3$ corresponding to two different forms: calcite (green zones) and vaterite (blue zones). The peak at 1085 cm^{-1} signifies calcite, while the peaks at 1080 and 1090 cm^{-1} represent vaterite, specifically

corresponding to the Ag internal mode derived from the v_1 symmetric stretching mode of the carbonate ion in each material. The v_4 in-plane bending mode of carbonate is observed at 712 cm^{-1} for calcite and 739–749 cm^{-1} for vaterite. It is noteworthy that the characteristic peak for vaterite was not detected in the case of PEG/h-BN and PEG/hBN-OH. However, the reason of the lack of this peak is not clear.

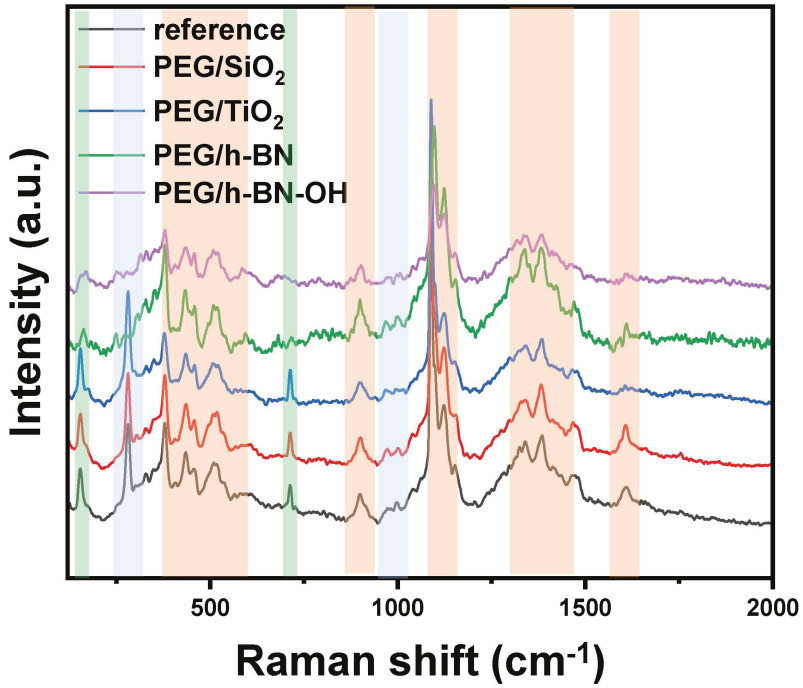

Figure 5. Raman spectra of reference paper and paper with different crosslinkers (PEG/SiO_2, PEG/TiO_2, PEG/h-BN, and PEG/h-BN-OH).

Figure 6 shows the X-ray diffraction patterns of the reference, PEG/SiO_2, PEG/TiO_2, PEG/h-BN, and PEG/h-BN-OH paper samples. In the patterns of all samples, two characteristic phases were identified, i.e., cellulose and calcium carbonate ($CaCO_3$). The three observed peaks (broad peaks) at 2θ = 16°, 22°, and 35° correspond to cellulose. However, a series of reflections at 2θ equal to ~23°, 29.4°, 36°, 39.4°, 43.2°, 47.5°, and 48.5° are characteristic for $CaCO_3$ (ICDD no. 00-005-2586). The XRD diffractograms also show two peaks (low intensity) at ~30.9° and 31.6°, which can be attributed to other calcium carbonate polymorphs (e.g., aragonite and vaterite) (ICDD no. 01-075-9984, 00-024-0030). The reflections, which correspond to the calcium carbonate, are narrow and intense (compared to the cellulose peaks, the peaks are wider and of lower intensity), which indicates the high crystallinity of the used $CaCO_3$. A lack of a significant effect of the fillers on the intensity and location of individual reflections was found, which may be attributed to the small amount of the additives.

To define the thermal behavior of the paper samples, thermogravimetric analysis (TGA) was applied. The TGA results for the reference and the PEG/SiO_2, PEG/TiO_2, PEG/h-BN, and PEG/h-BN-OH papers are presented in Figure 7. For all samples, three significant weight decreases are noticeable. First, weight loss is observed at 90 °C and is attributed to the evaporation of the adsorbed water or moisture present in the samples. Furthermore, two stages of cellulose degradation are observed. The first decomposition stage starts at 250 °C. Cellulose consists of glucose molecules linked together by β-1,4-glycosidic bonds [24]. During this stage, glycosidic bonds break, resulting in the release of volatile products and various volatile organic compounds, such as acetic acid and levoglucosan [25,26]. Next, a second decomposition stage starting at 350 °C is observed. During this stage, additional volatile products are formed as cellulose decomposes. Carbon dioxide (CO_2) and carbon monoxide (CO) are released at this stage as a result of the

breakdown of more complex cellulose structures. Starting with the reference, a gradual mass loss with increasing temperature leads to a residue of approximately 26%, indicating the ash content in the reference sample. In the cases of PEG/SiO_2, PEG/TiO_2, PEG/h-BN, and PEG/h-BN-OH, the thermal profiles display analogous mass loss curves, resulting in residual masses of about 27.0%, 25.7%, 25.5%, and 24.8%, respectively.

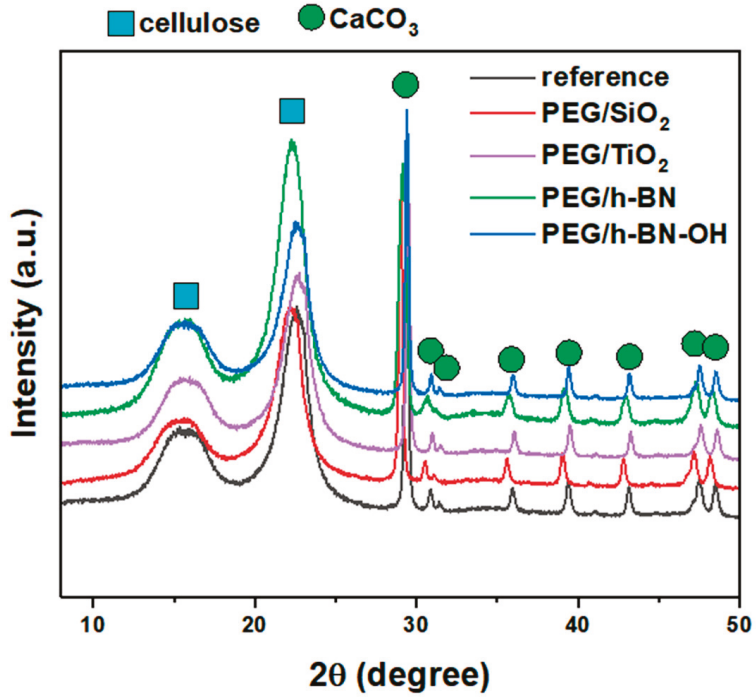

Figure 6. X-ray diffraction patterns of reference paper and paper with different crosslinkers: PEG/SiO_2, PEG/TiO_2, PEG/h-BN, and PEG/h-BN-OH.

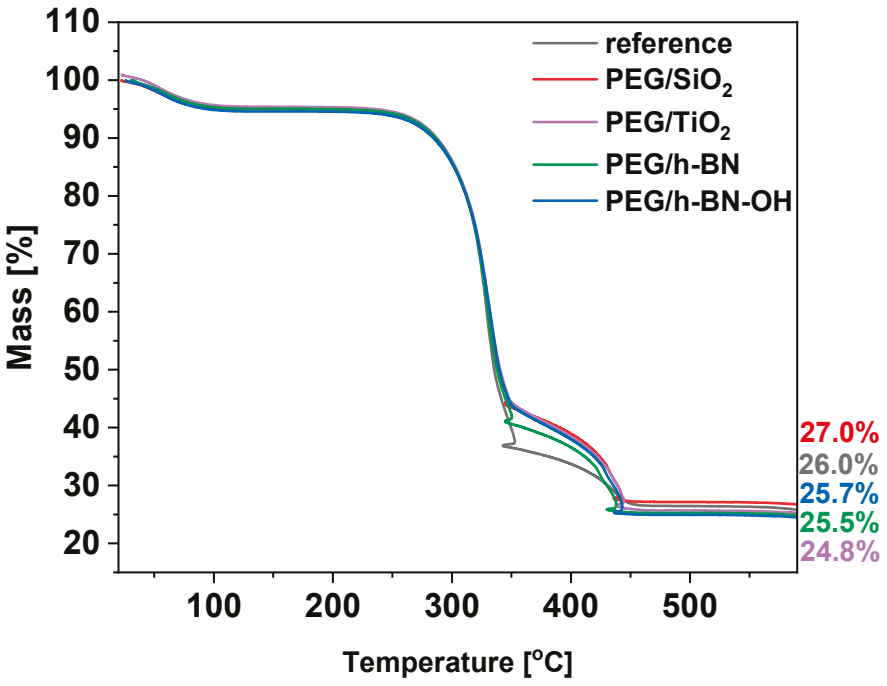

Figure 7. TGA plots of reference paper and paper with crosslinkers: PEG/SiO_2, PEG TiO_2, PEG/h-BN, and PEG/h-BN-OH.

To determine the ash content in the paper, the guidelines set by the International Organization of Standardization (ISO 1762:2001) were applied. The procedure was through sample ignition at 525 °C. The ash content in the reference and modified papers (PEG/SiO_2, PEG/TiO_2, PEG/h-BN, and PEG/h-BN-OH) are presented in Table 2.

Table 2. Data obtained from the International Organization of Standardization (ISO) standard (ISO 1762:2001) ash content for all samples.

	Ash Content (%)
Reference	28.1
PEG/SiO_2	**31.5**
PEG/TiO_2	25.7
PEG/h-BN	25.1
PEG/h-BN-OH	23.2

Based on the results presented in Table 2, the addition of SiO_2 nanoparticles increased the ash content in the paper significantly. This means that this facile strategy boosts $CaCO_3$ retention on cellulose fibers by 12.1% in the presence of PEG/SiO_2 as a nanofiller, which can be related to the abundance of active sites available for $CaCO_3$ bonding. The opposite trend can be observed for PEG/TiO_2, PEG/h-BN, and PEG/h-BN-OH, where ash content is 8.1, 11.1, and 17.5% lower compared to the reference paper, respectively.

In summary, based on the above results, it can be inferred that the addition of porous SiO_2 in the form of a PEG suspension is the most promising crosslinker increasing the affinity of $CaCO_3$ to cellulose fibers. This conclusion is supported by numerous analyses, such as TGA, and ISO 1762:2001 tests, which showed that the inorganic fillers content after the introduction of PEG/SiO_2 increased by 12.1%, which proves the potential of this facile strategy in practical application in the paper industry. This may be because SiO_2 possesses the largest specific surface area among other crosslinkers (TEM and N_2 adsorption/desorption), increasing affinity to cellulose fibers, resulting in higher inorganic filler content retention.

4. Conclusions

In summary, this study investigated the influence of various crosslinkers (TiO_2, SiO_2, h-BN, and h-BN-OH) on the inorganic filler content in paper samples. Raman spectroscopy and XRD confirmed that the chemical structure of the samples remained insignificantly changed upon the addition of these compounds. This study further delved into the molecular dynamics of cellulose through various Raman peaks associated with specific vibrational modes. Additionally, Raman spectroscopy identified characteristic peaks for $CaCO_3$, distinguishing between calcite and vaterite forms. Moreover, the introduction of h-BN and h-BN-OH led to the formation of agglomerates and uneven distribution of $CaCO_3$ particles on cellulose fibers, resulting in decreased ash content after testing. Among the crosslinkers, SiO_2 suspended in a PEG solution emerged as a promising candidate due to its excellent affinity to cellulose and high surface area, enhancing inorganic filler content in the paper. These findings contribute to a deeper understanding of how different crosslinkers impact the composition and structure of paper samples and allow the boosting of the content of inorganic compounds in the paper sheet, reducing the contribution of cellulose.

Author Contributions: Methodology, K.W. and T.K.; Investigation, W.B.; Writing—original draft, K.M. and K.S.; Visualization, B.Z.; Supervision, E.M.; Project administration, A.G.-K.; Funding acquisition, J.J. and G.M. All authors have read and agreed to the published version of the manuscript.

Funding: This research received funding from the National Centre for Research and Development (Poland): POIR.01.01.01-00-0272/19-00.

Institutional Review Board Statement: Not applicable.

Data Availability Statement: The data presented in this study are available from the corresponding author upon reasonable request.

Conflicts of Interest: The authors declare no conflict of interest.

References

1. Calcium Carbonate in the Paper Industry â¢ Blessing for Coated Papermaking and Curse for Recycling. Available online: https://imisrise.tappi.org/TAPPI/Products/14/NOV/14NOV47.aspx (accessed on 22 June 2023).
2. Dalas, E.; Klepetsanis, P.G.; Koutsoukos, P.G. Calcium Carbonate Deposition on Cellulose. *J. Colloid Interface Sci.* **2000**, *224*, 56–62. [CrossRef] [PubMed]
3. Fimbel, P.; Siffert, B. Interaction of calcium carbonate (calcite) with cellulose fibres in aqueous medium. *Colloids Surf.* **1986**, *20*, 1–16. [CrossRef]
4. Guerra-Garcés, J.; García-Negrete, C.A.; Pastor-Sierra, K.; Arteaga, G.C.; Barrera-Vargas, M.; de Haro, M.C.J.; Fernández, A. Morphologically diverse $CaCO_3$ microparticles and their incorporation into recycled cellulose for circular economy. *Mater. Today Sustain.* **2022**, *19*, 100166. [CrossRef]
5. Kandirmaz, E.A.; Yenido, S.; Aydemir, C.; Karademir, A. Effect of using calcium carbonate ($CaCO_3$) in surface coating on liquid absorption of paper and some printability parameters. *Cellul. Chem. Technol.* **2020**, *54*, 485–493. [CrossRef]
6. Su, N. Preparation and performance of retention and drainage aid made of cationic spherical polyelectrolyte brushes. *e-Polymers* **2022**, *22*, 676–685. [CrossRef]
7. Salfitra, M.; Putra, A. Effect of calcium carbonate (caco3) additives on the quality of cellulose-based biodegradable plastics bacteria-polyethylene glycol (peg)of coconut water (*Cocos nucifera*). *Electrolyte* **2023**, *2*, 65–72. [CrossRef]
8. Watcharamul, S.; Lerddamrongchai, S.; Siripongpreda, T.; Rodtassana, C.; Nuisin, R.; Kiatkamjornwong, S. Effects of Carboxymethyl Cellulose/Nano-Calcium Carbonate Hydrogel Amendment of Loamy Sand Soil for Maize Growth. *ACS Agric. Sci. Technol.* **2022**, *2*, 1071–1080. [CrossRef]
9. Zhang, Y.; Wang, Q.; Wang, C.; Wang, T. High-strain shape memory polymer networks crosslinked by SiO_2. *J. Mater. Chem.* **2011**, *21*, 9073–9078. [CrossRef]
10. Roy, S.; Zhai, L.; Kim, H.C.; Pham, D.H.; Alrobei, H.; Kim, J. Tannic-Acid-Cross-Linked and TiO_2-Nanoparticle-Reinforced Chitosan-Based Nanocomposite Film. *Polymers* **2021**, *13*, 228. [CrossRef]
11. Aki, D.; Ulag, S.; Unal, S.; Sengor, M.; Ekren, N.; Lin, C.C.; Yılmazer, H.; Ustundag, C.B.; Kalaskar, D.M.; Gunduz, O. 3D printing of PVA/hexagonal boron nitride/bacterial cellulose composite scaffolds for bone tissue engineering. *Mater. Des.* **2020**, *196*, 109094. [CrossRef]
12. Onyszko, M.; Markowska-Szczupak, A.; Rakoczy, R.; Paszkiewicz, O.; Janusz, J.; Gorgon-Kuza, A.; Wenelska, K.; Mijowska, E. Few Layered Oxidized h-BN as Nanofiller of Cellulose-Based Paper with Superior Antibacterial Response and Enhanced Mechanical/Thermal Performance. *Int. J. Mol. Sci.* **2020**, *21*, 5396. [CrossRef] [PubMed]
13. Zeng, X.; Liu, Y.; He, R.; Li, T.; Hu, Y.; Wang, C.; Xu, J.; Wang, L.; Wang, H. Tissue paper-based composite separator using nano-SiO_2 hybrid crosslinked polymer electrolyte as coating layer for lithium ion battery with superior security and cycle stability. *Cellulose* **2022**, *29*, 3985–4000. [CrossRef]
14. Zhang, W.; Rhim, J.W. Titanium dioxide (TiO_2) for the manufacture of multifunctional active food packaging films. *Food Packag. Shelf Life* **2022**, *31*, 100806. [CrossRef]
15. Chen, L.; Xiao, C.; Tang, Y.; Zhang, X.; Zheng, K.; Tian, X. Preparation and properties of boron nitride nanosheets/cellulose nanofiber shear-oriented films with high thermal conductivity. *Ceram. Int.* **2019**, *45*, 12965–12974. [CrossRef]
16. Ghimire, P.P.; Jaroniec, M. Renaissance of Stöber method for synthesis of colloidal particles: New developments and opportunities. *J. Colloid Interface Sci.* **2021**, *584*, 838–865. [CrossRef] [PubMed]
17. Liang, Y.; Ouyang, J.; Wang, H.; Wang, W.; Chui, P.; Sun, K. Synthesis and characterization of core–shell structured SiO_2@YVO_4:Yb^{3+},Er^{3+} microspheres. *Appl. Surf. Sci.* **2012**, *258*, 3689–3694. [CrossRef]
18. Chandraboss, V.L.; Kamalakkannan, J.; Senthilvelan, S. Synthesis of AC-Bi@SiO_2 Nanocomposite Sphere for Superior Photocatalytic Activity Towards the Photodegradation of Malachite Green. *Can. Chem. Trans.* **2016**, *3*, 410–429. [CrossRef]
19. Spurr, R.A.; Myers, H. Quantitative Analysis of Anatase-Rutile Mixtures with an X-ray Diffractometer. *Anal. Chem.* **1957**, *29*, 760–762. [CrossRef]
20. Awe, A.A.; Opeolu, B.O.; Fatoki, O.S.; Ayanda, O.S.; Jackson, V.A.; Snyman, R. Preparation and characterisation of activated carbon from *Vitis vinifera* leaf litter and its adsorption performance for aqueous phenanthrene. *Appl. Biol. Chem.* **2020**, *63*, 12. [CrossRef]
21. Lahiri, S.K.; Liu, L. Fabrication of a Nanoporous Silica Hydrogel by Cross-Linking of SiO_2-H_3BO_3-Hexadecyltrimethoxysilane for Excellent Adsorption of Azo Dyes from Wastewater. *Langmuir* **2021**, *37*, 8753–8764. [CrossRef]
22. Hsieh, Y.C.; Yano, H.; Nogi, M.; Eichhorn, S.J. An estimation of the Young's modulus of bacterial cellulose filaments. *Cellulose* **2008**, *15*, 507–513. [CrossRef]
23. Schenzel, K.; Fischer, S. NIR FT Raman spectroscopy—A rapid analytical tool for detecting the transformation of cellulose polymorphs. *Cellulose* **2001**, *8*, 49–57. [CrossRef]

24. Zhu, C.; Krumm, C.; Facas, G.G.; Neurock, M.; Dauenhauer, P.J. Energetics of cellulose and cyclodextrin glycosidic bond cleavage. *React. Chem. Eng.* **2017**, *2*, 201–214. [CrossRef]
25. Huang, Y.B.; Fu, Y. Hydrolysis of cellulose to glucose by solid acid catalysts. *Green Chem.* **2013**, *15*, 1095–1111. [CrossRef]
26. Paajanen, A.; Vaari, J. High-temperature decomposition of the cellulose molecule: A stochastic molecular dynamics study. *Cellulose* **2017**, *24*, 2713–2725. [CrossRef]

polymers

MDPI

Article

Applications of Xylan Derivatives to Improve the Functional Properties of Cellulose Foams for Noise Insulation

Silviu Marian Nastac [1,2,*], Petronela Nechita [1,*], Maria Violeta Guiman [2,*], Mirela Roman [1] and Ioan Calin Rosca [2]

[1] Research Center for Mechanics of Machines and Technological Equipment, Engineering and Agronomy Faculty in Braila, "Dunarea de Jos" University of Galati, 810017 Braila, Romania; mirela.roman@ugal.ro
[2] Faculty of Mechanical Engineering, "Transilvania" University of Brasov, 500024 Brasov, Romania; icrosca@unitbv.ro
* Correspondence: snastac@ugal.ro (S.M.N.); petronela.nechita@ugal.ro (P.N.); violeta.guiman@unitbv.ro (M.V.G.)

Abstract: Cellulose-based foams present a high potential for noise insulation applications. These materials are bio-degradable, eco-friendly by both embedded components and manufacturing process, have low density and high porosity, and are able to provide good noise insulation characteristics compared with available petroleum-based foams currently used on a large scale. This paper presents the results of some investigations performed by the authors in order to improve the functional characteristics in terms of free surface wettability and structural integrity. Native xylan and xylan-based derivatives (in terms of acetylated and hydrophobized xylan) were taken into account for surface treatment of cellulose foams, suggesting that hemicelluloses represent by-products of pulp and paper industry, and xylan polysaccharides are the most abundant hemicelluloses type. The investigations were mainly conducted in order to evaluate the level to which surface treatments have affected the noise insulation properties of basic cellulose foams. The results indicate that surface treatments with xylan derivatives have slowly affected the soundproofing characteristics of foams, but these clearly have to be taken into account because of their high decrease in wettability level and improving structural integrity.

Keywords: cellulose fiber; foam-forming; xylan derivatives; noise insulation; wettability; sound absorption; sound transmission loss

1. Introduction

Foam-formed cellulose biomaterials represent a promising technology for developing lightweight and sustainable materials, which are in high demand for packaging, cushioning, and insulation applications [1–4]. Cellulosic foams, derived from cellulose fibers, exhibit intriguing properties, including extremely low density [5–7], high fluid permeability [8–10], and effective sound and heat insulation [11–15]. In line with this trend, Cucharero et al. investigated sound-absorbing materials produced using foam-forming methods based on hardwood and softwood pulps as raw materials [16]. The foams exhibited sound absorption characteristics comparable to those of typical porous materials, commonly employed in contemporary soundproofing applications on a large scale. The findings from this study offer valuable insights into the optimization of wood-based noise insulation materials. Jahangiri et al. also proposed a novel biodegradable, low-density porous material based on wood fibers and produced in foam-laid media [17–19]. An experimental setup based on a three-microphone impedance tube was employed to investigate acoustical properties concerning the potential effects of various parameters (e.g., foam air content, thickness, porosity, and consistency of the foam–fiber solution).

In recent years, the authors of this article have developed cellulose fiber-based porous lightweight materials using foam-forming techniques and various types of cellulose fibers

as raw components [20]. These materials have primarily been applied for noise insulation [21–24], thermal insulation [25], and cushioning/packaging purposes [26,27]. Experimental investigations have generally shown that cellulose foams are able to provide insulation characteristics similar to or better than petroleum-based materials/composites, commonly used as a protective solution in most cases.

Despite the fact that wet-laying is a mature technology widely applied in specific industries, it typically involves the use of large volumes of water and is energy intensive [28]. In this regard, the foam-laying method offers a substantial reduction in water consumption during the fibrous network formation process and helps decrease the water content of the non-wovens produced before drying, thereby achieving a reduced energy demand [29–33]. An interesting and useful overview of the foam-forming technique was presented by Hjelt et al. in their paper [34], where they addressed both fundamental foam properties and practical forming methods. They also demonstrated how the material characteristics can be affected by foam–fiber interactions. Furthermore, the potential material characteristics were compared against key requirements in typical product applications. Another useful survey regarding applications of foam-formed cellulose-based materials for cushioning packaging was provided in [35], where the authors presented a comprehensive state-of-the-art overview of the materials involved, available methods, and the main properties of these foams.

Scientists have also focused on non-wood fibers as a viable alternative for the pulp and paper industry. In their article [36], Abd El-Sayed et al. showed that actual high-tech innovation has made non-wood more reasonable than wood as a raw material for the papermaking industry, even in countries with acceptable wood sources, due to environmental concerns. The foam-forming method also presents high interest in the exploitation of proven design concepts for advanced material solutions [37,38]. The authors of [39] proposed a foam structure that presents high-yield stress in the primary direction and excellent thermal insulation. In addition, cellulose-based foams offer an unlimited creative space for the design of green functional materials with a wide range of energy-related applications. Thus, the work [40] demonstrates that cellulose-based foams can exhibit solid–liquid phase change functionality and shows the versatility of the foam-forming process of cellulose-based materials in order to accommodate physical functionalities in materials with complex architectures. The authors developed foams that are recyclable, industrially scalable, and can be exploited as heat storage materials.

Regarding the subtle fiber–bubble interactions, the research [41] demonstrates that these interactions provide a suitable tool that can be used to alter both structural and mechanical material properties of foam-formed cellulose-based materials. A large ensemble of studies was developed within the area of soundproofing, being mainly focused on materials or composites suitable for applications in noise insulation practice [42–46].

Different types of fiber raw sources are used worldwide, related to available wood resources for a certain geographical area. For example, Malekzadeh et al. [47] demonstrated the potential of bamboo fiber-based porous materials as low-cost, lightweight structural materials. The authors of paper [5] present a new method to produce cellulose fiber-based lightweight materials, using eucalyptus pulp as raw material and fibers partially hydrolyzed with sulfuric acid. The advantage of this method is justified by a drying step easily performed at mild temperatures in a convection oven, thus eliminating the need for more sophisticated drying techniques. Moreover, the proposed method does not require surfactants or special foam-forming equipment.

Using pineapple leaf fibers with paper waste, a research group developed composites with good performances related to sound absorption and impact strength [48]. Ultra-lightweight cellulose foams with good mechanical properties were proposed in article [49]. The authors have observed that micro-pores (bubbles) inside the wet foams weakened the mechanical properties but increased these properties in the dried foams. Their investigations revealed good compressive strength of dried foams, which exhibited great potential for further development and comprehensive utilization of cellulose. Other groups of raw

sources for composites with very interesting characteristics and potential applications in sound insulation practice are cork sheets [50–53] and corn stalk fibers [54].

The required strength of cellulose-based foams can be achieved by optimally combining fibers and fines of different length scales [55]. In addition, the elasticity can be improved by adding polymers, which accumulate at fiber joints and help the network structure recover after compression. Within their study [55], the authors showed that structure and elastic properties were sensitive not only to the raw materials but also to the elastomer stiffness and foam properties. Additionally, an improved strain recovery makes the developed cellulose-based materials suitable for various applications, such as padding for insulation purposes.

By incorporating different additives (e.g., chitosan, cationic polyacrylamide), Meiyan et al. improved some functional properties of pulp foam (in terms of physical strength, fire-retardance, thermal insulation, antibiosis, and sound absorption) [56]. Interesting biodegradable chitosan-based foams were also proposed in study [57]. New bio-based packaging materials present high interest in replacing conventional fossil-based products for a more sustainable society [58]. The cellulose fiber-based foams containing chitosan provide both good water stability and good antibacterial and antifungal properties, demonstrating the feasibility of bio-based foam material with desired characteristics. Hereby, these foams can enable an interesting low-density packaging composite with protective mechanical and microbial properties without using any toxic compounds [56–58]. In addition, Seppänen et al. evaluated the wet strength properties of foam-formed fiber-based materials [59]. Novel lightweight cellulose fiber-based composites, embedding various strength-enhancing polymeric and fibrillar components, were developed by Pöhler and collaborators using the foam-forming technology [60]. During their research, increasing both inter-fiber bond strength and local material density was attempted.

As they are the second class after cellulose, hemicelluloses are heterogeneous polysaccharides that exist in almost all cell walls of lignocellulosic biomass. Xylan polysaccharides are the most abundant hemicellulose type, representing about 20–35%, mainly in hardwood and annual plants (wheat straw, corn stalks, and cobs) and also as a by-product of the pulp and paper industry [61,62].

Although it exists in large quantities, the industrial application of xylan hemicellulose is still limited. It is used to obtain the xylitol and bio-fuels by biological conversion of sugar, starch, and vegetable oils. In the packaging industry, xylan hemicellulose is used to improve the strength and biodegradability properties of plastic materials [63]. Generally, the limitation of industrial applications for xylan hemicellulose is due to its high hydrophilicity as a result of a larger number of OH groups in the structural unit. To enhance its hydrophobicity and processability by reducing the H-bonds, the hydrophobic groups are attached to the hemicellulose chains by different methods of chemical modification. Therefore, chemical modification with hydrophobic moieties was applied in order to improve the function of hemicelluloses for packaging and coating applications [64]. In addition, cationic xylan derivatives have a wide range of applications in the papermaking industry, such as cellulose fiber strength additives, flocculation aids, and antimicrobial agents [63].

Considering the good compatibility of xylan with cellulose fibers, this paper aims to utilize xylan derivatives to enhance the free surface wetting and structural integrity of cellulose fiber-based foams. This improvement enables the materials to be incorporated into sound insulation applications. To achieve this goal, native hardwood xylan hemicellulose, along with its acetylated and hydrophobized derivatives, was applied as coatings in a thin layer to treat the free surface of cellulose foams. The coated samples underwent analysis to assess noise insulation characteristics and performance, aiming to evaluate the impact of xylan-based coatings on soundproofing capabilities. This evaluation involved a comparison with untreated cellulose-based samples and a few samples of commercially available petroleum-based materials commonly used in sound insulation.

The originality of this study arises from several aspects: (i) the novel use of cellulose fiber foams in soundproofing applications; (ii) the imperative need to ensure appropriate wetting and surface structure integrity properties for these materials, enabling their practical utilization as noise insulation panels; and (iii) the utilization of hemicelluloses, by-products of the pulp and paper industry, with xylan polysaccharides being the most abundant hemicellulose type.

Essentially, based on available scientific reports, this type of surface coating (utilizing xylan derivatives) has not been thoroughly analyzed. The effects of this treatment must be rigorously evaluated concerning changes in noise insulation characteristics to validate its functional capability in practical applications. In addition, it has to be underlined that some other research groups, which have analyzed the necessity of foam-free surface coating, generally used synthetic petroleum-based solutions or with very complicated production technology (also environmental pollutants). Therefore, given the previously mentioned advantages, xylan-based derivatives offer a viable solution for enhancing the hydrophobicity and surface structure integrity of cellulosic foams.

2. Materials and Methods

2.1. Materials

The proposed porous lightweight materials were developed in a foam medium using virgin softwood cellulose fibers. Bleached softwood cellulose (typically providing 400–800 μm average fiber length and 15–35 μm diameter) was used as a raw fiber source [21,22,27]. Cellulose fibers, with 60 and 43 °SR beating degrees (according to the Schopper–Riegler evaluation method), and slurry pulp with 1.98% consistency were adopted within this research. The anionic surfactant used for foam forming was sodium dodecyl sulfate (SDS), commonly utilized in commercial regular cosmetics production. Based on these components (slurry pulp and surfactant), two types of foam-formed cellulose-based lightweight foams were obtained (please see details within Sections 2.2 and 3.1) [21–24,27,35].

Xylan hemicellulose with a molecular mass of (132)n from beechwood was purchased from Carl Roth Company, Karlsruhe, Germany, and used as received.

Acetylated xylan was obtained in laboratory conditions according to the procedure described by the authors in previous papers [26,65]. The procedure involved the esterification process of native xylan with acetic anhydride in two stages, at 50 °C for 1 h and a molar ratio of acetic anhydride to functional hydroxyl groups in the structural unit of xylan about 8:1. The degree of substitution was about 0.48 [26,65].

Hydrophobized xylan was obtained by reaction of native xylan with long chain anhydrides as alkyl ketene dimers at 20 °C and 24 h of magnetic stirrer at 1500 rpm. Alkyl Ketene Dimer of milky white liquid, odorless, total solids of 16.2% and viscosity of 4 cPs/t = 25 °C (as a commercial product, AquapelTM 210D—Solenis, Wilmington, DE, USA), was used for xylan hydrophobization [26,65]. All the other chemical reagents for esterification reaction (acetic anhydride, acetic acid, and sulfuric acid) have had analytical purity.

Both native xylan and xylan derivatives were used as water dispersion of 2.5% for coating by pulverization in a thin layer (about 5 g/m^2) on the surface of different samples of cellulose foams.

A schematic diagram of sample preparation is provided in Figure 1. The upper section of this scheme presents the basic procedure to obtain cellulose fiber-based foams [21–24,27,35]. At the same time, the lower section presents relevant aspects regarding the xylan-based coatings of foam-free surfaces in terms of magnetic stirrers used for homogenization of native xylan and xylan derivatives water dispersion, preparation of dispersion for sample surface treatment, and an example of xylan treatment laid on sample surface using the spraying method.

Four different commercially available petroleum-based materials currently used in sound insulation were also considered in order to provide a suitable reference for analyzing the performances of cellulose-based materials (with and without xylan-free surface

treatments). These materials include expanded polystyrene (EPS), extruded polystyrene (XEPS), polyurethane (PU), and expanded polyethylene (EPE).

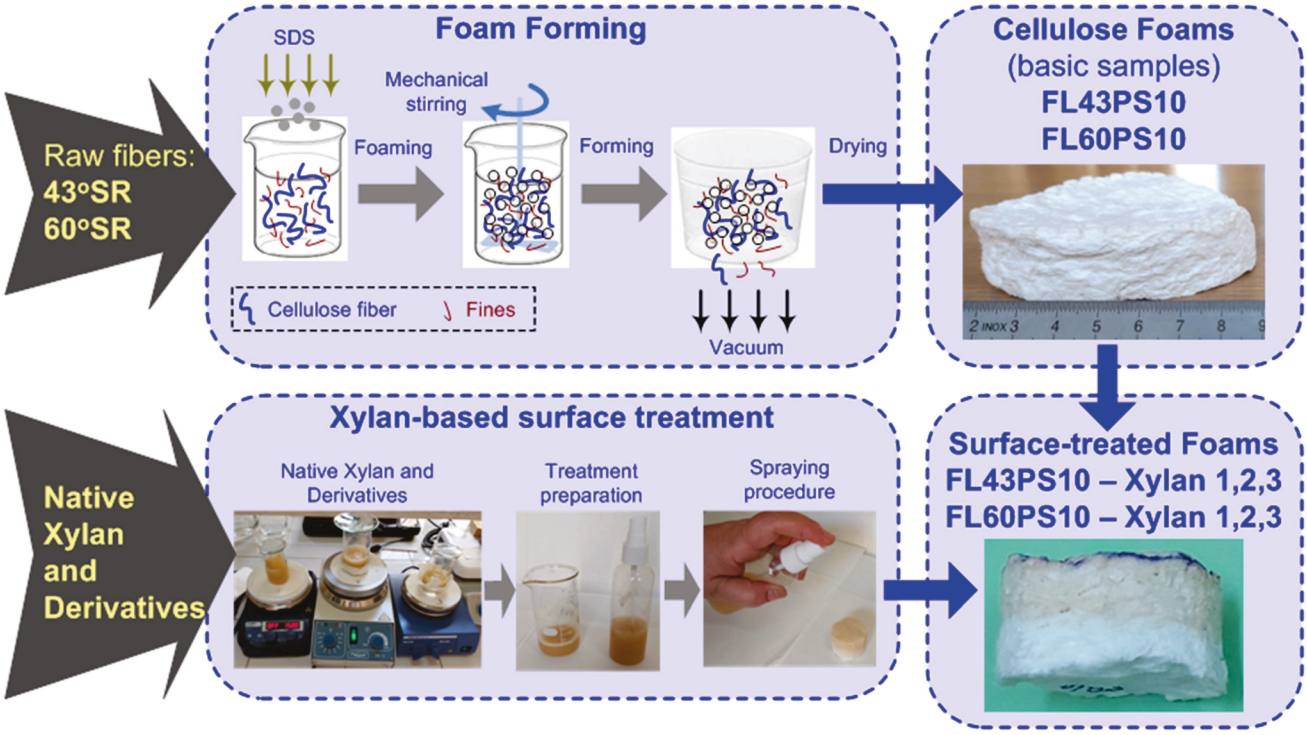

Figure 1. Schematic diagram of sample preparation, based on cellulose fiber foam-forming technique and xylan and xylan derivatives for free surface treatments.

2.2. Methods within Sample Forming Procedure

The cellulose fibers (resinous virgin cellulose fibers with 1.98% consistency) were soaked overnight (approx. 24 h) using distillate water with 1% sodium hydroxide (1 N concentration). Next, the slurry pulp was mixed using high shear velocity up to 2200 rpm for 20 min in order to facilitate air entraining. During the agitation process, a controlled percentage of surfactant (relative to the pulp weight) was added to obtain a suitable foam medium.

The authors have aimed to obtain and analyze two types of foam materials based on two different beating degrees of raw pulp with constant air content. Thereby, 4% of surfactant was adopted relative to the fiber weight (this is the mid value of the surfactant percentage range used in previous investigations [21]).

The suspension of fibers and foam was filtered and dewatered using a Buchner funnel and a sample holder with an inner diameter correlated to that required by equipment used in acoustical investigations (e.g., 100, 72, and 28.5 mm). A filter paper was used at a sample bottom, in addition to the filtering system of the Buchner funnel, aiming to obtain a sample surface as flat as possible. The filtering was developed at a low vacuum level for approx. 20 min, following both a suitable dewatering and the sample structural integrity. After dewatering, the samples were carefully transferred to the drying table, aiming to avoid structural integrity loss. Samples were dried at room temperature (around 22 °C) and 50–60% relative humidity for 24 to 48 h (please see details within Section 3.1) [21–24,27,35].

2.3. Methods within Contact Angle Evaluation

In order to evaluate the hydrophobicity of cellulose foams in terms of free surface wettability, the static water contact angle was measured according to the T-458 cm-04 Standard by static sessile drop method [66]. This procedure used the Ossila® contact angle

goniometer (Ossila BV, Leiden, The Netherlands), which is equipped with a high-resolution digital camera and suitable software for recording and processing the results.

The samples were placed on the test table, and water drops (approx. 5 μL) were deposited onto its surface with a micro-syringe. The value of the contact angle was recorded after 5 s of water–substrate contact time on each sample. The measurements were repeated at five different locations on the cellulose foam surface, and the average contact angle values were reported (please see details within Section 3.2).

2.4. Methods within FT-IR Investigations

The structural characteristics, which highlight the presence of specific chemical groups in the modified xylan samples, were analyzed using a Nicolet iS50 FT-IR spectrometer (Thermo Scientific, Waltham, MA, USA) equipped with an attenuated total reflection (ATR) accessory and a diamond crystal plate, in transmission mode. The spectrometer was placed in a temperature-controlled room (21 ± 2 °C). Infrared spectra were measured within the spectral range 4000–400 cm^{-1} at 2 cm^{-1} spectral resolution and 32 background/sample scans using OMNIC™ software (Thermo Fisher Scientific Inc., Waltham, MA, USA). The background spectrum was collected by taking air as a reference before each measurement, and the diamond crystal plate was cleaned with alcohol.

2.5. Methods within Noise Insulation Investigations

The foam samples, both untreated and xylan-based surface treated, were analyzed in order to estimate the acoustic insulation capabilities in terms of absorption and reflection coefficients and acoustic impedance, with all these parameters being evaluated at a normal incidence angle. Experimental investigations were conducted using an Impedance Tube Kit Type 4206® (Brüel&Kjær Sound and Vibration Measurement A/S, Nærum, Denmark), with a 29 mm diameter sample holder and a two-microphones setup configuration (Figure 2). The frequency range enabled by this tube is 500–6400 Hz (according to the technical specifications). A sound source (that generates broadband, stationary random sound waves) is mounted at one end of the impedance tube, and the sample of material is placed at the other end. The propagation, contact, and reflection result in a standing-wave interference pattern due to the superposition of forward- and backward-traveling waves inside the tube. Measuring the sound pressure at two fixed locations and evaluating the complex transfer function using a two-channel frequency analyzer result the sound absorption, complex reflection coefficients, and the normal acoustic impedance of the tested material within the sample holder. The measurements were developed based on the transfer function method and testing method described in ISO 10534-2 [67] and ASTM E1050-12 International Standards [68].

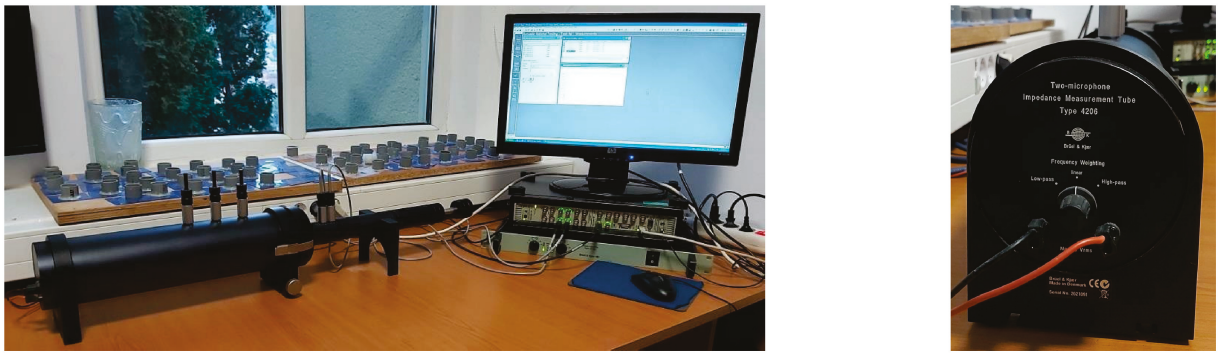

Figure 2. The Impedance Tube Kit Type 4206® (Brüel&Kjær) used for acoustical investigations.

Acoustic measurements were made with two 1/4″ Pressure-field Condenser Microphones Type 4187® (Brüel&Kjær Sound and Vibration Measurement A/S, Nærum, Denmark), which are supplied with a tube kit and are specially designed to reduce errors due to pressure leakage at high frequencies.

Data acquisition and primary processing were managed with the software platform PULSE Acoustic Material Testing Type 7758® (Brüel&Kjær Sound and Vibration Measurement A/S, Nærum, Denmark). Advanced computational developments were performed using a set of Matlab®R2018b (MathWorks, Natick, MA, USA) based applications.

3. Results

3.1. Cellulose-Based Foam Formed Samples with Xylan-Based Treatments

According to the methods presented in Section 2.2 and using the raw materials presented in Section 2.1, two types of resinous fibers cellulose-based foams were made: one type with a 43 °SR beating degree and another with a 60 °SR beating degree. Microphotographs within Figure 3 depict the micro-fibrous structure of external surfaces for each sample type. These images were acquired using optical microscopy technique, with transmitted dead white light, based on DELTA Optical Three-Ocular Microscope model SZ-450T® (Delta Optical, Minsk Mazowiecki, Poland), and Bresser MikrOkular Full HD Digital Camera® (Bresser GmbH, Rhede, Germany). Each image provides a dimensional grid, suitably marked on the picture and gained by a standard calibration grid lamella.

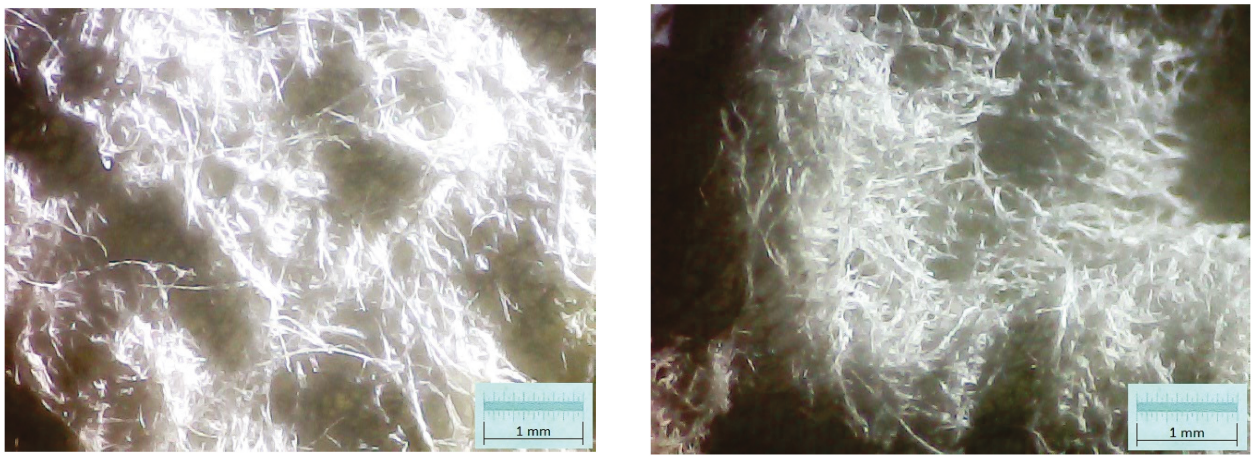

(**a**) (**b**)

Figure 3. Optical micro-photographs of cellulose-based foam-formed samples surface: (**a**) foam based on long fibers with 43 °SR beating degree; (**b**) foam based on long fibers with 60 °SR beating degree.

The samples with applied xylan-based surface treatments were depicted in Figure 4, where the sample codes have the following meanings: (43, 60)/(1, 2, 3)—base foam with 43 or 60 °SR beating degree and treatment with native xylan (1), AKD hydrophobized xylan (2), and acetylated xylan (3). The pictures in Figure 4 were acquired just after the xylan spraying procedure.

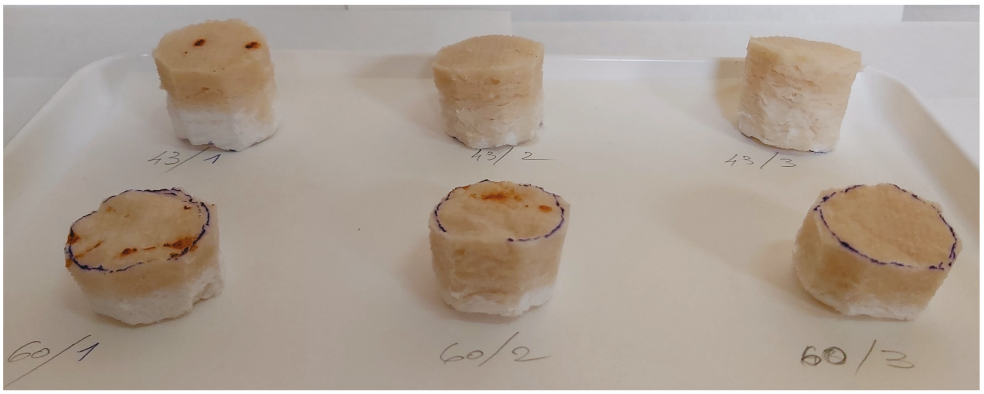

Figure 4. Photo of wet-state samples just after the xylan-based treatments (see text for sample coding details).

Surface-treated samples were dried on filter paper (in order to take over the possible xylan leakages through samples) at room temperature (approx. 22 °C) for 48 h. Dry-state samples (ready-to-use foams) were presented in Figure 5, where sample codes have the following meanings: FL(43, 60) PS10—Long Fiber with 43 or 60 °SR beating degree, and 4% surfactant (SDS); Xylan (1, 2, 3)—native xylan (1), AKD hydrophobized xylan (2), and acetylated xylan (3). The image within Figure 5 also contains the reference foams (denoted as "Basic"), enabling a comparative analysis between samples with and without surface treatments.

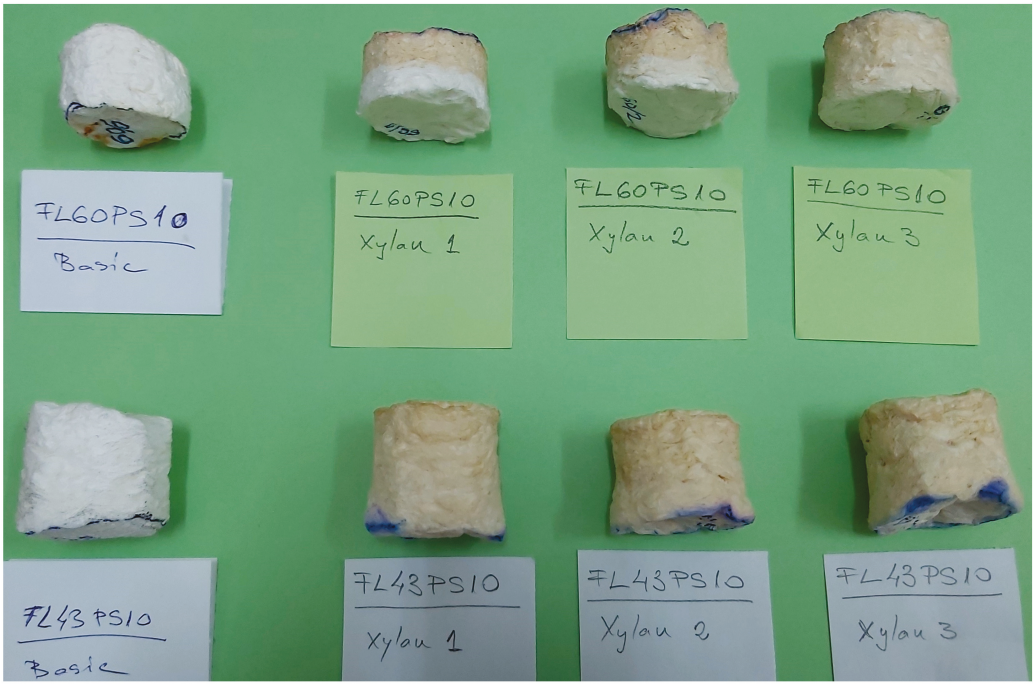

Figure 5. Photo of dry-state samples 48 h after the xylan-based treatments (see text for sample coding details).

In order to enable the analyses of xylan–foam interactions and the effects of treatment on the foam structure, a longitudinal section on samples was considered. Thus, a thin slice of 4 mm thickness was cut from each sample. These sectional samples were analyzed with both reflected and transmitted dead white light (without optical magnification) and with optical transmitted light microscopy.

The results are depicted in Figure 6 for 43 °SR beating degree basic material and Figure 7 for 60 °SR beating degree basic material. For each microphotograph, an etalon scale (enabled by a standard calibration grid lamella) was suitably marked on the picture.

3.2. Static Water Contact Angle

A set of snapshots within the contact angle evaluation procedure is presented in Figure 8, where the droplet on the sample surface can be observed, with marked left/right estimated angles through the image processing with data interpolation correlated procedure) and the angle distribution chart. The significance of each image is mentioned in the figure caption. According to the samples within Figure 8, Table 1 systematically presents values of each angle, average angle, and RMS errors of the estimation procedure (sample codes in Table 1 have the same meaning as those in Figure 5 (see Section 3.1)).

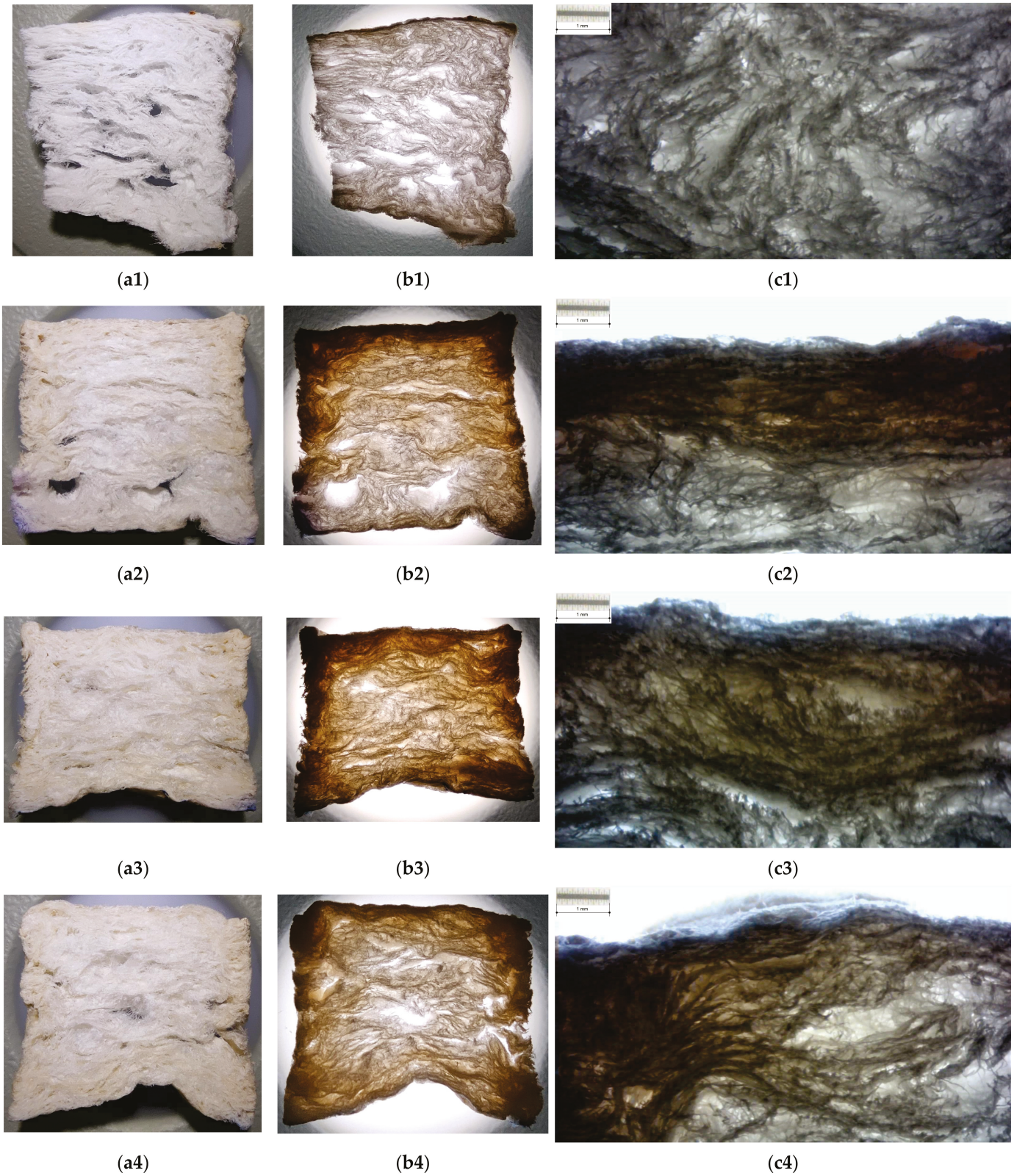

Figure 6. Images of longitudinal sections into samples based on 43 °SR beating degree: (**a**) photo on reflected light; (**b**) photo on transmitted light; (**c**) optical microphotograph of xylan–material interface (transmitted light, etalon scale marked on picture); (**1**) basic samples without xylan surface treatment; (**2**) samples with native xylan surface treatment; (**3**) samples with AKD hydrophobized xylan surface treatment; (**4**) samples with acetylated xylan surface treatment.

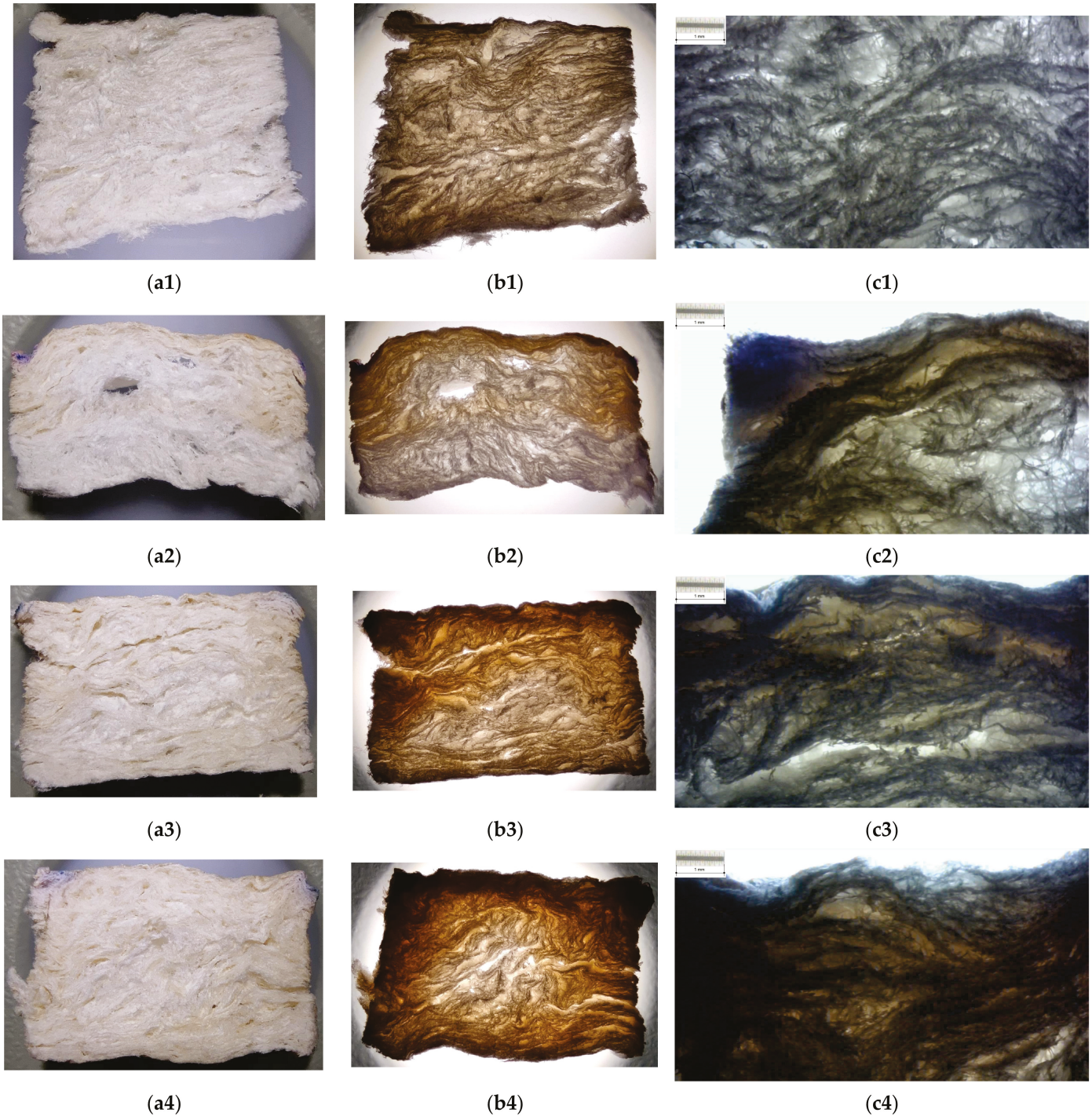

Figure 7. Images of longitudinal sections into samples based on 60 °SR beating degree: (**a**) photo on reflected light; (**b**) photo on transmitted light; (**c**) optical microphotograph of xylan–material interface (transmitted light, etalon scale marked on picture); (**1**) basic samples without xylan surface treatment; (**2**) samples with native xylan surface treatment; (**3**) samples with AKD hydrophobized xylan surface treatment; (**4**) samples with acetylated xylan surface treatment.

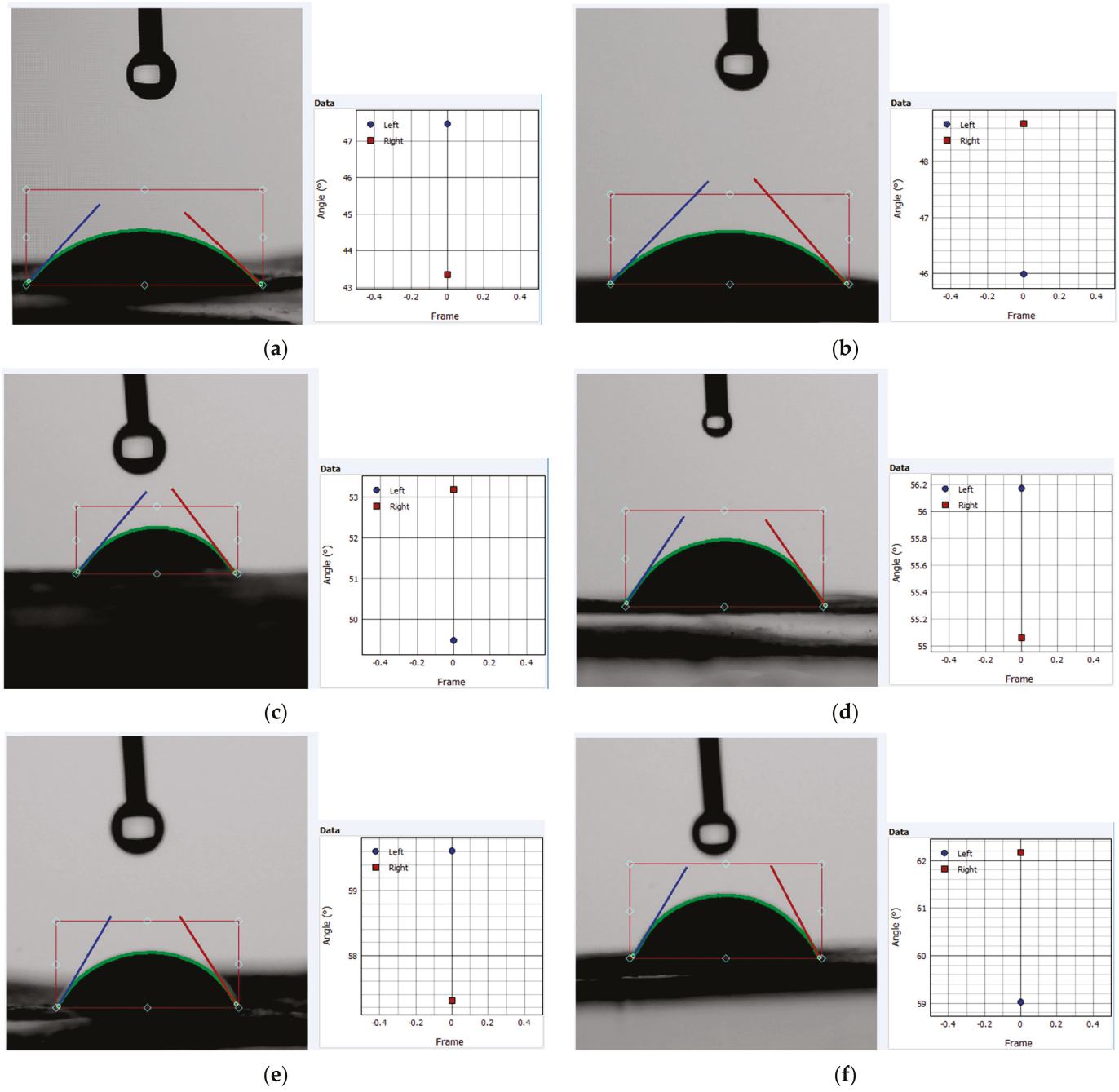

Figure 8. Snapshots within contact angle procedure for samples: (**a**) FL43PS10 with native xylan; (**b**) FL60PS10 with native xylan; (**c**) FL43PS10 with hydrophobized xylan; (**d**) FL60PS10 with hydrophobized xylan; (**e**) FL43PS10 with acetylated xylan; (**f**) FL60PS10 with acetylated xylan.

Table 1. Values of contact angle for all samples xylan-based treated.

Sample *	Left Angle (°)	Right Angle (°)	Average Angle (°)	Left RMSE **	Right RMSE **
FL43PS10/xylan 1	47.46	43.34	45.4	0.89234076	0.968734416
FL60PS10/xylan 1	45.98	48.67	47.32	0.45422208	0.476735329
FL43PS10/xylan 2	49.47	53.17	51.32	0.81973641	0.772447342
FL60PS10/xylan 2	56.17	55.06	55.61	0.58340201	0.430664096
FL43PS10/xylan 3	59.61	57.3	58.45	0.52365381	0.441699407
FL60PS10/xylan 3	59.02	62.16	60.59	0.69721882	0.628683974

* See text for samples coding details; ** RMSE: Root Mean Square Error.

3.3. FT-IR Analysis

The FT-IR spectral transmittance diagrams of xylan and xylan derivatives are presented in Figure 9. Compared with native xylan, the structural spectra of xylan derivatives indicated the presence of absorption peaks at 1746 cm^{-1}, which are associated with C=O vibration stretching from acetyl and −COOH groups, and the vibration stretching characteristic absorption peaks of β-ketone ester bond formed between xylan hemicelluloses and AKD within 1602 cm^{-1} and 1733 cm^{-1} (please see details in Figure 9b,c).

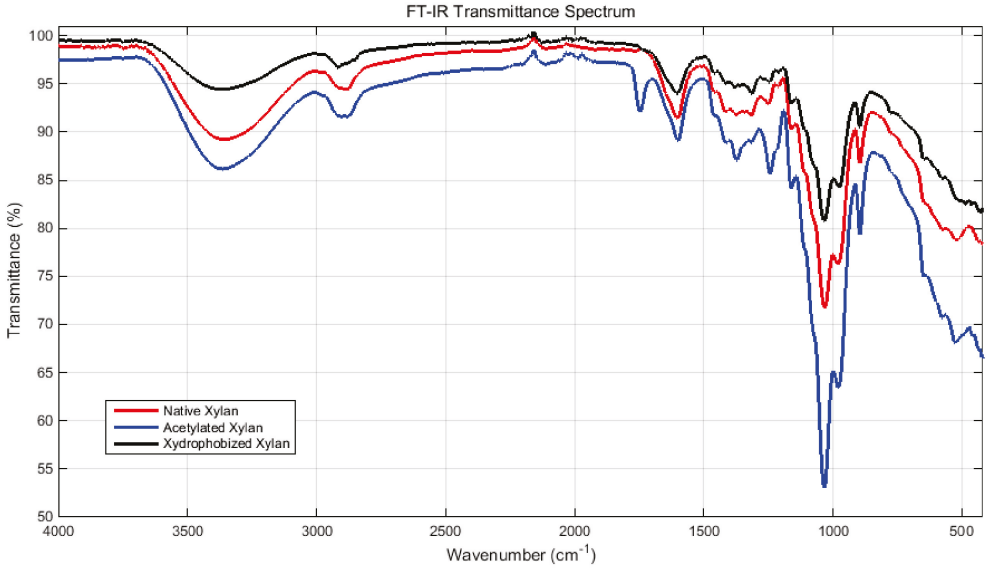

(**a**)

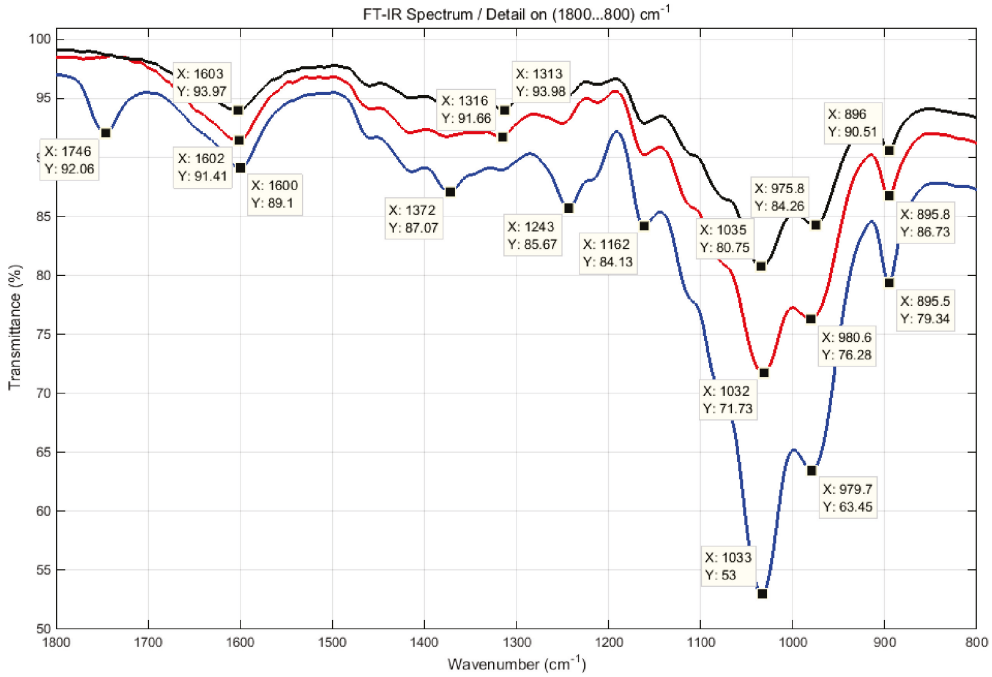

(**b**)

Figure 9. *Cont.*

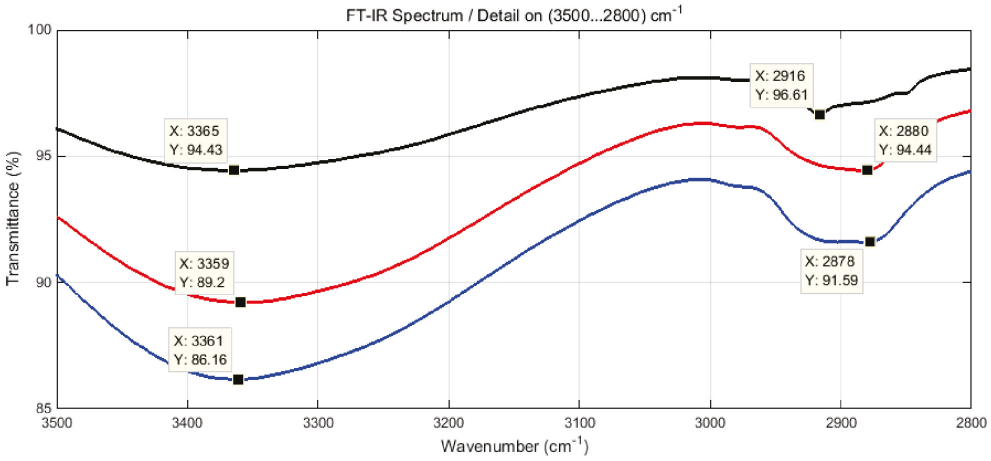

(**c**)

Figure 9. FT-IR spectra of softwood native xylan, acetylated xylan, and hydrophobized xylan: transmittance spectra of whole samples (**a**); detailed views with marked peaks (**b**,**c**).

3.4. Noise Insulation Characteristics

The investigations related to the noise insulation capability of xylan-based surface-treated foams were performed following the acoustic absorption coefficient, the acoustic reflection coefficient, and the surface acoustic impedance, with all of these supposing the normal sound incidence (according to the international standards and the experimental setup (see Section 2.5)). The raw data gained by experimental investigations were post-processed and managed using a Matlab®-based application in order to enable and facilitate comparative analyses between different categories of data.

Graphs in Figure 10 present the results related to the acoustic absorption coefficient with respect to the frequency range enabled by the impedance tube. Diagrams were grouped by the basic material, such as 43 and 60 °SR beating degree, and reference petroleum-based materials. In the same manner, the results related to the acoustic reflection coefficient are presented in Figure 11.

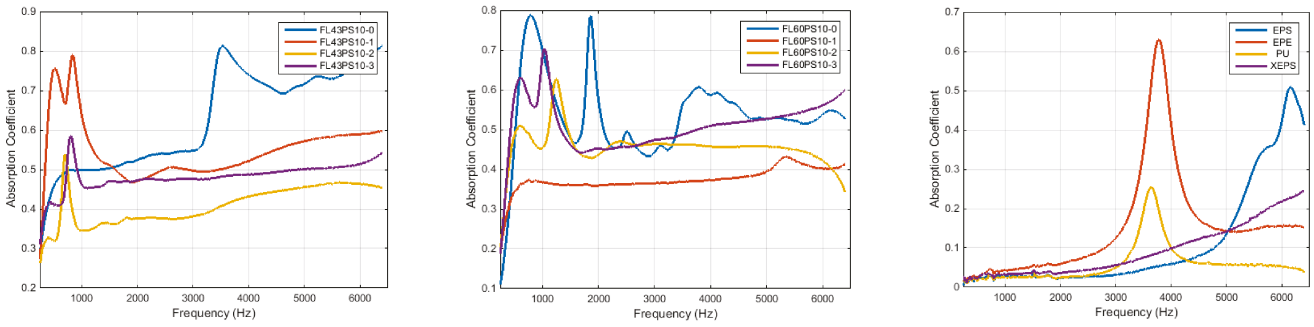

(**a**) (**b**) (**c**)

Figure 10. Acoustical absorption coefficient: (**a**) FL43PS10 basic material; (**b**) FL60PS10 basic material; (**c**) reference materials.

Taking into account the previous grouping rule (FL43PS10, FL60PS10, and reference materials), the surface acoustic impedance is presented in Figure 12 in terms of the magnitude (using a vertical semi-logarithmic scale representation) and angle.

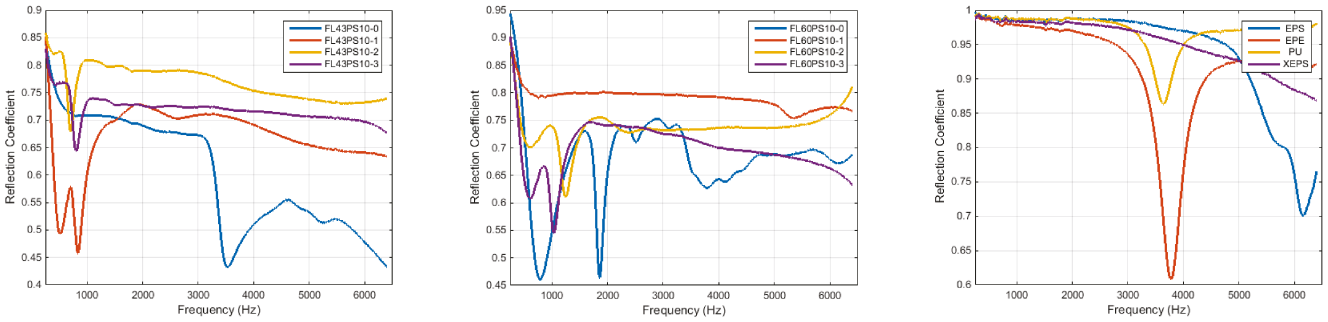

(**a**) (**b**) (**c**)

Figure 11. Acoustical reflection coefficient: (**a**) FL43PS10 basic material; (**b**) FL60PS10 basic material; (**c**) reference materials.

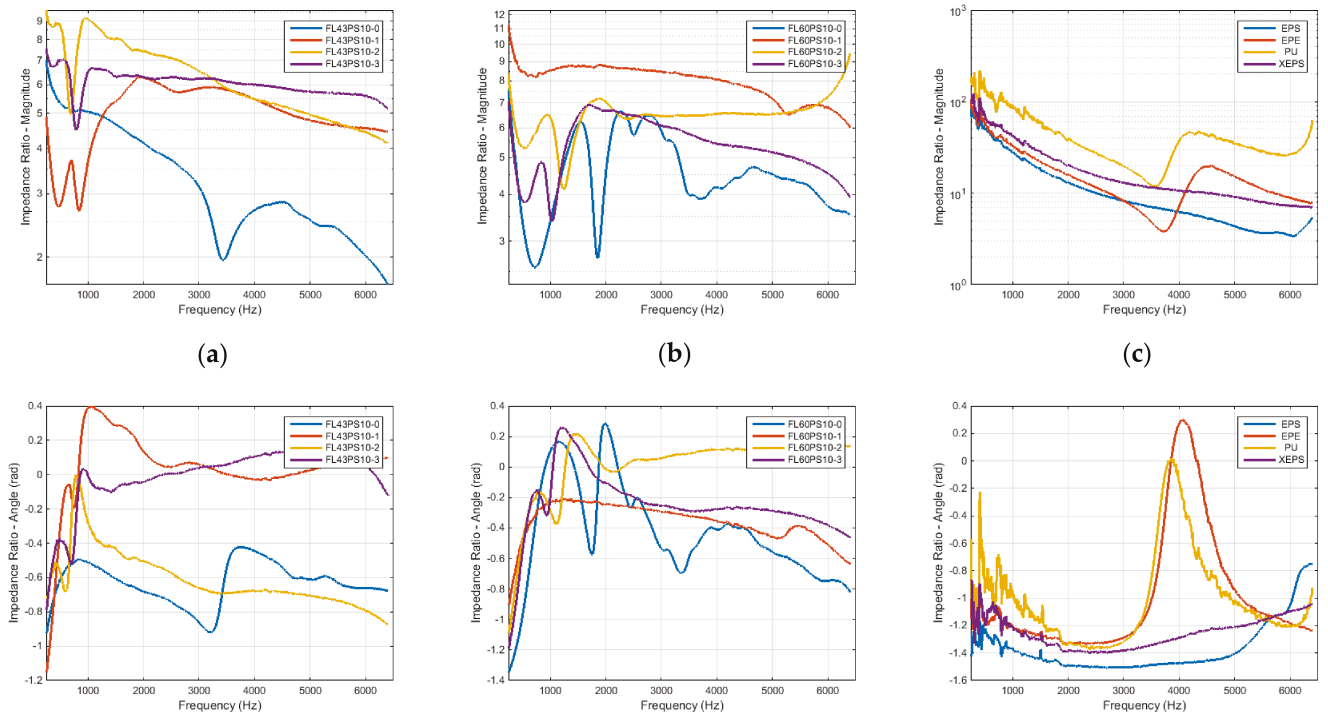

(**a**) (**b**) (**c**)

(**d**) (**e**) (**f**)

Figure 12. Surface acoustic impedance at normal sound incidence in terms of magnitude and angle: (**a**) FL43PS10 basic material—impedance magnitude; (**b**) FL60PS10 basic material—impedance magnitude; (**c**) reference materials—impedance magnitude; (**d**) FL43PS10 basic material—impedance angle; (**e**) FL60PS10 basic material—impedance angle; (**f**) reference materials—impedance angle.

A comparative analysis of the effect induced by xylan-based treatments on the sound-proofing ability of cellulose foams can be performed using the peak distribution of the acoustic absorption coefficient. Hereby, the maximum value and its corresponding frequency for each graph within Figure 10a,b is provided in Table 2.

Table 2. Peak values of acoustic absorption coefficient (α) with respect to the frequency.

CF Material *	Parameter	Surface Treatment			
		No Xylan	**Xylan 1 ***	**Xylan 2 ***	**Xylan 3 ***
FL43PS10	Freq. (Hz)	3528	840	704	808
	α	0.8131	0.7902	0.5384	0.5856
FL60PS10	Freq. (Hz)	792	5368	1248	1040
	α	0.7887	0.4325	0.6277	0.7029

* CF: Cellulose-based foam; Xylan 1: native xylan; Xylan 2: hydrophobized xylan; Xylan 3: acetylated xylan.

4. Discussion

By analyzing dried samples photos in Figure 5, it can be observed that xylan treatments penetrate the foam based on cellulose fibers much more, with a low beating degree (between 40% for native xylan and 60% for acetylated xylan, of sample high), comparative with the foams from high beating degree cellulosic fiber (between 60% and 70%).

These aspects are also present on the sample kernel and become visible on the longitudinal section slices (please see photos in Figures 6 and 7). Micrographs in Figures 6 and 7 show the way that xylan penetrates the porous structure of the foam and fills the pore between cellulose fibers, as well as the depth of this penetration. It was observed that an increase in the depth at the same time as native xylan, hydrophobized xylan, and acetylated xylan were applied. Thus, the xylan derivatives intensively fill in the pores, and this fact can affect the noise insulation ability of treated foam, especially for high frequencies, but it is able to increase this ability for low–medium frequencies. On the other hand, they increase the surface structure integrity and decrease the wettability of the surface. The slice photos qualitatively indicate that acetylated xylan treatment is able to provide better functional properties than the hydrophobized xylan, both exceeding the capability of native xylan-based treatment.

An additional indicator of changing wettability can be provided by the static water contact angle. Values within Table 1 enable a quantitative view of the ability of xylan-based surface treatments to decrease foam wettability. The hierarchy (native, hydrophobized, acetylated) of xylan, in order to improve the hydrophobicity of samples, can also be observed in snapshots in Figure 8. But, the average angle values (see Table 1) clearly supply this order and reveal that foams based on 60 °SR beating degree fibers overrun those with lower beating degree. This aspect can be justified by the relative length of cellulose fiber and different fine percentages between the two raw fiber components.

Taking into account the main goal of this research, it has to evaluate the new soundproofing abilities of surface-treated samples in order to identify and characterize changes produced by the xylan fill-in effect. The main aspect is provided by the acoustic absorption coefficient (see diagrams in Figure 10). Let us talk distinctively about the two groups of foams.

Thus, the group based on FL43PS10 basic material presents the following characteristics: (a) all treatments shift the frequency peak to the lower values (under 1000 Hz) compared with the basic foam sample; (b) all treatments decrease the absorption ability for medium–high frequencies (beyond 2000 Hz), but provide an approximately constant value ($\alpha \cong 0.4$–0.6, depending to the treatment type); (c) native xylan presents smallest changings; (d) hydrophobized xylan presents the worst solution because of its major decreasing of absorption ability; (e) acetylated xylan presents a relative constant characteristic ($\alpha \cong 0.45$–0.50) for the whole frequency range, and, by demonstrating the better performances related to the wettability, this treatment represents the better solution for this foam type.

On the other hand, the group based on FL60PS10 basic material presents different characteristics as follows: (a) all treatments reject the frequency peak around 2000 Hz; (b) native xylan substantially decreases the absorption ability for the entire frequency range and, thus, represents the worst solution; (c) hydrophobized xylan slowly decrease the

absorption, especially for high frequencies (greater than 3000 Hz); (d) acetylated xylan practically maintain the same characteristic trend than the surface untreated foam sample, thereby representing the better solution for this type of foam. By combining the acoustic absorption specificities of the two groups and supposing the previously presented wettability characteristics of each treatment type, it is shown that (a) native xylan can be used for low-level beating degree cellulose fibers but does not enable enough hydrophobicity contribution; (b) hydrophobized xylan represents a good choice for high-level beating degree cellulose fibers, especially for medium frequencies between 1000 and 5000 Hz; (c) acetylated xylan provide better treatment alternative at the same time with the increase in beating degree.

Compared with petroleum-based materials, good acoustic absorption performances of cellulose fiber-based foams (with or without surface treatments) are evident (please see diagrams within Figure 10). This fact and the previously presented specificities clearly result from the overlapped charts in Figure 13.

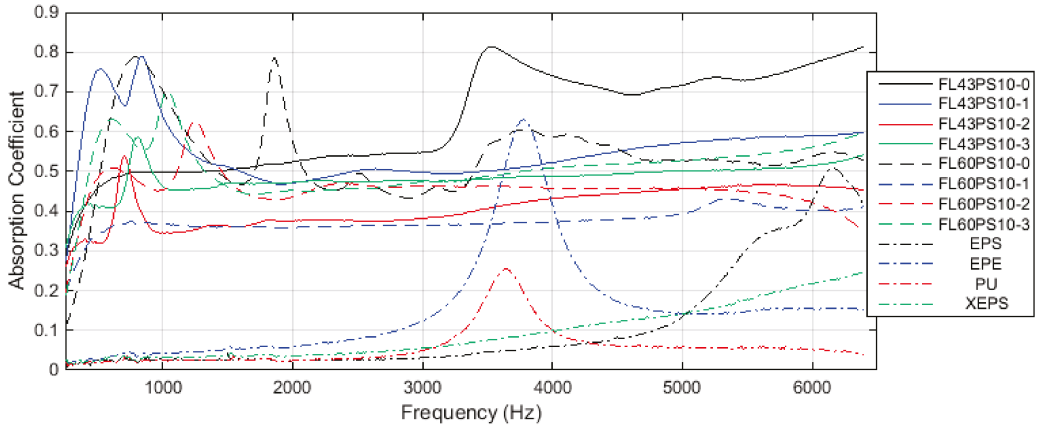

Figure 13. Comparative analysis of acoustic absorption coefficient (see text for coding details).

The relative decrease in absorption ability for treated samples, with respect to the basic foam structural characteristic and xylan derivatives, can be explained by a decrease in near-surface void number (through the xylan fill-in effect) and an increase in acoustic reflection coefficient. Thus, diagrams within Figure 11 clearly show this aspect. Additionally, the overlapped charts in Figure 14 reveal that commercially petroleum-based materials present maximum reflection abilities compared with cellulosic foams, but surface treatments increase, more or less, this foam's ability (to the absorption detriment). A good choice of acetylated xylan-based treatment also results from the comparative diagram of the acoustic reflection coefficient (see Figure 14).

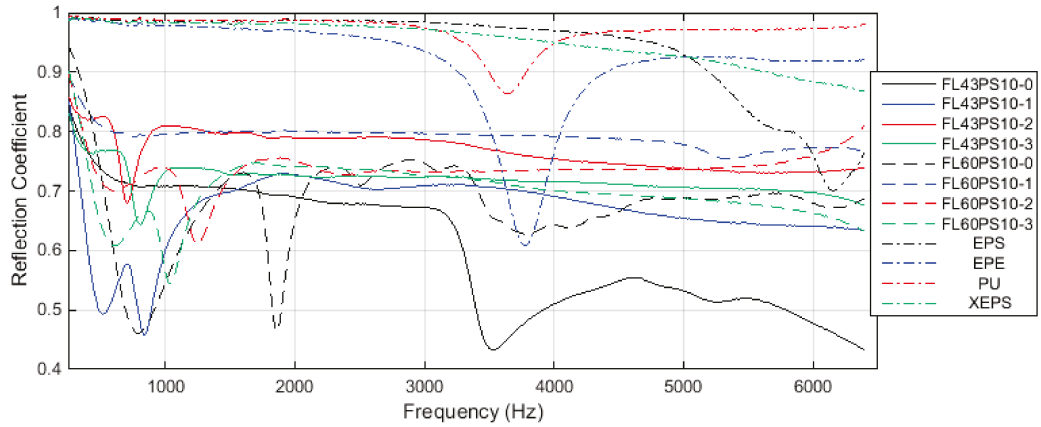

Figure 14. Comparative analysis of acoustic reflection coefficient (see text for coding details).

The diagrams of surface acoustic impedance at normal sound incidence (Figure 12) highlight previously presented aspects, especially in terms of impedance magnitude (impedance angle diagrams reveal the changes within magnitude evolutions). Greater values of petroleum-based materials' impedance sustain the concluding remark that cellulose foams (with or without surface hydrophobicity treatments) enable good acoustic absorption properties compared with these large-scale used materials in soundproofing applications.

5. Conclusions

The authors developed three types of surface-treated cellulosic foam-formed materials based on native xylan and xylan derivatives in order to acquire a potential consistent enhancement of foam hydrophobicity property. This improvement enables the materials to be incorporated into practical applications within the area of noise insulation.

The results reveal that acetylated xylan provides optimal performances in terms of both maintaining the noise insulation capability at a suitable level and decreasing the wettability of the basic foam to a serviceable acceptable level, according to the practice requirements. Hydrophobized xylan presents a selective application range with respect to the raw cellulosic fibers' characteristics and the incident noise frequency domain. On the other hand, native xylan does not strictly present a practical relevance due to its lowest capacity regarding the wettability protection of the external foam surface.

Future investigations will be performed in order to identify and evaluate other practical, suitable, and environmentally friendly solutions for surface treatments of cellulosic foam-formed materials with the highest performances in both soundproofing and additional required functional properties.

Author Contributions: Conceptualization, S.M.N. and P.N.; methodology, S.M.N., P.N. and I.C.R.; software, M.V.G. and M.R.; validation, S.M.N. and P.N.; formal analysis, S.M.N. and P.N.; investigation, S.M.N., P.N., M.V.G., M.R. and I.C.R.; resources, S.M.N., P.N. and I.C.R.; data curation, S.M.N., P.N., M.V.G. and M.R.; writing—original draft preparation, M.V.G. and M.R.; writing—review and editing, S.M.N. and P.N.; visualization, S.M.N. and P.N.; supervision, S.M.N. and P.N.; project administration, S.M.N. and P.N.; funding acquisition, S.M.N. and P.N. All authors have read and agreed to the published version of the manuscript.

Funding: This research was funded by the Ministry of Research, Innovation, and Digitization, CNCS—UEFISCDI, Romania, grant number PN-III-P4-PCE-2021-0714, and by "Dunarea de Jos" University of Galati, Romania, Grant number RF 9418/2023.

Institutional Review Board Statement: Not applicable.

Data Availability Statement: Data are contained within the article.

Conflicts of Interest: The authors declare no conflict of interest.

References

1. Miranda-Valdez, I.Y.; Coffeng, S.; Zhou, Y.; Viitanem, L.; Hu, X.; Jannuzzi, L.; Puisto, A.; Kostianien, M.A.; Makinen, T.; Kivisto, J.; et al. Foam-formed biocomposites based on cellulose products and lignin. *Cellulose* **2023**, *30*, 2253–2266. [CrossRef]
2. Immonen, K.; Jetsu, P.; Keränen, J.T.; Torvinen, K. Feasibility of foam forming technology for producing wood plastic composites. *J. Appl. Polym. Sci.* **2020**, *137*, e49404. [CrossRef]
3. Yan, W.; Liu, J.; Zheng, X.; Zhang, J.; Tang, K. Wood-derived high-performance cellulose structural materials. *e-Polymers* **2023**, *23*, 20230010. [CrossRef]
4. Mohammadi, B.; Ershad-Langroudi, A.; Mousa, A.A.; Mazourra, A.M. Foam for Sound Insulation, Polymeric Foams: Applications of Polymeric Foams. In *ACS Symposium Series, 1440*; American Chemical Society: Washington, DC, USA, 2023; Volume 2, Chapter 12; pp. 253–272. [CrossRef]
5. Ferreira, E.S.; Rezende, C.A. Simple Preparation of Cellulosic Lightweight Materials from Eucalyptus Pulp. *ACS Sustain. Chem. Eng.* **2018**, *6*, 14365–14373. [CrossRef]
6. Al-Qararah, A.M.; Hjelt, T.; Kinnunen, K.; Beletski, N.; Ketoja, J.A. Exceptional pore size distribution in foam-formed fibre networks. *Nord. Pulp Pap. Res. J.* **2012**, *27*, 226–230. [CrossRef]
7. Cervin, N.T.; Andersson, L.; Ng, J.B.S.; Olin, P.; Bergstorm, L.; Wagberg, L. Lightweight and strong cellulose materials made from aqueous foams stabilized by nano-fibrillated cellulose. *Biomacromolecules* **2013**, *14*, 503–511. [CrossRef]

8. Ferreira, E.S.; Dobrzanski, E.; Tiwary, P.; Agrawal, P.; Chen, R.; Cranston, E.D. Insulative wood materials templated by wet foams. *Mater. Adv.* **2023**, *4*, 641–650. [CrossRef]
9. Keranen, J.T.; Jetsu, P.; Turpeinen, T.; Koponen, A.I. Dewatering and Structural Analysis of Foam-Formed, Lightweight Fibrous Materials. *BioResources* **2023**, *18*, 531–549. [CrossRef]
10. Hurtado, P.L.; Rouilly, A.; Maréchal, V.V.; Raynaud, C. A review on the properties of cellulose fibre insulation. *Build. Environ.* **2016**, *96*, 170–177. [CrossRef]
11. Zhou, Y.; Yin, W.; Guo, Y.; Qin, C.; Qin, Y.; Liu, Y. Green. Preparation of Lightweight, High-Strength Cellulose-Based Foam and Evaluation of Its Adsorption Properties. *Polymers* **2023**, *15*, 1879. [CrossRef] [PubMed]
12. Silviana, S.; Prastiti, E.C.; Hermawan, F.; Setyawan, A. Optimization of the Sound Absorption Coefficient (SAC) from Cellu-lose–Silica Aerogel Using the Box–Behnken Design. *ACS Omega* **2022**, *7*, 41968–41980. [CrossRef] [PubMed]
13. Akıncı, T.C. Evaluation of sound absorption properties of natural fiber materials. *J. Nat. Fibers* **2018**, *15*, 336–349.
14. Taiwo, E.M.; Yahya, K.; Haron, Z. Potential of Using Natural Fiber for Building Acoustic Absorber: A Review. *J. Phys. Conf. Ser.* **2019**, *1262*, 012017. [CrossRef]
15. Arenas, J.P.; Rebolledo, J.; del Rey, R.; Alba, J. Sound absorption properties of unbleached cellulose loose-fill insulation material. *BioResources* **2014**, *9*, 6227–6240. [CrossRef]
16. Cucharero, J.; Ceccherini, S.; Maloney, T.; Lokki, R.; Hannien, T. Sound absorption properties of wood-based pulp fibre foams. *Cellulose* **2021**, *28*, 4267–4279. [CrossRef]
17. Jahangiri, P. Novel Cellulose based Foam-Formed Products: Applications and Numerical Studies. Ph.D. Thesis, University of Vancouver, Vancouver, BC, Canada, 2013.
18. Jahangiri, P.; Madani, A.; Korehei, R.; Zeinoddini, S.S.; Madani, A.; Sharma, A.; Phillion, A.; Martinez, M.D.; Olson, J.A. On filtration and heat insulation properties of foam formed cellulose based materials. *Nord. Pulp Pap.* **2014**, *29*, 584–591. [CrossRef]
19. Jahangiri, P.; Logawa, B.; Korehei, R.; Hodgson, M.; Martinez, D.M.; Olson, J.A. On acoustical properties of novel foam-formed cellulose-based material. *Nord. Pulp Pap. Res. J.* **2016**, *31*, 14–19. [CrossRef]
20. Stanciu, M.D.; Savin, A.; Nastac, S.M. Mechanical and surface properties of lignocellulosicfibres reinforced composites. *Stroj. Vestn* **2018**, *64*, 698–705.
21. Seciureanu, M.; Nastac, S.-M.; Guiman, M.-V.; Nechita, P. Cellulose Fibers-Based Porous Lightweight Foams for Noise Insulation. *Polymers* **2023**, *15*, 3796. [CrossRef]
22. Nechita, P.; Nastac, S. Foam-formed cellulose composite materials with potential applications in sound insulation. *J. Compos. Mater.* **2018**, *52*, 747–754. [CrossRef]
23. Debeleac, C.; Nechita, P.; Nastac, S. Computational investigations on soundproof applications of foam-formed cellulose materials. *Polymers* **2019**, *11*, 1223. [CrossRef]
24. Nastac, S.; Nechita, P.; Debeleac, C.; Simionescu, C.; Seciureanu, M. The Acoustic Performance of Expanded Perlite Composites Reinforced with Rapeseed Waste and Natural Polymers. *Sustainability* **2022**, *14*, 103. [CrossRef]
25. Ionescu, S.; Nechita, P. Thermo-Insulating Panels Based on Composite Structures from Vegetal Fibres and Polymeric Matrix. *Adv. Mater. Res.* **2017**, *1143*, 154–159.
26. Nechita, P.; Roman, M.; Nastac, S.M. Green Approaches on Modification of Xylan Hemicellulose to Enhance the Functional Properties for Food Packaging Materials—A Review. *Polymers* **2023**, *15*, 2088. [CrossRef] [PubMed]
27. Nastac, S.; Debeleac, C.; Nechita, P. Assessments On Shock Absorption Properties Of Foam-Formed Low Density Cellulose Composites. *Acta Tech. Napoc. Ser. -Appl. Math. Mech. Eng.* **2017**, *60*, 565–572.
28. Radvan, B.; Gatward, A. Formation of wet-laid webs by a foaming process. *Tappi* **1972**, *55*, 748.
29. Xiang, W.; Filpponen, I.; Saharinen, E.; Lappalainen, T.; Salminen, K.; Rojas, O.J. Foam Processing of Fibers As a Sustainable Alternative to Wet-Laying: Fiber Web Properties and Cause–Effect Relations. *ACS Sustain. Chem. Eng.* **2018**, *6*, 14423–14431. [CrossRef]
30. Madani, A.; Zeinoddini, S.; Varahmi, S.; Turnbull, H.; Phillion, A.B.; Martinez, M.D. Ultra-lightweight paper foams: Processing and properties. *Cellulose* **2014**, *21*, 2023–2031. [CrossRef]
31. Hasan, A.; Rabbi, M.S.; Billah, M. Making the lignocellulosic fibers chemically compatible for composite: A comprehensive review. *Clean. Mater.* **2022**, *4*, 100078. [CrossRef]
32. Tauhiduzzaman, M.; Hafez, I.; Bousfield, D.; Tajvidi, M. Multiscale modeling of lignocellulosic foams under compression. *Mater. Des.* **2023**, *225*, 111471. [CrossRef]
33. Leppänen, M.; Väätäinen, P. Environmental impact of cellulose-based insulation materials. *Energy Build.* **2018**, *166*, 246–254.
34. Hjelt, T.; Ketoja, J.A.; Kiiskinen, H.; Koponen, A.I.; Paakkonen, E. Foam forming of fiber products: A review. *J. Dispers. Sci. Technol.* **2022**, *43*, 1462–1497. [CrossRef]
35. Nechita, P.; Nastac, S.M. Overview on Foam Forming Cellulose Materials for Cushioning Packaging Applications. *Polymers* **2022**, *14*, 1963. [CrossRef]
36. Abd El-Sayed, E.; El-Sakhawy, M.; El-Sakhawy, M. Non-wood fibers as raw material for pulp and paper industry. *Nord. Pulp Pap. Res. J.* **2020**, *35*, 215–230. [CrossRef]
37. Cheng, F.; Lu, P.; Ren, P.; Chen, J.; Ou, Y.; Lin, M.; Liu, D. Preparation and properties of foamed cellulose-polymer microsphere hybrid materials for sound absorption. *BioResources* **2016**, *11*, 7394–7405. [CrossRef]

38. Maderuelo-Sanz, R. Characterizing and modelling the sound absorption of the cellulose acetate fibers coming from cigarette butts. *J. Environ. Health Sci. Eng.* **2021**, *19*, 1075–1086. [CrossRef]
39. Reichler, M.; Rabensteiner, S.; Törnblom, L.; Coffeng, S.; Viitanen, L.; Jannuzzi, L.; Makinen, T.; Mac Intyne, J.R.; Koivisto, J.; Puisto, A.; et al. Scalable method for bio-based solid foams that mimic wood. *Sci. Rep.* **2021**, *11*, 24306. [CrossRef] [PubMed]
40. Miranda-Valdez, I.Y.; Yazdani, M.R.; Mäkinen, T.; Coffeng, S.; Viitanen, L.; Koivisto, J.; Alava, M.J. Cellulose foams as scalable templates for phase change materials. *J. Energy Storage* **2023**, *73 Pt B*, 109036. [CrossRef]
41. Ketola, A.E.; Song, W.; Lappalainen, T.; Salminen, K.; Viitala, J.; Turpinen, T.; Lee, K.-Y.; Ketoja, J.A. Changing the Structural and Mechanical Anisotropy of Foam-Formed Cellulose Materials by Affecting Bubble−Fiber Interaction with Surfactant. *ACS Appl. Polym. Mater.* **2022**, *4*, 7685–7698. [CrossRef]
42. Neri, M.; Levi, E.; Cuerva, E.; Pardo-Bosch, F.; Zabaleta, A.G.; Pujadas, P. Sound Absorbing and Insulating Low-Cost Panels from End-of-Life Household Materials for the Development of Vulnerable Contexts in Circular Economy Perspective. *Appl. Sci.* **2021**, *11*, 5372. [CrossRef]
43. Ruan, J.; Tang, S.; Dai, J. Research on sound absorption property of natural cellulose fiber. In Proceedings of the 2018 2nd International Conference on Composite Material, Polymer Science and Engineering (CMPSE), Osaka, Japan, 21–22 September 2018; pp. 242–245.
44. Sombatsompop, N.; Niamsuwan, V. Acoustical properties of wood-based materials. In *Wood in Civil Engineering*; Springer: Berlin/Heidelberg, Germany, 2012; pp. 153–177.
45. Joutsimo, O.P.; Tyrväinen, P. The effect of fiber properties on sound absorption of soft fiberboards. *Appl. Acoust.* **2014**, *77*, 17–24.
46. Sahin, T.; Yılmaz, H. Sound absorption properties of wood-based insulation materials. *J. Acoust. Soc. Am.* **2016**, *140*, 3043.
47. Malekzadeh, H.; MdZaid, N.S.B.; Bele, E. Characterization and structural properties of bamboo fibre solid foams. *Cellulose* **2021**, *28*, 703–714. [CrossRef]
48. Sari, K.; Isnen, Y.Z.; Utomo, A.B.S.; Sunardi, S. Properties of pineapple leaf fibers with paper waste as an absorbing-composite to reduce noise. *J. Ilm. Pendidik. Fis. Al-Biruni* **2022**, *11*, 175–184. [CrossRef]
49. Li, R.; Du, J.; Zheng, Y.; Wen, Y.; Zhang, X.; Yang, Y.; Lue, A.; Zhang, L. Ultra-lightweight cellulose foam material: Preparation and properties. *Cellulose* **2017**, *24*, 1417–1426. [CrossRef]
50. Iannace, G.; Ciaburro, G.; Guerriero, L.; Trematerra, A. Use of Cork Sheets for Room Acoustic Correction. *J. Green Build.* **2020**, *15*, 45–55. [CrossRef]
51. Ciaburro, G.; Iannace, G. Membrane-type acoustic metamaterial using cork sheets and attached masses based on reused materials. *Appl. Acoust.* **2022**, *189*, 108605. [CrossRef]
52. Asdrubali, F.; Schiavoni, S.; Horoshenkov, K.V. A Review of Sustainable Materials for Acoustic Applications. *Build. Acoust.* **2012**, *19*, 283–311. [CrossRef]
53. Iannace, G.; Ciaburro, G. Modelling sound absorption properties for recycled polyethylene terephthalate-based material using Gaussian regression. *Build. Acoust.* **2021**, *28*, 185–196. [CrossRef]
54. Ciaburro, G.; Puyana-Romero, V.; Iannace, G.; Jaramillo-Cevallos, W.A. Characterization and Modeling of Corn Stalk Fibers tied with Clay using Support Vector Regression Algorithms. *J. Nat. Fibers* **2022**, *19*, 7141–7156. [CrossRef]
55. Paunonen, S.; Timofeev, O.; Torvinen, K.; Turpeinen, T.; Ketoja, J.A. Improving compression recovery of foam-formed fiber materials. *BioResources* **2018**, *13*, 4058–4074. [CrossRef]
56. Wu, M.; Yu, G.; Chen, W.; Dong, S.; Wang, Y.; Liu, C.; Li, B. A pulp foam with highly improved physical strength, fire-resistance and antibiosis by incorporation of chitosan and CPAM. *Carbohydr. Polym.* **2022**, *278*, 118963. [CrossRef] [PubMed]
57. Ergun, M.E. Activated Carbon and Cellulose-reinforced Biodegradable Chitosan Foams. *BioResources* **2023**, *18*, 1215–1231. [CrossRef]
58. Ottenhall, A.; Seppänen, T.; Ek, M. Water-stable cellulose fiber foam with antimicrobial properties for bio based low-density materials. *Cellulose* **2018**, *25*, 2599–2613. [CrossRef]
59. Seppänen, T.; Ketoja, J.; Pöhler, T.; Pääkkönen, E. Wet strength properties of foam formed fiber materials. In *Progress in Paper Physics Seminar: Abstract Book of the PPPS2020 Seminar (281–283)*; Kouko, J., Lehto, J., Tuovinen, T., Eds.; VTT Technical Research Centre of Finland: Espoo, Finland, 2020; Available online: https://publications.vtt.fi/pdf/technology/2020/T378.pdf (accessed on 7 November 2023).
60. Pöhler, T.; Ketoja, J.A.; Lappalainen, T.; Luukkainen, V.; Nurminen, I.; Lahtinen, P.; Torvinen, K. On the strength improvement of lightweight fibre networks by polymers, fibrils and fines. *Cellulose* **2020**, *27*, 6961–6976. [CrossRef]
61. Ramos, A.; Sousa, S.; Evtuguin, D.; Gamelas, J. Functionalized xylans in the production of xylan-coated paper laminates. *React. Funct. Polym.* **2017**, *117*, 89–96. [CrossRef]
62. Ebringerová, A.; Hromádková, Z.; Heinze, T. *Hemicellulose, Polysaccharides I: Structure, Characterization and Use, Advances in Polymer Science*; Springer: Berlin/Heidelberg, Germany, 2005; pp. 1–7. [CrossRef]
63. Petzold-Welcke, K.; Schwikal, K.; Daus, S.; Heinze, T. Xylan derivatives and their application potential—Mini-review of own results. *Carbohydr. Polym.* **2014**, *100*, 80–88. [CrossRef]
64. Zongquan, L.; Xuejun, P. Strategies to modify physicochemical properties of hemicelluloses from biorefinery and paper industry for packaging material. *Rev. Environ. SciBiotechnol.* **2018**, *17*, 47. [CrossRef]
65. Roman, M.; Nechita, P.; Simionescu, C.S. Evaluation of Barrier Properties of Food Packaging Papers Coated with Hemicellulose Biopolymers. *Bul. Inst. Polit. Iaşi* **2023**, *69*, 1–11. [CrossRef]

66. *T-458 cm-04*; Surface Wettability of Paper (Angle of Contact Method). TAPPI: Atlanta, GA, USA, 2004.
67. *ISO 10534-2*; Acoustics—Determination of Sound Absorption Coefficient and Impedance in Impedance Tubes—Part 2: Two-microphone Technique for Normal Sound Absorption Coefficient and Normal Surface Impedance. ISO: Geneva, Switzerland, 2023.
68. *ASTM E1050-12*; Standard Test Method for Impedance and Absorption of Acoustical Materials Using a Tube, Two Microphones and a Digital Frequency Analysis System. ASTM International: West Conshohocken, PA, USA, 2012.

polymers

MDPI

Article

Spray Drying Enzyme-Treated Cellulose Nanofibrils

Sungjun Hwang [1,2,*], Colleen C. Walker [3], Donna Johnson [3], Yousoo Han [1,2,*] and Douglas J. Gardner [1,2]

[1] Advanced Structures and Composites Center, University of Maine, 35 Flagstaff Road, Orono, ME 04469-5793, USA; douglasg@maine.edu
[2] School of Forest Resources, University of Maine, 5755 Nutting Hall, Orono, ME 04469-5755, USA
[3] Process Development Center, University of Maine, 5737 Jenness Hall, Orono, ME 04469-5737, USA; colleen.walker@maine.edu (C.C.W.); donna.johnson@maine.edu (D.J.)
* Correspondence: sungjun.hwang@maine.edu (S.H.); yousoo.han@maine.edu (Y.H.)

Abstract: Enzyme-treated cellulose nanofibrils (CNFs) were produced via a lab-scale mass colloider using bleached kraft pulp (BKP) to evaluate their processability and power requirements during refining and spray-drying operations. To evaluate the energy efficiency in the CNF refining process, the net energy consumption, degree of polymerization (DP), and viscosity were determined. Less energy was consumed to attain a given fines level by using the endoglucanase enzymes. The DP and viscosity were also decreased using the enzymes. The morphological properties of the enzyme-pretreated spray-dried CNF powders (SDCNFs) were measured. Subsequently, the enzyme-pretreated SDCNFs were added to a PP matrix with MAPP as a coupling agent. The mixture was then compounded through a co-rotating twin-screw extruder to determine whether the enzyme treatment of the CNFs affects the mechanical properties of the composites. Compared to earlier studies on enhancing PMCs with SDCNF powders, this research investigates the use of enzyme-pretreated SDCNF powders. It was confirmed that the strength properties of PP increased by adding SDCNFs, and the strength properties were maintained after adding enzyme-pretreated SDCNFs.

Keywords: enzyme treatment; cellulose nanofibrils; spray-drying; polypropylene

1. Introduction

The major chemical components of natural fibers are cellulose, lignin, and hemicellulose. Cellulose, the most abundant polymer on earth, is organized into microfibrils of amorphous and strongly hydrogen-bonded crystalline regions (α-cellulose) [1]. Cellulose contains β (1, 4)-linked glucopyranoside monomer units, predominantly located in the secondary cell wall [2]. The three hydroxyl groups on the glucose monomer are attributable to hydrogen bonding among the fibers [3]. The micrometer-sized cellulose can be manufactured into nanometer-sized cellulose by mechanical, chemical, and biological treatments [4]. The generated higher specific surface area with an increased number of hydroxyl groups on each nanofiber leads to an increase in hydrogen bonding, resulting in creating a strong network within the fibers [5].

Cellulose nanofibrils (CNFs) manufactured through mechanical treatment via grinding, refining, and/or homogenization are the most cost-effective production methods and have a very high production rate compared to other methods [6]. Therefore, CNFs are widely used as reinforcing fillers in thermoplastic matrix composites to increase the mechanical properties [7]. However, CNFs have a relatively bigger width and longer fibrils which result in a broad fiber size distribution compared with cellulose nanocrystals (CNCs). Therefore, high energy consumption is required to defibrillate pulp fibers to smaller sizes [8]. Many researchers are actively conducting research to produce CNFs more economically [9].

Conventionally, the bleaching chemicals used in pulping before the refining process eliminate lignin and hemicellulose that act as binding agents between cellulose fibrils, leading to the reduction of refining efficiency [10]. Moreover, TEMPO-oxidation, carboxylation,

and sulfonation are widely used to reduce the energy consumption in the refining process; however, those chemical methods are harmful to the environment [11–13]. Enzyme pretreatment includes using endoglucanases, cellobiohydrolases (CBHs), and β-glucosidases (BGs), which are well-known environmentally friendly methods for the reduction of refining costs as biodegradable cellulases are neutral and produce no emissions of harmful chemicals [14]. Endoglucanases are the primary enzymatic pretreatment for CNFs among other enzyme treatments. Endoglucanases specifically cleave the cellulose β-1, 4 linkages in the amorphous regions without affecting the crystalline regions. This leads to a reduction in fiber length and an increase in crystallinity, while preserving the mechanical properties of polymer matrix composites (PMCs). Because of their features, many researchers have used endoglucanases as an aid in fiber defibrillation for high efficiency during the production of cellulose nanofibrils [15–18].

Polymer matrix composites (PMCs) are composed of plastic matrices and reinforcement additives [19]. Polypropylene (PP) is a very common commodity thermoplastic, and it has been widely applied in the automotive and packaging industries because of its advantageous properties such as low price, good processability, resistance to weathering, and recyclability, which make PP accepted worldwide with a demand of over 21 million pounds per year [20,21]. Inorganic reinforcing materials including glass, carbon, and aramid fibers are commonly used in the PP matrix to increase its mechanical properties [22,23]. However, compared to conventional inorganic fillers, natural fibers have many significant advantages including biodegradability and relatively high tensile strength. Particularly, a significant enhancement of thermal and mechanical properties occurs with the addition of a small amount of CNFs into the polymer matrix [24]. However, the aqueous slurry CNFs are challenging to use in the manufacturing PMCs industry using the current melt compounding processes [25].

Spray drying is a fast, simple, cost-effective, and scalable method, so it is used in various industries including pharmaceutical, food, and chemical manufacturing [26,27]. Furthermore, SDCNFs have been reported to have higher thermal stability and superior crystallinity index than fibers dried by other drying methods including air-drying, oven-drying, freeze-drying, and supercritical-drying [28–32]. Spray-dried cellulose nanofibrils (SDCNFs) have the property of excellent dispersion and distribution in the plastic matrix attributable to their micrometer size with the spherical shape of individual particles [33]. There are typically three different atomizing techniques: a rotary disk atomizer, two-fluid nozzle, and ultrasonic atomizer [34]. Among the three different spray-drying techniques, the pilot-scale rotary disk atomizer offers a larger capacity and improved drying efficiency compared to the other two techniques scaled for laboratory use, attributable to its centrifugal technology that minimizes feed blockage [35]. In a pilot-scale rotary disk atomizer, the feedstock in liquid suspension is transported into the atomizer by a feed pump. The hot air and the centrifugal energy generated by the rotating disk atomizer are delivered to the suspensions. The disintegration of the liquid film results in the formation of droplets by the centrifugal force, and the water in droplets is evaporated, creating dry particles. After the disintegration of liquid film into the formation of droplets, the droplets evaporate, creating dry particles. The resulting particles collide with the surface of the cyclone, leading to a loss of kinetic energy and causing the particles to fall into the collector [36–38].

A serious problem of natural fiber use with non-polar polymers is the polar hydroxyl groups on the surface of the fibrils that are incompatible with most plastic matrices [39]. Furthermore, it is believed that the agglomeration of cellulose occurs because of the incompatibility between filler (hydrophilic) and matrices (hydrophobic) as the hydrophilic cellulose fibers can be agglomerated together by the hydrogen bonding among fibrils. Chemical modification on the fibril surfaces can make them hydrophobic, resulting in improved interfacial bonding between PMCs and reinforcing fillers materials [40]. The use of maleic anhydride-grafted polypropylene (MAPP) leads to an increase in the interfacial bonding between fibers and the PP matrix. MAPP can be bonded with the hydroxyl group

of cellulose by esterification or hydrogen bonding. At the same time, the PP tail on the MAPP becomes entangled with the melted polypropylene matrix [41,42].

In this research, the net energy consumption, the degree of polymerization (DP), and the low shear viscosity of enzyme- and non-treated CNFs were compared, and they were also compared based on enzyme dosage. The morphological and size analyses of SDCNFs dried from enzyme- and non-treated CNFs were compared. To determine the effect of the enzyme-pretreated SDCNFs on the PP matrix, the enzyme- and non-pretreated SDCNF powders were used as a reinforcing filler in a PP matrix, and the MAPP was used as a coupling agent between two materials, followed by comparing the mechanical properties of two composites. Compared to previous studies that explored the enhancement of PMCs with the incorporation of SDCNF powders, this research evaluates the effects of using SDCNF powders derived from enzyme-treated CNFs instead of non-treated CNFs. It also examines the relationship between the degree of polymerization (DP) and particle production. By reducing the manufacturing cost of CNFs and the subsequent production cost of SDCNFs, we believe this material is viable for use in commodity products and the interior components of the automotive industry.

2. Materials and Methods

2.1. Enzyme-Pretreated CNFs Production

The enzyme pretreatments and CNFs production were conducted by the Process Development Center (PDC) at the University of Maine, Orono, ME, USA. CNFs were made using bleached softwood kraft pulp (BSK) (US Patent, US 20170073893A1), after enzyme pretreatment. The enzyme used in this work was pure endoglucanase purchased from FiberCare (Novozymes, Kalundborg, Denmark), and the enzyme activity is 4500 ECU/g. The pretreatments were conducted at two enzyme levels—Low: 0.05% or High: 0.5%—as a percentage of the oven-dried pulp weight. Before addition to the pulp, the enzyme was diluted at a 3:40 ratio with DI water, and the pulp was diluted with the enzyme solution and water to the final treatment consistency of ~4%. The temperature was maintained at 50 °C throughout the treatment by placing the treatment container in a circulatory water bath, and the pulp was constantly mixed with a standing mixer at 1000 rpm. pH was adjusted to 5.5–6.5 by adding 10% H_2SO_4 solution as needed. The pulp was held at temperature for a 1 h treatment period. After treatment, the enzyme was denatured by heating the slurry at 90 °C for 25 min. In a representative experiment, 85 g of oven-dried bleached softwood kraft pulp (2219 g slurry at 3.83% consistency) was placed in a container in the water bath. The slurry was stirred until its temperature reached 50 °C. Prior to enzyme addition, the pH of the slurry was adjusted to 6.2. Then, 6.07 g of diluted enzyme solution was added (0.5% enzyme dose) and stirred continuously for one hour. After the treatment time, the mixture was denatured. The enzyme- and non-treated pulps were processed into CNF suspensions by using a mass colloider (Masuku Super, Model MKCA6-2, Tokyo, Japan) at 1800 rpm using 'fine" plates (MK-E6-46-DD). The pulps were diluted to 1.5% consistency by adding tap water. The pulp was then processed through the mass colloider in a single-pass fashion, repeating until the pulp was fibrillated to low (~50%), medium (~80%), and high (~95%) fines content.

2.2. Determination of Fines Level and Energy Consumption

In this study, the fines content (level) of CNF suspensions was reported based on the percentage of under 200 μm length fibers in the total amount of fibers [43]. The fines content was measured via the MorFi Fiber Analyzer (TechPap, Gières, France), and the measurement was made using two cameras that measured the fibers in a 50-micrometer-wide chamber and then delivered the data to the software. The net energy consumption was measured by monitoring the consumption of electricity during the grinding process.

2.3. Characterization of Enzyme-Pretreated CNFs

The low shear viscosity of enzyme- and non-treated CNF suspensions were measured via a Brookfield viscometer with spindle #64 at 100 RPM. The degree of polymerization (DP) was estimated based on the intrinsic viscosity according to TAPPI Test Method T237cm-98. *DP* was calculated by the Mark-Houwink-Sakurada equation [44]:

$$[\eta] = K \cdot DP^a$$

*η is the intrinsic viscosity; *K and a are the Mark Houwink parameters: K = 2.28, a = 0.76.

2.4. Spray Drying

Cellulose nanofibrils (CNFs) in dry powder form were produced by utilizing a pilot-scale spray dryer. The drying conditions are listed in Table 1. The solids content of all samples was set to 1.5 wt.% before they were spray-dried.

Table 1. Conditions of spray drying.

Conditions	Inlet Temp, °C	Outlet Temp, °C	Bag House Temp, °C	Spinning Disk, RPM	Feeding Rate, kg/h	Air Fan Speed, %
	248	123	117	30,000	17	85

2.5. Composite Manufacturing

The following two polymers were used as a matrix and coupling agent for the formulation: polypropylene (PP) (Pro-fax 6525, LyondellBasell, Rotterdam, The Netherlands); maleic anhydride modified homopolymer polypropylene (MAPP) (Polybond 3200, Lawrenceville, GA, USA). SDCNFs-reinforced PP composite was melt-compounded using a co-rotating twin-screw extruder (C. W. Brabender Instruments, South Hackensack, NJ, USA). The extruder process parameters were 180 °C across the heating sections with an extrusion speed of 50 rpm. The composite extrudate passed through a two-nozzle die with a nozzle diameter of 2.7 mm. Cooled extrudates were ground using a granulator (Hellweg MDS 120/150, Hackensack, NJ, USA). A masterbatch compounding process was used in this research to improve the dispersion and distribution of filler within the PP matrix. Table 2 shows the compounding conditions of treated and non-treated SDCNFs-reinforced PP composites. The MAPP ratio was fixed to 5 wt.%, and the PP ratio was changed according to the SDCNF ratios of 5 wt.% and 10 wt.%. For the masterbatching process, the input contents of SDCNFs, MAPP, and PP were 50%, 25%, and 25%, respectively, in the first compounding, followed by adding the neat PP to dilute the masterbatch in the second compounding. The input contents of neat PP and produced masterbatch were 60% and 40%, respectively, as listed in Table 3. The PP composites with 5 wt.% of SDCNFs added were not affected by the masterbatch, so the masterbatch was applied only in the PP composites filled with 10 wt.% of filler content. An injection molder Model #50 "Minijector" with a ram pressure of 2500 psi at 200 °C was used to produce specimens according to ASTM D 638, D 790, and D 256 for tensile, flexural, and IZOD impact tests, respectively.

2.6. Morphological Properties of SDCNFs Powders

The SEM images of SDCNFs were obtained via the Hitachi Tabletop Microscope SEM TM 3000 (Hitachi High-Technologies Corporation, Tokyo, Japan). SDCNF powders were placed on the SEM stub covered with carbon tape using a lab scoop. Air flow was then used to secure minor particles to the carbon tape. The set accelerating voltage was 15 kV and various magnifications were adjusted automatically. The particle size distribution was measured via a laser diffractometer Mastersizer 2000 (Malvern, Worcestershire, UK). One gram of SDCNF powders was placed on the tray in the Scirocco 2000 attachment (Malvern, Worcestershire, UK), and the powders were analyzed with a particle refractive index of 1.53 [45]. The aspect ratio and circularity of SDCNFs particles were measured

via a Morphologi-G3-ID morphologically directed optical microscope system (Malvern, Worcestershire, UK). The following two equations are Circularity and Aspect Ratio:

$$\text{Circularity} = \frac{2\times\sqrt{\pi \times \text{Area}}}{\text{Perimeter}}$$

$$\text{Aspect Ratio} = \frac{\text{Width}}{\text{Length}}$$

Perimeter (μm): Actual perimeter of particle; Area (μm^2): Actual area of a particle in square microns [46].

Table 2. Polymers and SDCNFs powder formulation (wt.%).

No.	Composite	PP	SDCNFs	MAPP
1	Neat PP	100	0	0
2	Control 5% (non-enzyme-treated)	90	5	5
3	Control 10% (non-enzyme-treated)	85	10	5
4	Enzyme 5% (enzyme-treated)	90	5	5
5	Enzyme 10% (enzyme-treated)	85	10	5

Table 3. Masterbatch formulation (wt.%).

1st Compounding Formulation	2nd Compounding Formulation	SDCNFs	MAPP	PP
SDCNFs50%:MAPP50%:PP25%	Masterbatch40%:PP60%	10	5	85

2.7. Mechanical Properties of SDCNFs-Reinforced PP Composite

Tensile strength and MOE were performed according to the ASTM D 638-10 standard [47] and under a displacement control loading with a speed of loading of 5 mm/min. An extensometer was employed to determine the elongation of the specimens. Flexural strength and MOE were performed according to ASTM D790-10 [48] and under a displacement control loading with a speed of 1.27 mm/min. Izod impact strength was measured according to ASTM D256-10 [49] using a Ceast pendulum impact tester (Model Resil 50B). Notching was produced on the impact specimens using a Ceast notch cutting machine.

3. Results and Discussion

3.1. Effect Enzyme Pretreatment on Energy Consumption

Figure 1 shows the net energy vs. fines curves for the enzyme- and non-treated CNF suspensions. The enzyme-treated pulps required much less energy by up to 64% to reach a 90% fines level than non-treated pulp, and the difference in net energy consumption between the two enzyme dosages was insignificant. The net energy consumption after enzyme treatment was lowered to 70% and 77% compared to the non-treated pulp at the 80% fines level after adding 0.05% and 0.5% enzyme doses, respectively. The reduction rate of energy consumption was the same as 63% at the 90% fines level for two enzyme doses.

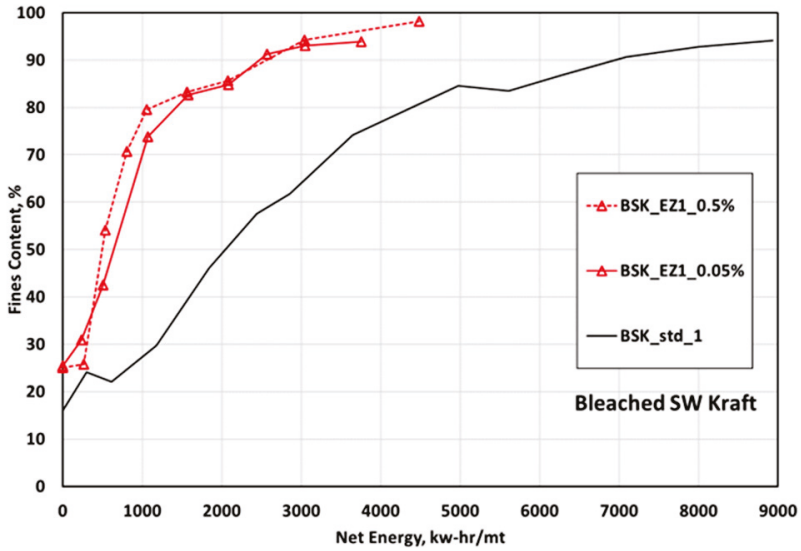

Figure 1. Energy vs. fines for CNFs made from enzyme-pretreated (EZ1) bleached softwood kraft pulp at two doses of the enzyme, 0.5% and 0.05%.

Figures 2 and 3 represent the low shear viscosity and the degree of polymerization (DP), respectively. As fines levels increased for both enzyme- and non-treated CNF suspensions, the viscosity increased and the degree of polymerization (DP) decreased, which is consistent with previous research [50,51]. After the grinding process, the increased surface area and aspect ratio of fibers can generate more hydrogen bonding and entanglement between fibers, resulting in strong interfibril interactions. This can restrict suspension flow, leading to increased viscosity [52,53]. DP might be decreased, attributable to the shortened fiber length by the grinding process [54]. In addition, the change rate in viscosity increased, while DP was consistent, as the fine levels increased. In general, longer grinding can further increase the aspect ratio of the fiber because the reduction rate of the fiber width is higher than that of the fiber length. The decreased fiber width with unchanged fiber length increases the aspect ratio, increasing the viscosity change rate and decreasing the change rate of DP [55].

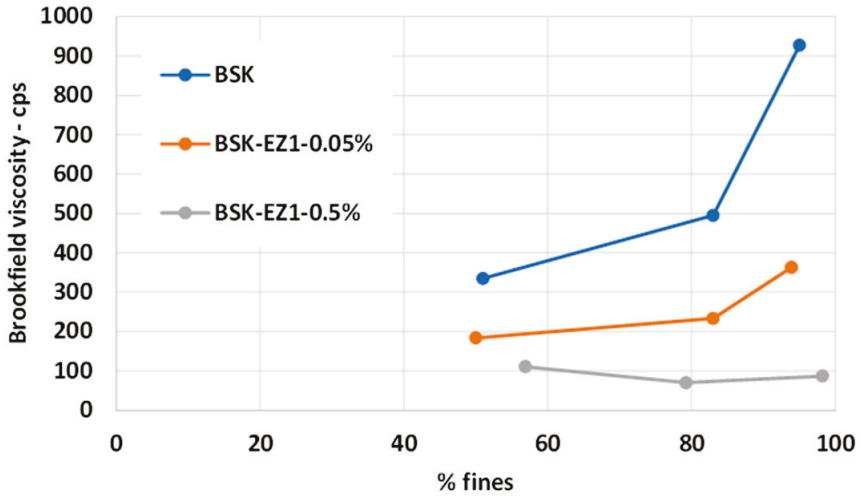

Figure 2. Low shear viscosity vs. fines for CNFs made from enzyme-pretreated (EZ1) bleached softwood kraft pulp at two doses of the enzyme, 0.5% and 0.05%.

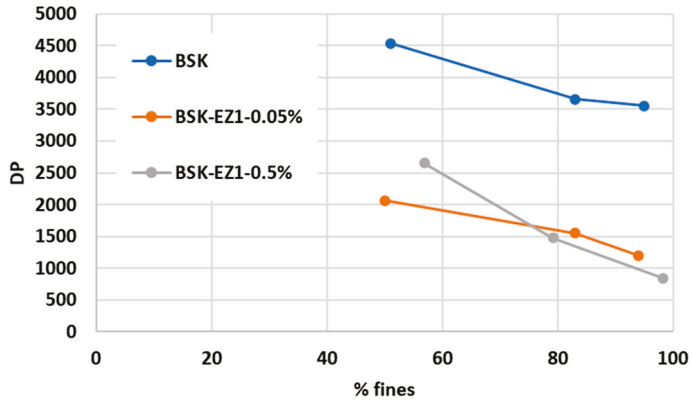

Figure 3. Degree of polymerization vs. fines for CNFs made from enzyme-pretreated (EZ1) bleached softwood kraft pulp at two doses of the enzyme, 0.5% and 0.05%.

Enzyme-treated 90% fines CNF suspensions had lower DP and viscosity than untreated CNFs by up to 69% and 88%, respectively. DP might be decreased, attributable to the shorter fibers resulting from the cleavage of amorphous regions in cellulose chains by the endoglucanases [56]. In addition, the shorter fiber length by endoglucanases might lead to decreased fiber-fiber interactions, forming a less tight network between fibers resulting in lowered viscosity. Furthermore, the swelling effect resulting from the endoglucanase might make fibers more flexible, leading to separate fiber bundles and reducing fiber-fiber contact sites, resulting in a decrease in the viscosity. A 0.5% dose of endoglucanase had lower viscosity than a 0.05% dose at entire fines levels, attributable to increased binding sites between the fiber surface and the endoglucanase. DP of the 0.5% dose CNFs was higher by 20% compared to a 0.05% dose of endoglucanase at the lower fines levels. However, DP of the 0.5% dose was somewhat lower than that of the 0.05% dose after 80% fines levels, and this is likely attributable to a 0.05% dose of endoglucanase readily removing the exposed cellulose surface chains. In contrast, the rapid removal of cellulose chains might have occurred from the 0.5% dose [57].

It can be concluded that the net energy consumption during a grinding process to reach the targeted fines level decreased with the reduction of viscosity and DP of CNF suspensions attributable to the shortened fiber length and separated fiber bundles by the endoglucanase. In addition, based on the measurement of viscosity and DP, using 0.05% of endoglucanase had enough effect to reduce the net energy consumption during grinding. In this study, only a 0.05% dose of endoglucanase was selected for spray drying and composite manufacture.

3.2. Production of SDCNFs Powder

Generally, fine powder spray-dried without a fibrous material might be considered to mean high drying efficiency. In our previous research, good-quality powders without fibrous materials were produced using a 1.5 wt.% CNFs suspension fibrillated by a pilot scale thermo-mechanical refiner. In this research, 1.5 wt.% CNF suspensions were fibrillated through a laboratory-scale mass colloider with a lower fibrillation performance than a pilot-scale thermos-mechanical refiner. All produced SDCNF powders using CNF suspensions fibrillated by the mass colloider included fine powders and fibrous materials after spray drying. This is likely attributable to the fact that CNF suspensions manufactured through a Masuku Super mass colloider are less defibrillated and contain many long fibers, resulting in reduced drying efficiency. The long fibers can be entangled with each other during the drying process, leading to a heavy accumulation of materials on the drying chamber wall and plugging of the spinning disk atomizer holes [58].

As shown in Figure 4, the No. 20 mesh sifting screen (the medium-size U.S. Standard mesh size with an 833 μm nominal sieve opening) was used to sift the SDCNF powders spray-dried from enzyme- and non-treated CNF suspensions and then collect only the fine

powders except for the fluffy, fibrous material. Figure 5 represents the SEM images of sifted fine particles and fibrous materials. The spherical-shaped small particles were observed in the collected fine particles. The collected fine powders from enzyme- and non-treated CNF suspensions were used to measure the morphological properties of SDCNF powders and their utilization as the reinforcing material in the polymer matrix.

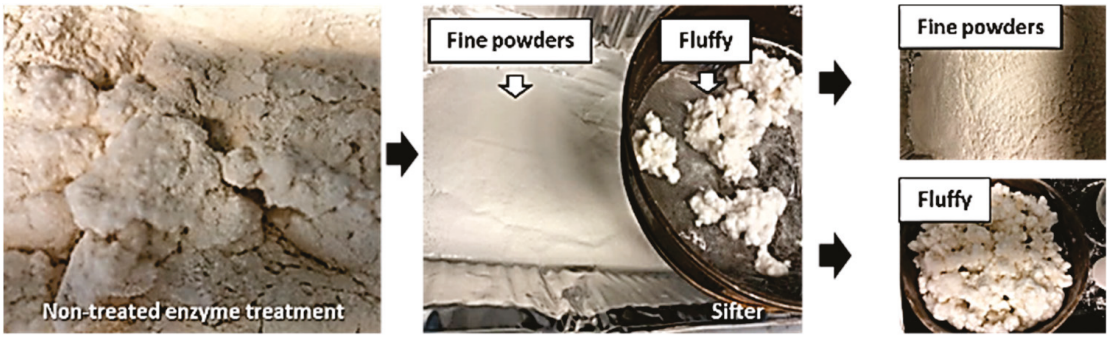

Figure 4. Procedure of sifting SDCNF powders.

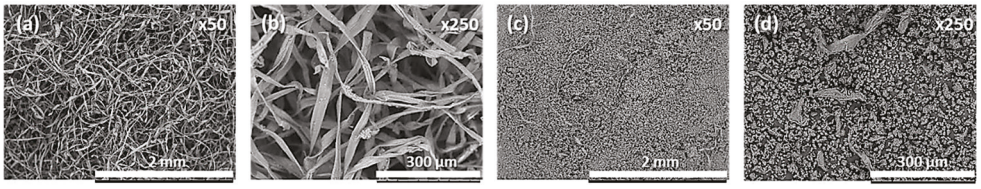

Figure 5. SEM micrographs of sifted fibrous materials (**a**,**b**) and fine powders (**c**,**d**).

3.3. Effect of Enzyme Pretreatment on Spray Drying

A 90% fines level of CNFs suspension was used for both enzyme- and non-pretreated SDCNFs, and the enzyme-pretreated SDCNFs included 0.05% of endoglucanase. The collected contents of sifted fine powders in enzyme- and non-pretreated SDCNFs were 94% and 84%, respectively. It can be concluded that the spray-drying production efficiency is improved by the enzyme treatment, producing less fibrous material. Figure 6 shows the morphological properties and the particle size distribution of the enzyme- and non-pretreated SDCNFs. For scanning electron microscopy (SEM), particle size distribution (PSD), and Morphologi-G3, the subjected samples were only fine powders separated from fibrous materials; it must be noted that the morphology and size analysis may not perfectly represent the whole samples collected from the spray drying. The CEDs given in the chart are the arithmetical mean values of the particle samples based on the surface area [D3.2] of the samples, and the [D3.2] values were considered as the mean particle size of SDCNF powders in this study [59]. The mean particle sizes of treated and non-treated SDCNFs were 13 µm and 19 µm, respectively. The mean particle size of the 0.05% enzyme-pretreated SDCNFs is slightly smaller than that of the non-pretreated SDCNFs, and this is likely attributable to the endoglucanase reducing the DP of pulp fibers during grinding, leading to more fine particles forming with smaller particle sizes after spray drying. In addition, the fiber bundles might be further separated into individual fibers by a swelling effect resulting from the endoglucanase [60]. The particle size distributions of all samples are well matched with the scanning electron microscopy (SEM) images.

The aspect ratio and circularity of enzyme- and non-enzyme-pretreated SDCNFs were measured via G3-Morphologi (Figure 7). The aspect ratio and circularity values lying between 0 to 1 indicate the particles' shapes in Morphologi-G3. For example, the closer their value to 1, the closer the shape of the circle, while the closer it is to 0 indicates a more prolonged rod shape [46]. For the aspect ratio in Morphologi-G3, the result value is presented reciprocal to the general result of the aspect ratio. A result value of 1 in Morphologi-G3 means that the length and width of the fibers are the same. Overall, the

circularity values were over 85% between 0.8 to 1, and the aspect ratio values were also over 85% in the 0.6 to 1 range, which means that the enzyme- and non-pretreated SDCNFs include spherical-shaped fine particle forms. However, the difference between the two samples was insignificant.

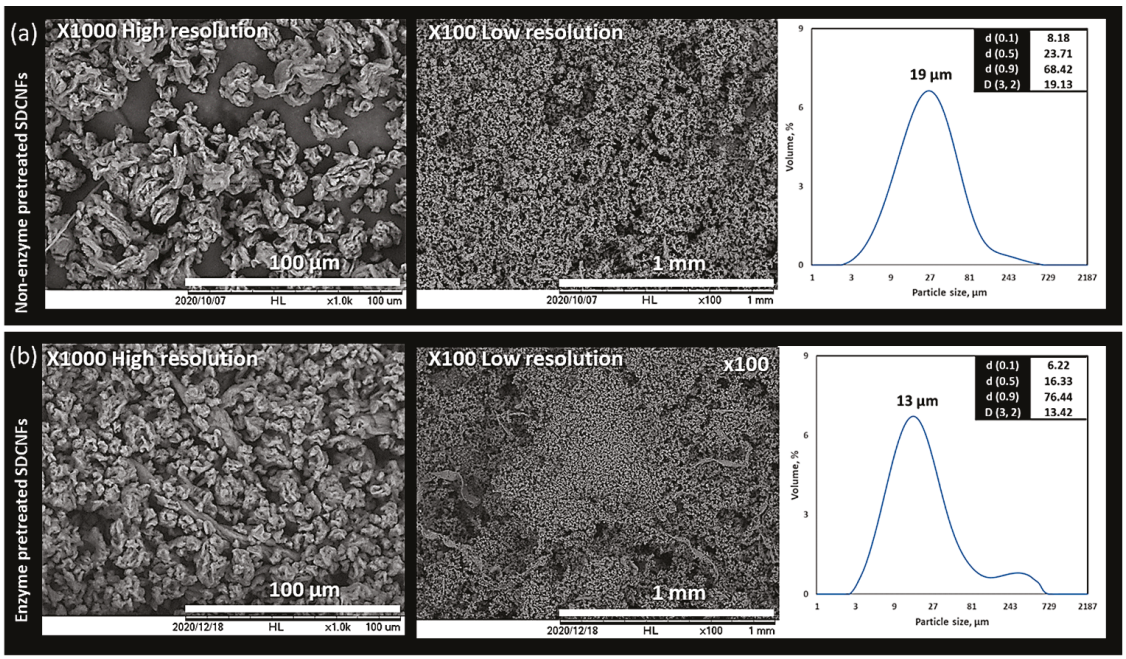

Figure 6. SEM micrographs of non-enzyme-treated (**a**) and enzyme-treated (**b**) cellulose nanofibrils with size distributions and mean CED.

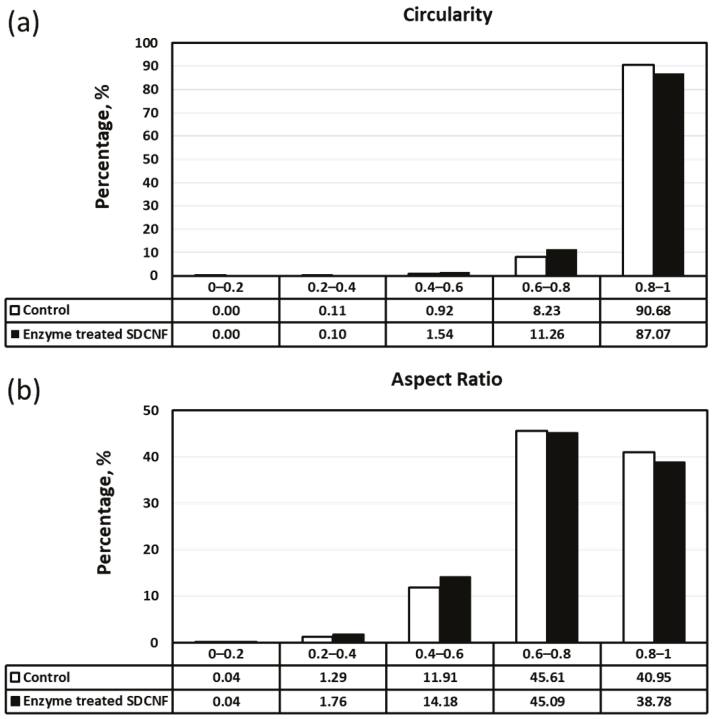

Figure 7. Morphological properties of non-enzyme-treated and enzyme-treated cellulose nanofibrils with circularity (**a**) and aspect ratio (**b**).

3.4. Enzyme-Pretreated SDCNFs Reinforced PP Composites

The enzyme-pretreated SDCNFs were utilized for composite sample manufacturing to evaluate the reinforcing functionality of the CNFs in polymeric matrices. Non-enzyme-pretreated SDCNFs denoted as control SDCNFs in this research were used as a control group to understand the effect of enzyme treatment on the mechanical properties of PP composites. Figure 8 shows the SEM images of 5 wt.% enzyme-treated and non-treated SDCNFs-reinforced PP composites using fractured specimens after the impact test. It can be confirmed that all SDCNFs were embedded in the PP matrix with good dispersion and distribution by the masterbatch system applied using a double compounding process. The tensile strength and tensile MOE of composites increased by adding 5 wt.% and 10 wt.% of enzyme-pretreated and non-pretreated SDCNFs into the PP matrix compared to neat PP; however, there was no significant difference in the increased feeding rate between 5 wt.% and 10 wt.% of fillers added. As shown in Figure 9, the maximum increased rate of tensile strength and tensile MOE were 20% and 45%, respectively. It can be concluded that SDCNFs were well distributed in the PP matrix, and the SDCNFs played the role of reinforcing material properly to the plastic matrix. In addition, the interfacial bonding between hydrophilic SDCNFs and hydrophobic PP matrix is increased by the MAPP coupling agent. Furthermore, it was confirmed that there was no difference in tensile properties even if enzyme-pretreated SDCNFs were added to the PP matrix. The flexural properties showed a similar tendency to tensile properties, and the maximum increase rate of flexural strength and flexural MOE were 7% and 45%, respectively (Figure 10). The impact strength of 5 wt.% SDCNFs-reinforced PP composite increased, and the maximum increase rate of impact strength was approximately 15% (Figure 11). It can be concluded that adding the SDCNFs as a reinforcing material in polymer matrices overcomes the reduction in impact strength attributable to the decreased fiber size with spherical-shaped powders, which reduced the contact site between fibrils and matrices. On the contrary, the impact strength decreased with the addition of 10 wt.% SDCNFs in the PP matrix, and it might be attributed to the result of an excessive amount of filler embedded in the PP matrix. Generally, it is difficult to improve the impact strength using cellulosic materials because of intrinsic long fibrils' properties resulting in stress concentration that leads to crack initiation in polymer matrices. The further reduction in impact strength occurred when the coupling agent was applied because the strong interfacial adhesion between the fibrils and matrix reduces polymer mobility, and it can prevent fiber pull-outs from the matrix, resulting in a decrease in impact strength [61–63]. There was no decrease in mechanical properties, including tensile and flexural properties, and impact strength, even though enzyme treatment was applied to CNFs, which is likely attributable to the result of endoglucanase breaking the amorphous region except the crystalline region of cellulose.

It has been observed that the addition of a small amount of SDCNFs to the polymer matrix in this research significantly enhances mechanical properties, a finding consistent with previous research [33]. According to Peng et al. [33], after adding 6 wt.% of SDCNFs and 2 wt.% of MAPP into the PP matrix, the tensile strength, tensile MOE, flexural strength, and flexural MOE increased by up to 11%, 36%, 7%, and 21%, respectively, compared to the neat PP. In Peng et al., the increase in tensile and flexural properties was lower, and the impact strength was higher than that of this research. The main reason for the different values of mechanical properties might be the different spray-drying techniques used to dry the CNFs suspension. Peng et al. used a lab-scale spray dryer, which utilized a pneumatic two fluid nozzle (TFN) to atomize the droplets of the fluid feed [64], while a pilot-scale rotary atomizer was used in this research. The 4 μm particle size produced by the lab-scale spray dryer was smaller than our powders containing an average of about 13 μm. CNFs dried from a rotary disk atomizer contained bigger particle sizes and more fibrous material with a higher aspect ratio, resulting in better stress transfer between the matrix and the fibers, leading to higher tensile and flexural properties compared to the SDCNFs dried by the lab-scale dryer [65]. In terms of the impact strength, it is believed that the small-sized particles dried by a lab-scale spray dryer prevented more crack initiation, resulting in a higher impact strength [33,66].

Overall, individual SDCNF particles exceeding 10 μm with a higher aspect ratio might be more advantageous for tensile and flexural properties, whereas these larger particles are not as beneficial for impact strength as the finer 4 μm particles.

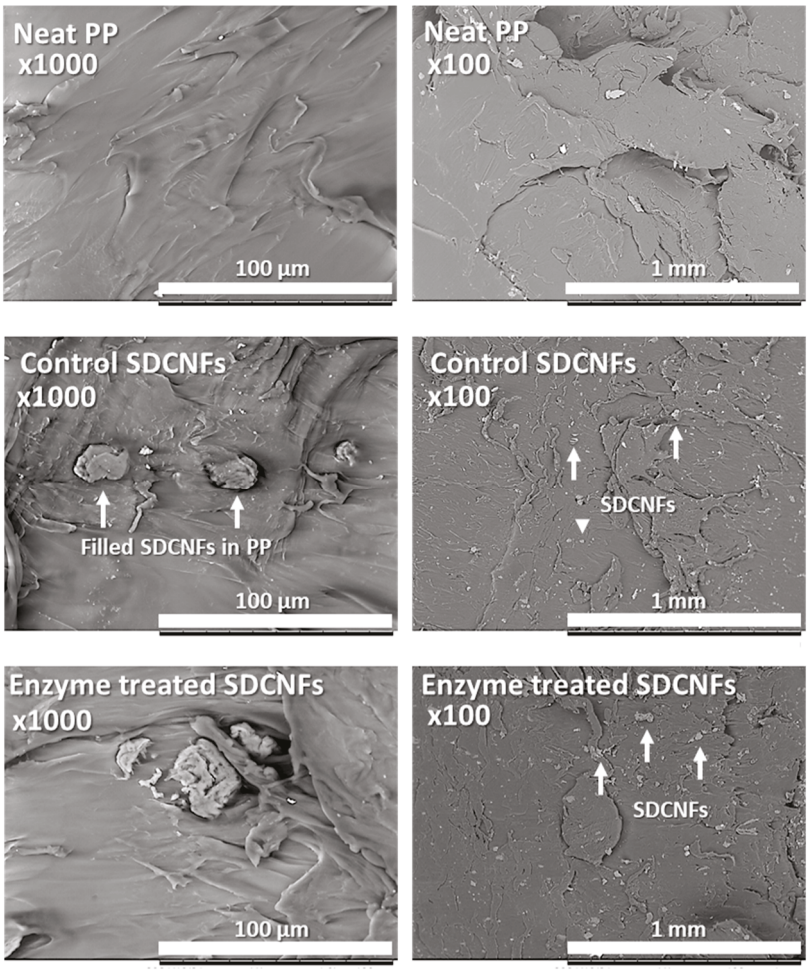

Figure 8. SEM images of fractured neat PP and 5 wt.% reinforced enzyme-treated and non-treated SDCNFs-PP composites.

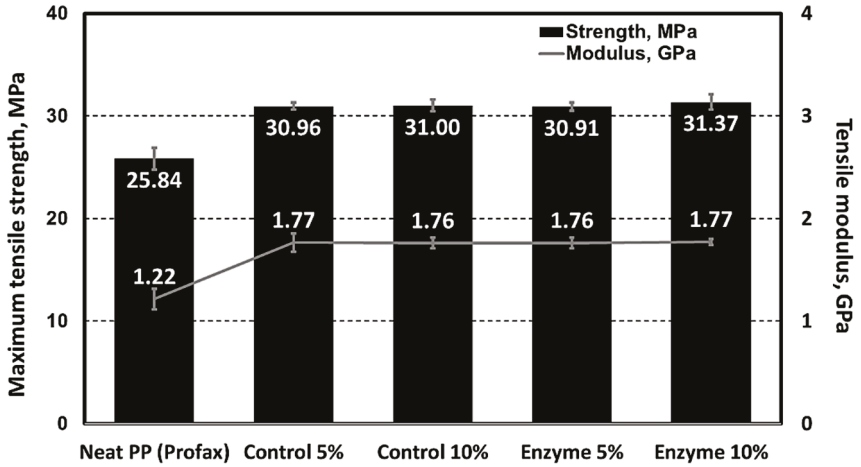

Figure 9. Tensile properties of enzyme-treated and non-treated SDCNFs-reinforced PP composites.

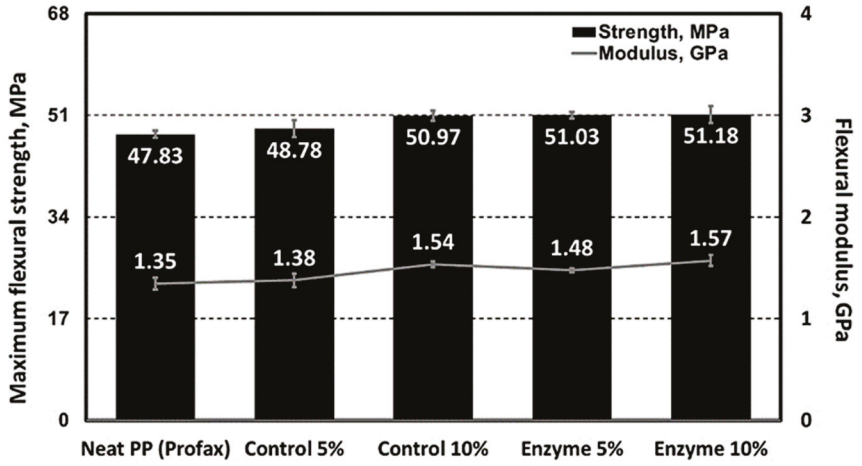

Figure 10. Flexural properties of enzyme-treated and non-treated SDCNFs-reinforced PP composites.

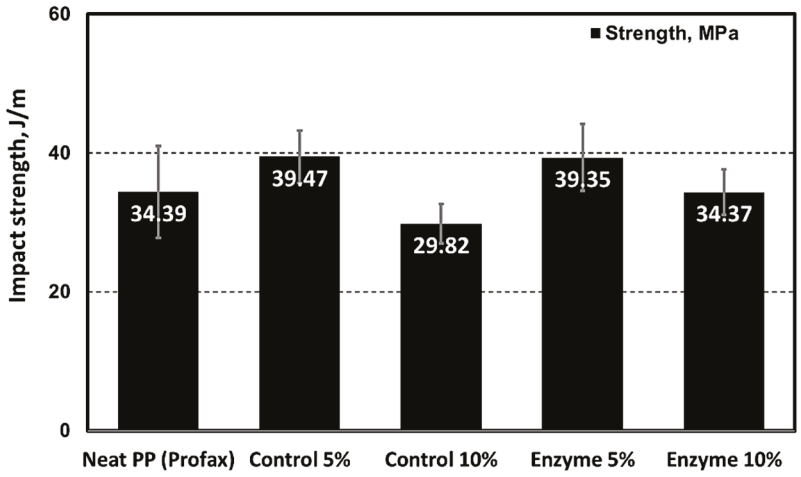

Figure 11. Impact strength of enzyme-treated and non-treated SDCNFs-reinforced PP composites.

4. Conclusions

In this study, an attempt to reduce the energy consumption used in the CNF grinding process was made through an enzymatic treatment using endoglucanase. It was confirmed that the DP and viscosity of CNFs were reduced by up to 66% and 88%, respectively, and the net energy consumption was lowered by up to 64% at a 90% fines level, attributable to the effect of the enzyme treatment. The enzyme-treated CNF suspensions were successfully dried using a conventional spray dryer, and their sizes are smaller than the control CNFs powder; even the morphologies are similar to each other. The size and morphological differences of the CNFs between the fibrillation methods (super mass collider and disk grinder) need to be studied in the future. The thermoplastic composite samples filled with enzyme-treated SDCNFs showed significant increases in mechanical performance, but no differences from that of composite samples filled with regular SDCNFs. The increase in composite samples was up to 20% and 45% in strength and modulus, respectively. SDCNFs are already known as effective reinforcing materials in PMCs; however, the study of enzyme-treated SDCNFs is limited. Utilizing enzyme treatment on CNF suspensions could reduce SDCNFs manufacturing costs, making them more viable for wider industry applications.

Author Contributions: S.H., Y.H. and D.J.G. wrote the main manuscript text. C.C.W. and D.J. reviewed and commented on the manuscript. All authors have read and agreed to the published version of the manuscript.

Funding: US Department of Energy (DOE), Office of Energy Efficiency and Renewable Energy, Advanced Materials and Manufacturing Office under CPS Agreement 35863.

Institutional Review Board Statement: Not applicable.

Data Availability Statement: All of the material is owned by the authors and/or no permissions are required.

Acknowledgments: This material is based upon work supported by the US Department of Energy (DOE), Office of Energy Efficiency and Renewable Energy, Advanced Materials and Manufacturing Office under CPS Agreement 35863, and Manufacturing Renew3D Oak Ridge National Laboratory/University of Maine Hub & Spoke Program team.

Conflicts of Interest: The authors declare no conflict of interest.

References

1. Zhang, B.; Biswal, B.K.; Zhang, J.; Balasubramanian, R. Hydrothermal treatment of biomass feedstocks for sustainable production of chemicals, fuels, and materials: Progress and perspectives. *Chem. Rev.* **2023**, *123*, 7193–7294. [CrossRef]
2. Chibrikov, V.; Pieczywek, P.M.; Zdunek, A. Tailor-made biosystems-bacterial cellulose-based films with plant cell wall polysaccharides. *Polym. Rev.* **2023**, *63*, 40–66. [CrossRef]
3. Elango, B.; Shirley, C.P.; Okram, G.S.; Ramesh, T.; Seralathan, K.K.; Mathanmohun, M. Structural diversity, functional versatility and applications in industrial, environmental and biomedical sciences of polysaccharides and its derivatives—A review. *Int. J. Biol. Macromol.* **2023**, *250*, 126193. [CrossRef] [PubMed]
4. Leong, M.Y.; Kang, Y.L.; Harun, M.Y.; Looi, C.Y.; Wang, W.F. Current advances of nanocellulose application in biomedical filed. *Carbohydr. Res.* **2023**, *532*, 108899. [CrossRef]
5. Nitodas, S.; Skehan, M.; Liu, H.; Shah, R. Current and potential applications of green membranes with nanocellulose. *Membranes* **2023**, *13*, 694. [CrossRef]
6. Spence, K.L.; Venditti, R.A.; Rojas, O.J.; Habibi, Y.; Pawlak, J.J. A comparative study of energy consumption and physical properties of microfibrillated cellulose produced by different processing methods. *Cellulose* **2011**, *18*, 1097–1111. [CrossRef]
7. Seydibeyoğlu, M.Ö.; Dogru, A.; Wang, J.; Rencheck, M.; Han, Y.; Wang, L.; Seydibeyoğlu, E.A.; Zhao, X.; Ong, K.; Shatkin, J.A.; et al. Review on hybrid reinforced polymer matrix composites with nanocellulose, nanomaterials, and other fibers. *Polymers* **2023**, *15*, 984. [CrossRef]
8. Zielinska, D.; Szentner, K.; Waskiewicz, A.; Borysiak, S. Production of nanocellulose by enzymatic treatment for application in polymer composites. *Materials* **2021**, *14*, 2124. [CrossRef]
9. Balea, A.; Merayo, N.; Fuente, E.D.L.; Negro, C.; Blanco, A. Assessing the influence of refining, bleaching and TEMPO-mediated oxidation on the production of more sustainable cellulose nanofibers and their application as paper additives. *Ind. Crops Prod.* **2017**, *97*, 374–387. [CrossRef]
10. Li, M.C.; Liu, X.; Lv, K.; Sun, J.; Dai, C.; Liao, B.; Liu, C.; Mei, C.; Wu, Q.; Hubbe, M. Cellulose nanomaterials in oil and gas industry: Current status and future perspectives. *Prog. Mater. Sci.* **2023**, *139*, 101187. [CrossRef]
11. Gorski, D.; Hill, J.; Engstrand, P.; Johansson, L. Review: Reduction of energy consumption in TMP refining through mechanical pretreatment of wood chips. *Nord. Pulp Pap. Res. J.* **2010**, *25*, 156–161. [CrossRef]
12. Levanic, J.; Senk, V.P.; Nadrah, P.; Polijasek, I.; Oven, P.; Haapala, A. Analyzing TEMPO-Oxidized cellulose fiber morphology: New insights into optimization of the oxidation process and nanocellulose dispersion quality. *ACS Sustain. Chem. Eng.* **2020**, *8*, 17752–17762. [CrossRef]
13. Liu, Y.; Zhang, S.; Lin, R.; Li, L.; Li, M.; Du, M.; Tang, R. Potassium permanganate oxidation as a carboxylation and defibrillation method for extracting cellulose nanofibrils to fabricate films with high transmittance and haze. *Green Chem.* **2021**, *23*, 8069–8078. [CrossRef]
14. Pere, J.; Tammelin, T.; Niemi, P.; Lille, M.; Virtanen, T.; Penttila, P.A.; Ahvenainen, P.; Gronqvist, S. Production of high solid nanocellulose by enzyme-aided fibrillation coupled with mild mechanical treatment. *ACS Sustain. Chem. Eng.* **2020**, *8*, 18853–18863. [CrossRef]
15. Bondancia, T.J.; Florencio, G.; Baccarin, G.S.; Farinas, C.S. Cellulose nanostructures obtained using enzymatic cocktails with different compositions. *Int. J. Biol. Macromol.* **2022**, *207*, 299–307. [CrossRef]
16. Igarashi, K.; Ishida, T.; Hori, C.; Samejima, M. Characterization of an endoglucanase belonging to a new subfamily of glycoside hydrolase family 45 of the Basidiomycete Phanerochaete chrysosporium. *Appl. Environ. Microbiol.* **2008**, *74*, 5628–5634. [CrossRef]
17. Nie, S.; Zhang, K.; Lin, X.; Zhang, C.; Yan, D.; Liang, H.; Wang, S. Enzymatic pretreatment for the improvement of dispersion and film properties of cellulose nanofibrils. *Carbohydr. Polym.* **2018**, *181*, 1136–1142. [CrossRef] [PubMed]
18. Bian, H.; Dong, M.; Chen, L.; Zhou, X.; Ni, S.; Fang, G.; Dai, H. Comparison of mixed enzymatic pretreatment and post-treatment for enhancing the cellulose nanofibrillation efficiency. *Bioresour. Technol.* **2019**, *293*, 122171. [CrossRef] [PubMed]
19. Taj, S.; Munawar, M.A.; Khan, S. Natural fiber-reinforced polymer composites. *Proc.-Pak. Acad. Sci.* **2007**, *44*, 129–144.
20. Yang, H.S.; Kiziltas, A.; Gardner, D.J. Thermal analysis and crystallinity study of cellulose nanofibril-filled polypropylene composites. *J. Therm. Anal. Calorim.* **2013**, *113*, 673–682. [CrossRef]
21. Wang, L. Spray-Dried Cellulose Nanofibril-Reinforced Polypropylene Composites for Extrusion-Based Additive Manufacturing. Ph.D. Thesis, University of Maine, Orono, ME, USA, December 2017.

22. Yang, G.; Park, M.; Park, S.J. Recent progresses of fabrication and characterization of fibers-reinforced composites: A review. *Compos. Commun.* **2019**, *14*, 34–42. [CrossRef]
23. Hartikainen, J.; Hine, P.; Szabo, J.S.; Lindner, M.; Harmia, T.; Duckett, R.A.; Friedrich, K. Polypropylene hybrid composites reinforced with long glass fibres and particulate filler. *Compos. Sci. Technol.* **2005**, *65*, 257–267. [CrossRef]
24. Dufresne, A.; Belgacem, M.N. Cellulose-reinforced composites: From micro-to nanoscale. *Polimeros* **2013**, *23*, 277–286. [CrossRef]
25. Gardner, D.J.; Oporto, G.S.; Mills, R.; Samir, M.A.S.A. Adhesion and surface issue in cellulose and nanocellulose. *J. Adhes. Sci. Technol.* **2008**, *22*, 545–567. [CrossRef]
26. Gallardo, G.; Guida, L.; Martinez, V.; Lopez, M.C.; Bernhardt, D.; Blasco, R.; Pedroza, I.R.; Hermida, L.G. Microencapsulation of linseed oil by spray drying for functional food application. *Food Res. Int.* **2013**, *52*, 473–482. [CrossRef]
27. Sosnik, A.; Seremeta, K.P. Advantages and challenges of the spray-drying technology for the production of pure drug particles and drug-loaded polymeric carriers. *Adv. Colloid Interface Sci.* **2015**, *223*, 40–54. [CrossRef]
28. Eyholzer, C.; Bordeanu, N.; Lopez, S.F.; Rentsch, D.; Zimmermann, T.; Oksman, K. Preparation and characterization of water-redispersible nanofibrillated cellulose in powder form. *Cellulose* **2010**, *17*, 19–30. [CrossRef]
29. Peng, Y.; Gardner, D.J.; Han, Y. Drying cellulose nanofibrils: In search of a suitable method. *Cellulose* **2012**, *19*, 91–102. [CrossRef]
30. Peng, Y.; Han, Y.; Gardner, D.J. Spray-drying cellulose nanofibrils: Effect of drying process parameters on particle morphology and size distribution. *Wood Fiber Sci.* **2012**, *44*, 448–461.
31. Peng, Y.; Gardner, D.J.; Han, Y.; Cai, Z.; Tshabalala, M.A. Influence of drying method on the surface energy of cellulose fibrils determined by inverse gas chromatography. *J. Colloid Interface Sci.* **2013**, *405*, 85–95. [CrossRef]
32. Gardner, D.J.; Han, Y.; Peng, Y. Method for Drying Cellulose Nanofibrils. U.S. Patent 8,372,320 B2, 12 February 2013.
33. Peng, Y.; Gallegos, S.A.; Gardner, D.J.; Han, Y.; Cai, Z. Maleic anhydride polypropylene modified cellulose nanofibril polypropylene nanocomposites with enhanced impact strength. *Polym. Compos.* **2016**, *37*, 782–793. [CrossRef]
34. Schmid, K.; Arpagaus, C.; Friess, W. Evaluation of the nano spray dryer B-90 for pharmaceutical applications. *Pharm. Dev. Technol.* **2011**, *16*, 287–294. [CrossRef]
35. Huang, L.X.; Kumar, K.; Mujumdar, A.S. A comparative study of a spray dryer with rotary disc atomizer and pressure nozzle using computational fluid dynamic simulations. *Chem. Eng. Process.* **2006**, *45*, 461–470. [CrossRef]
36. Teunou, E.; Poncelet, D. Rotary disc atomisation for microencapsulation applications-prediction of the particle trajectories. *J. Food Eng.* **2005**, *71*, 345–353. [CrossRef]
37. Woo, M.W.; Daud, W.R.W.; Tasirin, S.M.; Talib, M.Z.M. Optimization of the spray drying operating parameters-A quick trial-and-error method. *Dry. Technol.* **2007**, *25*, 1741–1747. [CrossRef]
38. Chegini, G.R.; Bashiri, B.; Mesbahi, M.H. Comparison of pumped air characteristics from a rotary atomizer with three types of wheels. *Exp. Tech.* **2012**, *36*, 63–68. [CrossRef]
39. Wang, L.; Sanders, J.E.; Gardner, D.J.; Han, Y. In-situ modification of cellulose nanofibrils by organosilanes during spray drying. *Ind. Crops Prod.* **2016**, *93*, 129–135. [CrossRef]
40. Kalia, S.; Boufi, S.; Celli, A.; Kango, S. Nanofibrillated cellulose: Surface modification and potential applications. *Colloid Polym. Sci.* **2014**, *292*, 5–31. [CrossRef]
41. Melo, J.C.P.; Filho, E.C.S.; Santana, S.A.A.; Airoldi, C. Maleic anhydride incorporated onto cellulose and thermodynamics of cation-exchange process at the solid/liquid interface. *Colloids Surf. A Physicochem. Eng.* **2009**, *346*, 138–145. [CrossRef]
42. Rowell, R.M. Advances and challenges of wood polymer composites. In Proceedings of the 8th Pacific Rim Bio-Based Composites Symposium, Kuala Lumpur, Malaysia, 20–23 November 2006; pp. 2–11.
43. Guay, D.; Sutherland, N.R.; Rantanen, W.; Malandri, N.; Stephens, A.; Mattingly, K.; Schneider, M. Comparison of fiber length analyzers. In Proceedings of the 2005 TAPPI Practical Papermaking Conference, Milwaukee, WI, USA, 22–26 May 2005.
44. Henriksson, M.; Berglund, L.; Isaksson, P.; Lindstro¨m, T.; Nishino, T. Cellulose nanopaper structures of high toughness. *Biomacromolecules* **2008**, *9*, 1579–1585. [CrossRef]
45. Liu, Q.; Smalyukh, I.I. Liquid crystalline cellulose-based nematogels. *Sci. Adv.* **2017**, *3*, e1700981. [CrossRef] [PubMed]
46. Ulusoy, U.; Kursun, I. Comparison of different 2D image analysis measurement techniques for the shape of talc particles produced by different media milling. *Miner. Eng.* **2011**, *24*, 91–97. [CrossRef]
47. Kwon, H.J.; Sunthornvarabhas, J.; Park, J.W.; Lee, J.H.; Kim, H.J.; Piyachomkwan, K.; Sriroth, K.; Cho, D. Tensile properties of kenaf fiber and corn husk flour reinforced poly(lactic acid) hybrid bio-composites: Role of aspect ratio of natural fibers. *Compos. Part B* **2014**, *56*, 232–237. [CrossRef]
48. Appels, F.V.W.; Camere, S.; Montalti, M.; Karana, E.; Jansen, K.M.B.; Dijksterhuis, J.; Krijgsheld, P.; Wosten, H.A.B. Fabrication factors influencing mechanical, moisture and water related properties of mycelium-based composites. *Mater. Des.* **2019**, *161*, 64–71. [CrossRef]
49. Wang, L.; Kiziltas, A.; Mielewski, D.F.; Lee, E.C.; Gardner, D.J. Closed-loop recycling of polyamide 12 powder from selective laser sintering into sustainable composites. *J. Clean. Prod.* **2018**, *195*, 765–772. [CrossRef]
50. Syverud, K.; Carrasco, G.C.; Toledo, J.; Toledo, P.G. A comparative study of Eucalyptus and Pinus radiate pulp fibres as raw materials for production of cellulose nanofibrils. *Carbohydr. Polym.* **2011**, *84*, 1003–1038. [CrossRef]
51. Im, W.; Lee, S.; Abhari, A.R.; Youn, H.J.; Lee, H.L. Optimization of carboxymethylation reaction as a pretreatment for production of cellulose nanofibrils. *Cellulose* **2018**, *25*, 3873–3883. [CrossRef]

52. Shin, S.; Park, S.; Park, M.; Jeong, E.; Na, K.; Youn, H.J.; Hyun, J. Cellulose nanofibers for the enhancement of printability of low viscosity gelatin derivatives. *BioResources* **2017**, *12*, 2941–2954. [CrossRef]
53. Lglesias, M.C.; Shivyari, N.; Norris, A.; Sampedro, R.M.; Eugenio, M.E.; Lahtinen, P.; Auad, M.L.; Elder, T.; Jiang, Z.; Frazier, C.E.; et al. The effect of residual lignin on the rheological properties of cellulose nanofibril suspensions. *J. Wood Chem. Technol.* **2020**, *40*, 370–381. [CrossRef]
54. Park, S.Y.; Lee, S.H.; Im, W.H.; Lee, H.L.; Youn, H.J. Combined enzymatic pretreatment of pulp for production of CNF. *J. Korea TAPPI* **2021**, *53*, 5–15. [CrossRef]
55. Palma, G.A.; Ching, D.; Andrade, A.; Gallegos, S.H.; Mendonca, R.T.; Pereira, M. Relationships between size distribution, morphological characteristics, and viscosity of cellulose nanofibrils dispersions. *Polymers* **2022**, *14*, 3843. [CrossRef] [PubMed]
56. Wang, W.; Mozuch, M.D.; Sabo, R.C.; Kersten, P.; Zhu, J.Y.; Jin, Y. Production of cellulose nanofibrils from bleached encalyptus fibers by hyperthermostable endoglucanase treatment and subsequent microfluidization. *Cellulose* **2015**, *22*, 351–361. [CrossRef]
57. Gourlay, K.; Zwan, T.V.D.; Shourav, M.; Saddler, J. The potential of endoglucanases to rapidly and specially enhance the rheological properties of micro/nanofibrillated cellulose. *Cellulose* **2018**, *25*, 977–986. [CrossRef]
58. Huang, L.X.; Mujumdar, A.S. The effect of rotary disk atomizer RPM on particle size distribution in a semi industrial spray dryer. *Dry. Technol.* **2008**, *26*, 1319–1325. [CrossRef]
59. Linsinger, T.P.J.; Gerganova, T.; Kestens, V.; Got, J.C. Preparation and characterisation of two polydisperse, non-spherical materials as certified reference materials for particle size distribution by static image analysis and laser diffraction. *Powder Technol.* **2019**, *343*, 652–661. [CrossRef]
60. Berto, G.L.; Mattos, B.D.; Rojas, O.J.; Arantes, V. Single-step fiber pretreatment with monocomponent endoglucanase: Defibrillation energy and cellulose nanofibril quality. *ACS Sustain. Chem. Eng.* **2021**, *9*, 2260–2270. [CrossRef]
61. Karmarkar, A.; Chauhan, S.S.; Modak, J.M.; Chanda, M. Mechanical properties of wood–fiber reinforced polypropylene composites: Effect of a novel compatibilizer with isocyanate functional group. *Compos. Part A Appl. Sci. Manuf.* **2007**, *38*, 227–233. [CrossRef]
62. Feldmann, M.; Heim, H.P.; Zarges, J.C. Influence of the process parameters on the mechanical properties of engineering biocomposites using a twin-screw extruder. *Compos. Part A Appl. Sci. Manuf.* **2016**, *83*, 113–119. [CrossRef]
63. Thomason, J.L.; Fernandez, J.L.R. A review of the impact performance of natural fiber thermoplastic composites. *Front. Mater.* **2018**, *5*, 60. [CrossRef]
64. Chen, B.; Gao, D.; Li, Y.; Chen, C.; Wang, Z.; Zhong, Q.; Sun, P.; Wang, Z.; Wu s Zhao, J. Experimental analysis of spray behavior and lubrication performance under twin-fluid atomization. *J. Manuf. Process* **2021**, *61*, 561–573. [CrossRef]
65. Ashori, A. Wood-plastic composites as promising green-composites for automotive industries. *Bioresour. Technol.* **2008**, *99*, 4661–4667. [CrossRef] [PubMed]
66. Lee, B.H.; Kim, H.J.; Yu, W.R. Fabrication of long and discontinuous natural fiber reinforced polypropylene biocomposites and their mechanical properties. *Fibers Polym.* **2009**, *10*, 83–90. [CrossRef]

polymers

MDPI

Article

Cellulose Fibers-Based Porous Lightweight Foams for Noise Insulation

Mihai Seciureanu [1], Silviu-Marian Nastac [1,2,*], Maria-Violeta Guiman [2,*] and Petronela Nechita [1,*]

[1] Engineering and Agronomy Faculty in Braila, "Dunarea de Jos" University of Galati, 810017 Braila, Romania; mihai.seciureanu@gmail.com

[2] Faculty of Mechanical Engineering, "Transilvania" University of Brasov, 500024 Brasov, Romania

* Correspondence: snastac@ugal.ro or silviu.nastac@unitbv.ro (S.-M.N.); violeta.guiman@unitbv.ro (M.-V.G.); petronela.nechita@ugal.ro (P.N.)

Abstract: This paper examines effective and environmentally friendly materials intended for noise insulation and soundproofing applications, starting with materials that have gained significant attention within last years. Foam-formed materials based on cellulose fibers have emerged as a promising solution. The aim of this study was to obtain a set of foam-formed, porous, lightweight materials based on cellulose fibers from a resinous slurry pulp source, and to investigate the impact of surfactant percentage of the foam mixtures on their noise insulation characterisitcs. The basic foam-forming technique was used for sample assembly, with three percentages of sodium dodecyl sulphate (as anionic surfactant) related to fiber weight, and a standardised sound transmission loss tube procedure was used to evaluate noise insulation performance. Results were obtained as observations of internal structural configurations and material characteristics, and as measurements of sound absorption/reflection, sound transmission loss, and surface acoustic impedance. Based on the findings within this study, the conclusions highlight the strong potential of these cellulosic foams to replace widely used synthetic materials, at least into the area of practical noise insulation applications.

Keywords: cellulose fiber; foam-forming; surfactant; noise insulation; sound absorption; sound transmission loss

1. Introduction

In the past 10 years, the potential of foam-formed materials based on cellulose fibers (CF) has been harnessed in the pursuit of sustainable and environmentally friendly materials and has gained significant attention [1–6]. Indeed, foam-formed materials based on CF have emerged as a promising solution. By combining the inherent properties of CF with the unique characteristics of foam-forming, these materials offer a wide range of applications and demonstrate great potential in various industries [7–11].

The use of CF in noise insulation and soundproofing (NISp) applications combines their natural properties, sustainability, and cost-effectiveness, providing an attractive solution for creating quieter and more comfortable environments [1,2,5–7,10,12–17]. Below is a brief description of the advantages of using foams, particularly those based on CF, for NISp applications. (i) Foams with excellent sound absorption, including CF-based foams, possess a porous structure that effectively absorbs sound waves, reducing noise transmission; the interconnected void spaces in foams allow for the dissipation of sound energy through friction and air resistance [15,16]. (ii) Lightweight foams, including CF-based foams, are easy to handle and install; this characteristic is particularly beneficial for NISp applications as it minimizes additional weight on structures and systems [2,3]. (iii) Sustainable and environmentally friendly, CF-based foams are derived from renewable sources such as wood, making them a sustainable choice; these foams are biodegradable and can be produced from recycled materials, reducing environmental impact [1,4]. (iv) CF-based foams are typically non-toxic and safe for human health; they do not release harmful chemicals or

volatile organic compounds (VOCs) into the environment, making them suitable for use in residential and commercial settings [6]. (v) CF-based foams have versatility and adaptability; i.e., they can be easily shaped, molded, or cut to fit various spaces and applications; this versatility allows customized solutions for NISp needs [5]. (vi) In addition to sound insulation, foams have thermal insulation properties, helping to regulate temperature and improve energy efficiency by reducing heat transfer [17]. (vii) CF-based foams can offer cost advantages compared to some synthetic alternatives; their production cost is often lower, making them a cost-effective option for NISp applications [10].

Ultra-light porous materials find significant applications in sound and energy absorption, thermal insulation, radiation shielding, and filtration [18–22]. Another class of materials, namely cellulose-containing materials, has gained attention in foam forming technology. In recent studies [7,8], a lightweight, highly porous, and three-dimensional, shaped, cellulose-based material called foam-paper was introduced. The production process of foam-paper shares similarities with papermaking, but offers several advantages over traditional papermaking techniques: prevention of fiber flocculation, the presence of a three-dimensional porous structure, and reduced water and energy consumption during manufacturing. Foam-paper exhibits versatility and can be applied in various fields such as insulation, packaging, filtration, and acoustics [7,9].

1.1. State of the Art in Materials Based on Cellulose Fibers and Foam Forming

The concept of incorporating foam into the papermaking process was initially proposed by Radvan and Gatward [23] in 1972 and later by Smith and Punton [24] in 1974, with an aim to enhance paper uniformity. Radvan and Gatward [23] utilized foam to prevent fiber flocculation caused by long fibers and high pulp suspension consistency. They introduced the Radfoam process, a foam forming technique employing a discontinuous foam forming unit connected to a small paper machine. Another study on the Radfoam process [25] demonstrated that Radfoam-made sheets exhibit a 20 to 30% higher specific volume (bulk) compared to standard handsheets. In a study by Smith et al. [26] focusing on the structure and characteristics of Radfoam-made materials, it was found that surface tension and bubble spacing within the foam significantly influence the properties of the final product, while chemical effects were deemed insignificant. Tringham [25] and Smith [26] further confirmed that Radfoam-produced material possesses improved uniformity, porosity, and strength. More recently, Al-Qararah et al. [27] from the VTT Technical Research Centre of Finland investigated the impact of various parameters on bubble size distribution in foam-formed cellulose fibers. The study revealed that increasing the rotational speed of mixing led to a decrease in average bubble size and a reduction in air content, resulting in an increased average bubble radius.

In response to the growing demand for sustainable and eco-friendly products, there has been a notable rise in interest in the reintroduction of the foaming process for the development of innovative cellulose-based materials [20,28–31]. Numerous studies have explored the creation of lightweight porous materials using nanofibrillated cellulose (NFC) through various methods [28–31].

In latest years, some recent studies also assessed practical aspects of foam-formed composites based on CF for insulation applications. Thus, the main purpose of the study [32] was the identification of physical, chemical, and mechanical properties of soundproofing materials. The review [33] investigated the potential of CF-based polymeric composites for automotive applications, and it concluded that cellulosic (natural) fiber-based polymeric composites offer an efficient alternative to man-made synthetic fibers within the automotive sector. Within their research, Tauhiduzzaman et al. [34] focused on the production of lignocellulosic foams using wood flour or thermo-mechanical pulp (TMP) fibers bound with cellulose nanofibrils (CNFs). Multiscale modelling was proposed to predict the mechanical properties. Hasan et al. [35] have explored various chemical modifications of lignocellulosic fiber to make it more compatible for use as reinforcement in composite materials. In addition, the applications of natural fiber composite were broadly discussed.

The study [36] summarized the recent progress within the fields of preparation methods and high-performance cellulose structural material properties. The concluding remarks within the work of Xu et al. [37] suggests that thin layers of sustainable natural materials such as CF can be used to significantly improve the capability of traditional porous media to absorb noise. CF-based materials suitable for filtering, insulation, protective, and hygiene applications can be formed/obtained using aqueous foam as a carrier phase [38–42]. The subtle fiber−bubble interaction provides a very useful tool that can be utilized to alter both structural and mechanical material properties. Indeed, the results within the study by Ketola et al. [38] revealed that there was a clear variation in structure and strength properties between the samples made using different fibers and surfactants. Following the previous idea, the work [43] presents and discusses mechanisms that underlie the formation process, and thus, influence physical properties of formed fiber networks. Another useful conclusion of this work was that the foam rheology is affected by added fibers, which is highly important to the development of foam-forming processes.

Miranda-Valdez et al. [44] concluded that foam-formed cellulose bio-composites are a promising technology for developing lightweight and sustainable packaging materials. Their results showed that organosolv lignin enhances many properties of cellulose bio-composite foams, which are mainly required in practical applications of insulation, packaging, and cushioning. More practically, the paper [45] systematically presents and discusses the technical parameters that can be controlled in practice during foam-forming processes with cellulosic materials, in order to obtain the required properties. The focus of this analysis was on the identification of feasible solutions to compensate for decreased strength, caused by the reduced density and poor water resistance of foam-formed cellulose composites. An innovative foam/natural fiber composite was successfully developed within the work [46]. The authors demonstrated an alternative way to produce composites with promising enhanced mechanical properties. Moreover, the results presented into the study [47] can serve as a basic reference for preparation of highly stable, cellulose-based solid foams, with very good adsorption properties.

Taiwo et al. [48] have proposed an evaluation of the potential of natural fibers for building acoustics absorbers. They have concluded two main ideas: many studies have shown that sound absorbing composites based on natural fibers present good acoustic properties in a high frequency range, similar to synthetic fibers, and natural fibers have been proven as a feasible alternative to synthetic fibers for building acoustic absorbers, thereby alleviating some sustainability issues associated with synthetics.

Cellulose fibers are a natural, environmentally friendly material often used in sound insulation products. However, they do have some negative aspects when compared to other commonly used polymeric materials. Here are some of the drawbacks of using cellulose fibers in NISp applications [36,48–59]. (i) Moisture sensitivity, (ii) poor fire resistance, (iii) pest attraction, (iv) settling and decomposition, (v) dust and allergen release and (vi) limited applications mean that CFs may not be ideal for situations where moisture or fire resistance is a critical concern. (vii) While CFs are a natural and renewable resource, their production process may involve the use of chemicals and energy; thus, they have a negative environmental impact. Additionally, the need for fire-retardant treatments can add to the environmental impact. It is important to note that the choice between CFs and synthetic polymeric materials for NISp depends on specific project requirements and priorities, including cost, environmental concerns, and performance criteria.

Within the past 10 years, researchers have focused on CF-based foams, developing and analysing different types, based on various properties of CFs and additives, and optimizing the forming process [45,58–67], in order to obtain the highest performance for practical applications of noise insulation [58–60,64–67], shock absorption [62], cushioning [45], packaging [45,63], and thermal isolation [61]. The investigations were mainly conducted on experimental tests [45,58,60–67], but computational simulations were also considered [45,59,62,64], modeling potential insulation characteristics compared to widely-used synthetic materials.

1.2. Aim of This Study

The goal of this study examined surfactant charges influence the fibrous structural configuration (fibrous network) of foam-formed cellulosic materials, as they influence sound insulation performance. In this paper, the authors have presented the experimental results for a set of foam-formed materials based on virgin, long cellulosic fibers (resinous fibers), using low-level beating, variable surfactant percentages, and a basic laboratory foam-forming technique. The results were presented and discussed in terms of noise insulation characteristics, related to fibrous network structure and specific mass. The novelty of this study is justified by: (i) a comparative analysis of noise insulation ability, in relation to the percentage of surfactant, (ii) a comparative analysis of results against those of two of the most-commonly used synthetic materials, and (iii) development of a simple and environmentally friendly formation process.

2. Materials and Methods

2.1. About Materials

2.1.1. Cellulose-Based Foam-Formed Materials

The authors had developed the porous lightweight materials in a foam medium, based on virgin cellulose long fibers (resinous type fibers). The bleached softwood cellulose (typically supplying 400–800 μm average fiber length, with 15–35 μm diameter) has been used as fiber source for the foam material. Cellulose fibers with 20 °SR beating degree (according to the Shopper-Riegler method) and slurry pulp with 1.98% consistency.

The anionic surfactant used for foam forming was sodium dodecyl sulphate (SDS), commonly utilized in commercial cosmetics production. With these basic materials (slurry pulp and surfactant), three types of cellulose-based lightweight foams were obtained (please see details within Section 2.2).

2.1.2. Commercial Sound Absorbers

Two different commercially available petroleum-based materials, currently used in sound insulation, were also tested, in order to provide a reference basis for analysing the performance of the CF-based foams. These materials include samples of expanded polystyrene (EPS) and extruded polystyrene (XEPS) (ISOVER, Saint-Gobain Construction Products SA (Pty) Ltd.), with specific masses presented in Section 3.1.

2.2. Methods Used for Forming Samples

2.2.1. Foam-Forming Method

Foam-formed materials based on cellulose fibers consist of a matrix of cellulose fibers embedded within a foam structure. Cellulose fibers, derived from plant sources such as wood, cotton, or hemp, serve as the reinforcing material. The manufacturing process involves several stages, starting with the disintegration of the cellulose fibers into a water suspension. This suspension is then mixed with foaming agents and additives to create a foam-like structure. Subsequently, the foam is consolidated and dried to form a solid material. Diagrams and pictures in Figure 1 present the main difference between water- and foam-forming techniques, highlighting clearly the advantages of the last procedure.

The foam-forming technique is briefly described. The cellulose fibers (resinous virgin cellulose fibers) with a pre-determined weight to obtain a slurry pulp with 1.98% consistency were soaked overnight (approx. 24 h) using distillate water with 1% sodium hydroxide (1 N concentration).

Next, the slurry pulp was mixed at high shear velocity (up to 2200 rpm) for 20 min, in order to increase the porosity of final foam structure by air entraining (Figure 2a). During the agitation process, a controlled percentage of surfactant (relative to the pulp weight) was added, to produce foam. The authors proposed to analyse three types of materials with various air contents. Hence, three different quantities of surfactant were used as follows: 2%, 4%, and 6%, relative to the fiber weight.

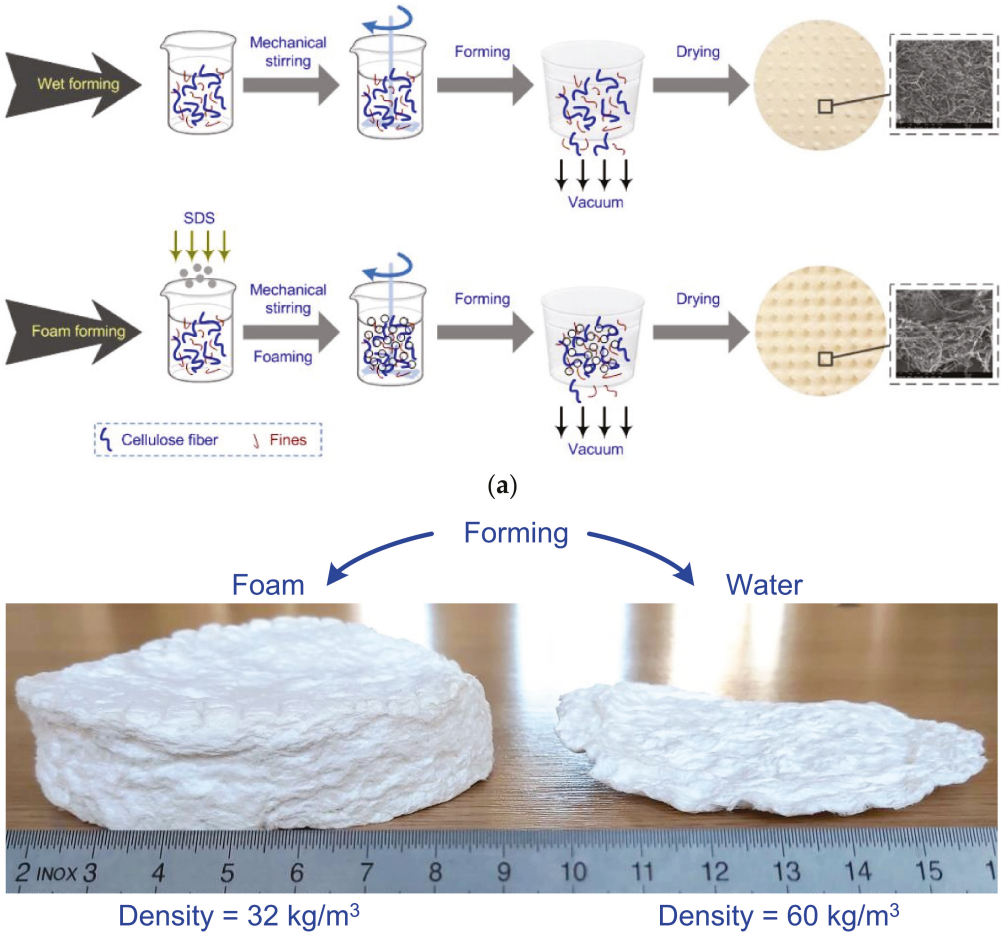

Figure 1. Differences between water- and foam-forming techniques, in terms of schematic diagrams [45] (**a**) and an example of final products (**b**).

Figure 2. Equipment used in foam-forming procedure: (**a**) Mixer for homogenization of slurry pulp and SDS; (**b**) Buchner funnel with vacuum pump for dewatering.

The mixture of foam and fibers in suspension were filtered and dewatered, using a Buchner funnel (Figure 2b), with sample holder diameter correlated to the requirements of equipment used in experimental investigations (e.g., 100, 72 and 28.5 mm). A filter paper

was used at a sample bottom, in addition to the filtering system of the Buchner funnel, in order to obtain a sample surface as flat as possible. The filtering was developed at a low level of vacuum, for approx. 20 min, to insure a suitable dewatering, while maintaining the sample structural integrity.

2.2.2. Drying Methods

After dewatering, the samples of foam material were carefully transferred, to avoid destroying of their integrity, from the Buchner funnel to the drying table in a mould with a specific diameter appropriate for the equipment used in acoustical investigations. The samples were dried at room temperature (approximately 22 °C) and 50–60% relative humidity, for 24 to 48 h.

2.3. Methods for Investigation of Noise Insulation Ability

The foam samples, obtained according to the previously described procedure, were analysed in order to estimate the acoustic insulation capabilities, in terms of absorption/reflection coefficients, sound transmission loss, and acoustic impedance. All parameters were evaluated at normal incidence.

Experimental investigations were conducted using a transmission-loss tube setup, containing two types of conventional acoustic tubes (Kundt tubes), for samples with 100 and 28.5 mm diameters (Figure 3). The frequency ranges for each tube are (10–2000) Hz for the large diameter tube (denoted K1 within this paper), and (100–7000) Hz for the small diameter tube (denoted K2 within this paper). Both devices enable floating anechoic termination and four-microphone setup configuration.

Figure 3. Transmission loss tubes used for evaluation of noise insulation ability of foams.

Based on the transfer matrix method, the "two-load" technique was adopted for all experimental investigations, which uses two different tube loads, such as "nearly–anechoic" and "free" terminations. Both acoustic tubes enable this requirement.

The tubes include suitable holders for the PCB–130E20 ICP® Electret Array Microphone (PCB Piezotronics Inc., Depew, NY, USA) acoustic transducers. Digital acquisition of acoustic signals was practically assured with the NI-USB-9233/9162® (NI, Austin, TX, USA) pair devices, and managed using a specific NI-LabVIEW® (NI, USA) application. A high sampling rate (25 kHz) was used, in order to provide highest accuracy of acquired signals, and enabling a consistent/conformal computational post-processing procedure. The computational developments were performed using a set of Matlab® R2014b (MathWorks, USA) applications.

The measurements were developed based on the transfer function method according to ISO 10534-2 and ASTM E1050-12 international standards for absorption coefficient and ASTM E2611-17 for transmission loss [58,64,66].

3. Results

3.1. Cellulose Fiber-Based Porous Lightweight Materials

The authors obtained three types of foam materials using cellulose fibers from resinous slurry pulps with 20 °SR. Optical micrographs in Figure 4 present the internal fibrous structure of slurry pulp before starting the foam-forming process, with few marked measurements related to fiber length and diameter respectively. Photos were obtained using an optical microscopy technique, with transmitted dead white light, based on a DELTA Optical Three-Ocular Microscope model SZ-450T® (Delta Optical, Minsk Mazowiecki, Poland), and Bresser MikrOkular Full HD Digital Camera® (Bresser GmbH, Rhede, Germany). Each photo provides a dimensional grid gained by a standard calibration grid lamella.

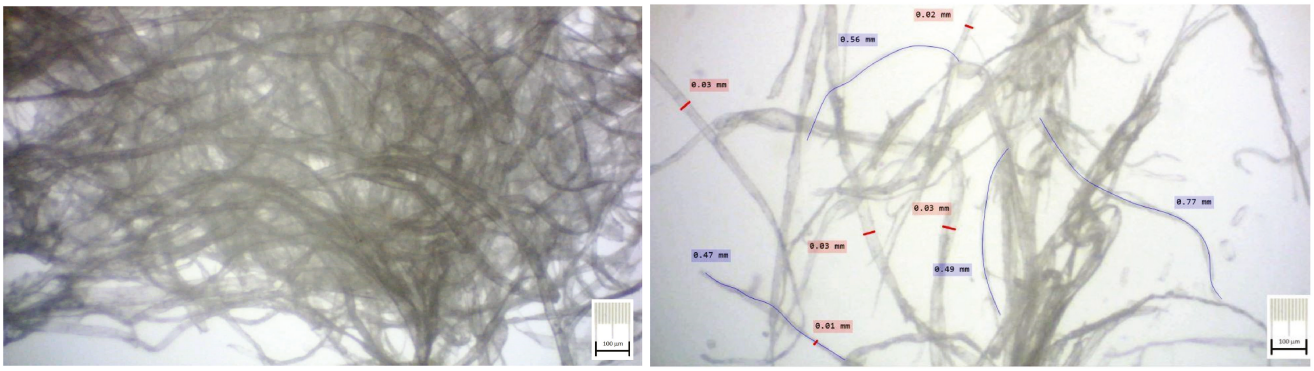

(**a**) (**b**)

Figure 4. Micropgraphs of slurry pulp used for foam-forming materials: (**a**) general view; (**b**) detail view with length and diameter measurement.

Foam density is strongly related to the structure and strength of fibrous network, which is quantified as the numbers of contacts between fibers. Foam bubbles limit the possible localization of fibers, thus, resulting in more open pores, and also in more fiber contacts at areas in-between the bubbles.

Micrographs in Figure 5 reveal these facts, for the three different types of samples. It was observed that higher SDS percentage leads to larger foam-bubbles, increasing the void between fibers, and, thereby, increasing the possibility to obtain high porosity of foam.

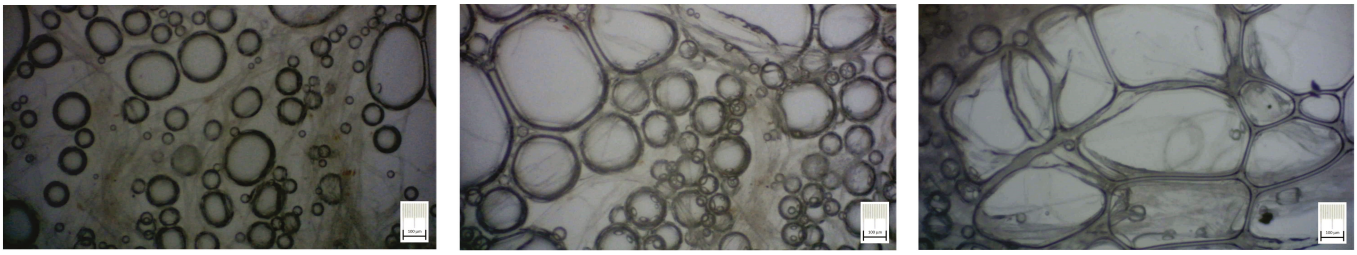

(**a**) (**b**) (**c**)

Figure 5. Micrographs of cellulose fibers in foam (wet samples, at the end of mixing process), for different SDS percentage: (**a**) S1 sample with 2% SDS; (**b**) S2 sample with 4% SDS; (**c**) S3 sample with 6% SDS.

This latter remark will be validated through mass and density measurements. However, the micrographs presented in Figure 6, for a certain foam sample, reveal a porous, fibrous internal structure in its final material (after dewatering and drying processes) compared to the initial structure of slurry pulp (see Figure 4a). Photos in Figures 5 and 6a were obtained using the same technique and equipment presented in the previous paragraph, and photo in Figure 6b was obtained through SEM technique (using available equipment at "Dunarea de Jos" University of Galati, RO).

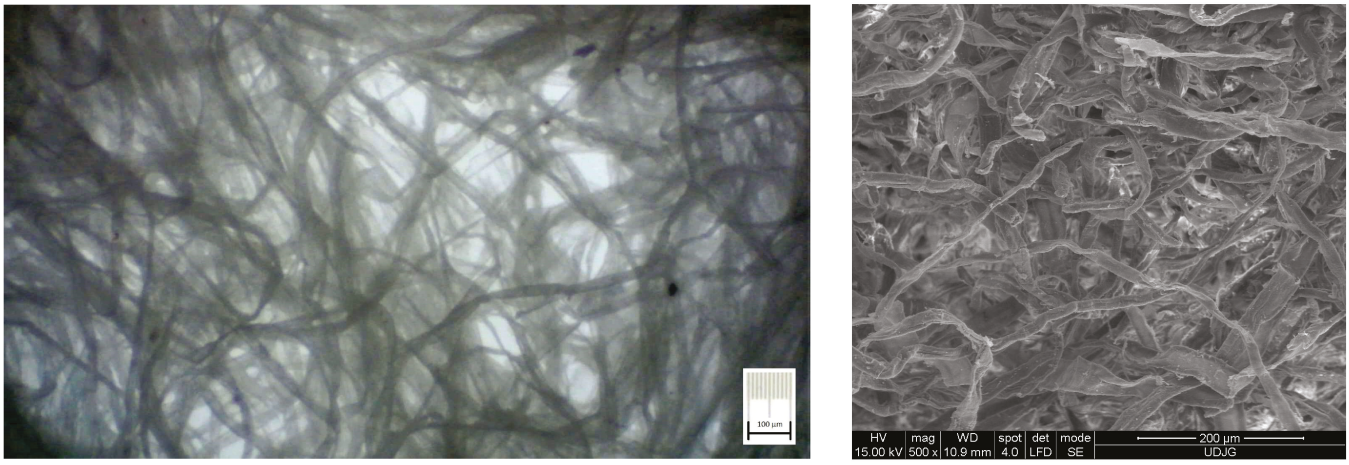

(**a**) (**b**)

Figure 6. Internal fibrous structure of S1 sample at the end of drying process: (**a**) Optical micrograph; (**b**) SEM micrograph.

For acoustical investigations using the normal incidence hypothesis, the quality of the external surface is an important aspect. Thus, in Figure 7, are depicted three micrographs related to each category of samples. It was easily observed that an improvement of surface airy porous structure is obtained with an increasing SDS percentage.

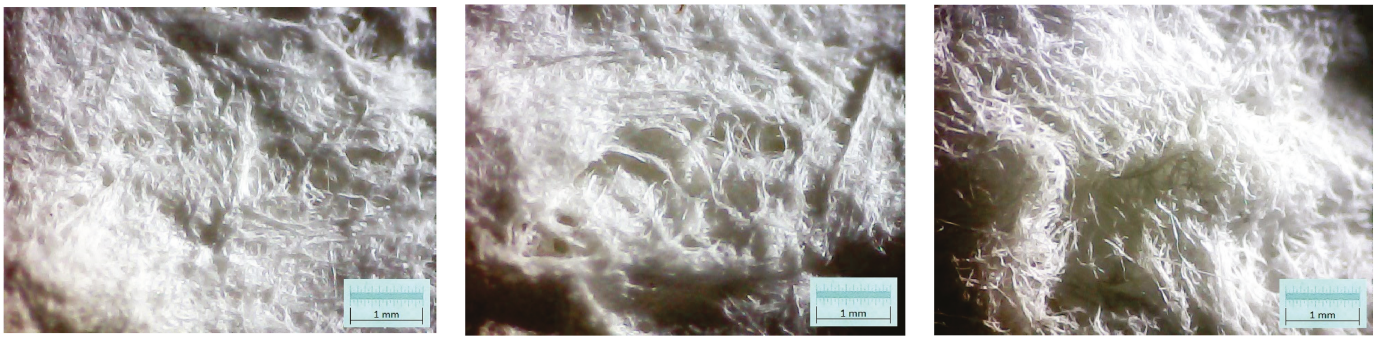

(**a**) (**b**) (**c**)

Figure 7. Optical micrographs of the samples external surface (dry and ready-to-use samples) for: (**a**) S1 sample; (**b**) S2 sample; (**c**) S3 sample.

A set of samples from each category are presented in Figure 8, where S(1,2,3) samples denote (2,4,6)% of SDS (relative to the fibres content of slurry pulp) into the initial foam-forming mixture, and S0 is the reference sample, simply obtained by water-forming procedure (without SDS addition).

The air content was computed for each sample, based on the initial volume of slurry pulp and SDS and the final volume of foamed mixture (directly evaluated after stopping of mixing process). The average values of air content, for each type of foam samples are provided in Table 1 (where STD means standard deviation).

Table 1. Average values of air content.

Sample	Inital Volume (mL)	Final Volume [1] (mL)	Air Content (%)	STD
S1	500	710	42	0.122
S2	500	760	52	0.141
S3	500	800	60	0.135

[1] Average values (20 items for each sample).

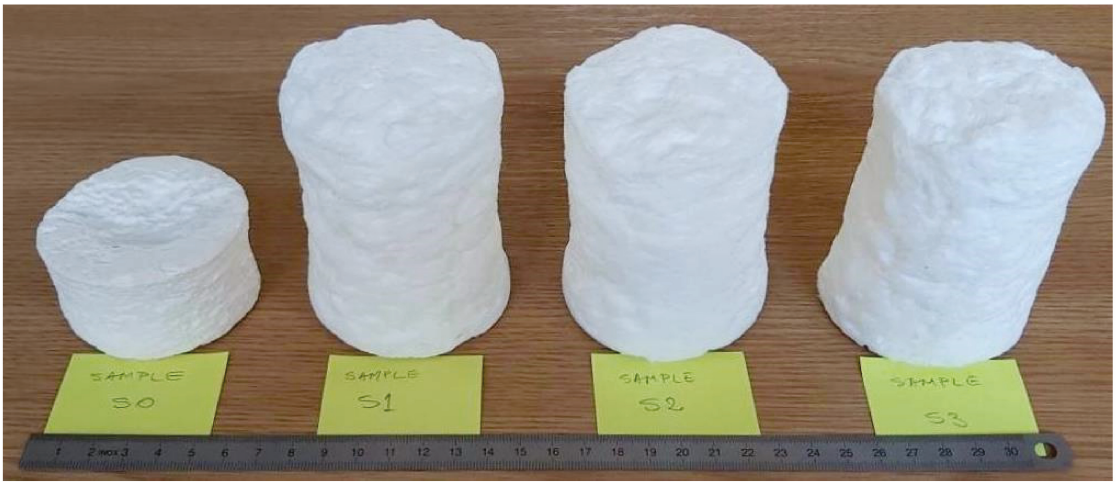

Figure 8. A set of samples used for noise insulation investigations.

The density and mass of the foam samples were evaluated, and the values were presented in Table 2 (table contains average values for samples S0, S1, S2, and S3). A stochastical analysis was performed for each parameter, and the comparative results were provided in graphical form. The stochastic parameters for sample density are depicted in the boxplots in Figure 9, and the surface/bar plots in Figure 10 illustrate the behaviour of statistical parameters in relation to the acquired values of density. Similarly, diagrams within Figures 11 and 12 show the statistical parameters in relation to the mass.

Table 2. Average values of samples density and mass.

Sample	EPS	XEPS	S0 [1]	S1 [1]	S2 [1]	S3 [1]
Density (kg/m^3)	25.000	32.000	47.9095	28.4846	27.8818	27.1249
Mass ($\times 10^{-3}$ kg)	9.969	12.760	10.183	10.265	10.322	10.366

[1] Average values (20 items for each sample).

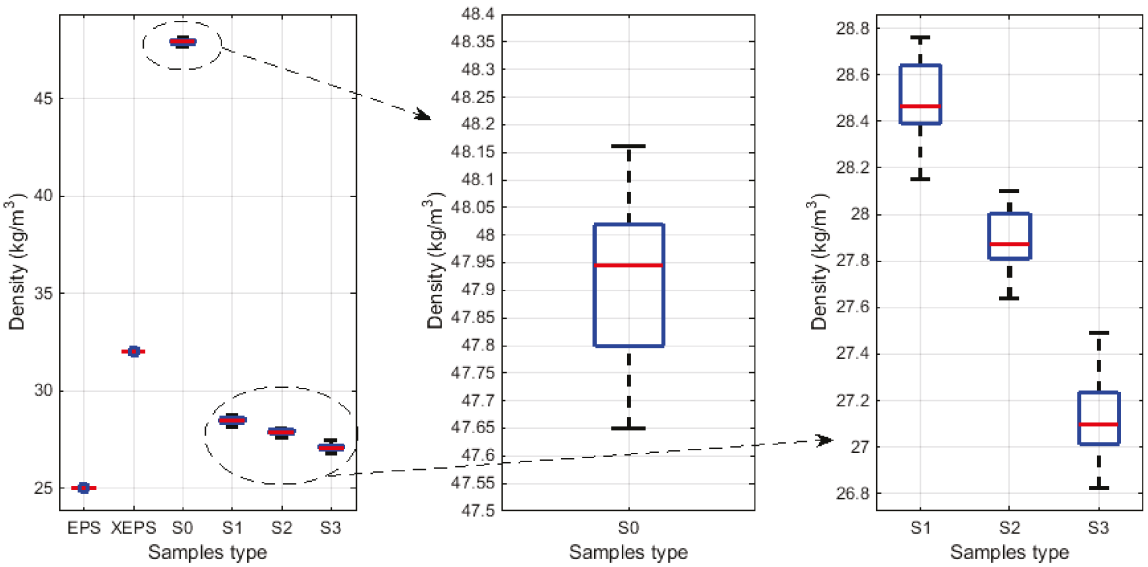

Figure 9. The stochastic diagram related to the samples density (general view for all samples, and details of water- and foam-formed foams respectively).

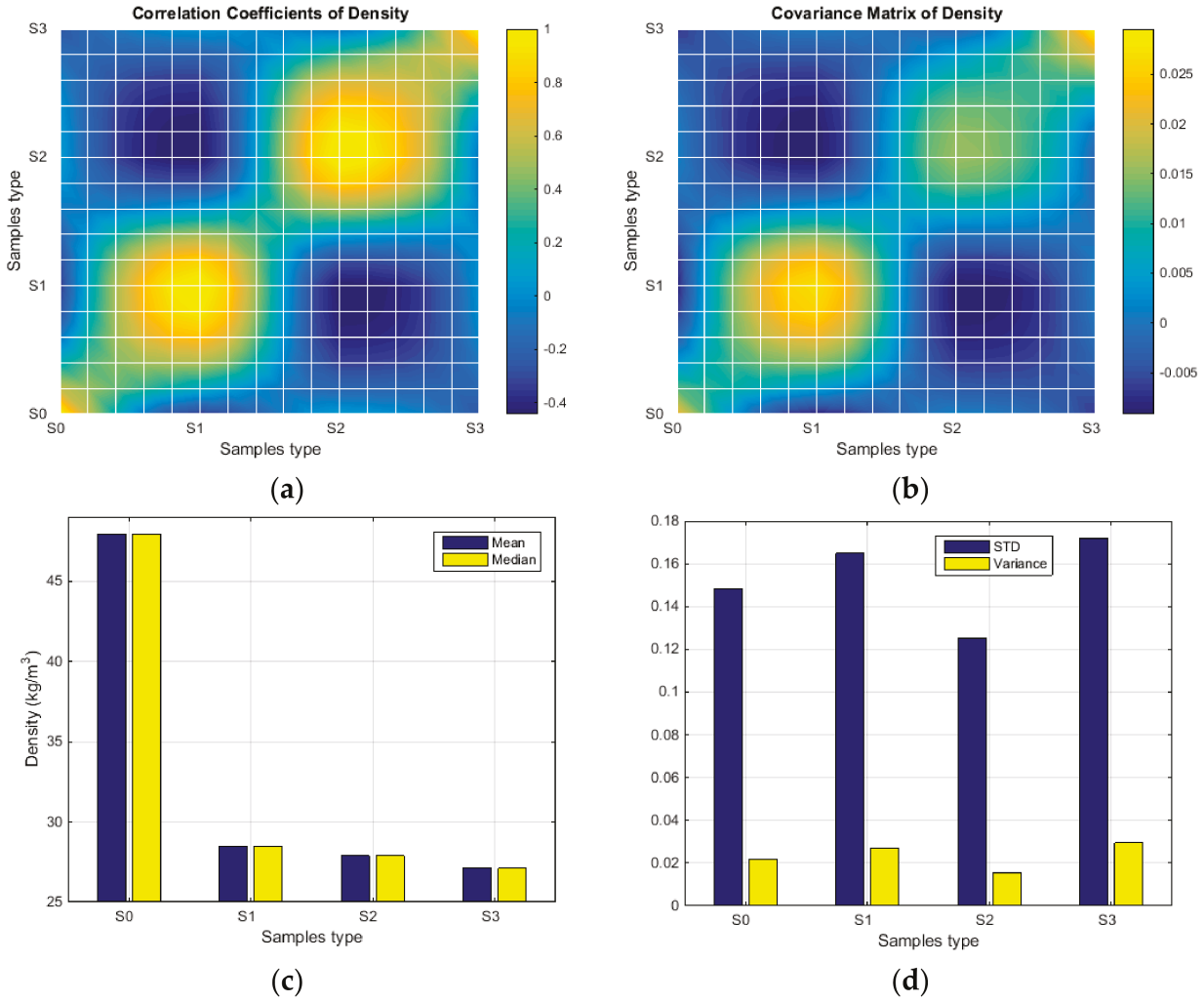

Figure 10. Statistical parameters of density in respect to material type: (**a**) Correlation coefficient; (**b**) Covariance matrix; (**c**) Mean and median values; (**d**) Standard deviation and variance.

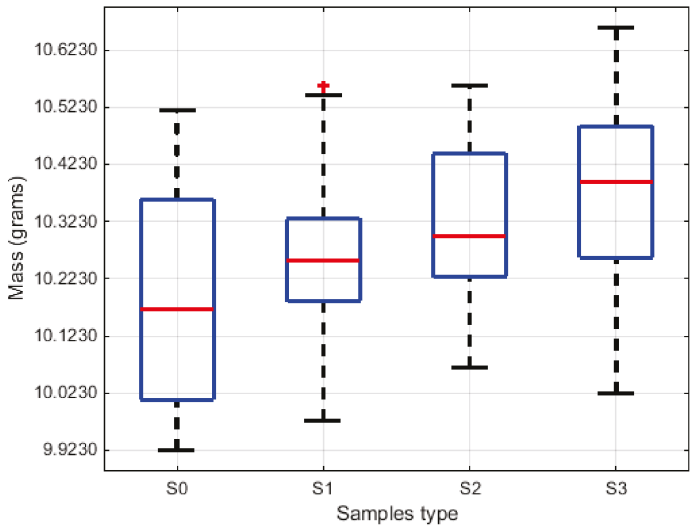

Figure 11. The stochastic diagram related to the samples' mass.

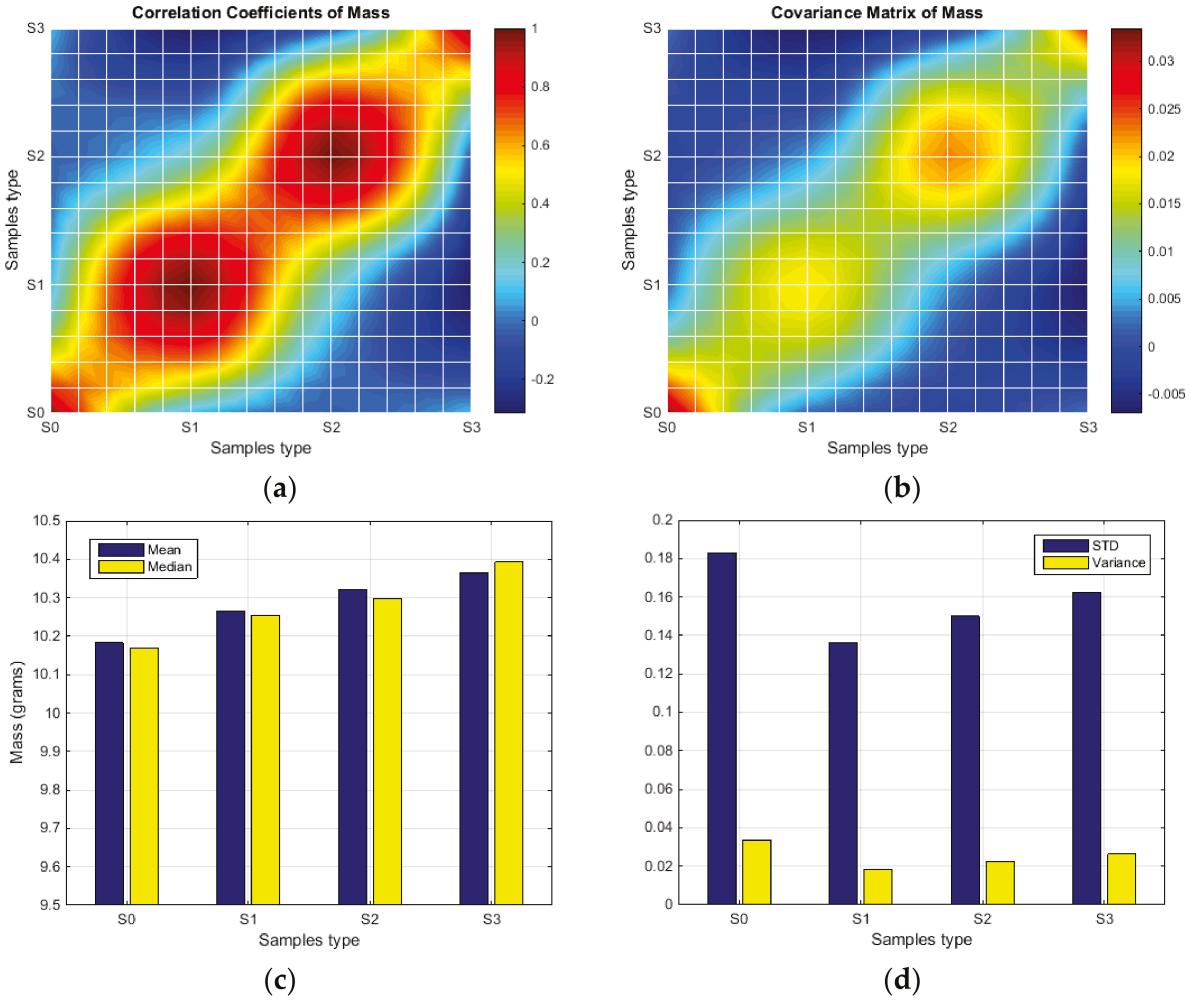

Figure 12. Statistical parameters of mass in respect to material type: (**a**) Correlation coefficient; (**b**) Covariance matrix; (**c**) Mean and median values; (**d**) Standard deviation and variance.

3.2. Noise Insulation Characteristics

The noise insulation ability of proposed materials were evaluated in terms of following parameters: normal incidence absorption (α)/reflection (R) coefficients, normal incidence sound transmission loss (STL), and impedance at normal incidence (Z). Whole parameters were evaluated based on both transmission loss tubes (K1 and K2). Complex domain parameter R has been adopted only the magnitude for this study, because this is commonly presented in the technical literature related to comparative analyses regarding noise insulation capabilities of different materials. However, the Z parameter, also complex, was presented in terms of both magnitude and phase, in order to reveal the conformity of sound spectrum evaluations. All parameters were presented with respect to frequency (suitable for each tube's capability). Thus, the diagrams were grouped as follows: absorption and reflection coefficients in Figure 13, STL in Figure 14, and impedance components in Figure 15.

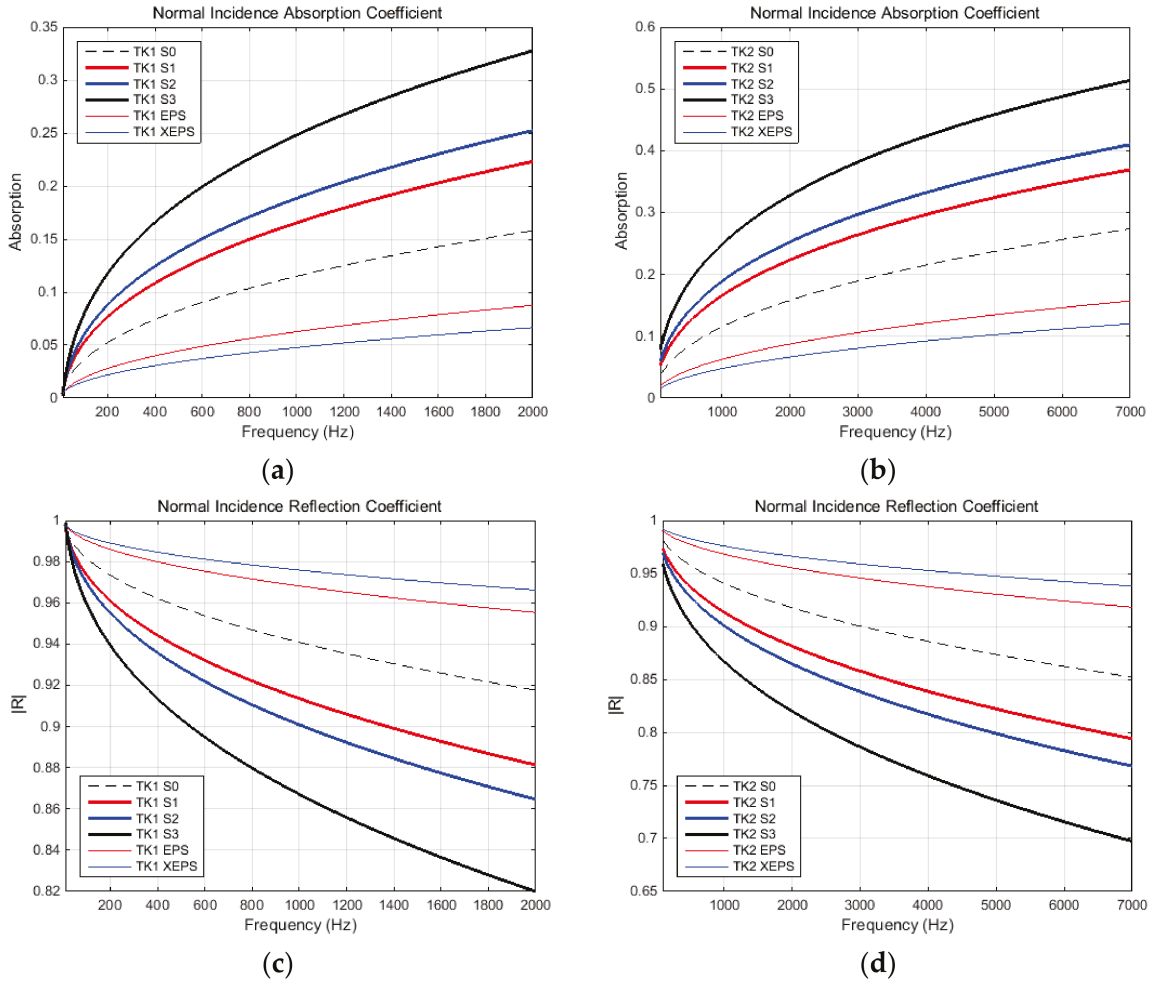

Figure 13. Sound absorption and reflection ability of samples at normal incidence, in terms of: Absorption coefficient recorded in tube K1 (**a**) and tube K2 (**b**) respectively; Reflection coefficient recorded in tube K1 (**c**) and tube K2 (**d**) respectively.

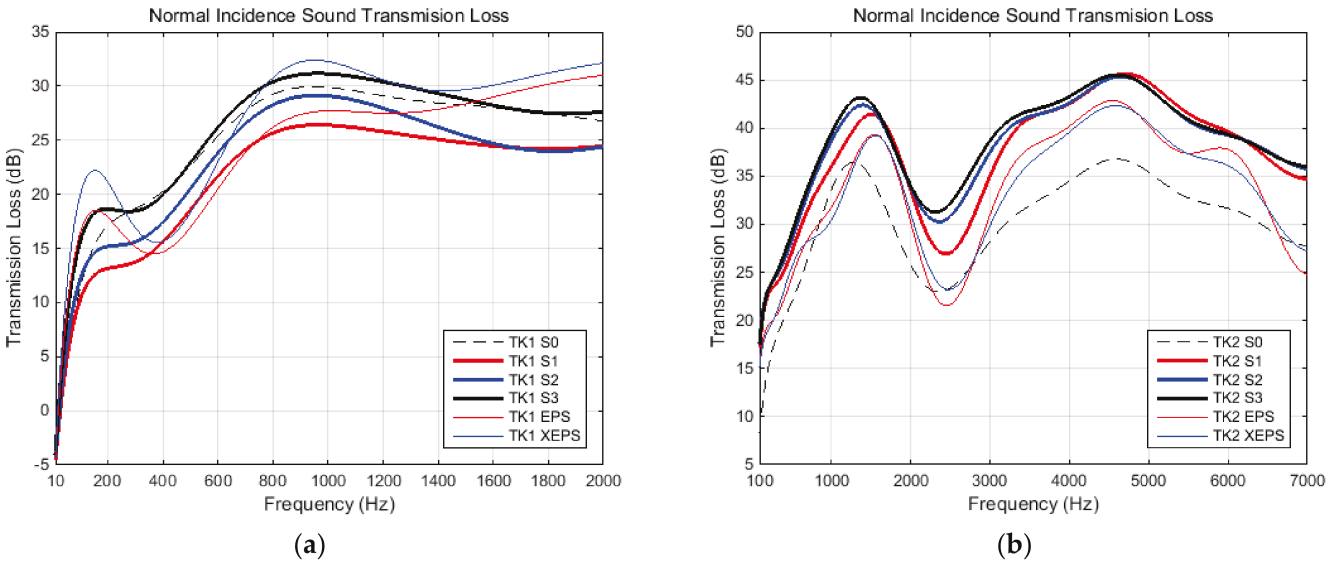

Figure 14. Sound transmission loss characteristic at normal incidence, recorded in tube K1 (**a**) and tube K2 (**b**) respectively.

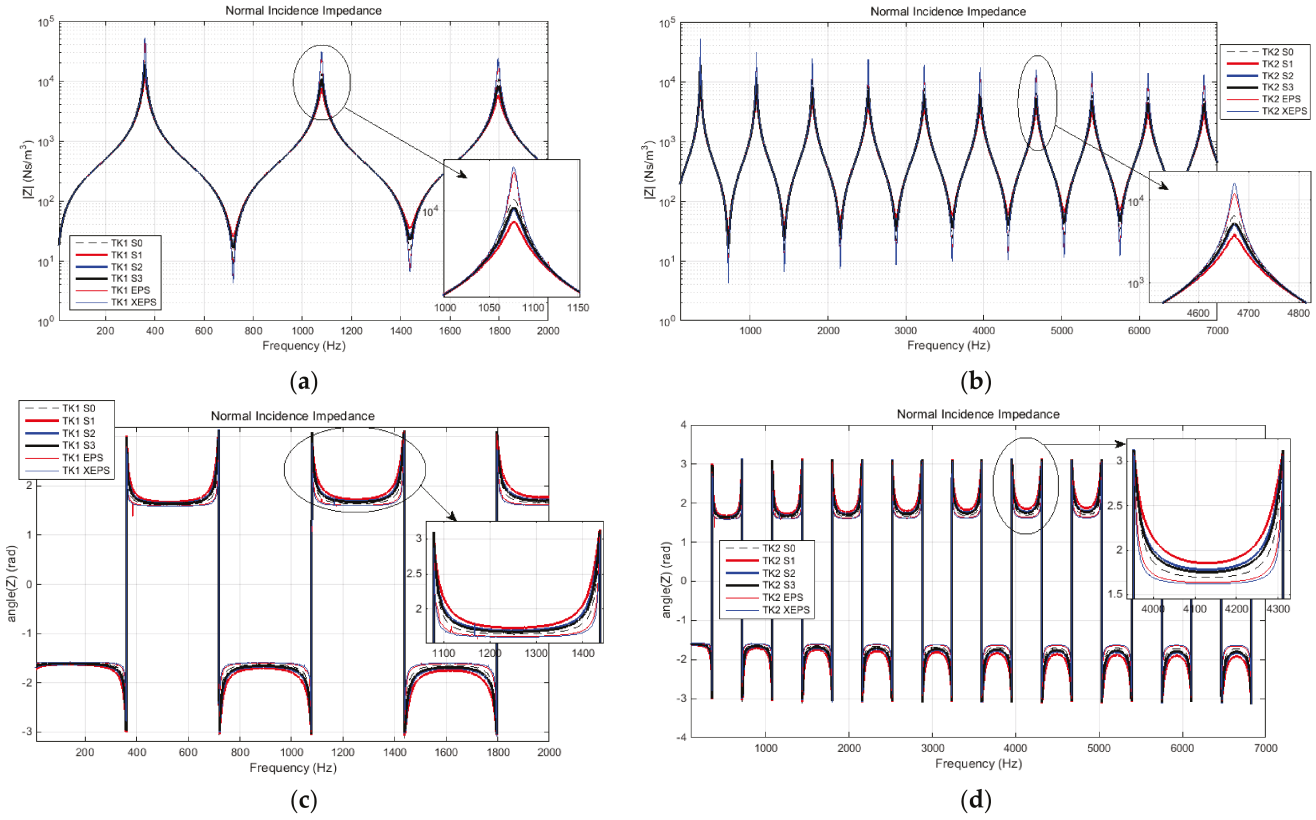

Figure 15. The impedance at normal incidence of sound, in terms of: impedance magnitude for signals recorded in tube K1 (**a**) and tube K2 (**b**); and impedance phase (angle) for siganls recorded in tube K1 (**c**) and tube K2 (**d**).

In addition to previously presented parameters, in the acoustics technical literature another indicator is typically used, which is related to noise insulation capability, particularly for middle-range frequencies. This is known as the Noise reduction coefficient (abbreviated NRC; introduced by W. R. Farrell in the early 1950s [68]), and this is represented by a single number, ranging from 0.0 to 1.0, which describes the average sound absorption performance of a material. NRC is the arithmetic average, rounded to the nearest multiple of 0.05, of the sound absorption coefficients for a specific material and mounting condition, evaluated at the octave band centre frequencies of 250, 500, 1000, and 2000 Hz. Within this study, NRC is given as raw values (unrounded) because this research was based on impedance tube for the noise absorption investigation, and authors have proposed to comparatively characterize the raw materials, not within practical dimensional and mounting conditions. The raw values of NRC, for each tube and sample type, were presented in Table 3. A graphical representation was presented in Figure 16 in order to facilitate comparative analysis.

Table 3. Noise reduction coefficients (NRCs) as raw, unrounded values.

Sample	EPS	XEPS	S0 [1]	S1 [1]	S2 [1]	S3 [1]
NRC—tube K1	0.0566	0.0432	0.1037	0.1489	0.1696	0.2231
NRC—tube K2	0.0594	0.0454	0.1099	0.1586	0.1832	0.2376

[1] Average values (20 items for each sample).

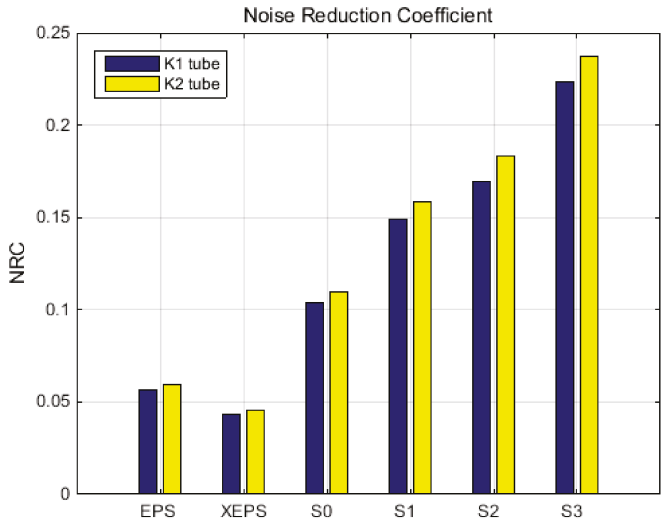

Figure 16. Noise reduction coefficient, average, for both transmission loss tubes (K1 and K2).

4. Discussion

The results have clearly shown a suitable foam structure for noise insulation applications; the microphotographs in Figure 5 present the initial bubble structure (wet state during the mixing process of foam-forming process) of the proposed material, with increasing percentage of SDS, inducing larger bubbles in fiber-based foam. The positive effect of the airy wet structure can be observed in the final state of samples (see optical and SEM micrographs in Figure 6) as they compare to the initial state of the slurry pulp (see Figure 4a). Moreover, the surface microphotographs presented in Figure 7 clearly reveal a porous structure for each type of material, with air content improving with increasing SDS. In addition to the wet state air content (see values in Table 1), the density values (see Table 2) support this concluding remark, with final air content percentages of 70, 74, and 80 for S1, S2, and S3, respectively. Statistical analyses (see Figures 9–12) highlight good correlation coefficient matrices for the results, with very close mean and median values, small variances and standard deviations, and a very small covariance matrix.

Based on the results within Section 3.1, it can be stated that the initial aim of obtaining a highly porous internal structure was reached. The maximum SDS percentage was limited by sample structural stability (based on visual investigations). Systematically, through repeated tests with various SDS percentages, we have shown that the high level of air-bubbles within the pulp structure had a role in the structural stability loss of the out-of-mould sample (final stage sample, ready-to-use). The minimum SDS percentage was based on relevant air-bubbles volumes in foam mixtures (microscope-based investigations).

Previously mentioned findings were validated through noise insulation characteristics. The results within Section 3.2 validate the structural morphology-based remarks. In terms of acoustical parameters, we found that the normal incidence absorption/reflection coefficients (see diagrams in Figure 13) indicated improved absorption, but poorer reflection, with increasing SDS percentage. Even the reference sample (water-formed sample, S0) had better absorption/reflection properties than synthetic materials (EPS, XEPS). This aspect has been supported by the very open pore structures of the fiber-based materials, compared to the closed structures of EPS/XEPS. A distinct increase in absorption capacity was observed in the S3 sample (with a higher percentage of air-content), as evidenced by its very high porosity (and tortuosity) parameter. The poor reflection coefficient of the highly porous S3 sample (also the others fiber-based samples) can be explained by the surface's rugged profile (please see micrographs in Figure 7), which induces sparse reflections, compared to the smooth surface of reference synthetic materials which enable directional reflection. It should be noted there was a good correlation between the results obtained from the two acoustic tubes (K1 and K2).

Sound transmission loss (STL) at normal incidence represents another important parameter used in sound insulation characterization. Diagrams within Figure 14 show the evolution at this parameter in respect to frequency (according to each tube's capability). The conclusions from these results are listed here. (i) The large tube (K1) provides relevant information for low- and mid-range frequencies, while the small tube (K2) provides information for a whole significant range in noise insulation practice. (ii) Overall, the S3 sample performed better than the other foam-formed materials (S2, S1; performance level decreasing in this order). (iii) S1–S3 foam-formed materials, in comparison to synthetic references (EPS, XEPS), for low-middle range frequencies, have clearly better STL performance in the whole range. (iv) The reference, water-formed fiber-based material (S0) provided better STL performance compared to the S3 sample, but only for low-middle range frequencies; its other characteristics were poorer than those of synthetic reference materials (EPS, XEPS).

The proposed foam-formed cellulose fiber-based materials are able to provide comparable STL performances to those of widely used synthetics.

Diagrams within Figure 15 depict the impedance characteristic of sample's surfaces, at normal incidence, in terms of magnitude and phase. The graphs were relatively identical in general shape; however, detailed views of the diagrams, particularly those of the resonance domain (randomly adopted for each graph) reveal some observations. (i) The similitude of shape for both magnitude and phase reveals a correlation of the sample geometry according to the acoustic transmission loss tube used for investigation. (ii) Detailed views provide very useful information regarding damping capability of each sample, which has a direct implication on its capacity for noise insulation. For example, it can be easily observed that the group of foam-formed samples (S1–S3) enable higher damping ratios than did the other reference samples. Within this group of samples, S1 provides better damping and S3 has the poorest dampling. This aspect can be explained by the fiber density, which is greater for S1 than S3, as the damping is supplied by fiber deformations. In contrast, the S0 sample enabled a high damping ratio compared to synthetic materials, because of its open-pore structure, which had internal mechanisms of wave propagation and pore wall (fiber-based) deformations.

Finally, the values used for NRC computing were acquired from sound absorption coefficient diagrams (see Figure 13a,b). Analyses of the numerical results in Table 3 and the graphical representation in Figure 16 show a good correlation between the two acoustic tube investigations. NRC increases with sample porosity; thus, a better NRC was provided by the foam-formed materials compared to the reference samples, especially the synthetics. The small differences between values computed for the two tubes are due to the different functional characteristics of each tube, and by the homogeneity of samples. The latter also impacts the absorption/reflection coefficients, and acoustic impedance diagrams.

5. Conclusions

The objectives of this research were met: Cellulose fiber-based, porous, lightweight materials were obtained using the basic foam-forming technique, and preliminary results (through material and structural characterization) have shown a suitable ability for noise insulation applications, as verified in specific acoustic investigations. The authors' assumption that the SDS percentage influences noise insulation performances was also experimentally tested and validated. Indeed, increasing SDS charge results in an improved noise insulation capability thorough its porous internal configuration (with greater voids structure and spatial distribution). Additional results obtained during the experimental tests (e.g., dimensional and structural stability) were not directly presented into this paper (such as discussed diagrams or tables), but were obviously included within the adopted hypotheses for this study.

Foam-formed materials based on cellulose fibers present a sustainable and promising alternative to conventional materials. Leveraging the mechanical properties of cellulose fibers and the advantages of foam forming, these materials offer enhanced strength, low density, and environmental benefits. In the future, advancements in processing techniques

and the development of hybrid materials using cellulose fibers with other reinforcing materials, such as natural or synthetic polymers, could further expand the range of applications and enhance the overall performance of foam-formed materials.

Author Contributions: Conceptualization, S.-M.N. and P.N.; methodology, S.-M.N., M.-V.G. and P.N.; software, M.S. and S.-M.N.; validation, S.-M.N., M.-V.G. and P.N.; formal analysis, M.S.; investigation, M.S., S.-M.N., M.-V.G. and P.N.; resources, S.-M.N. and P.N.; writing—original draft preparation, S.-M.N.; writing—review and editing, S.-M.N., M.-V.G. and P.N.; visualization, S.-M.N.; supervision, S.-M.N., M.-V.G. and P.N.; project administration, S.-M.N.; funding acquisition, S.-M.N. and P.N. All authors have read and agreed to the published version of the manuscript.

Funding: This research was funded by "Dunarea de Jos" University of Galati, Romania, Grant number RF 9418/2023.

Institutional Review Board Statement: Not applicable.

Data Availability Statement: Not applicable.

Acknowledgments: The authors thank for support of the Research Centre for Mechanics of Machines and Technological Equipments—MECMET, within Engineering and Agronomy Faculty in Braila, "Dunarea de Jos" University of Galati, Romania.

Conflicts of Interest: The authors declare no conflict of interest.

References

1. Leppänen, M.; Väätäinen, P. Environmental impact of cellulose-based insulation materials. *Energy Build.* **2018**, *166*, 246–254.
2. Ruan, J.; Tang, S.; Dai, J. Research on sound absorption property of natural cellulose fiber. In Proceedings of the 2018 2nd International Conference on Composite Material, Polymer Science and Engineering (CMPSE), Osaka, Japan, 21–22 September 2018; IEEE: Piscataway, NJ, USA, 2018; pp. 242–245.
3. Acikgoz, S. *Noise and Vibration Control Engineering: Principles and Applications*; John Wiley & Sons: Hoboken, NJ, USA, 2016.
4. Torgal, F.; Jalali, S. *Eco-Efficient Construction and Building Materials: Life Cycle Assessment (LCA), Eco-Labelling and Case Studies*; Woodhead Publishing: Thorston, UK, 2017.
5. Tarnawski, W.; Krucinska, I. Acoustic properties of natural insulation materials. *Arch. Acoust.* **2017**, *42*, 103–110.
6. Jaeger, P. Insulation materials for buildings. In *Handbook of Environmental Engineering*; Springer: Berlin/Heidelberg, Germany, 2014; pp. 111–136.
7. Jahangiri, P. Novel Cellulose Based Foam-Formed Products: Applications and Numerical Studies. Ph.D. Thesis, University of British Columbia, Vancouver, BC, Canada, 2013.
8. Madani, A.; Zeinoddini, S.; Varahmi, S. Turnbull, T.; Phillion, A.B.; Olson, J.A.; Martinez, D.M. Ultra-lightweight paper foams: Processing and properties. *Cellulose* **2014**, *21*, 2023–2031.
9. Jahangiri, P.; Madani, A.; Korehei, R.; Zeinoddini, S.S.; Madani, A.; Sharma, Y.; Phillion, A.; Martinez, D.M.; Olson, J.A. On filtration and heat insulation properties of foam formed cellulose based materials. *Nord. Pulp Pap. Res. J.* **2014**, *29*, 584–591.
10. Acikgoz, S.; Durgun, I. A new acoustic absorber material from cotton and polyurethane foam wastes. *Build. Environ.* **2008**, *43*, 1626–1633.
11. Tianjian, L. Ultralight porous metals: From fundamentals to applications. *Acta Mech. Sin.* **2002**, *18*, 457–479.
12. Tanpichai, S.; Boonmahitthisud, A.; Soykeabkaew, N.; Ongthip, L. Review of the recent developments in all-cellulose nanocomposites: Properties and applications. *Carbohydr. Polym.* **2022**, *286*, 119192. [CrossRef]
13. Sombatsompop, N.; Niamsuwan, V. Acoustical properties of wood-based materials. In *Wood in Civil Engineering*; Springer: Berlin/Heidelberg, Germany, 2012; pp. 153–177.
14. Joutsimo, O.P.; Tyrväinen, P. The effect of fiber properties on sound absorption of soft fiberboards. *Appl. Acoust.* **2014**, *77*, 17–24.
15. Sahin, T.; Yılmaz, H. Sound absorption properties of wood-based insulation materials. *J. Acoust. Soc. Am.* **2016**, *140*, 3043.
16. Akıncı, T.C. Evaluation of sound absorption properties of natural fiber materials. *J. Nat. Fibers* **2018**, *15*, 336–349.
17. Kim, H.C.; Lee, J.W.; Kim, J.H. Acoustic absorption property of porous polymer materials made of vegetable fibers. *J. Mech. Sci. Technol.* **2012**, *26*, 2595–2601.
18. Chen, N.; Pan, Q. Versatile fabrication of ultralight magnetic foams and application for oil-water separation. *ACS Nano* **2013**, *7*, 6875–6883. [CrossRef] [PubMed]
19. Yin, J.; Li, X.; Zhou, J.; Guo, W. Ultralight three-dimensional boron nitride foam with ultralow permittivity and superelasticity. *Nano Lett.* **2013**, *13*, 3232–3236. [CrossRef] [PubMed]
20. Xu, S.; Bourham, M.; Rabiei, A. A novel ultra-light structure for radiation shielding. *Mater. Des.* **2010**, *31*, 2140–2146. [CrossRef]
21. Tillotson, T.M.; Hrubesh, L.W. Transparent ultralow-density silica aerogels prepared by a two-step sol-gel process. *J. Non-Cryst. Solids* **1992**, *145*, 44–50. [CrossRef]

22. Tappan, B.C.; Huynh, M.H.; Hiskey, M.A.; Chavez, D.E.; Luther, E.P.; Mang, J.T.; Son, S.F. Ultralow-density nanostructured metal foams: Combustion synthesis, morphology, and composition. *J. Am. Chem. Soc.* **2006**, *128*, 6589–6594. [CrossRef]
23. Radvan, B.; Gatward, A. Formation of wet-laid webs by a foaming process. *Tappi* **1972**, *55*, 748.
24. Smith, M.; Punton, V. The role of the forming process in determining the structure and properties of paper. *Pulp Pap. Can.* **1975**, *76*, 114–117.
25. Tringham, R. New developments in radfoam process. *Pap. Technol. Ind.* **1974**, *15*, 288–294.
26. Smith, M.; Punton, V.; Rixson, A. Structure and properties of paper formed by a foaming process. *Tappi* **1974**, *57*, 107–111.
27. Al-Qararah, A.M.; Hjelt, T.; Kinnunen, K.; Beletski, N.; Ketoja, J.A. Exceptional pore size distribution in foam-formed fibre networks. *Nord. Pulp Pap. Res. J.* **2012**, *27*, 226–230. [CrossRef]
28. Cervin, N.T.; Andersson, L.; Ng, J.B.S.; Olin, P.; Bergström, L.; Wågberg, L. Lightweight and strong cellulose materials made from aqueous foams stabilized by nanofibrillated cellulose. *Biomacromolecules* **2013**, *14*, 503–511. [CrossRef] [PubMed]
29. Deng, M.; Zhou, Q.; Du, A.; van Kasteren, J.; Wang, Y. Preparation of nanoporous cellulose foams from cellulose-ionic liquid solutions. *Mater. Lett.* **2009**, *63*, 1851–1854. [CrossRef]
30. Sehaqui, H.; Salajkova, M.; Zhou, Q.; Berglund, L.A. Mechanical performance tailoring of tough ultra-high porosity foams prepared from cellulose I nanober suspensions. *Soft Matter* **2010**, *6*, 1824. [CrossRef]
31. Ali, Z.M.; Gibson, L.J. The structure and mechanics of nanofibrillar cellulose foams. *Soft Matter* **2013**, *9*, 1580–1588. [CrossRef]
32. Mohammadi, B.; Ershad-Langroudi, A.; Moradi, G.; Safaiyan, A.; Kahnamuei, F.H. Foam for Sound Insulation. In *Polymeric Foams: Applications of Polymeric Foams (Volume 2)*; ACS Symposium Series; American Chemical Society: Washington, DC, USA, 2023; Volume 1440, Chapter 12; pp. 253–272. [CrossRef]
33. Dua, S.; Khatri, H.; Naveen, J.; Jawaid, M.; Jayakrishna, K.; Norrrahim, M.N.F.; Rashedi, A. Potential of natural fiber based polymeric composites for cleaner automotive component production—A comprehensive review. *J. Mater. Res. Technol.* **2023**, *25*, 1086–1104. [CrossRef]
34. Tauhiduzzaman, M.; Hafez, I.; Bousfield, D.; Tajvidi, M. Multiscale modeling of lignocellulosic foams under compression. *Mater. Des.* **2023**, *225*, 111471. [CrossRef]
35. Hasan, A.; Rabbi, M.S.; Billah, M. Making the lignocellulosic fibers chemically compatible for composite: A comprehensive review. *Clean. Mater.* **2022**, *4*, 100078. [CrossRef]
36. Yan, W.; Liu, J.; Zheng, X.; Zhang, J.; Tang, K. Wood-derived high-performance cellulose structural materials. *e-Polymers* **2023**, *23*, 20230010. [CrossRef]
37. Xu, W.; Horoshenkov, K.V.; Jin, Y. The influence of a thin, natural cellulose fibre membrane on the acoustic absorption of a layer of melamine foam. *Build. Acoust.* **2023**, *30*, 1–16. [CrossRef]
38. Ketola, A.E.; Song, W.; Lappalainen, T.; Salminen, K.; Viitala, J.; Turpeinen, T.; Miettinen, A.; Lee, K.-Y.; Ketoja, J.A. Changing the Structural and Mechanical Anisotropy of Foam-Formed Cellulose Materials by Affecting Bubble−Fiber Interaction with Surfactant. *ACS Appl. Polym. Mater.* **2022**, *4*, 7685–7698. [CrossRef]
39. Keranen, J.T.; Jetsu, P.; Turpeinen, T.; Koponen, A.I. Dewatering and Structural Analysis of Foam-Formed, Lightweight Fibrous Materials. *BioResources* **2023**, *18*, 531–549. [CrossRef]
40. Ergun, M.E. Activated Carbon and Cellulose-reinforced Biodegradable Chitosan Foams. *BioResources* **2023**, *18*, 1215–1231. [CrossRef]
41. Ferreira, E.S. Insulative wood materials templated by wet foams. *Mater. Adv.* **2023**, *4*, 641–650. [CrossRef]
42. Cucharero, J.; Ceccherini, S.; Maloney, T.; Lokki, T. Sound absorption properties of wood-based pulp fibre foams. *Cellulose* **2021**, *28*, 4267–4279. [CrossRef]
43. Hjelt, T.; Ketoja, J.A.; Kiiskinen, H.; Koponen, A.I.; Pääkkönen, E. Foam forming of fiber products: A review. *J. Dispers. Sci. Technol.* **2022**, *43*, 1462–1497. [CrossRef]
44. Miranda-Valdez, I.Y.; Coffeng, S.; Zhou, Y.; Viitanen, L.; Hu, X.; Jannuzzi, L.; Puisto, A.; Kostiainen, M.A.; Mäkinen, T.; Koivisto, J. Foam-formed biocomposites based on cellulose products and lignin. *Cellulose* **2023**, *30*, 2253–2266. [CrossRef]
45. Nechita, P.; Nastac, S.M. Overview on Foam Forming Cellulose Materials for Cushioning Packaging Applications. *Polymers* **2022**, *14*, 1963. [CrossRef] [PubMed]
46. Sriprom, W.; Sirivallop, A.; Choodum, A.; Limsakul, W.; Wongniramaikul, W. Plastic/Natural Fiber Composite Based on Recycled Expanded Polystyrene FoamWaste. *Polymers* **2022**, *14*, 2241. [CrossRef]
47. Zhou, Y.; Yin, W.; Guo, Y.; Qin, C.; Qin, Y.; Liu, Y. Green Preparation of Lightweight, High-Strength Cellulose-Based Foam and Evaluation of Its Adsorption Properties. *Polymers* **2023**, *15*, 1879. [CrossRef]
48. Taiwo, E.M.; Yahya, K.; Haron, Z. Potential of Using Natural Fiber for Building Acoustic Absorber: A Review. *J. Phys. Conf. Ser.* **2019**, *1262*, 012017. [CrossRef]
49. Maderuelo-Sanz, R. Characterizing and modelling the sound absorption of the cellulose acetate fibers coming from cigarette butts. *J. Environ. Health Sci. Eng.* **2021**, *19*, 1075–1086. [CrossRef] [PubMed]
50. Arenas, J.P.; Rebolledo, J.; del Rey, R.; Alba, J. Sound absorption properties of unbleached cellulose loose-fill insulation material. *BioResources* **2014**, *9*, 6227–6240. [CrossRef]
51. Hurtado, P.L.; Rouilly, A.; Maréchal, V.V.; Raynaud, C. A review on the properties of cellulose fibre insulation. *Build. Environ.* **2016**, *96*, 170–177. [CrossRef]

52. Silviana, S.; Prastiti, E.C.; Hermawan, F.; Setyawan, A. Optimization of the Sound Absorption Coefficient (SAC) from Cellulose–Silica Aerogel Using the Box–Behnken Design. *ACS Omega* **2022**, *7*, 41968–41980. [CrossRef]
53. Neri, M.; Levi, E.; Cuerva, E.; Pardo-Bosch, F.; Zabaleta, A.G.; Pujadas, P. Sound Absorbing and Insulating Low-Cost Panels from End-of-Life Household Materials for the Development of Vulnerable Contexts in Circular Economy Perspective. *Appl. Sci.* **2021**, *11*, 5372. [CrossRef]
54. Cheng, F.; Lu, P.; Ren, P.; Chen, J.; Ou, Y.; Lin, M.; Liu, D. Preparation and properties of foamed cellulose-polymer microsphere hybrid materials for sound absorption. *BioResources* **2016**, *11*, 7394–7405. [CrossRef]
55. Maderuelo-Sanz, R.; García-Cobos, F.J.; Sánchez-Delgado, F.J. Study of the acoustic performance of composites made from recycled cellulose acetate and polymer waste. *Build. Acoust.* **2022**, *29*, 445–457. [CrossRef]
56. Krucińska, I.; Gliścińska, E.; Michalak, M.; Ciechańska, D.; Kazimierczak, J.; Bloda, A. Sound-absorbing green composites based on cellulose ultra-short/ultra-fine fibers. *Text. Res. J.* **2015**, *85*, 646–657. [CrossRef]
57. Kolya, H.; Jang, E.S.; Hashitsume, K.; Kang, C.W. Effects of ammonium persulfate on coconut wood (Cocos nucifera L.) cellulose, hemicellulose, and lignin polymers: Improved sound absorption capacity. *J. Appl. Polym. Sci.* **2022**, *139*, e52674. [CrossRef]
58. Nechita, P.; Nastac, S. Foam-formed cellulose composite materials with potential applications in sound insulation. *J. Compos. Mater.* **2018**, *52*, 747–754. [CrossRef]
59. Debeleac, C.; Nechita, P.; Nastac, S. Computational investigations on soundproof applications of foam-formed cellulose materials. *Polymers* **2019**, *11*, 1223. [CrossRef] [PubMed]
60. Stanciu, M.D.; Curtu, I.; Cosereanu, C.; Lica, D.; Nastac, S. Research regarding acoustical properties of recycled composites. In Proceedings of the 8th International DAAAM Baltic Conference Industrial Engineering, Tallinn, Estonia, 19–21 April 2012; Otto, T., Ed.; Tallinn University of Technology, Estonia: Tallinn, Estonia, 2012; pp. 741–746.
61. Ionescu, S.; Nechita, P. Thermo-Insulating Panels Based on Composite Structures from Vegetal Fibres and Polymeric Matrix. *Adv. Mater. Res.* **2017**, *1143*, 154–159.
62. Nastac, S.; Debeleac, C.; Nechita, P. Assessments on Shock Absorption Properties of Foam-Formed Low Density Cellulose Composites. *Acta Tech. Napoc. Ser.-Appl. Math. Mech. Eng.* **2017**, *60*, 565–572.
63. Stanciu, M.D.; Savin, A.; Nastac, S.M. Mechanical and surface properties of lignocellulosic fibres reinforced composites. *Stroj. Vestn* **2018**, *64*, 698–705. [CrossRef]
64. Nastac, S.; Nechita, P.; Debeleac, C.; Simionescu, C.; Seciureanu, M. The Acoustic Performance of Expanded Perlite Composites Reinforced with Rapeseed Waste and Natural Polymers. *Sustainability* **2022**, *14*, 103. [CrossRef]
65. Seciureanu, M.; Guiman, M.V.; Nastac, S.M.; Nechita, P.; Debeleac, C.N.; Capatana, G.F. On Experimental Evaluation of Tortuosity for Cellulose-based Highly Porous Composites used within Noise Insulation Applications. In Proceedings of the 17th International Conference "Acoustics and Vibration of Mechanical Structures", Springer Proceedings in Physics, Timisoara, Romania, 26–27 May 2023.
66. Nechita, P.; Seciureanu, M.; Guiman, M.V. Sandwich Biocomposites Structures based on Foam and Cellulose Fibers intended to Noise Insulation. In Proceedings of the 24th International Symposium in the Fields of Pulp, Paper, Packaging and Graphics, Belgrade, Republic of Serbia, 21–22 June 2023.
67. Seciureanu, M. Innovative Bio-Foam-Formed Composites for Soundproofing Applications. In Proceedings of the 29th International Congress on Sound and Vibration ICSV29, Prague, Czech Republic, 9–13 July 2023.
68. Farrell, W.R. Acoustical Materials for Use in Monumental Spaces. *Noise Control* **1958**, *4*, 32–39. [CrossRef]

polymers

MDPI

Article

Compressible Cellulose Wood Prepared with Deep Eutectic Solvents and Its Improved Technology

Wenhao Wang, Mengyao Chen and Yan Wu *

College of Furnishings and Industrial Design, Nanjing Forestry University, Nanjing 210037, China
* Correspondence: wuyan@njfu.edu.cn

Abstract: Elastic materials have a wide range of applications in many industries, but their widespread use is often limited by small-scale production methods and the use of highly polluting chemical reagents. In this study, we drew inspiration from research on wood softening to develop an environmentally friendly and scalable approach for producing a new type of compressible wood material called CW from natural wood. To achieve this, we employed a top-down approach using a novel type of "ionic liquid" eutectic solvent (DES) that is cost-effective, environmentally friendly, and recyclable. After treatment with DES, the resulting CW demonstrated good elasticity and durable compressibility, which was achieved by removing some lignin and hemicellulose from the wood and thinning the cell walls, thereby creating a honeycomb structure that allows for sustained compression and rebound. However, we found that the wood treated with a single eutectic solvent showed some softening (CW-1), although there was still room for further improvement of its elasticity. To address this, we used a secondary treatment with sodium hydroxide alkali solution to produce a softer and more elastic wood (CW-2). We conducted a series of comparative analyses and performance tests on natural wood (NW) and CW, including microscopic imaging; determination of chemical composition, mechanical properties, and compressive stress effects; and laser confocal testing. The results show that the DES and sodium hydroxide alkali solution treatments effectively removed some lignin, hemicellulose, and cellulose from the wood, resulting in the thinning of the cell walls and creating a more elastic material with a sustainable compression rebound rate of over 90%. The various properties of CW, including its elasticity, durability, and sustainability, provide great potential for its application in a range of fields, such as sensors, water purification, and directional tissue engineering.

Keywords: wood chemistry; deep eutectic solvents; cellulose nanofiber; mechanical compressibility; elastic porous structure

1. Introduction

Cellular materials, especially those that are hydrated, have garnered significant research interest due to their unique characteristics. These materials have the ability to contain water, are biocompatible and environmentally friendly, and have a wide range of applications in various fields such as biomedicine [1,2], pharmaceutics [3], energy storage and batteries [4,5], water purification [6], agriculture [7], and other industries. Bottom-up approaches, such as using cellulose nanofibers [8], graphene oxide [9], and bamboo nanofibers [10], have been popular methods for fabricating cellular hydrated materials. However, these approaches often involve complex manufacturing processes, high energy consumption, and the use of toxic chemicals, which can lead to unsatisfactory mechanical properties. Despite the advantages of blending with additional components, a new manufacturing method that is fast, clean, and efficient is needed to produce cellular materials.

To reduce costs and improve efficiency, a top-down approach has been implemented to manufacture cellular materials [11]. Song et al. proposed a method whereby entire blocks of wood are used, chemicals are removed from wood cells through chemical treatment,

and freeze drying is employed to shape them into cellular materials. However, traditional chemical treatments that utilize methods such as NaOH-Na_2SO_3 and $NaClO_2$-H_2O_2 treatments tend to destroy the cellulose crystal structure [12]. As a result, the mechanical properties of wood are compromised [13], leading to poor mechanical properties in the final cellular material. Additionally, these methods can produce a lot of pollution, which is not environmentally friendly.

Deep eutectic solvents (DESs) a new class of ionic liquid analogues, which are low-temperature eutectic mixtures composed of hydrogen bond donors (HBD) and hydrogen bond acceptors (HBA), such as quaternary ammonium salts and metal salts, in a certain mole ratio. DESs are green solvents exhibiting low vapor pressure, high thermal stability, low toxicity, and biodegradability [14]. The combined diversity of eutectic solvents allows for adjustment of their physical and chemical properties, providing tremendous potential for industrial applications such as electrochemistry [15], gas absorption [16], extraction [17], and biopharmaceuticals [18]. DESs composed of choline chloride and lactic acid or oxalic acid have been reported to be effective in removing lignin and hemicellulose from wood [16]. Lignin is dissolved in the DES system and subsequently separated, while the ability of C-C chemical bonds in lignin remains unaffected, allowing most of the characteristics and activities of natural lignin to be maintained [19]. Compared to traditional methods, DES delignification treatment does not damage the cellulose structure, and the stiff cell wall becomes more flexible [20]. DES treatment is a safe and efficient process, as it is a physical dissolution process rather than a chemical decomposition process [21], and DESs can be recycled after the termination of reactions. Economically and environmentally, using DES for the delignification of wood enables the production of cellulose-based wood scaffolds, making it a vital process.

In this study, a simple, clean, and scalable top-down approach was employed to fabricate elastic and compressible cellulose wood (also known as elastic material) from natural wood. The process involved treating natural wood with a DES solution to remove a portion of lignin and hemicellulose and soften the cell walls of the wood. An alkali solution was then used to further remove hemicellulose in the wood cell wall. In addition, chemical treatment and freeze drying of the ice templates led to thinner cell walls of the wood that adhered to each other, forming a honeycomb structure. compressible woodis highly porous and can be compressed under high strain (e.g., 70%). However, natural wood is prone to fracture and cannot fully recover to its original state after deformation. In contrast, as shown in Figure 1, compressible wood exhibits a high degree of recoverability, almost fully recovering to its original state even when compressed under high strain (e.g., 70%). To analyze the treatment effect of the reagents, two different methods were employed. The first method involved treating natural wood with DES alone, while the second method involved treating natural wood with both DES and an alkali solution. To distinguish between the two types of wood, the pretreated wood is referred to as NW, and the post-treated wood is called CW. The CW-1 samples were treated with DES alone, while the CW-2 samples were treated with both DES and alkali solution.

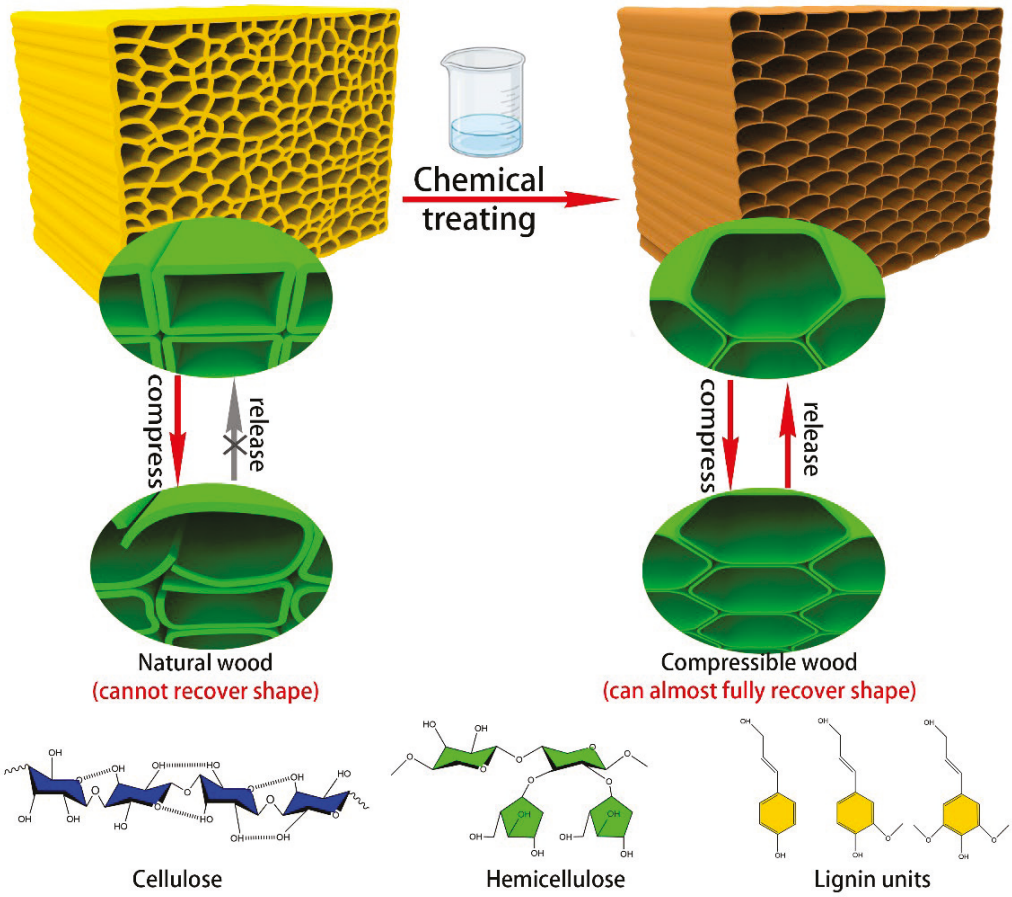

Figure 1. Comparison between natural wood and compressible wood.

2. Materials and Methods

2.1. Materials

The experiment utilized ash wood (Populus tomentosa Carr.) samples with dimensions of 15 × 15 × 15 mm, which were provided by Yihua Life Technology Co., Ltd. located in Shantou, China. Anhydrous ethanol was sourced from Guangdong Guanghua Sci-Tech Co., Ltd., Guangdong, China, while acetone was provided by Sinopharm Chemical Reagent Co., Ltd., Beijing, China. Choline chloride (AR, 98%) was supplied by Shanghai Canspec Scientific Instruments Co., Ltd., Shanghai, China, and lactic acid (AR, Content 85%~92%) was obtained from Tianjin Fuyu Fine Chemical Co., Ltd., Tianjin, China. Sodium hydroxide (AR, 98%) was procured from Shanghai Aladdin Biochemical Technology Co., Ltd., Shanghai, China. All chemicals used were of analytical grade.

2.2. Experimental Procedure for Compressible Wood

2.2.1. Preprocessing

To prepare the ash wood blocks for the subsequent experiments, a preprocessing step was conducted. First, the wood blocks were immersed in a solution of anhydrous ethanol and acetone at a 1:1 volume ratio for 10 h to remove gums and resins in the wood. Next, the blocks were air-dried in an oven at 102 °C for 6 h to completely remove the solvents and any residual moisture. This preprocessing step ensured that the ash wood blocks were clean and free of impurities that could interfere with the subsequent treatments.

2.2.2. DES Solution Treatment

To make deep eutectic solvents, chloride choline and lactic acid were mixed in a 1:5 molar ratio, added to a beaker, and stirred with a magnetic stirrer at 60 °C until a colorless and transparent liquid was formed. Detailed reaction equations are shown in Figure 2. Then, the

Ash wood samples were fully immersed in the DES solution (at a mass ratio of 1:10) and heated in a 120 °C oil bath for 5 h, resulting in DES-treated wood. Studies have shown that as the treatment time increases and the temperature rises, more lignin is removed from wood materials . It was discovered that DESs can be synthesized at various molar ratios of HBA to HBD (HBA:HBD). The acid containing a hydroxyl group (such as lactic acid) is capable of forming DESs with an HBA ratio of 1:1, while other HBAs may require a ratio of 1:2 or more [22]. In this study, we used lactic acid as HBDs at a molar ratio 1:5; additional HBDs may lead to the dissolution of more lignin. In this experiment, a molar ratio of 1:5 and a high-temperature, short-duration treatment method was adopted to remove lignin while preserving a certain level of mechanical properties of the wood blocks.

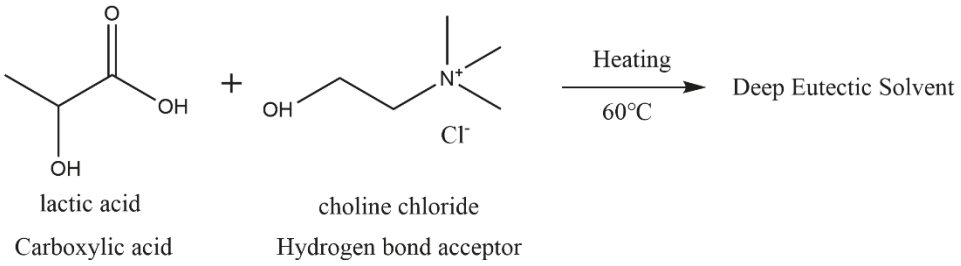

Figure 2. Choline chloride reacted with hydrogen bond acceptor to produce deep eutectic solvents.

2.2.3. Alkaline Solution Treatment

To further modify the properties of the DES-treated wood, the compressible cellulose wood samples were washed with deionized water and subsequently treated with a 5 wt% sodium hydroxide solution for a 3 h reaction at 80 °C (The mass ratio of solid to liquid was 1:10), resulting in alkaline-treated wood. During this process, more lignin and hemicellulose were removed, further enhancing the flexibility and elasticity of the wood.

2.2.4. Freeze Drying

All the samples, were prefrozen at −15 °C for 6 h, then evacuated at −56 °C for 36 h. It is worth noting that dry compressible cellulose wood can be converted back to compressible wood by absorbing approximately 60% of its weight in water. This was achieved by immersing the dry compressible wood into water. The water not only penetrated the porous cell wall but also filled in empty spaces within the compressible wood.

2.3. Characterization

2.3.1. Scanning Electron Microscopy

To observe the morphological characteristics of the sample, an FEI Quanta 200 scanning electron microscope (SEM) was utilized with an acceleration voltage of 30 kV. First, the natural wood and compressible wood samples were cut into small pieces using a glass knife while maintaining the integrity of the sample structure. Next, the pieces were fixed onto conductive carbon glue with tweezers and sprayed with gold films for 30 s using a vacuum coating instrument. Finally, the vessels, cell walls, and cell cavities of the sample were observed with SEM.

2.3.2. X-ray Diffraction and Fourier Infrared Spectroscopy

To characterize the molecular structure of the samples, an X-ray diffractometer (Ultima IV, from Rigaku Co., Ltd., Tokyo, Japan) was utilized. First, all samples were crushed into small, uniform powders, and an appropriate amount was flattened in the sample tank. The X-ray diffractometer was then used to scan the sample with a scanning voltage of 40 kV, a scanning range of 2θ = 5–60°, and a scanning speed of 10°/min. The crystallinity index (I_c) was determined using Formula (1) based on the height of the 200 peak (I_{200}, 2θ = 22.5°) and the minimum between the 200 and 110 peaks (I_{am}, 2θ = 18°). It is worth

noting that I_{200} represents both crystalline and amorphous materials, while Iam only represents amorphous material [23].

$$I_c = \left[\frac{I_{200} - I_{am}}{I_{200}}\right] \times 100\% \quad (1)$$

To characterize the infrared spectra of functional groups of samples, a Fourier transform infrared spectrometer (VERTEX 80V, from Bruker Co., Ltd., Bremen, Germany) was used. The method involved grinding samples into wood powder of 80 to 100 mesh, mixing and tableting the powder with KBr, then placing it into a sample pool. The sample was then scanned to obtain the infrared spectrum, allowing for the identification of functional groups present in the samples.

2.3.3. Chemical Composition Content Test

To determine the cellulose, hemicellulose, and lignin contents of the samples, the laboratory analytical procedure (LAP) described by the National Renewable Energy Laboratory was employed. First, the wood powders were hydrolyzed with 72% concentrated sulfuric acid, and the resulting solution was diluted to 4% and filtered using a G3 glass sand funnel. The acid-insoluble lignin content was calculated by weighing the filtered residue, while the acid-soluble lignin content was determined by measuring the ultraviolet absorbance of the filtered filtrate. The sugar content was then analyzed by high-performance liquid chromatography (HPLC) after diluting the filtrate by a certain multiple. Finally, the contents of cellulose, hemicellulose, and lignin were calculated according to Formula (2).

$$\text{content} = \frac{M_S}{M_W} \times 100\% \quad (2)$$

In the formula, M_S refers to the mass of each chemical component in the sample, and M_W refers to the total mass of the samples.

2.3.4. Mechanical Performance Test

A compression test was conducted using a computer-controlled electronic universal testing machine (AG-IC/100KN, Shimadzu Co., Ltd., Kyoto, Japan). The samples were loaded at a speed of 2 mm/min until the compressive strain reached 70%, and the resulting stress–strain curves were recorded by a computer. Loading–unloading cyclic compression experiments were also performed using the same machine at 30% compression strain and a loading speed of 4 mm/min. The data obtained from these experiments were used to analyze the mechanical properties of the samples.

2.3.5. Laser Confocal Test

The fluorescence emission spectra of lignin were acquired using a confocal laser microscope (LSM710, Carl Zeiss AG Co., Ltd., Kupferzell, Germany) by exciting the lignin with a laser at a wavelength of 488 nm. The samples were cut into slices that were 0.5 mm thick and placed on a slide. A cover slide was then applied, and the sample was observed under the confocal laser microscope to obtain the fluorescence emission spectra of the lignin.

3. Results and Discussion

3.1. Morphology Analysis

Ash wood is a widely available, fast-growing tree species in China with several advantageous characteristics, including wide adaptability, a long annual growth period, and fast production speed. Due to these features, it was selected as the experimental material for this study. The morphology of samples can be visualized by SEM images. Specifically, NW mainly consists of tough wood fibers, vessels, and ray cells; the tough wood fiber cells have a small cell cavity and a thick cell wall and are randomly distributed among the uniform single-row xylem rays (Figure 3a,b). After DES treatment, the cellular

structure was maintained, but cracks appeared between cells, and the cell wall collapsed (Figure 3c,d) [20]. It is worth noting that no significant thinning of cell walls was observed, perhaps because DES selectively removes lignin between cells and does not affect the structural components of cell walls significantly. Upon treatment with NaOH solution, cell walls became thinner, and adjacent cell walls stuck together, forming a highly porous network structure.

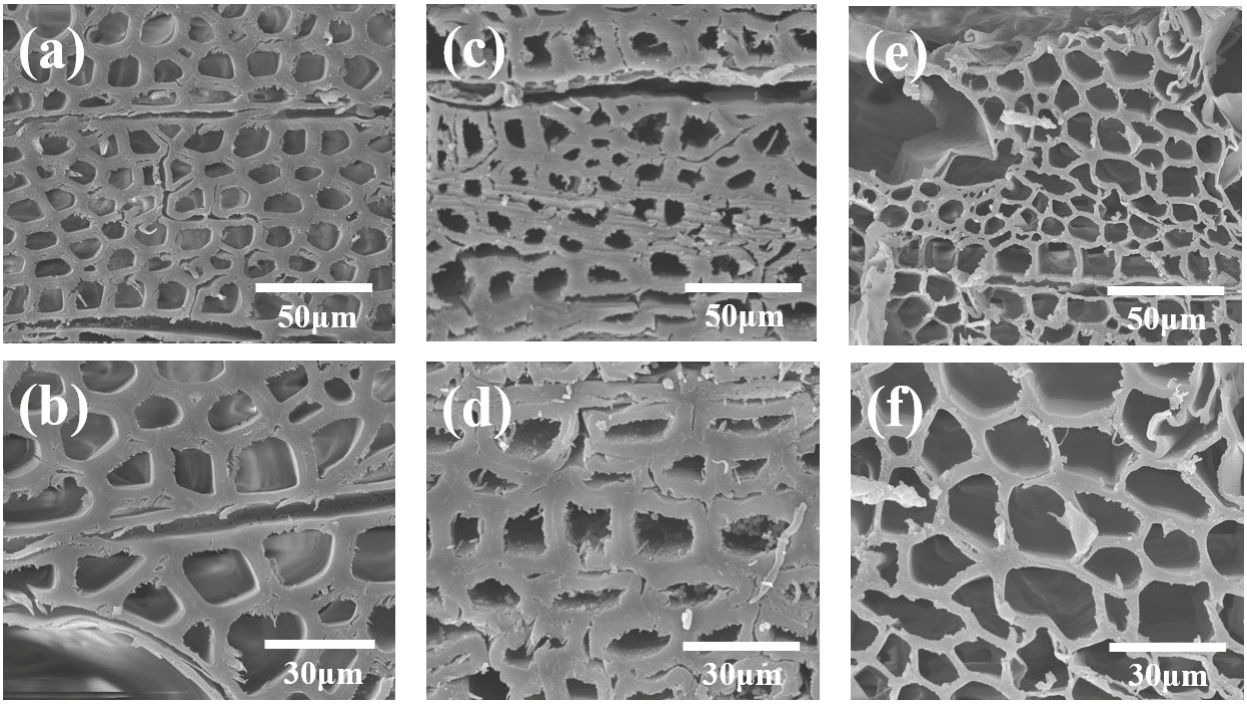

Figure 3. Morphological and structural characterizations of NW and CW. (**a**,**b**) SEM images of NW. (**c**,**d**) SEM images of CW-1. (**e**,**f**) SEM images of CW-2.

3.2. Chemical Structure Analysis

As shown in Figure 4a, the characteristic absorption peaks of NW are the same as those reported in previous studies, with absorption peaks at 3327 cm^{-1} (O–H stretching vibration), 2915 cm^{-1} (C–H stretching vibration), 1032 cm^{-1} (ether bond vibration), 1735 cm^{-1} (C=O stretching vibration), 1242 cm^{-1} (C–O stretching vibration), 1505, and 1592 cm^{-1} (aromatic nucleus skeleton vibration). The infrared spectra presented in Figure 4a show that a significant intensity reduction appears in peaks of CW-2 at 1735 cm^{-1}, which represents hemicellulose acetyl groups, and at 1238 cm^{-1}, which represents the C–O stretching vibration in lignin and hemicellulose, indicating the partial removal of hemicellulose. The characteristic absorption peak strengths of lignin at 1590 and 1505 cm^{-1} were also reduced, indicating the partial removal of lignin. In addition, compared with NW, the absorption peak intensities of CW-1 at 1238 cm^{-1} and 1735 cm^{-1} increased, which may be due to the residual lactic acid in the wood.

The crystal structure of cellulose shows the characteristic diffraction peaks of cellulose in the Figure 4b.Tthe positions of the main diffraction peaks of samples are almost the same at $2\theta = 15.6^\circ$ (101 plane), 22.5° (002 plane), and 34.4° (040 crystal plane), indicating that both CW-1 and CW-2 retain the crystal structure of cellulose I [24]. As shown in Figure 4b, CW-2 has the highest crystallinity (about 80%), followed by CW-1 (about 78%), and NW has the lowest crystallinity of about 62%. The diffraction peak intensity of CW increases at $2\theta = 15.6$ and 22.5°, which may be due to the fact that after partial lignin removal by DES and alkali solution, the cellulose chain tightly wrapped by lignin remains basically parallel, making it easier to crystallize into cellulose type I, and under high-temperature and acidic environment, the hydroxyl group in DES and the primary hydroxyl

group in cellulose participate in the alkylation of cellulose selectively. Additionally, the removal of substances such as lignin, hemicellulose, and amorphous cellulose dominated the pretreatment process, resulting in thinning of the cell wall, which is consistent with the results presented in Figure 3 [25].

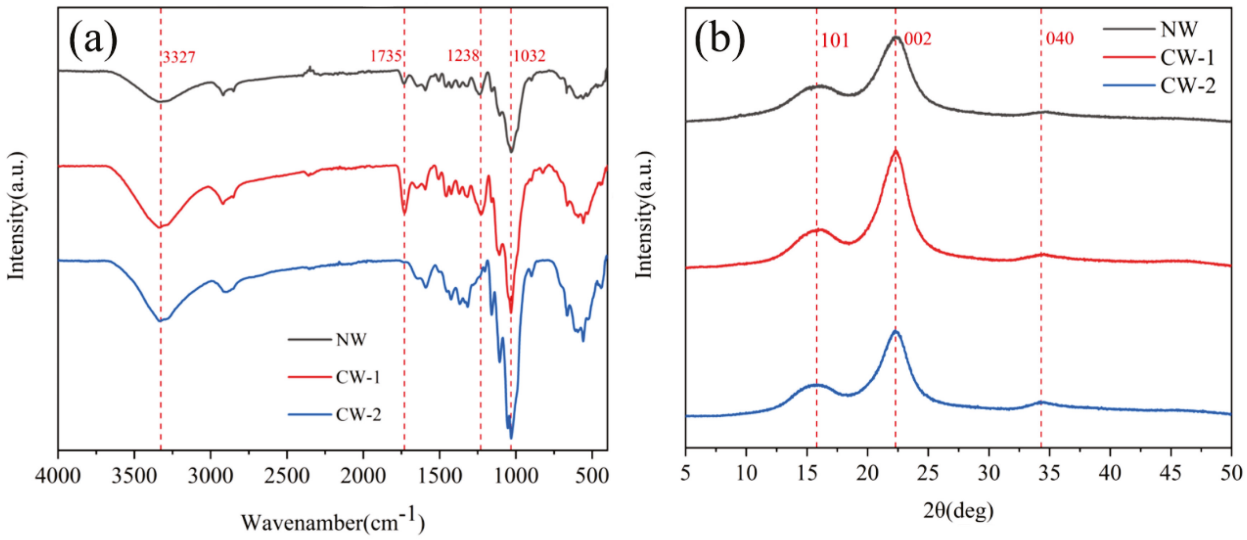

Figure 4. (**a**) FT-IR spectra of NW and CW. (**b**) XRD patterns of NW and CW.

3.3. Mechanical Performance

The compressive stress–strain curves of samples were obtained as shown in Figure 5. The curves exhibited typical three-state behavior, with a low-strain linear elastic deformation region of less than 4%, followed by a steady-state region in which the stress between 4 and 60% strain remained relatively constant, and finally, a region where the stresses increased sharply with strain. NW showed a significant inflection point at a strain of about 4%, indicating the onset of nonlinear elastic deformation. However, after the stress was released, the strain could not be fully recovered, and partial plastic deformation occurred. In contrast, CW required less stress to achieve the same strain and benefited from its honeycomb structure and hydration network, showing rapid recovery properties when releasing the applied pressure [26]. In contrast, it was almost impossible for NW to regain its shape when released from the same compressive strain. To assess their fatigue resistance, the samples were subjected to 50 load–unload cyclic compression tests at a constant strain of 30% (Figure 5). The results show that after 50 compression cycles, the height retention rate of CW-1 and CW-2 was about 90% and 96%, respectively, indicating good mechanical compressibility and fatigue resistance. Moreover, the plastic deformation produced by CW was much smaller than that of NW (10% and 4%, respectively), demonstrating that CW has superior mechanical properties over NW.

3.4. Chemical Composition Content Analysis

Wood cell walls are composed of linear polysaccharide cellulose, heterohemicellulose, and structurally variable lignin, which are interconnected through hydrogen and covalent bonding [27]. The cellular interlocking structure of wood is critical, and chemical treatment and freeze drying can impact this structure. Figure 6 shows that the content of cellulose decreased from 45.4% (NW) to 40.2% (CW-1) to 39.7% (CW-2), while the content of hemicellulose decreased from 13.9% (NW) to 9.3% (CW-1) to 3.1% (CW-2). The content of lignin decreased from 29.6% (NW) to 25.6% (CW-1) to 18.7% (CW-2). The DES treatment dissolved and removed part of the lignin and hemicellulose and a small amount of cellulose. The subsequent alkaline solution treatment further removed part of the lignin and hemicellu-

lose, particularly a large amount of hemicellulose in the cell wall, which led to thinning of the cell wall, as shown in Figure 3.

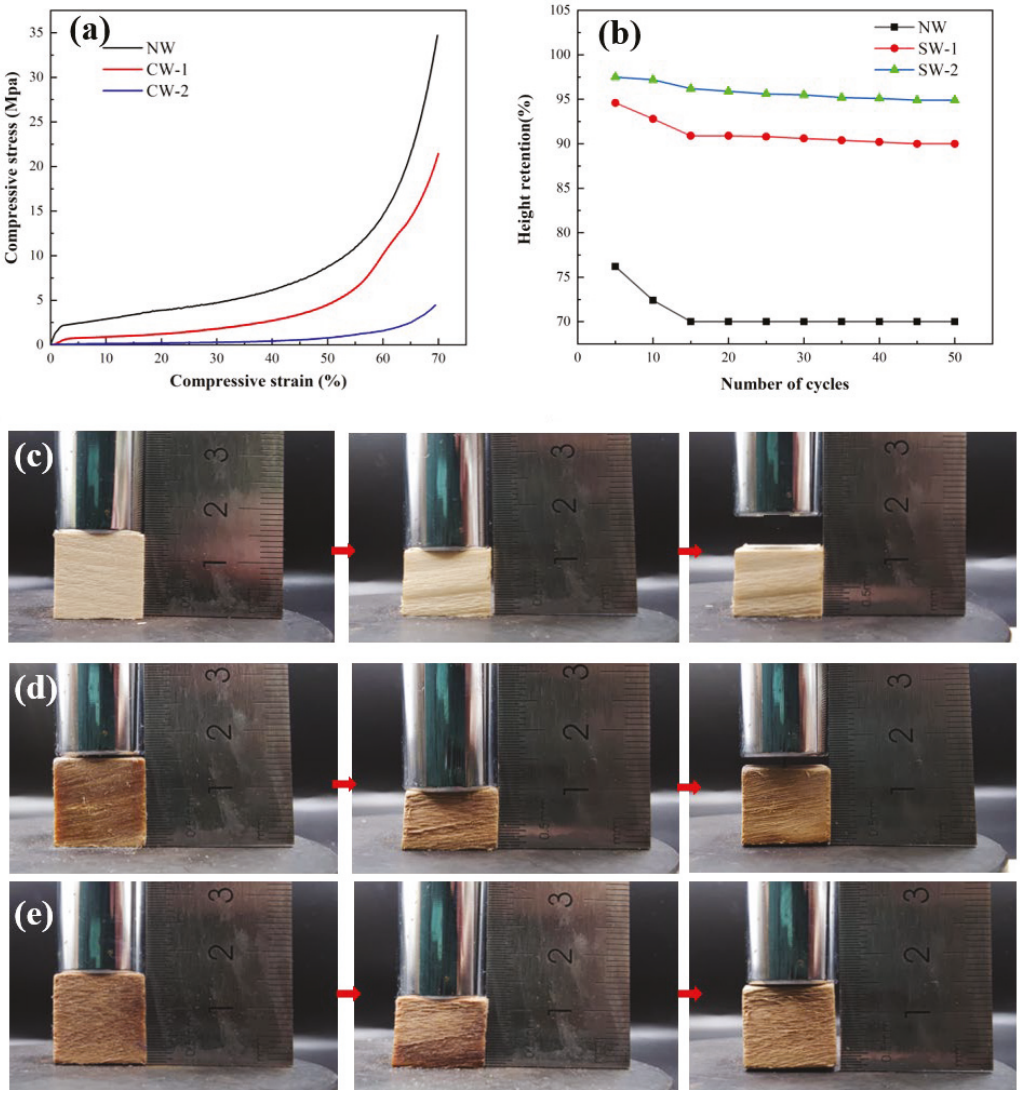

Figure 5. Mechanical properties of NW and CW. (**a**) Stress–strain curves of NW and CW during compression. (**b**) Height retention of NW and CW under cyclic compression with a compression strain of 30%. (**c**) Compression resilience picture of NW. (**d**) Compression resilience picture of CW-1. (**e**) Compression resilience picture of CW-2.

3.5. Confocal Fluorescence Figure

The distribution of lignin in wood is not uniform, with a general trend of lower content at collection sites closer to the top of the plant. Lignin is concentrated in the intercellular layer, followed by the secondary wall inner layer, and the concentration of lignin in the cell interior is the lowest. To determine the content and location of lignin in cells, confocal laser testing is necessary. Confocal laser imaging allows for the estimation of lignin deposition in plant samples and provides spatial quantitative information on the relative amount and composition of lignin [28]. Qualitative observation of the microdistribution of lignin content can be achieved using blue light with a wavelength of 488 nm. The brighter the fluorescence, the higher the density and concentration of lignin. Figure 7a shows that NW has the highest brightness, followed by CW-1 (Figure 7b), and CW-2 is the darkest (Figure 7c). These results are consistent with the chemical composition content determination shown in Figure 6. In NW, lignin is distributed heavily in the cell wall and cell cavity. In CW-1, the confocal

fluorescence figure shows a general dimming in brightness, indicating that some lignin was removed. In CW-2, fluorescence intensity is barely observed within the cells, with only a faint glow seen between the cells, indicating that lignin was almost completely removed from the cell wall.

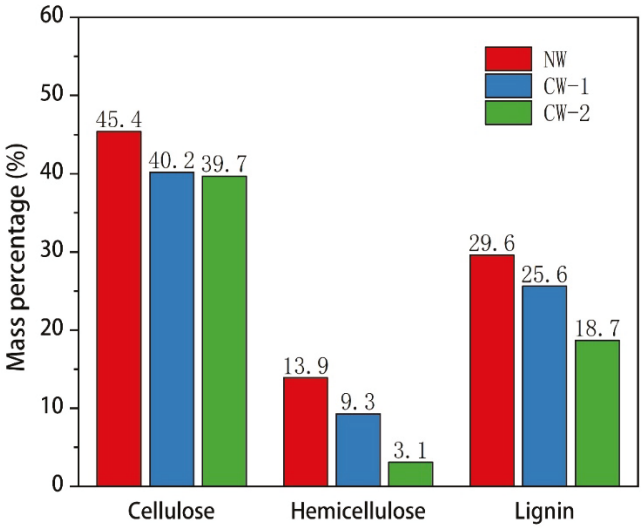

Figure 6. Cellulose, hemicellulose, and lignin contents of NW and CW.

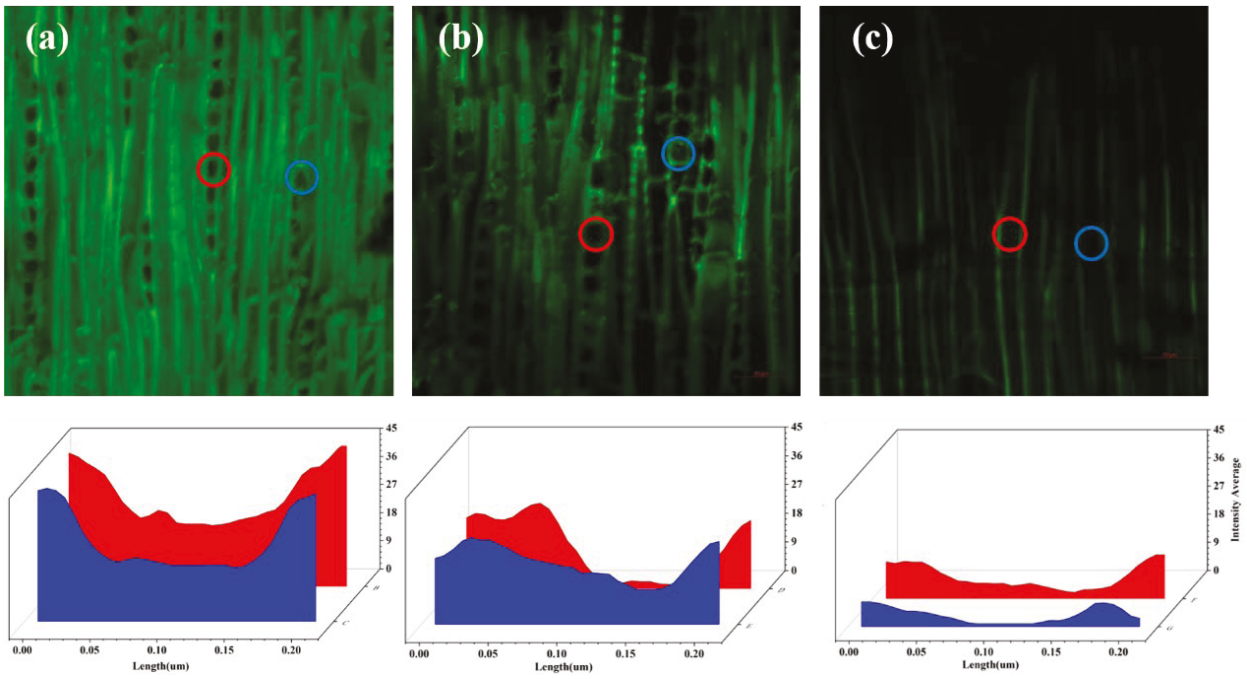

Figure 7. Confocal fluorescence figure of NW and CW under blue light with a wavelength of 488 nm. (**a**) Confocal fluorescence figure of NW. (**b**) Confocal fluorescence figure of CW-1. (**c**) Confocal fluorescence figure of CW-2. Circles indicate the regions of interest for the analysis of the fluorescence intensity by confocal microscopy at corresponding positions of the cells.

3.6. Thermal Property

Figure 8 shows the typical TGA and DTG curves of natural wood and compressible wood. All curves exhibit a minor weight loss below 100 °C, which can be attributed to water evaporation. Above 200 °C, the weight loss rate gradually increased, and a distinct weight loss was observed between 200 and 400 °C. The first weight loss stage was due to water evaporation, while the first degradation event occurred between 200 and 300 °C and

can be attributed to the decomposition of hemicelluloses and the slower decomposition of lignin. The second degradation stage above 300 °C can be attributed to the degradation of cellulose. These findings are consistent with previously reported results [29,30].

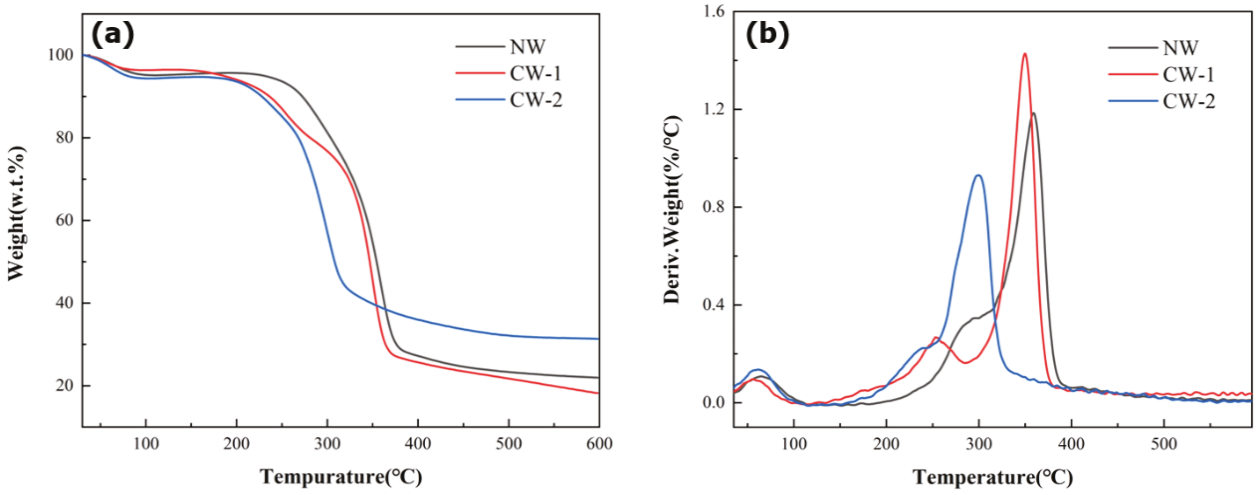

Figure 8. Typical TGA curves (**a**) and DTG curves (**b**) of NW and CW.

The Table 1 shows the rmogravimetric data of NW and CW. The T_{max}, which refers to the temperature at which the maximum weight loss occurs during decomposition, was found to be lower for the compressible wood compared to the natural wood. In addition, the charcoal residue of CW-2 increased by 42.7% compared to NW. This increase in char residue can be attributed to the removal of low-molecular-weight polysaccharides and some inorganic matter or extractives during the compressible wood treatment process, resulting in a lower decomposition temperature and a higher amount of char formation [31]. These findings suggest that the flame retardancy of treated wood could be improved.

Table 1. The rmogravimetric data of NW and CW.

Sample	T0 (°C)	Tf (°C)	Tmax (°C)	Residue at 600 °C(%)
NW	249.51	377.38	368.54	21.95
CW-1	212.20	367.24	355.72	18.19
CW-2	207.13	332.01	297.15	31.33

4. Conclusions

In this study, we present a top-down approach for producing long-lasting compressible cellulose materials by chemically treating natural wood with DES and alkaline solutions, followed by freeze drying. The chemical treatment process removes some of the lignin and hemicellulose, which not only softens the cell walls but also causes them to adhere to each other and form a honeycomb structure. The resulting resilient wood can be more easily compressed and exhibits a sustainable rebound. DES is an environmentally friendly chemical that can be recycled after use, making this approach a sustainable option. These compressible wood materials have potential applications in fields such as sensors, directional tissue engineering, and water purification.

Author Contributions: Conceptualization, W.W. and Y.W.; methodology, W.W.; software, W.W.; validation, W.W., Y.W. and M.C.; formal analysis, W.W.; investigation, W.W.; resources, W.W.; data curation, W.W.; writing—original draft preparation, W.W.; writing—review and editing, W.W., Y.W. and M.C.; visualization, W.W.; supervision, Y.W.; project administration, W.W., Y.W. and M.C.; funding acquisition, Y.W. All authors have read and agreed to the published version of the manuscript.

Funding: This research was funded by The National Natural Science Foundation of China (32071687 and 32001382).

Institutional Review Board Statement: Not applicable.

Data Availability Statement: The data presented in this study are available on request from the corresponding author.

Conflicts of Interest: The authors declare no conflict of interest.

References

1. Khademhosseini, A.; Langer, R. Microengineered hydrogels for tissue engineering. *Biomaterials* **2007**, *28*, 5087–5092. [CrossRef] [PubMed]
2. Zhao, H.; Liu, M.; Zhang, Y.; Yin, J.; Pei, R. Nanocomposite hydrogels for tissue engineering applications. *Nanoscale* **2020**, *12*, 14976–14995. [CrossRef] [PubMed]
3. Emi, T.T.; Barnes, T.; Orton, E.; Reisch, A.; Tolouei, A.E.; Madani, S.Z.M.; Kennedy, S.M. Pulsatile Chemotherapeutic Delivery Profiles Using Magnetically Responsive Hydrogels. *ACS Biomater. Sci. Eng.* **2018**, *4*, 2412–2423. [CrossRef]
4. Zhang, W.; Feng, P.; Chen, J.; Sun, Z.; Zhao, B. Electrically conductive hydrogels for flexible energy storage systems. *Prog. Polym. Sci.* **2019**, *88*, 220–240. [CrossRef]
5. Wu, H.; Yu, G.; Pan, L.; Liu, N.; McDowell, M.T.; Bao, Z.; Cui, Y. Stable Li-ion battery anodes by in-situ polymerization of conducting hydrogel to conformally coat silicon nanoparticles. *Nat. Commun.* **2013**, *4*, 1943. [CrossRef]
6. Pakdel, P.M.; Peighambardoust, S.J. Review on recent progress in chitosan-based hydrogels for wastewater treatment application. *Carbohydr. Polym.* **2018**, *201*, 264–279. [CrossRef]
7. Demitri, C.; Scalera, F.; Madaghiele, M.; Sannino, A.; Maffezzoli, A. Potential of Cellulose-Based Superabsorbent Hydrogels as Water Reservoir in Agriculture. *Int. J. Polym. Sci.* **2013**, *2013*, 435073. [CrossRef]
8. Xing, C.; Chen, S.; Liang, X.; Liu, Q.; Qu, M.; Zou, Q.; Li, J.; Tan, H.; Liu, L.; Fan, D.; et al. Two-Dimensional MXene (Ti3C2)-Integrated Cellulose Hydrogels: Toward Smart Three-Dimensional Network Nanoplatforms Exhibiting Light-Induced Swelling and Bimodal Photothermal/Chemotherapy Anticancer Activity. *ACS Appl. Mater. Interfaces* **2018**, *10*, 27631–27643. [CrossRef] [PubMed]
9. Xu, Y.; Lin, Z.; Huang, X.; Wang, Y.; Huang, Y.; Duan, X. Functionalized Graphene Hydrogel-Based High-Performance Supercapacitors. *Adv. Mater.* **2013**, *25*, 5779. [CrossRef]
10. Zhang, X.; Wang, Y.; Lu, C.; Zhang, W. Cellulose hydrogels prepared from micron-sized bamboo cellulose fibers. *Carbohyd. Polym.* **2014**, *114*, 166–169. [CrossRef]
11. Song, J.; Chen, C.; Wang, C.; Kuang, Y.; Li, Y.; Jiang, F.; Li, Y.; Hitz, E.; Zhang, Y.; Liu, B.; et al. Superflexible Wood. *ACS Appl. Mater. Interfaces* **2017**, *9*, 23520–23527. [CrossRef]
12. Xiong, Y.; Xu, L.; Nie, K.; Jin, C.; Sun, Q.; Xu, X. Green Construction of an Oil-Water Separator at Room Temperature and Its Promotion to an Adsorption Membrane. *Langmuir* **2019**, *35*, 11071–11079. [CrossRef] [PubMed]
13. Wang, K.; Liu, X.; Tan, Y.; Zhang, W.; Zhang, S.; Li, J. Two-dimensional membrane and three-dimensional bulk aerogel materials via top-down wood nanotechnology for multibehavioral and reusable oil/water separation. *Chem. Eng. J.* **2019**, *371*, 769–780. [CrossRef]
14. Chen, Z.; Ragauskas, A.; Wan, C. Lignin extraction and upgrading using deep eutectic solvents. *Ind. Crops Prod.* **2020**, *147*, 112241. [CrossRef]
15. Fang, Y.; Jiang, X.; Sun, X.; Dai, S. New ionic liquids based on the complexation of dipropyl sulfide and AlCl3 for electrodeposition of aluminum. *Chem. Commun.* **2015**, *51*, 13286–13289. [CrossRef]
16. Carriazo, D.; Gutierrez, M.C.; Luisa Ferrer, M.; Del Monte, F. Resorcinol-Based Deep Eutectic Solvents as Both Carbonaceous Precursors and Templating Agents in the Synthesis of Hierarchical Porous Carbon Monoliths. *Chem. Mater.* **2010**, *22*, 6146–6152. [CrossRef]
17. Rogosic, M.; Kucan, K.Z. Deep eutectic solvent based on choline chloride and propylene glycol as a potential medium for extraction denitrification of hydrocarbon fuels. *Chem. Eng. Res. Des.* **2020**, *161*, 45–57. [CrossRef]
18. Wikene, K.O.; Bruzell, E.; Tonnesen, H.H. Improved antibacterial phototoxicity of a neutral porphyrin in natural deep eutectic solvents. *J. Photochem. Photobiol. B* **2015**, *148*, 188–196. [CrossRef]
19. Jablonsky, M.; Skulcova, A.; Kamenska, L.; Vrska, M.; Sima, J. Deep Eutectic Solvents: Fractionation of Wheat Straw. *Bioresources* **2015**, *10*, 8039–8047. [CrossRef]
20. Bi, Z.; Li, T.; Su, H.; Ni, Y.; Yan, L. Transparent Wood Film Incorporating Carbon Dots as Encapsulating Material for White Light-Emitting Diodes. *ACS Sustain. Chem. Eng.* **2018**, *6*, 9314–9323. [CrossRef]
21. Chen, Z.; Dang, B.; Luo, X.; Li, W.; Li, J.; Yu, H.; Liu, S.; Li, S. Deep Eutectic Solvent-Assisted In Situ Wood Delignification: A Promising Strategy To Enhance the Efficiency of Wood-Based Solar Steam Generation Devices. *ACS Appl. Mater. Interfaces* **2019**, *11*, 26032–26037. [CrossRef] [PubMed]
22. Tan, Y.T.; Ngoh, G.C.; Chua, A.S.M. Effect of functional groups in acid constituent of deep eutectic solvent for extraction of reactive lignin. *Bioresour. Technol.* **2019**, *281*, 359–366. [CrossRef] [PubMed]
23. Mandal, A.; Chakrabarty, D. Isolation of nanocellulose from waste sugarcane bagasse (SCB) and its characterization. *Carbohyd. Polym.* **2011**, *86*, 1291–1299. [CrossRef]

24. Dong, Y.; Yan, Y.; Ma, H.; Zhang, S.; Li, J.; Xia, C.; Shi, S.Q.; Cai, L. In-Situ Chemosynthesis of ZnO Nanoparticles to EndowWood with Antibacterial and UV-Resistance Properties. *J. Mater. Sci. Technol.* **2017**, *33*, 266–270. [CrossRef]
25. Pinkert, A.; Goeke, D.F.; Marsh, K.N.; Pang, S. Extracting wood lignin without dissolving or degrading cellulose: Investigations on the use of food additive-derived ionic liquids. *Green Chem.* **2011**, *13*, 3124–3136. [CrossRef]
26. Yang, C.; Suo, Z. Hydrogel ionotronics. *Nat. Rev. Mater.* **2018**, *3*, 125–142. [CrossRef]
27. Zhang, N.; Li, S.; Xiong, L.; Hong, Y.; Chen, Y. Cellulose-hemicellulose interaction in wood secondary cell-wall. *Model. Simul. Mater. Sci. Eng.* **2015**, *23*, 085010. [CrossRef]
28. Decou, R.; Serk, H.; Menard, D.; Pesquet, E. Analysis of Lignin Composition and Distribution Using Fluorescence Laser Confocal Microspectroscopy. *Methods Mol. Biol.* **2017**, *1544*, 233–247. [CrossRef]
29. Kim, H.S.; Kim, S.; Kim, H.J.; Yang, H.S. Thermal properties of bio-flour-filled polyolefin composites with different compatibilizing agent type and content. *Thermochim. Acta* **2006**, *451*, 181–188. [CrossRef]
30. Shebani, A.N.; van Reenen, A.J.; Meincken, M. The effect of wood extractives on the thermal stability of different wood species. *Thermochim. Acta* **2008**, *471*, 43–50. [CrossRef]
31. Shebani, A.N.; Van Reenen, A.J.; Meincken, M. The Effect of Wood Species on the Mechanical and Thermal Properties of Wood-LLDPE Composites. *J. Compos. Mater.* **2009**, *43*, 1305–1318. [CrossRef]

polymers

MDPI

Review

From Nature to Lab: Sustainable Bacterial Cellulose Production and Modification with Synthetic Biology

Vid Potočnik [1], Selestina Gorgieva [2] and Janja Trček [1,3,*]

[1] Department of Biology, Faculty of Natural Sciences and Mathematics, University of Maribor, 2000 Maribor, Slovenia; vid.potocnik.2@gmail.com
[2] Faculty of Mechanical Engineering, Institute of Engineering Materials and Design, University of Maribor, 2000 Maribor, Slovenia; selestina.gorgieva@um.si
[3] Faculty of Chemistry and Chemical Engineering, University of Maribor, 2000 Maribor, Slovenia
* Correspondence: janja.trcek@um.si; Tel.: +386-(0)2-22-93-749

Abstract: Bacterial cellulose (BC) is a macromolecule with versatile applications in medicine, pharmacy, biotechnology, cosmetology, food and food packaging, ecology, and electronics. Although many bacteria synthesize BC, the most efficient BC producers are certain species of the genera *Komagataeibacter* and *Novacetimonas*. These are also food-grade bacteria, simplifying their utilization at industrial facilities. The basic principles of BC synthesis are known from studies of *Komagataeibacter xylinus*, which became a model species for studying BC at genetic and molecular levels. Cellulose can also be of plant origin, but BC surpasses its purity. Moreover, the laboratory production of BC enables in situ modification into functionalized material with incorporated molecules during its synthesis. The possibility of growing *Komagataeibacter* and *Novacetimonas* species on various organic substrates and agricultural and food waste compounds also follows the green and sustainable economy principles. Further intervention into BC synthesis was enabled by genetic engineering tools, subsequently directing it into the field of synthetic biology. This review paper presents the development of the fascinating field of BC synthesis at the molecular level, seeking sustainable ways for its production and its applications towards genetic modifications of bacterial strains for producing novel types of living biomaterials using the flexible metabolic machinery of bacteria.

Keywords: acetic acid bacteria; *Komagataeibacter*; *Novacetimonas*; bacterial cellulose; sustainable production; agricultural waste; food waste; genetic engineering; synthetic biology; biomaterial

1. Review Contents

The Scheme 1 gives an overview of the sections covered in this review.

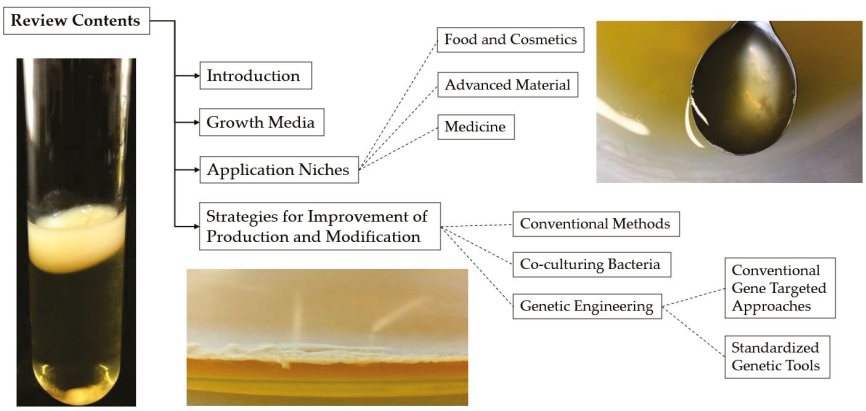

Scheme 1. An overview of the sections covered in this review.

2. Bacterial Cellulose as Featured Nanomaterial

2.1. Introduction to Bacterial Cellulose

Although cellulose is widely known, even outside the scientific community, to be the main structural component of many plant tissues, the biosynthesis of this homopolysaccharide not only takes place in plant cells, but similar anabolic reactions also occur in the world of microorganisms [1,2]. Prominent cellulose-producing microorganisms include certain algae, the Gram-positive bacterium *Sarcina ventriculi*, and a variety of Gram-negative genera such as *Achromobacter*, *Azotobacter*, *Pseudomonas*, *Rhizobium*, and *Salmonella* [3]. Some of the best-known producers of bacterial cellulose (BC) undoubtedly belong to the genera of acetic acid bacteria (AAB)—rod-shaped, Gram-negative obligate aerobes classified in the family *Acetobacteraceae* [4,5]. These α-*Proteobacteria*, capable of oxidizing alcohols, aldehydes, sugars, and sugar alcohols to acetic acid in the presence of oxygen, are of great economic importance [6]. In the food industry, they enable the production of vinegar, kombucha tea (Figure 1a), and nata de coco. Due to their high productivity and rapid biosynthesis, they are considered primary commercial BC-producing bacteria [7]. Two genera, *Komagataeibacter* and the recently described *Novacetimonas*, are characterized by their tolerance to low pH, efficient conversion of ethanol to acetic acid, and secretion of large amounts of BC [8,9]. Both genera occur in nature mainly as colonizers of fruits. The AAB species *Komagataeibacter europaeus*, *Komagataeibacter medellinensis*, *Komagataeibacter rhaeticus*, *Komagataeibacter xylinus*, and *Novacetimonas hansenii* are considered the best cellulose producers among bacteria and serve as model organisms for studying BC and its applications [10–12].

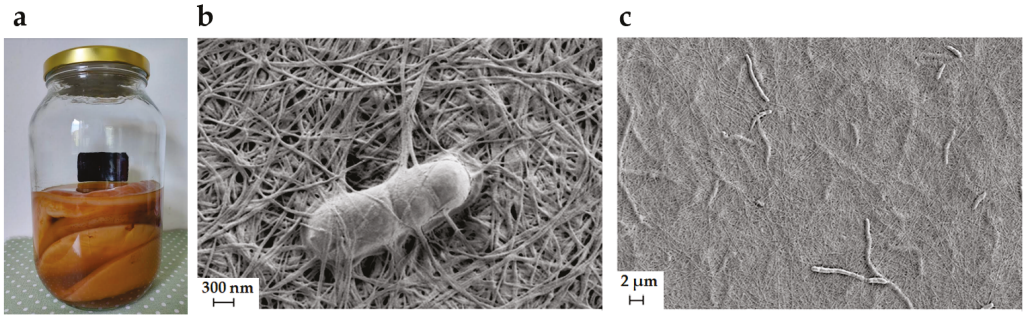

Figure 1. (**a**) Homemade kombucha tea with a visible mass of BC; (**b**,**c**) micrographs of *Komagataeibacter melomenusus* embedded in a cellulose network, taken with the scanning electron microscope.

Microbial cells surrounded by cellulose fibers (Figure 1b,c) form a biofilm. This defensive layer can protect organisms from lack of water and the associated desiccation, damage caused by ultraviolet radiation, unfavorable pH conditions, and the accumulation of toxic substances [1]. BC is not essential for survival, but it gives the microorganisms that produce it a competitive advantage by supporting attachment, adherence, and following colonization of substrates [3].

Although the molecular formula of bacterial and plant cellulose is identical—both are biopolymers composed of D-glucose monomers linked by β-1,4-glycosidic bonds—these two types of cellulose differ in their microfibrillar structure [13]. The *Komagataeibacter* can biosynthesize two allomorphic forms of cellulose (Figure 2a) with the dominant cellulose I allomorph, which is less stable and more crystalline, and the cellulose II allomorph, which is thermodynamically more stable and present in a smaller proportion [14].

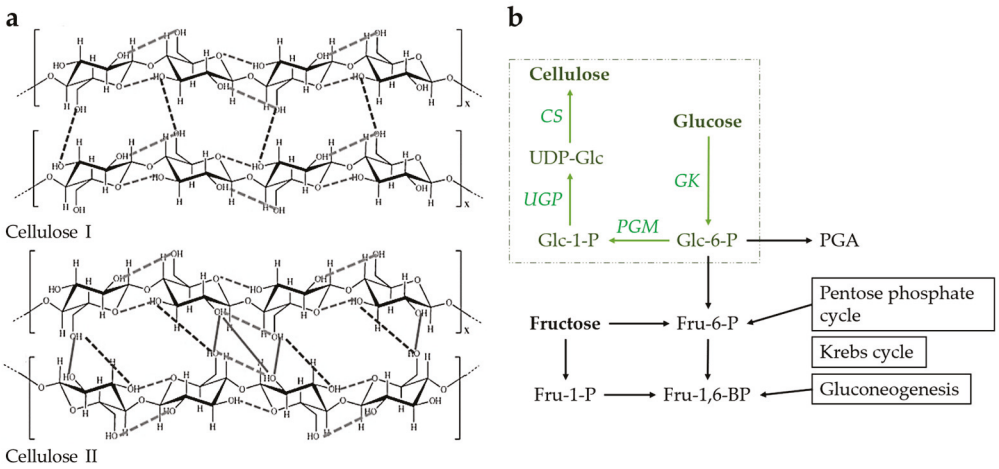

Figure 2. (**a**) Different allomorphs of cellulose: cellulose I (**top**), and cellulose II (**bottom**) (adapted from Ferro et al. [15] (CC BY)); (**b**) schematic representation of the biosynthetic BC pathway with steps from glucose to cellulose in green (GK—glucokinase, PGM—phosphoglucomutase, UGP—UDP-glucose pyrophosphorylase, CS—cellulose synthase).

The biosynthetic BC pathway consists of four crucial enzymatic steps when glucose molecules are a carbon source (Figure 2b). These include glucose phosphorylation to glucose-6-phosphate (Glc-6-P) by glucokinase, Glc-6-P isomerization to glucose-1-phosphate (Glc-1-P) by phosphoglucomutase, and UDP-glucose (UDP-Glc) synthesis by UDP-glucose pyrophosphorylase [13]. The resulting UDP-Glc is a monomer that polymeryzes into a series of β-1,4-glucan chains. The cell immediately secretes these chains into the external environment, where they first self-assemble into fibrils and then into larger cellulose fibers. BC biosynthesis and export are primarily controlled by the *bcsABCD* operon, which encodes four major proteins comprising the bulk of cellulose synthase. The BcsA protein catalyzes the polymerization of UDP-Glc units and enables allosteric regulation of BC synthesis by cyclic di-GMP. Together with the BcsB protein, it forms a pore in the cytoplasmic membrane. The periplasmic protein BcsC forms a β-barrel pore in the outer membrane through which the growing glucan chain enters the external environment. Another periplasmic protein called BcsD controls the correct orientation of the cellulose synthase complex. The molecular mechanisms described allow polymerization at up to 200,000 glucose molecules per second [16,17].

Cellulose nanofibers, typically 25–100 nm in diameter and several micrometers in length, intertwine in large numbers to form a structure known as a cellulose lattice. As new fibers accumulate, the cellulose network increases in volume and density, eventually forming a mat visible to the human eye—a so-called pellicle [16]. BC-producing bacteria can be grown in static or agitated cultures. In the first case, bacteria grow at the liquid–air interface, where a higher oxygen concentration allows high-quality aerobic growth, forming a pellicle (Figure 3a). In the second case, where oxygenated air is added directly to the liquid growth medium, the cellulose fibers form millimeter-scale pellets, spheres, or a fibrous suspension with irregular shape [18].

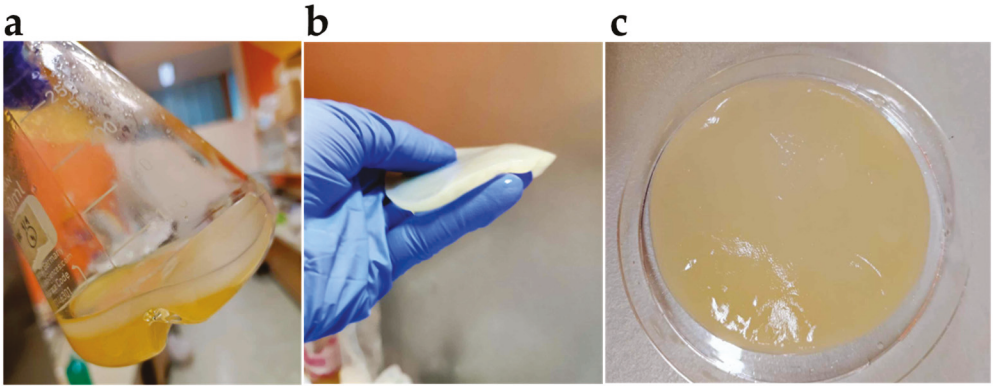

Figure 3. (**a**) Pellicle formed by *K. xylinus* in static culture; (**b**) bacterial pellicle—elastic and conformable, yet very robust material; (**c**) typical cellulose pellicle has a high water-holding capacity and possesses hydrogel-like properties.

Its unique physicochemical properties, which include a high degree of crystallinity, high tensile strength, excellent permeability, high water content, hydrophilicity, high porosity, large specific surface area, high elasticity, and conformability (Figure 3b), low density, high degree of polymerization, high purity, biocompatibility, and biodegradability, make BC an exciting platform for materials science [19].

The individual glucan chains are linked by van der Waals forces and intra- and intermolecular hydrogen bonds that form between the hydroxyl groups of the glucose monomers. This promotes the parallel stacking of cellulose molecules into crystalline nanofibers, which further assemble into cellulose nanofibrils. The strong molecular bonds contribute to a high degree of crystallinity and high tensile strength. A single BC nanofiber has a tensile strength of at least 2 GPa and Young's modulus of about 138 GPa. BC also has a high water-holding capacity due to the specific arrangement and large number of hydroxyl groups in the glucose molecules, enabling the cellulose fibers to bind many water molecules. Hydrated BC has a very high water content (>98% w/v) and exhibits hydrogel-like properties (Figure 3c) [2,14].

The main advantage of BC over plant-derived cellulose is its high purity, as BC-producing bacteria do not co-produce other substances (e.g., hemicellulose, lignin, and pectin) alongside cellulose. The absence of these heterologous polymers and other impurities makes BC biocompatible. Plant-derived cellulose requires pre-processing, an energy-intensive and environmentally harmful purification process that involves numerous mechanical and chemical separation steps. BC produced by fermentation usually contains only traces of impurities (mainly microbial cells and their components, or the culture medium components), which significantly simplifies the purification process. In most cases, BC is purified using alkalis such as potassium hydroxide and sodium hydroxide or organic acids such as acetic acid, or it is repeatedly washed in a reverse osmosis process [13].

The market demand for BC is steadily increasing, and its commercialization is exponentially growing due to the wide range of BC applications in various sectors. In 2023, the global market for BC was estimated to be USD 480.1 million, and the expected market value is projected to reach USD 608.71 million by 2025 and USD 771.76 million by 2027, with a compound annual growth rate (CAGR) of 12.6% from 2019 through 2027 [20]. Despite BC production being capital-intensive, the research focus is on new, optimized production approaches aimed at cost reduction. These approaches include, but are not limited to, investigating new, low-cost media, discovering new bacterial strains, and utilizing synthetic biology tools to enhance production yields or achieve new properties.

2.2. Growth Media for Bacterial Cellulose Production

Human civilization has relied on various natural materials for thousands of years. In recent times, known as the age of advanced materials, society has been striving toward green technologies that significantly emphasize the circular economy—a new driver of innovation. Due to the emerging trend of more sustainable production processes, cost-effective yet efficient growth media are at the forefront.

BC is industrially exciting because it can be obtained quickly, inexpensively, and sustainably. Although the glucose in the growth medium for bacteria cultivation is the preferred carbon source for BC synthesis, other sugars, such as xylose, lactose, galactose, mannose, arabinose, fructose, and sucrose present in different agricultural and food waste materials, and industrial byproducts can also be used [21–24]. The efficiency of BC production on carbon sources other than glucose is different, but also, in the case of being lower, it is still attractive due to low or zero media prices and companies' increasing awareness of the circular economy importance.

The most widely used synthetic complex growth medium for BC production is the Hestrin–Schramm (HS) medium, with glucose as a carbon source for bacterial growth and BC synthesis [25]. The BC production yield in this medium and media prepared from agricultural and industrial organic waste materials depends on the bacterial strain, the vessel used for bacteria cultivation, oxygen supply, pH of the medium, and cultivation time [2]. Depending on these parameters, the cellulose pellicle forms within a few (3–14) days and in high yields, reaching up to 10 g of dry weight per liter [22,23,26,27].

During the last 10 years, many research studies have been performed using different natural raw organic materials for BC production. The preferred natural organic material for BC production varies among countries depending on the climate suitable for growing fruits and grain types. Very appropriate raw organic waste materials are fruits since they contain high sugar content, but also since the medium can be easily prepared in a blender with the addition of some water followed by filtering and centrifugation. Jozala et al. [28] achieved an extremely high 60 g/L dry BC yield after 4 days of *Komagataeibacter xylinus* cultivation in a medium prepared from rotten fruits composed of plums, green grapes, pineapples, and apples. From industrial residues of the cashew apple juice processing, the BC was, after centrifugation, also directly produced at 3.1 g/L dry BC yield in 12 days of static cultivation [29]. When using industrial beverage waste material, such as fruit peels and pomace, more harsh conditions are necessary for preparing growth media, including enzymatic treatment or acid hydrolysis. Fan et al. [26] reported producing a 5.7 g/L dry BC yield after 9 days in medium from enzymatically treated citrus peel and pomace. Potato peel waste acid hydrolysate was also successfully used for BC production at 4.7 g/L dry yield after 6 days of cultivation [30]. Recently, Gorgieva et al. [23] prepared BC membranes using a novel species, *Komagataeibacter melomenusus*, in grape pomace hydrolysate in only 4 days with a 1.2 g/L dry BC yield. Also, the liquid industrial waste byproducts can be used directly, without any treatment, and as a sole medium without any supplements, such as cheese whey [31], thin stillage, which is a liquid byproduct that remains after microbial ethanol fermentation of carbohydrates by yeast and subsequent distillation of the fermented mash [22], and olive oil mill wastewater [32]. Other liquid waste materials, such as corn-steep liquor and laundry effluent for jeans processing, were also used directly but just as a replacement for a part of the synthetic HS medium [33]. The BC can also be produced in hot-water-extracted wood, a residual material originating from pulp mills and lignocellulosic biorefineries, although at only 0.15 g/L dry BC yield after 10 days of static cultivation [21], or glucose obtained from algae hydrolysate at 1.1 g/L dry BC yield after 7 days of static cultivation [27]. Tobacco waste extract was, after nicotine removal, also successfully used for BC production at 2.27 g/L dry BC yield after 7 days of static cultivation [24].

2.3. Application Niches of Bacterial Cellulose

BC possesses many applicable properties, making this nanomaterial attractive in diverse areas, from the food and paper industry to the cosmetic industry and medical engineering (Figure 4). In general, the commercial niche of BC is guided by the shape and macro-appearance of the produced material, which depends on the fermentation method. The agitated fermentation ends up with hydrocolloid-like material used in the food industry as a thickener or suspending agent. In contrast, the pellicle-like material obtained at static cultivation is useful in the medical, pharmaceutical, and cosmetic fields and packaging [34].

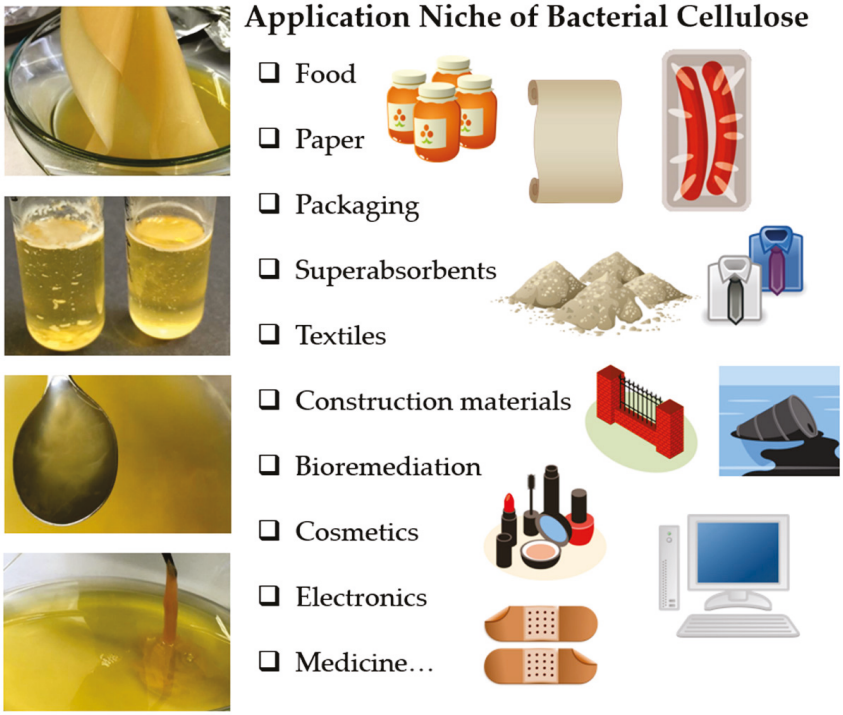

Figure 4. BC's remarkably wide application niche, stemming from its unique and convenient physicochemical properties, encompasses diverse areas, including the food industry, superabsorbent-polymers market, production of sustainable microbial textiles, and biomedical engineering.

2.3.1. Application of Bacterial Cellulose in Food and Cosmetics

BC has immense potential in the food industry due to its ultra-pure, low-calorie nature and ability to hold large amounts of water. As a naturally occurring food rich in dietary fiber, it benefits the consumer's health by reducing the risk of developing chronic diseases such as diabetes, obesity, and cardiovascular diseases [35]. In recognition of its safety, The United States Food and Drug Administration (FDA) granted BC the status of "generally recognized as safe" (GRAS) in the year 1992, enabling numerous FDA-approved products to use its convenient material properties [36].

Unprocessed BC is tasteless and has a rigid structure, but it can be softened by treatment with alginate, calcium chloride, or sugar alcohols. Due to having excellent water-holding properties and not compromising structural integrity, BC is often added to processed foods to help maintain their original properties for extended periods. With its gelling, thickening, stabilizing, suspending, and emulsifying ability, cellulose is a suitable candidate for various food products such as pastries, salads, and yogurts. A significant area of the food industry is diet-food production, where BC is frequently included as a quality, low-calorie substitute for fats (Figure 5a) [35]. Recent toxicological experiments in mice related to acute, subacute, and subchronic oral toxicity assays after consumption of BC demonstrated the absence of reproductive toxicity, embryotoxicity, teratogenicity, and genotoxicity effects [37]. Another comprehensive review on the toxicology and dietetic

role of BC when tested on animals and in vitro [38] also showed that BC is not toxic after ingestion, it is not carcinogenic, tumor-promoting, pyrogenic, or a developmental or reproductive toxicant and thus it is not expected to pose any adverse side effects when used in human foods.

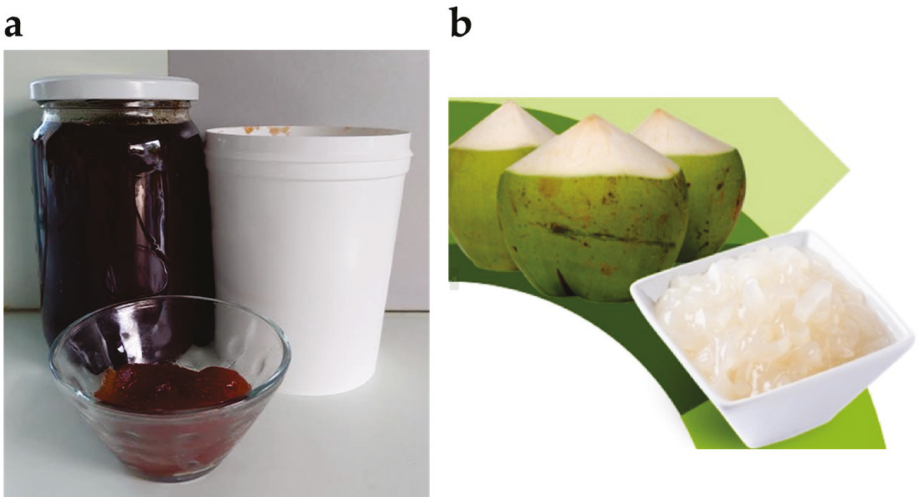

Figure 5. (**a**) Because of its low-calorie properties, BC is often a fat substitute in meat or bulking agent in jam; (**b**) coconut fruits and gelatinous cubs of nata de coco—a sweet Asian dessert based on BC (adapted from Rachtanapun et al. [39] (CC BY)).

The beginning of BC utilization in food industry dates back to the 1960–1970s in the Philippines, for producing healthy coconut gel, known as nata de coco (Figure 5b), where the BC is formed in the sugar syrup. This sweet dessert is commercially produced in several Asian countries, including Malaysia, Thailand, and Vietnam, as well as the Philippines. The production process of this cube-shaped delicacy involves the acetic acid bacterium *K. xylinus* metabolizing various carbohydrates, coconut water, and amino acids. Nata de coco is exploited in drinks, yogurts, pies, salads, and sausages, bringing a new flavour or texture to the formulations [40,41].

The use of various probiotics capable of enhancing gut microbiota and improving digestion has recently been rising. However, their usefulness is significantly limited by a short shelf life and instability. One possible solution to this problem is the encapsulation of probiotics with biocompatible and antibacterial materials, capable of enhancing the stability of probiotics over a long period, improving their resistance to adverse manufacturing conditions, and protecting them from the acidic conditions of the human digestive system. Due to its unique physicochemical properties, especially high crystallinity, biocompatibility, and non-toxicity, BC is highly suitable for encapsulating probiotics [35]. For instance, Fijałkowski et al. [42] showed that BC is a good carrier for immobilizing probiotic *Lactobacillus* spp., as it provides high-level protection of the microorganisms against the influence of gastric acid juice and bile salts, while Oliveira-Alcântara et al. [43] prepared BC/cashew gum films with probiotic *Bacillus coagulans* and/or prebiotic fructooligosaccharides and observed very good storage stability of probiotics. Aside from application in the gut, a recent study demonstrated the effectiveness of BC containing *Lactobacillus fermentum* and *Lactobacillus gasseri* against pathogens on skin [44]. Here, it strongly reduces the viability of *Staphylococcus aureus* and *Pseudomonas aeruginosa*, the most active pathogens in severe skin infections and chronic wounds and inhibits the proliferation of methicillin-resistant *S. aureus*.

BC also has significant potential in the cosmetic industry due to its valuable properties such as biocompatibility, water-holding capacity, adhesiveness, absorption, and release of substances. As a sustainable material, it could replace many non-biodegradable cosmetic ingredients. Among the commercially available cosmetic BC products, skin masks are particularly well-represented. Membranes made from BC nanofibers can incorporate a

wide range of cosmetic actives (for example, moisturizers and astringents), allowing these skin masks to not only hydrate and moisturize the skin but also serve as carriers for various active ingredients [45]. In addition to skin masks, cellulose makeup pads and BC-derived cosmetic additives are also available [2].

2.3.2. Application of Bacterial Cellulose as Advanced Material

Deforestation is a pressing issue in the conventional paper industry and has led to the intensive search for alternative methods of paper production using sustainable sources. Recyclable paper and paper pulp based on herbaceous (non-woody) plant fibers are becoming increasingly popular. The current challenge lies in the superior quality of traditionally produced paper compared to recycled paper, as the latter often fails to maintain the original physical and mechanical properties. One of the alternatives includes utilization of BC, which can enhance the mechanical properties of the materials it is merged with [46]. Therefore, it represents a suitable candidate for the sustainable production of high-quality paper pulp and paper [47]. Basta and El-Saied [48] demonstrated that adding modified BC, produced in the culture medium in the presence of glucose phosphate, to the wood pulp significantly improves kaolin retention, strength, and fire-resistance properties of the resulting functional paper. A recent mini review [49] provides a summary of specialized types of papers, containg BC as a modifier, such as conductive, fluorescent, and fire-resistant papers.

The inevitable consequence of the exponential growth of the human population is the persistent increase in consumption, followed by greater demand for products and services, as evidenced by the widespread use of plastic packaging. Petrochemically produced synthetic plastic has numerous adverse effects, particularly concerning its accumulation and incineration, leading to a growing focus on reducing and potentially eliminating such packaging in favor of biodegradable packaging materials. Plant-derived cellulose currently dominates in green packaging, which often relies at least partially on cellulose fibers. However, BC fibers offer a more reasonable alternative, as they are inherently ultra-pure and do not require pre-processing, resulting in lower production costs [50,51].

In their dry state, superabsorbent polymers can spontaneously absorb a volume of liquid twenty times their weight (a 2000% change in volume) while retaining their original identity. Currently, the majority of superabsorbents are produced from non-renewable and non-biodegradable polymers. This creates a significant market potential for biodegradable and natural polymers with high water-holding capacity, such as BC. Commercial superabsorbent polymers are found in baby diapers, adult incontinence products, and female hygiene products and are used in agriculture for the controlled release of fertilizers [35,52].

Due to new environmental policies, sustainable post-petroleum synthetic textiles originating from bacteria and fungi are gaining importance. The textile and leather industries are among major environmental polluters—agricultural production and industrial processing contribute to greenhouse gas emissions, and tanning and dyeing contaminate water. At the same time, synthetic fibers gradually break down into microplastic particles. Natural biomaterials, such as hair and skin, use their cells to produce pigments, thus sustainably coloring the material. In contrast, the analogous process of industrial textile dyeing (Figure 6a,b) requires a series of chemical reactions and has a significant environmental impact. Alternative dyeing methods must be explored to achieve fully sustainable green textiles, including BC-derived ones. For instance, self-dyeing BC produced by a strain of genetically engineered acetic acid bacteria that synthesize melanin due to recombinant tyrosinase expression holds excellent potential [53].

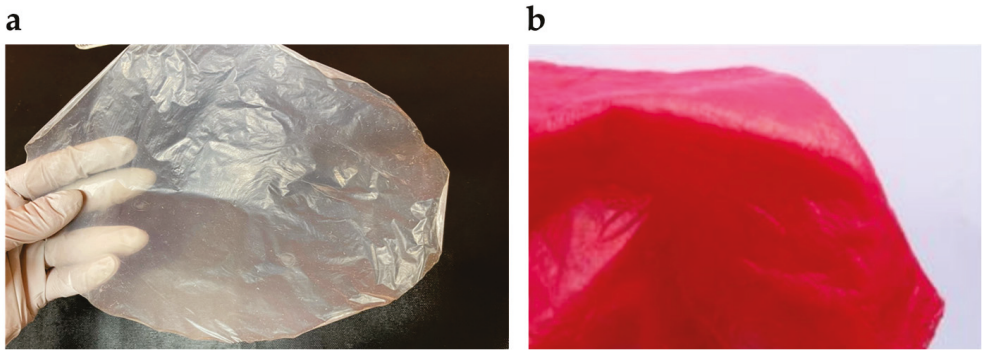

Figure 6. (**a**) As dried BC membranes are inherently beige, the dyeing process is an essential yet often ecologically damaging step in BC textile production; (**b**) a BC composite dyed with Procion Red H-E3N reactive dye (adapted from Fernandes et al. [54] (CC BY)).

There is a growing demand for sustainable construction materials with multifunctional properties. Nanoparticles have been popular for several decades for enhancing cement hydration, serving as reinforcement, and densifying microstructures, leading to reduced porosity and increased mechanical strength [55,56]. Green, non-toxic, and multifunctional nanocellulose materials hold a special place within the class of nanoparticles. Among them, plant-based cellulose nanofibers are widely known. Additionally, bacteria-derived cellulose, produced through uncomplicated fermentation and with a more cost-effective production process, represents a favorable alternative for obtaining bioconcrete [57].

Bioremediation, specifically microbial remediation, involves using various microorganisms to transform pollutants into simpler molecules such as carbon dioxide and water. It is a practical approach for containing and detoxifying different forms of contamination. There are several bioremediation applications of BC: modified BC adsorbs specific contaminants [58], cellulose-based ultrafiltration membranes filter polluted liquids [59], and composites of BC and other materials degrade pollutants [60].

In consumer electronics, many prominent developers and manufacturers follow a marketing strategy focusing on developing sustainable and flexible devices. BC is being used to achieve sustainability and recyclability, as it is a quality natural biopolymer with outstanding biodegradability, mechanical performance, piezoelectricity, and dielectricity [35,61]. One of the notable processing techniques is the carbonization of BC, where the entire cellulose structure is transformed into a highly conductive carbon network, resulting in carbonized BC (CBC) [62]. Fully or at least partially BC-based devices and their components include electronic paper, transistors, flexible electrodes, organic light-emitting diodes (OLEDs), digital displays, battery separators, and acoustic diaphragms for headphones and speakers [63]. BC-made commercial products also include biodegradable deformation sensors, essential sensor devices in virtual and augmented reality recreational markets, and gaming. Several major electronics companies, including Acer, Audioquest, Creative, Klipsch, Panasonic, and Sony, sell headphones equipped with BC-based diaphragms in the consumer electronics market [35].

An emerging field concerning BC production, engineered living materials (ELMs), has recently evolved. Natural biomaterials possess various unique and valuable properties that interest materials science, and organisms that produce such materials can transform simple raw materials to form large and complex natural biomaterials. However, their properties are restricted to the evolved set of genetic information. The emerging field of ELMs addresses these limitations, dedicated to constructing BC-based engineered living materials as well [64]. ELMs, which lie at the intersection of microbiology, materials science, and synthetic biology, utilize molecular biology tools to reprogram living cells at the DNA molecule level [53]. Broadly, ELMs can be defined as dynamic and responsive materials with programmable properties, where genetically engineered cells comprise an integral part [36]. The living biological entities that shape ELMs are responsible for their fabrication,

assembly, and functionalization [14]. The foremost goal is to create new or enhanced biomaterials tailored for specific applications in textile, fashion, and later also in other industries.

2.3.3. Application of Bacterial Cellulose in Medicine

Due to their useful physicochemical properties such as exceptional safety, high permeability, high water-holding capacity, excellent flexibility, pronounced biocompatibility, and biodegradability, BC-made dressings and bandages have great potential in wound and burn treatment [65] (Figure 7a,b). High-quality materials used for wound recovery are known to be non-toxic, non-allergenic, maintain a moist wound environment, absorb exudates, enhance re-epithelization, exhibit high porosity and gas permeability, and are suitable for functionalization with antibiotics, as well as convenient for drug delivery [13]. Since wound recovery involves complex interactions among various cell types, soluble compounds and extracellular matrix components, the candidate material should be an appropriate interface to facilitate this process [66] (Figure 7c).

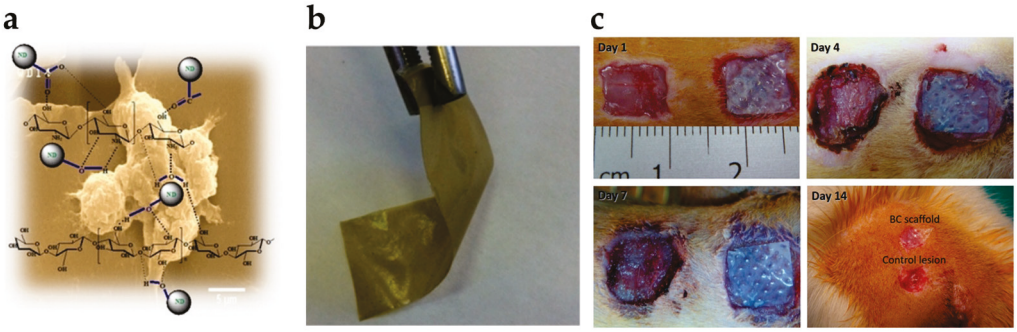

Figure 7. (**a**,**b**) Chitosan/BC composite films with diamond nanoparticles are among numerous BC-derived platforms for wound dressings (reproduced from Ostadhossein et al. [67] (CC BY)); (**c**) comparison of wound recovery on a rat model without (**left side**) or with (**right side**) BC bioscaffold covering (reproduced from Cherng et al. [68] (CC BY)).

The still predominant clinical approach, in which wounds are dressed with antibiotic-containing dressings, can be expensive, ineffective, and may contribute to the development of bacterial resistance to antibiotics [65]. Alternatively, BC, which does not possess intrinsic antimicrobial properties in its natural state, can be functionalized with antimicrobial substances [69]. Some examples are therapeutic metals and antibacterial nanomaterials (e.g., copper, silver, zinc, zinc oxide, titanium dioxide, and montmorillonite), natural polymers (e.g., chitosan), synthetic polymers (e.g., polyethyleneimine), and different antibiotics (e.g., amoxicillin).

In combination with other materials, BC is suitable for controlled drug delivery. Graphene nanoparticles are appropriate drug carriers capable of preventing the premature release of active substances. Since they tend to aggregate in aqueous solutions, embedding them in a BC network may offer a proper solution [70]. As a material enabling prolonged drug release, BC is a convenient carrier for therapeutic agents in cancer treatment. BC allows for controlled and localized chemotherapy, resulting in a higher drug concentration at the tumor site while minimizing exposure to surrounding tissues and reducing unwanted side effects [71,72]. Modified BC can trap cancer cells by implanting cellulose membranes functionalized with chemoattractants at the site of tumor removal [73].

Using various BC composites as scaffolds in tissue engineering is becoming increasingly common. Some pioneering ideas include 3D porous microspheres made from BC and collagen [74], BC with plant-derived cellulose nanocrystals and hydroxyapatite added in situ [75], and BC incorporated with the bone phosphoprotein osteopontin [76]. Gorgieva and Hribernik [77] proposed a combination of BC with microstructured gelatin to develop scaffolding membrane for guided tissue regeneration. The biocompatibility, fine archi-

tecture of cellulose fibers, and excellent tensile strength of BC enable the production of artificial blood vessels. Furthermore, due to its ability to promote neovascularization, BC is suitable for stimulating the growth of new native blood vessels [78].

3. Strategies for Improvement of Bacterial Cellulose Production and Modification

3.1. Conventional Methods for Improvements of Bacterial Cellulose Production and Modification

Applications and commercialization of BC were initially significantly limited by low yields in laboratory fermenters and inefficient scale-up of the production process to an industrial scale, as economically justified yields were not achievable in industrial bioreactors [14]. Consequently, researchers dedicated several years of studies to optimizing bioprocess factors by modifying culturing strategies and conditions. They investigated the influence of essential medium components, carbon sources, various additives, temperature, pH, dissolved oxygen concentration, dimensions of laboratory vessels, and different fermentation techniques, focusing on static and agitated cultures (Figure 8) and bioreactors [79–84].

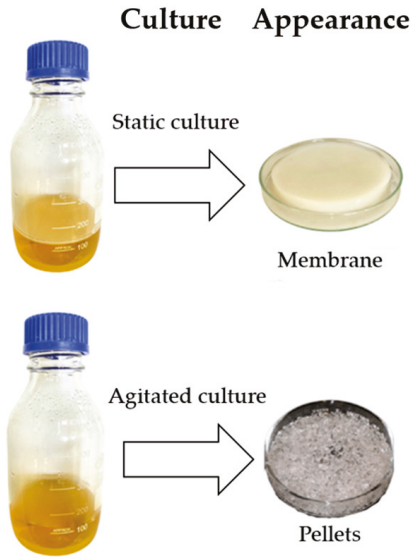

Figure 8. BC's final appearance depends on the fermentation technique, with static culture (**top**) resulting in BC membranes (pellicles) that form at the liquid–air interface and assume the shape of the laboratory vessel, and agitated culture (**bottom**) leading to the submerged formation of irregular BC pellets (adapted from de Amorim et al. [85] (CC BY)).

Static culture—the most popular strategy for producing BC, in which microorganisms form a cellulose pellicle at the liquid–air interface—is limited by long cultivation times. This drawback can be overcome by the agitation fermentation technique, where bacteria are incubated on a shaker, resulting in BC with a similar chemical structure. Although bacterial growth in agitated culture is higher than in static culture, shaking can lead to the occurrence of mutants in cellulose operons, which do not contribute to the final BC yield [14].

Researchers have attempted to improve the original medium to optimize cellulose production by adding a cheaper nitrogen source, such as corn steep liquor, incorporating various sulfates and phosphates, and removing organic acids [86,87]. The carbon source is one the most extensively studied components of the growth medium, as it significantly affects the BC yield. BC-producing bacteria vary in their ability to assimilate and utilize different carbon sources [14]. To enhance the BC yield, a wide range of primary metabolites have been tested, including various types of carbohydrates such as monosaccharides (e.g., D-xylose, D-xylulose, fructose, galactose, glucose), disaccharides (e.g., lactose, maltose, sucrose), oligosaccharides, organic acids, and sugar alcohols (e.g., ethanol, mannitol) [88–95].

Before the introduction of genetic engineering techniques in BC production, the artificial selection of strains was considered a relatively simple genetic intervention capable of influencing the production process. Various species of bacteria used in industrial BC production exhibit different yields depending on the growth medium and culturing conditions. They also differ in the properties of the final product, particularly in its purity and crystallinity. Artificial selection, combined with naturally occurring mutations, allowed researchers to identify the most successful strains with the highest product yield and quality for each species [7,96,97]. While such a non-targeted approach can be successful, it cannot gain the speed and precision of genetic engineering. Furthermore, it is unsuitable for introducing new functionalities into microorganisms since the necessary genes are commonly missing [12].

Like any natural or synthetic material, BC has limited usability, which can be expanded through various conventional functionalization methods. Based on the approach of modifying the material, three types of cellulose are distinguished: bacterial nanocellulose (BNC), cellulose nanocrystals (CNCs), and cellulose nanofibrils (CNFs). BNC is produced through a bottom-up approach by bacteria metabolizing low molecular weight carbohydrates [98]. Applying the top-down approach to BNC enables the production of CNCs and CNFs. CNCs are formed through treatment with chemicals, such as ionic liquids, lithium hydroxide, N,N dimethylacetamide/lithium chloride, N-methylmorpholine-N-oxides, and NaOH-urea/thiourea [99–103]. CNFs are obtained through mechanical processes, such as high-pressure homogenization and grinding combined with enzymatic pretreatments [104,105]. Particular challenges accompany the production of cellulose nanomaterials. The limited selection of suitable solvents leads to the use of toxic and hazardous chemicals, which pollute the environment and limit the recyclability and disposal of products. Meanwhile, mechanical processing methods may compromise the physical properties of the biopolymer.

Conventionally, without using genetic engineering methods, numerous composites can be produced where BC is combined with other materials. In principle, we can distinguish two different strategies. In the first strategy, the in situ strategy, various reinforcement materials are added directly into the growth medium and incorporated by microorganisms during the biosynthesis of BC. Commonly added substances capable of improving the functional properties of BC include agar [82], aloe vera [106], carboxymethyl cellulose [107], conductive polymers (polyaniline, PEDOT:PSS, polypyrrole) [108], graphene oxide [109], metal nanoparticles [110], multiwalled carbon nanotubes [111], poly-3-butyrate [112], and sodium alginate [113]. Some issues associated with this kind of strategy include the precipitation of added substances and the unsuccessful incorporation of reinforcement materials into the pellicle. In the second strategy, the ex situ strategy, physical absorption or hydrogen bond formation is employed to establish connections between additives and the cellulose matrix. Such nanocomposites are often developed by combining BC with carbon nanotubes, chitosan [114], collagen [115], conductive polymers [116], hyaluronic acid [117], hydroxyapatite [118], metal nanoparticles [119], metal oxides [120], and montmorillonite [121]. The use of these reinforcement materials enhances the mechanical, electrical, and antimicrobial properties of BC. The utility of this strategy is mainly restricted by the non-uniform size of additives and cellulose pores, as well as the hydrophilic nature of BC, which hinders interactions with hydrophobic reinforcement materials [14].

Gao et al. [122] showed the production of functional BC by *K. sucrofermentans* where instead of genetically engineering the microorganisms, they modified glucose into synthetic 6-carboxyfluorescein glucose (6-CF-Glc). The bacteria grown in the modified glucose medium synthesized a cellulose pellicle with unnatural green fluorescing capabilities (Figure 9). The fluorescence intensity was controlled by varying the concentration of 6-CF-Glc in the growth medium.

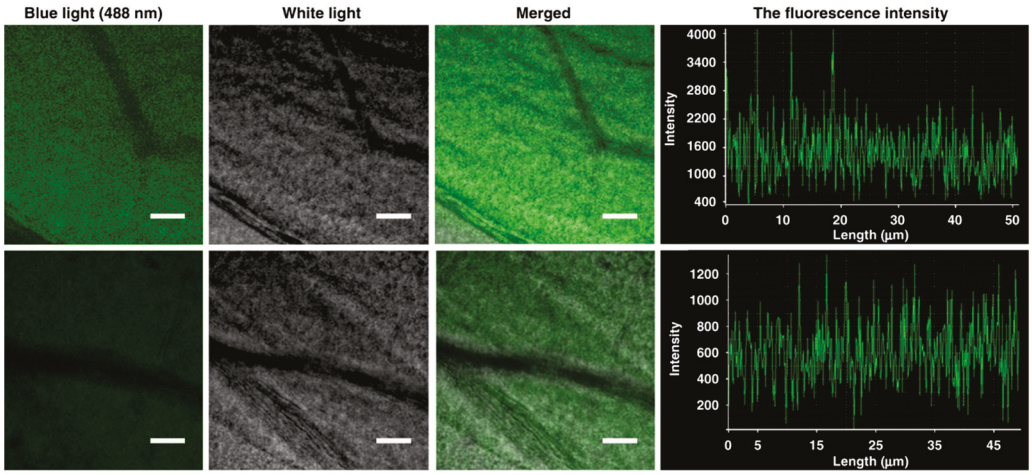

Figure 9. The fluorescence intensity of functional BC grown in the presence of 6-carboxyfluorescein glucose (6-CF-Glc) depends on the substrate concentration; a high concentration of 6-CF-Glc (**top**) and low concentration of 6-CF-Glc (**bottom**) with average fluorescence intensities of 1492 a.u. and 612 a.u., respectively (adapted from Gao et al. [122] (CC BY)).

3.2. Co-Culturing Bacteria for Improvements of Bacterial Cellulose Production and Functionality

Several examples exist of using the co-culture approach for BC production (Figure 10). In one of the early studies, *K. xylinus* and *Lactobacillus mali* were co-cultured in corn- steep liquor supplemented with sucrose [123]. The authors noted a 3-fold improvement in BC production compared to the monoculture of *K. xylinus*, due to cell–cell interactions and the exopolysaccharide produced by *L. mali*. BC made in *N. hansenii* and *E. coli* ATCC 700728 co-culture displayed superior mechanical properties [124]. In the co-culture of *N. hansenii* ATCC 23769 and *Lactococcus lactis* APJ3, a copolymer of BC and hyaluronic acid was successfully produced, showing improved water-holding capacity compared to regular cellulose pellicles [125]. Similarly, in the co-culture of *K. xylinus* and *Ralstonia eutropha*, a mechanically superior nanocomposite of BC and polyhydroxybutyrate was developed [126]. Gunduz et al. [127] expanded this approach by co-culturing *N. hansenii* ATCC 23769 with a consortium of microorganisms (e.g., *Lactobacillus casei*, *L. lactis*, *Rhodopseudomonas palustris*, and *S. cerevisiae*) that assists the display of multiple functionalities. They achieved a 40-fold increase in water-holding abilities compared to the monoculture of *K. xylinus*.

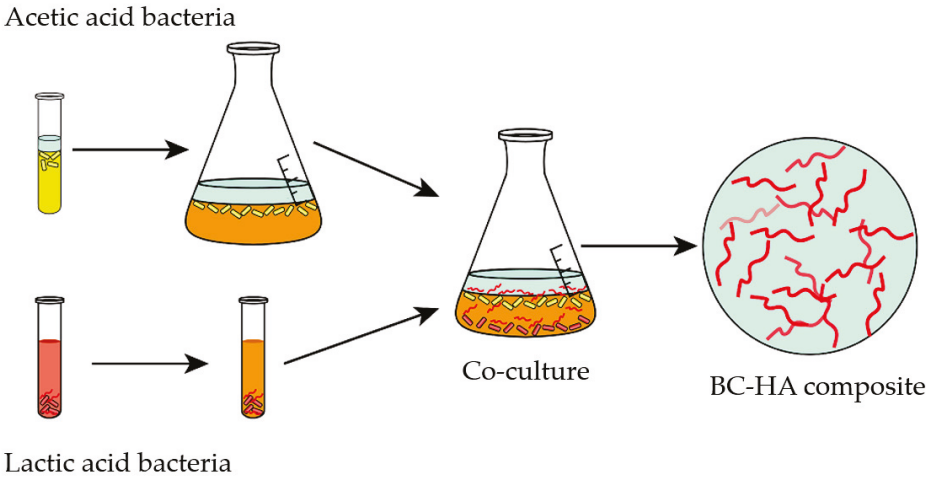

Figure 10. Schematic representation of co-culture approach for obtaining BC and hyaluronic acid (HA) composite (adapted from Brugnoli et al. [128] (CC BY)).

Taking a slightly different approach inspired by the symbiotic culture of bacteria and yeast (SCOBY) used for fermenting kombucha tea, Gilbert et al. [63] produced BC in a

co-culture of genetically modified yeast and a wild-type strain of *K. rhaeticus*. They focused on genetically modifying the yeast *S. cerevisiae*, a well-known model organism that can be genetically manipulated in ways not possible with the *Komagataeibacter* genus. The authors initially aimed to genetically engineer the yeast, known for its excellent protein secretion capabilities, to secrete proteins that would functionalize the developing cellulose pellicle. They tested this concept using β-lactam hydrolyzing enzyme TEM1 β-lactamase, and apparent enzymatic activity was detected in the pellicles produced in the co-culture containing both BC-producing bacteria and genetically modified yeast. This activity was preserved even after the functionalized BC was dried and rehydrated. Furthermore, they designed a yeast strain that modifies pellicles' physical properties. The microorganisms simultaneously secreted different cellulose-degrading enzymes, including β-glucosidase, cellobiohydrolases, endoglucanase, and lytic polysaccharide monooxygenases. They found that the BC production was not significantly reduced, but some of the pellicle's physical properties, especially its tensile strength and Young's modulus, were weakened. Co-culturing acetic acid bacteria and yeast was also used to investigate whether the living BC-based hybrid materials can sense and react. They designed a yeast biosensor system based on the synthetic transcription factor Z3EV and the reporter gene encoding the green fluorescent protein (GFP), whose transcription could be induced by the estrogen steroid hormone β-estradiol (BED). Since the cellulose pellicle grown in such co-culture displayed intense green fluorescence when exposed to externally applied BED, the authors concluded that the living BC-based hybrid materials can sense environmental stimuli and react correspondingly.

3.3. Genetic Engineering of Bacterial Cellulose Producing Strains

Although genetic engineering has been one of the critical tools in biotechnological research and industrial biotechnology since the 1980s, until recently, it was not extensively used for improving the production or modification of BC. This may be attributed to numerous non-genetic interventions that researchers and manufacturers employed effectively to enhance production, increase yield, modify the properties of the biopolymer, and introduce new functionalities to the resulting material. However, in the last two decades (Table 1), several examples proved that using genetic engineering of *Komagataeibacter* species can render additional improvements to BC production.

Table 1. Timeline of key examples intending to improve BC production and modification.

Year	Test Organism	Short Description	Reference
1999	*Acetobacter xylinum* subsp. *sucrofermentans* BPR 2001 (*K. sucrofermentans*)	Introducing the sucrose synthase gene enables sucrose metabolism and improves BC production	[129]
2004	*Acetobacter* ITDI 2.1 (*K. xylinus*)	Introducing the β-galactosidase-encoding gene (*lacZ*) enables lactose metabolism and improves BC production	[130]
2005	*G. xylinus* BPR 2001 (*K. sucrofermentans*)	Knocking out the glucose dehydrogenase-encoding gene (*gdh*) improves BC production	[131]
2006	*A. xylinum* BCRC 12334 (*K. xylinus*)	Expressing the *Vitreoscilla* hemoglobin gene (*vhb*) improves oxygen regulation, cell growth, and BC production	[132]
2006	*G. xylinus* st-60-12 (*K. xylinus*), *L. mali* JCM 1116	Co-culturing *K. xylinus* and *L. mali* improves BC production	[123]
2010	*G. xylinus* ATCC 10245 (*K. xylinus*)	Introducing the UDP-N-acetylglucosamine-synthesizing operon enables the production of BC/chitin copolymer with improved in vivo degradability	[133]
2014	*E. coli* XL1-Blue	Co-expressing cellulose synthase genes for proteins BcsA, BcsB, and diguanylate cyclase (DGC) enables the production of amorphous BC in *E. coli*	[134]

Table 1. *Cont.*

Year	Test Organism	Short Description	Reference
2015	*G. xylinus* AY201 (*K. xylinus*)	Introducing the curdlan-synthesizing gene (*crdS*) enables the production of BC/curdlan composite	[135]
2016	*K. rhaeticus* iGEM	• The first standardized genetic toolkit for *K. rhaeticus*, isolated from kombucha tea pellicle, is developed • An N-acyl-homoserine lactone (AHL) enables spatial patterning, as shown through red fluorescence (RFP) • An RNA-based silencing system repressing the UGPase-encoding gene (*galU*) stops BC production	[136]
2018	*E. coli* GM HMS174 (DE3), *E. coli* GM C41 (DE3)	Introducing cellulose synthase-encoding operon (*bcsABCD*) enables recombinant biosynthesis of BC in *E. coli*	[137]
2019	*K. xylinus* DSM 2325	Overexpressing two carbon metabolism genes (*pgi* and *gnd*) improves BC production	[138]
2019	*K. xylinus* DSM 2325	Introducing the phosphofructokinase-encoding gene (*pfkA*) establishes a glycolytic pathway, increases the level of intracellular ATP, enhances cell growth, and improves BC production	[139]
2019	*K. rhaeticus* iGEM	Co-culturing AHL-inducible and AHL-synthesizing cells enables the developing BC to initiate its red fluorescence	[140]
2019	*G. hansenii* ATCC 53582 (*N. hansenii*), *G. xylinus* ATCC 700178 (*K. xylinus*), *K. rhaeticus* iGEM	• The standardized genetic toolkit is expanded and used in several *Komagataeibacter* species • Employing CRISPR-mediated inhibition of two BC biosynthesis genes (*acsAB* and *acsD*) reduces the BC yield	[141]
2019	*K. sucrofermentans*	Adding 6-carboxyfluorescein glucose (6-CF-Glc) to the growth medium enables the production of BC with unnatural green fluorescing capabilities	[122]
2019	*K. hansenii* ATCC 23769 (*N. hansenii*)	Varying the expression of two motility genes (*motA* and *motB*) changes BC morphology	[142]
2019	*Enterobacter* sp. FY-07	Inducing the expression of the colanic acid-encoding operon (*wca*) improves BC water-holding capacity	[143]
2019	*G. hansenii* ATCC 23769 (*N. hansenii*), *E. coli* ATCC 700728	Co-culturing *N. hansenii* and *E. coli* enables the production of BC with improved mechanical properties	[124]
2019	*G. hansenii* ATCC 23769 (*N. hansenii*), *L. lactis* APJ3	Co-culturing *N. hansenii* and *L. lactis* enables the production of BC/hyaluronic acid copolymer	[125]
2019	*A. xylinum* ATCC 23769 (*N. hansenii*), *L. casei*, *L. lactis*, *S. cerevisiae*, *R. palustris*	Co-culturing *N. hansenii* and effective microorganism (EM) improves BC water-holding capacity	[127]
2020	*K. xylinus* CGMCC 2955	Varying the expression of the UGPase-encoding gene (*galU*) changes the crystallinity and porosity of BC	[144]
2021	*K. rhaeticus* iGEM, *S. cerevisiae*	• The genetically engineered yeast secretes proteins able to functionalize BC • The genetically engineered yeast secretes cellulose-degrading enzymes • A yeast-based biosensor system is designed, exhibiting green fluorescence when exposed to β-estradiol (BED)	[63]
2021	*G. xylinus* ATCC 700178 (*K. xylinus*), *R. eutropha* H16 (DSM-428)	Co-culturing *K. xylinus* and *R. eutropha* enables the production of mechanically superior BC/polyhydroxybutyrate nanocomposite	[126]

3.3.1. Conventional Gene Targeted Approaches for Modification of Bacterial Cellulose Production

Initially, genetic modifications of *Komagataeibacter* spp. were confined to plasmid vector backbones, such as pSA and pBBR122, and focused on adding or removing genes to enhance BC production [13]. The first more significant demonstration of genetic engineering in cellulose-producing bacteria was reported in a study from 1999, where a DNA sequence encoding the sucrose synthase of mung bean (*Vigna radiata*) was introduced into

K. sucrofermentans [129]. The genetically modified bacteria produced more BC than the wild-type strain when sucrose was present in the growth medium. Among the positive effects of the described genetic manipulation, which enabled acetic acid bacteria to metabolize sucrose, was increased BC yield and the possibility of using cheaper sucrose-based growth media.

An alternative method to improve BC yield using an inexpensive growth medium was developed by Battad-Bernardo et al. [130]. Their genetically modified bacteria could metabolize a low-cost lactose-based medium derived from whey. By inserting the *E. coli* β-galactosidase-encoding gene (*lacZ*) into *K. xylinus*, researchers achieved a 28-fold increase in BC production.

On the other hand, Chien et al. [132] aimed to enhance BC production by improving cells' oxygen utilization. They induced the expression of the *vhb* gene, which encodes *Vitreoscilla* hemoglobin, in *K. xylinus* BCRC 12334. As a result, the genetically engineered strain showed better oxygen regulation than the wild-type strain. The expression of the *vhb* gene led to 50% higher cell growth and 20% higher BC production when the bacteria were incubated on a shaker.

During BC production, the cell oxidizes glucose to gluconic acid, leading to acidification of the growth medium, which in turn slows down BC production. Shigematsu et al. [131] attempted to address this issue by knocking out the *gdh* gene, which encodes glucose dehydrogenase, the enzyme responsible for converting glucose to gluconic acid. The authors reported a 1.7-fold improvement in BC production in the genetically modified strain compared to its wild-type counterpart.

As part of an extensive study to improve BC production, Jang et al. [138] used data from the sequenced genome and metabolome analysis of *K. xylinus* to construct a genome-scale metabolic model. Initially, they overexpressed two carbon metabolism-connected genes, *pgi* (coding for glucose-6-phosphate isomerase), and *gnd* (coding for phosphogluconate dehydrogenase), originating from *E. coli* or *Corynebacterium glutamicum*, resulting in a 2-fold increase in BC yield. In their model, they discovered that the intracellular level of adenosine triphosphate (ATP) plays a critical role in determining the BC yield. The enzyme glucose-6-phosphate dehydrogenase, encoded by the *zwf* gene, acts as a branching point where the cellular mechanism decides whether to metabolize glucose or use it for biosynthetic reactions. Since the activity of this enzyme is significantly inhibited by high levels of intracellular ATP, an increase in intracellular ATP concentration redirects more glucose molecules toward cellulose synthesis reactions. To maximize the intracellular ATP level, Gwon et al. [139] used a plasmid containing the *pfkA* gene, which encodes phosphofructokinase, an enzyme critical for glycolysis absent in the genus *Komagataeibacter*. Heterologous expression of the *E. coli pfkA* gene established the glycolytic pathway in *K. xylinus* (where glucose is usually metabolized via the alternative pentose phosphate pathway), resulting in a four-fold increase in intracellular ATP concentration, higher growth, and improved BC production.

In another significant study, Yadav et al. [133] introduced a *bla* promoter-controlled operon consisting of three genes from *Candida albicans* into *K. xylinus*, thereby altering the flow of cellular metabolites during the BC biosynthesis. This genetic intervention enabled the incorporation of the chitin monomer, activated cytoplasmic UDP-N-acetylglucosamine (UDP-GlcNAc), into the glucan chains alongside UDP-Glc. When both glucose and N-acetylglucosamine were available in the growth medium, the cellulose synthase of the genetically modified strain used UDP-Glc and UDP-GlcNAc to synthesize a copolymer of cellulose and chitin (Figure 11). The resulting cellulose/chitin copolymer exhibited improved in vivo degradability due to the susceptibility of chitin to degradation by enzymes in animal lysosomes. The authors also found that partial or complete glucose replacement with GlcNAc significantly reduced the final cellulose production.

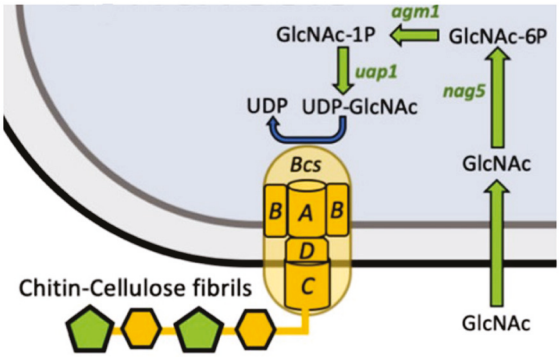

Figure 11. Schematic representation of cellulose/chitin copolymer production in genetically modified strain of *K. xylinus* expressing operon of three genes from *C. albicans* (GlcNAc—N-acetylglucosamine, UDP-GlcNAc–UDP-N-acetylglucosamine) (adapted from Singh et al. [12] (CC BY)).

The properties of produced BC were also investigated by Jacek et al. [142], who studied how the motility genes *motA* and *motB* influence the morphology of the cellulose pellicle in *N. hansenii*. Overexpression of the two genes resulted in a loosening of the intramembrane structure and fiber thickening. In contrast, disrupting the same genes, causing reduced mobility, led to a denser and more compact BC with improved mechanical properties.

Liu et al. [143] focused on improving another fundamental physicochemical property of BC, which is its water-holding capacity. Working on *Enterobacter* sp. FY-07, they induced the expression of the *wca* operon, carrying the genetic code for colanic acid, a water-soluble polysaccharide. By varying the concentration of the inducer, cellulose hydrogels differing in crystallinity, rheological properties, and water-holding capacity were developed. Their water-holding capacity was 1.7 times higher than that of the pellicle produced by the wild-type strain.

3.3.2. Standardized Genetic Tools for Bacterial Cellulose Production with Advanced Characteristics

Florea et al. [136] were the first to develop a standardized genetic toolkit (Figure 12) for BC-producing bacteria, specifically for the *K. rhaeticus* iGEM strain isolated from a kombucha tea pellicle. Their study selected five replicative plasmid backbones, including pSEVA321, pSEVA331, pSEVA351, pBAV1K-T5-sfGFP, and pBla-Vhb-122. Their genetic toolkit also included reporter genes encoding various fluorescent proteins, terminator sequences, synthetic promoters of different strengths, and two types of regulated promoters. The inducible promoters were regulated by transcription factors, chemically inducible with anhydrotetracycline, which is an antibiotic analog, or N-acyl-homoserine lactone (AHL), a quorum sensing molecule involved in intercellular communication. They designed their genetic toolkit to a standardized cloning format named BioBricks, which allows for quick assembly of variously combined modular DNA parts in *E. coli* plasmids and subsequent introduction into *K. rhaeticus*. To demonstrate the usefulness of the new standardized genetic toolkit, the authors genetically engineered bacteria to respond to different concentrations of AHL. Afterward, they induced the production of red fluorescence only on one side of the developing pellicle or only in its newest layers, thus illustrating that spatial patterning is achievable with their tools. Furthermore, they replaced the module for red fluorescence with another one that expressed a synthetic RNA-based silencing system designed to repress the chromosomal gene for the enzyme UDP-glucose pyrophosphorylase, which is crucial for BC synthesis. As a result of this genetic intervention, they obtained a genetically modified bacterium that stopped producing a BC pellicle when a sufficient concentration of AHL was added to the growth medium.

In the following study [140], the same group of researchers successfully demonstrated, through an innovative experiment, that the induction of gene expression in plasmids of the aforementioned bacterial cells can be controlled by other genetically modified cells grown in the same co-culture. The genetically engineered strain producing a red fluorescent protein

(RFP) when induced with AHL, was combined with another recombinant strain capable of constitutively expressing the gene for the AHL-synthesizing LuxI enzyme. The new strain, consisting of the so-called sender cells, secreted AHL molecules into the medium where co-culture was grown. When these molecules reached a sufficient concentration and were near the so-called receiver cells, controlled by AHL, they initiated the production of RFP (Figure 13). Through this experiment, the researchers illustrated that the two genetically modified cells coexisted in co-culture while producing BC capable of creating red fluorescence. Perhaps more significantly, this study revealed that it is possible to grow materials that autonomously detect borders between different populations of genetically modified cells and induce gene expression only at those specific locations.

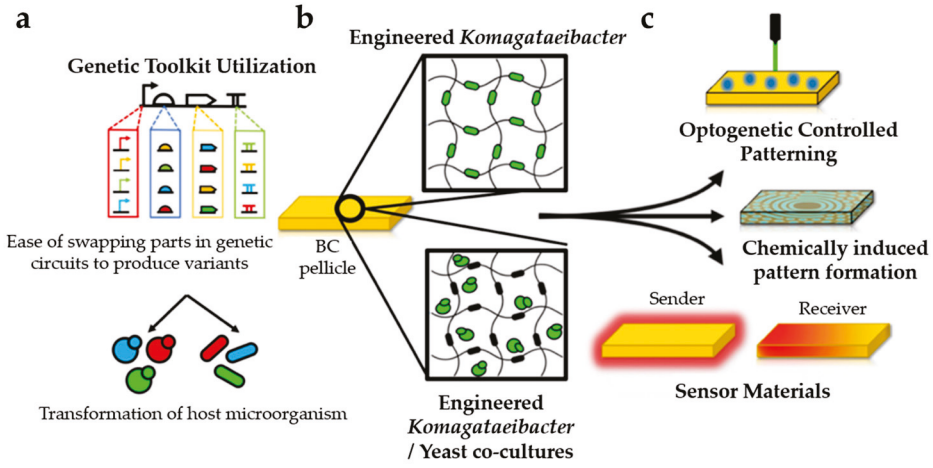

Figure 12. Overview of standard synthetic biology methods that are utilized for the development of living and functional BC-based hybrid materials; (**a**) synthetic libraries comprise modular DNA parts (including promoters, ribosome-binding sites (RBSs), coding sequences (CDSs), and terminators) which can be joined together into gene constructs for transformation into a host microorganism, such as yeast (circles) or *Komagataeibacter* (rods); (**b**) genetically modified cells secrete cellulose nanofibers into their surroundings and gradually form a BC pellicle within which they are contained; (**c**) BC pellicle encompasses living genetically modified cells that can sense and react as a response to selected externally applied signals, such as light, chemicals, and diffusible signaling molecules (adapted from Singh et al. [12] (CC BY)).

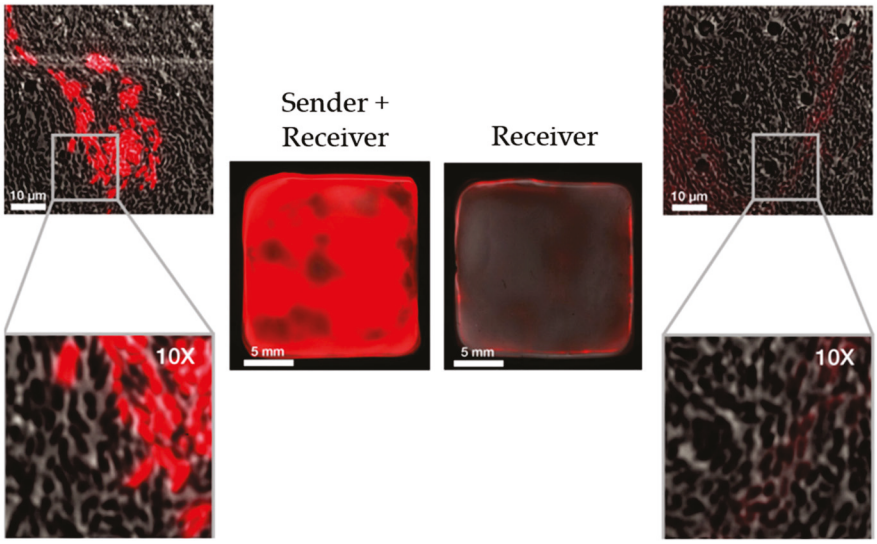

Figure 13. Comparison of red fluorescence response in the co-culture of sender and receiver cells (**left**) and monoculture of receiver cells (**right**) (adapted from Walker et al. [140] (CC BY)).

Teh et al. [141] extended the existing genetic toolkit by introducing several additional modular parts, such as new constitutive promoters and terminator sequences. They incorporated an arabinose-inducible promoter (P_{BAD}) that reacts to high sugar concentrations (4%). Through different experiments, they demonstrated that the standardized genetic toolkit was efficient not only for *K. rhaeticus* but also for various strains of *K. xylinus* and *N. hansenii*. They also described programmable regulation of gene expression using the Clustered Regularly Interspaced Short Palindromic Repeats (CRISPR) approach. By employing CRISPR-mediated inhibition of two genes involved in BC synthesis, namely *acsAB* and *acsD*, they successfully reduced the BC yield by 15% in the first case and 5% in the second case.

In a similar experiment, another group used CRISPR-mediated inhibition to regulate the UGPase-encoding *galU* gene expression in *K. xylinus* CGMCC 2955. They found that changing the gene's expression could influence the crystallinity and porosity of the BC pellicle. When repressing this gene, the porosity of BC increased by 0.5-fold. In contrast, the crystallinity of the cellulose network only increased to a certain extent with increasing expression (when the *galU* expression was 30 times higher than in the control group, the crystallinity started to decrease) [144].

The promising opportunities of genetic toolkits extend to BC-composite production where bacteria synthesize another polymer alongside cellulose. Fang et al. [135] demonstrated the biosynthesis of such composites by inserting the curdlan-synthesizing gene (*crdS*) from *Agrobacterium* into *K. xylinus* AY201. The genetically modified bacteria co-produced cellulose and curdlan with minimal changes in the crystallinity of the resulting composite. However, due to the variable pore size, the surface properties of the composite were slightly altered.

To accelerate BC production and make it more cost-effective, researchers came up with the idea of transferring the ability to biosynthesize the cellulose pellicle, which is characteristic of the *Komagataeibacer* genus, to better-studied model organisms with advanced genetic toolkits [13]. Although successful reconstitution of cellulose synthase in *E. coli* was achieved through the heterologous co-expression of genes for proteins BcsA, BcsB, and diguanylate cyclase, the genetically modified bacteria produced amorphous cellulose, highlighting the significance of genes responsible for export and crystallization, namely genes for proteins BcsC and BcsD [134]. Buldum et al. [137] took it further by introducing the entire *bcsABCD* operon into *E. coli*, resulting in the recombinant biosynthesis of cellulose with an exceptional fiber structure measuring from 10 to 20 μm in diameter.

4. Conclusions and Perspectives

This review highlights the remarkable potential of BC as an ultrafine nanomaterial comprised of versatile macromolecules with wide-ranging applications. The promising trajectory of BC research offers exciting perspectives for numerous industries and scientific domains. BC's versatile properties are poised to revolutionize medicine, with potential applications in tissue engineering, wound dressings, and targeted drug-delivery systems. Pharmaceutical advancements may harness BC's encapsulation capabilities to improve drug stability and bioavailability. Additionally, BC shows great potential in cosmetology, offering opportunities for enhanced skincare products, hair treatments, and wound-healing materials. In electronics and biotechnology, the integration of BC promises the development of flexible and biocompatible materials, facilitating the creation of innovative electronic devices, biosensors, and bioelectronics.

Using synthetic biology tools to genetically engineer BC-producing bacteria introduces a new era of living biomaterials with tailored functionalities, unlocking further possibilities for advanced bioproducts. While these prospects are promising, scaling up BC production remains a challenge that requires continued research to optimize fermentation processes, refine production techniques, and explore sustainable substrates.

By embracing sustainable approaches and employing synthetic biology, BC's transformative potential can be harnessed across various applications, paving the way for

groundbreaking developments in biomaterials and biotechnology. Collaborative efforts across disciplines will be crucial in fully realizing the applications of BC and shaping a more sustainable and innovative future.

Author Contributions: Conceptualization, V.P., S.G. and J.T.; writing—original draft preparation, V.P.; writing—review and editing, V.P., S.G. and J.T.; funding acquisition, S.G. and J.T. All authors have read and agreed to the published version of the manuscript.

Funding: This research was funded by the Slovenian Research and Innovation Agency through research programs P2-0006, P2-0118 and research project J2-2487.

Institutional Review Board Statement: Not applicable.

Data Availability Statement: Data sharing not applicable.

Acknowledgments: We acknowledge Urška Jančič, Bernarda Karničnik, Kim Fijok, and Eva Cepec from the University of Maribor for providing Figure 1b,c, Figures 3 and 4 (left panel), and Figure 6a, respectively.

Conflicts of Interest: The authors declare no conflict of interest.

References

1. Gullo, M.; La China, S.; Falcone, P.M.; Giudici, P. Biotechnological production of cellulose by acetic acid bacteria: Current state and perspectives. *Appl. Microbiol. Biotechnol.* **2018**, *102*, 6885–6898. [CrossRef] [PubMed]
2. Gorgieva, S.; Trček, J. Bacterial cellulose: Production, modification and perspectives in biomedical applications. *Nanomaterials* **2019**, *9*, 1352. [CrossRef] [PubMed]
3. Römling, U.; Galperin, M.Y. Bacterial cellulose biosynthesis: Diversity of operons, subunits, products, and functions. *Trends Microbiol.* **2015**, *23*, 545–557. [CrossRef]
4. Marič, L.; Cleenwerck, I.; Accetto, T.; Vandamme, P.; Trček, J. Description of *Komagataeibacter melaceti* sp. nov. and *Komagataeibacter melomenusus* sp. nov. Isolated from Apple Cider Vinegar. *Microorganisms* **2020**, *8*, 1178. [CrossRef]
5. La China, S.; Bezzecchi, A.; Moya, F.; Petroni, G.; Di Gregorio, S.; Gullo, M. Genome sequencing and phylogenetic analysis of K1G4: A new *Komagataeibacter* strain producing bacterial cellulose from different carbon sources. *Biotechnol. Lett.* **2020**, *42*, 807–818. [CrossRef] [PubMed]
6. Adachi, O.; Moonmangmee, D.; Toyama, H.; Yamada, M.; Shinagawa, E.; Matsushita, K. New developments in oxidative fermentation. *Appl. Microbiol. Biotechnol.* **2003**, *60*, 643–653. [CrossRef] [PubMed]
7. Ryngajłło, M.; Kubiak, K.; Jędrzejczak-Krzepkowska, M.; Jacek, P.; Bielecki, S. Comparative genomics of the *Komagataeibacter* strains—Efficient bionanocellulose producers. *Microbiologyopen* **2019**, *8*, e731. [CrossRef]
8. Brandão, P.R.; Crespo, M.T.B.; Nascimento, F.X. Phylogenomic and comparative analyses support the reclassification of several *Komagataeibacter* species as novel members of the *Novacetimonas* gen. nov. and bring new insights into the evolution of cellulose synthase genes. *Int. J. Syst. Evol. Microbiol.* **2022**, *72*, 005252. [CrossRef]
9. Trček, J.; Mira, N.P.; Jarboe, L.R. Adaptation and tolerance of bacteria against acetic acid. *Appl. Microbiol. Biotechnol.* **2015**, *99*, 6215–6229. [CrossRef]
10. Bimmer, M.; Mientus, M.; Klingl, A.; Ehrenreich, A.; Liebl, W. The Roles of the Various Cellulose Biosynthesis Operons in *Komagataeibacter hansenii* ATCC 23769. *Appl. Environ. Microbiol.* **2022**, *88*, e02460-21. [CrossRef]
11. Anguluri, K.; La China, S.; Brugnoli, M.; Cassanelli, S.; Gullo, M. Better under stress: Improving bacterial cellulose production by *Komagataeibacter xylinus* K2G30 (UMCC 2756) using adaptive laboratory evolution. *Front. Microbiol.* **2022**, *13*, 994097. [CrossRef] [PubMed]
12. Singh, A.; Walker, K.T.; Ledesma-Amaro, R.; Ellis, T. Engineering Bacterial Cellulose by Synthetic Biology. *Int. J. Mol. Sci.* **2020**, *21*, 9185. [CrossRef] [PubMed]
13. Buldum, G.; Mantalaris, A. Systematic Understanding of Recent Developments in Bacterial Cellulose Biosynthesis at Genetic, Bioprocess and Product Levels. *Int. J. Mol. Sci.* **2021**, *22*, 7192. [CrossRef]
14. Vadanan, S.V.; Basu, A.; Lim, S. Bacterial cellulose production, functionalization, and development of hybrid materials using synthetic biology. *Polym. J.* **2022**, *54*, 481–492. [CrossRef]
15. Ferro, M.; Mannu, A.; Panzeri, W.; Theeuwen, C.H.J.; Mele, A. An integrated approach to optimizing cellulose mercerization. *Polymers* **2020**, *12*, 1559. [CrossRef]
16. Abidi, W.; Torres-Sánchez, L.; Siroy, A.; Krasteva, P.V. Weaving of bacterial cellulose by the Bcs secretion systems. *FEMS Microbiol. Rev.* **2022**, *46*, fuab051. [CrossRef]
17. Li, G.; Wang, L.; Deng, Y.; Wei, Q. Research progress of the biosynthetic strains and pathways of bacterial cellulose. *J. Ind. Microbiol. Biotechnol.* **2022**, *49*, kuab071. [CrossRef]
18. Ullah, M.W.; Ul Islam, M.; Khan, S.; Shah, N.; Park, J.K. Recent advancements in bioreactions of cellular and cell-free systems: A study of bacterial cellulose as a model. *Korean J. Chem. Eng.* **2017**, *34*, 1591–1599. [CrossRef]

19. Gorgieva, S. Bacterial Cellulose as a Versatile Platform for Research and Development of Biomedical Materials. *Processes* **2020**, *8*, 624. [CrossRef]
20. Bacterial Cellulose Market by Product Type. Available online: https://www.profsharemarketresearch.com/bacterial-cellulose-market-report/ (accessed on 25 July 2023).
21. Erbas Kiziltas, E.; Kiziltas, A.; Gardner, D.J. Synthesis of bacterial cellulose using hot water extracted wood sugars. *Carbohydr. Polym.* **2015**, *124*, 131–138. [CrossRef]
22. Revin, V.; Liyaskina, E.; Nazarkina, M.; Bogatyreva, A.; Shchankin, M. Cost-effective production of bacterial cellulose using acidic food industry by-products. *Brazilian J. Microbiol.* **2018**, *49*, 151–159. [CrossRef] [PubMed]
23. Gorgieva, S.; Jančič, U.; Cepec, E.; Trček, J. Production efficiency and properties of bacterial cellulose membranes in a novel grape pomace hydrolysate by *Komagataeibacter melomenusus* AV436^{T} and *Komagataeibacter xylinus* LMG 1518. *Int. J. Biol. Macromol.* **2023**, *244*, 125368. [CrossRef] [PubMed]
24. Ye, J.; Zheng, S.; Zhang, Z.; Yang, F.; Ma, K.; Feng, Y.; Zheng, J.; Mao, D.; Yang, X. Bacterial cellulose production by *Acetobacter xylinum* ATCC 23767 using tobacco waste extract as culture medium. *Bioresour. Technol.* **2019**, *274*, 518–524. [CrossRef] [PubMed]
25. Hestrin, S.; Schramm, M. Synthesis of cellulose by *Acetobacter xylinum*. II. Preparation of freeze-dried cells capable of polymerizing glucose to cellulose. *Biochem. J.* **1954**, *58*, 345–352. [CrossRef]
26. Fan, X.; Gao, Y.; He, W.; Hu, H.; Tian, M.; Wang, K.; Pan, S. Production of nano bacterial cellulose from beverage industrial waste of citrus peel and pomace using *Komagataeibacter xylinus*. *Carbohydr. Polym.* **2016**, *151*, 1068–1072. [CrossRef]
27. Uzyol, H.K.; Saçan, M.T. Bacterial cellulose production by *Komagataeibacter hansenii* using algae-based glucose. *Environ. Sci. Pollut. Res.* **2017**, *24*, 11154–11162. [CrossRef]
28. Jozala, A.F.; Pértile, R.A.N.; dos Santos, C.A.; de Carvalho Santos-Ebinuma, V.; Seckler, M.M.; Gama, F.M.; Pessoa, A. Bacterial cellulose production by *Gluconacetobacter xylinus* by employing alternative culture media. *Appl. Microbiol. Biotechnol.* **2015**, *99*, 1181–1190. [CrossRef]
29. Guimarães, D.T.; de Oliveira Barros, M.; de Araújo e Silva, R.; Silva, S.M.F.; de Almeida, J.S.; de Freitas Rosa, M.; Gonçalves, L.R.B.; Brígida, A.I.S. Superabsorbent bacterial cellulose film produced from industrial residue of cashew apple juice processing. *Int. J. Biol. Macromol.* **2023**, *242*, 124405. [CrossRef]
30. Abdelraof, M.; Hasanin, M.S.; El-Saied, H. Ecofriendly green conversion of potato peel wastes to high productivity bacterial cellulose. *Carbohydr. Polym.* **2019**, *211*, 75–83. [CrossRef]
31. Salari, M.; Sowti Khiabani, M.; Rezaei Mokarram, R.; Ghanbarzadeh, B.; Samadi Kafil, H. Preparation and characterization of cellulose nanocrystals from bacterial cellulose produced in sugar beet molasses and cheese whey media. *Int. J. Biol. Macromol.* **2019**, *122*, 280–288. [CrossRef]
32. Sar, T.; Yesilcimen Akbas, M. Potential use of olive oil mill wastewater for bacterial cellulose production. *Bioengineered* **2022**, *13*, 7659–7669. [CrossRef]
33. Costa, A.F.S.; Almeida, F.C.G.; Vinhas, G.M.; Sarubbo, L.A. Production of bacterial cellulose by *Gluconacetobacter hansenii* using corn steep liquor as nutrient sources. *Front. Microbiol.* **2017**, *8*, 2027. [CrossRef]
34. Zhong, C. Industrial-Scale Production and Applications of Bacterial Cellulose. *Front. Bioeng. Biotechnol.* **2020**, *8*, 605374. [CrossRef]
35. Gregory, D.A.; Tripathi, L.; Fricker, A.T.R.; Asare, E.; Orlando, I.; Raghavendran, V.; Roy, I. Bacterial cellulose: A smart biomaterial with diverse applications. *Mater. Sci. Eng. R Rep.* **2021**, *145*, 100623. [CrossRef]
36. Jin, K.; Jin, C.; Wu, Y. Synthetic biology-powered microbial co-culture strategy and application of bacterial cellulose-based composite materials. *Carbohydr. Polym.* **2022**, *283*, 119171. [CrossRef] [PubMed]
37. Lin, D.; Liu, Z.; Shen, R.; Chen, S.; Yang, X. Bacterial cellulose in food industry: Current research and future prospects. *Int. J. Biol. Macromol.* **2020**, *158*, 1007–1019. [CrossRef] [PubMed]
38. Dourado, F.; Gama, M.; Rodrigues, A.C. A Review on the toxicology and dietetic role of bacterial cellulose. *Toxicol. Rep.* **2017**, *4*, 543–553. [CrossRef]
39. Rachtanapun, P.; Klunklin, W.; Jantrawut, P.; Leksawasdi, N.; Jantanasakulwong, K.; Phimolsiripol, Y.; Seesuriyachan, P.; Chaiyaso, T.; Ruksiriwanich, W.; Phongthai, S.; et al. Effect of monochloroacetic acid on properties of carboxymethyl bacterial cellulose powder and film from nata de coco. *Polymers* **2021**, *13*, 488. [CrossRef]
40. Gallegos, A.M.A.; Carrera, S.H.; Parra, R.; Keshavarz, T.; Iqbal, H.M.N. Bacterial Cellulose: A Sustainable Source to Develop Value-Added Products—A Review. *BioResources* **2016**, *11*, 5641–5655. [CrossRef]
41. Azeredo, H.M.C.; Barud, H.; Farinas, C.S.; Vasconcellos, V.M.; Claro, A.M. Bacterial Cellulose as a Raw Material for Food and Food Packaging Applications. *Front. Sustain. Food Syst.* **2019**, *3*, 7. [CrossRef]
42. Fijałkowski, K.; Peitler, D.; Rakoczy, R.; Zywicka, A. Survival of probiotic lactic acid bacteria immobilized in different forms of bacterial cellulose in simulated gastric juices and bile salt solution. *LWT—Food Sci. Technol.* **2016**, *68*, 322–328. [CrossRef]
43. Oliveira-Alcântara, A.V.; Abreu, A.A.S.; Gonçalves, C.; Fuciños, P.; Cerqueira, M.A.; Gama, F.M.P.; Pastrana, L.M.; Rodrigues, S.; Azeredo, H.M.C. Bacterial cellulose/cashew gum films as probiotic carriers. *LWT—Food Sci. Technol.* **2020**, *130*, 109699. [CrossRef]
44. Sabio, L.; González, A.; Ramírez-Rodríguez, G.B.; Gutiérrez-Fernández, J.; Bañuelo, O.; Olivares, M.; Gálvez, N.; Delgado-López, J.M.; Dominguez-Vera, J.M. Probiotic cellulose: Antibiotic-free biomaterials with enhanced antibacterial activity. *Acta Biomater.* **2021**, *124*, 244–253. [CrossRef] [PubMed]

45. Bianchet, R.T.; Vieira Cubas, A.L.; Machado, M.M.; Siegel Moecke, E.H. Applicability of bacterial cellulose in cosmetics—Bibliometric review. *Biotechnol. Rep.* **2020**, *27*, e00502. [CrossRef] [PubMed]
46. Kalyoncu, E.E.; Pesman, E. Bacterial Cellulose as Reinforcement in Paper Made from Recycled Office Waste Pulp. *BioResource* **2020**, *15*, 8496–8514. [CrossRef]
47. Choi, S.M.; Rao, K.M.; Zo, S.M.; Shin, E.J.; Han, S.S. Bacterial Cellulose and Its Applications. *Polymers* **2022**, *14*, 1080. [CrossRef]
48. Basta, A.H.; El-Saied, H. Performance of Improved Bacterial Cellulose Application in the Production of Functional Paper. *J. Appl. Microbiol.* **2009**, *107*, 2098–2107. [CrossRef]
49. Janbade, A.; Zaidi, S.; Vats, M.; Kumar, N.; Dhiman, J.; Gupta, M.K. A Mini Review on Current Advancement in Application of Bacterial Cellulose in Pulp and Paper Industry. In *Proceedings of the International Conference on Innovative Technologies for Clean and Sustainable Development (ICITCSD—2021)*; Springer: Berlin/Heidelberg, Germany, 2022.
50. Dikshit, P.K. Production of Low-Cost Nano-Functionalized Bacterial Cellulose Films for Smart/Intelligent Packaging. *Mater. Proc.* **2023**, *14*, 58. [CrossRef]
51. Cazón, P.; Vázquez, M. Bacterial cellulose as a biodegradable food packaging material: A review. *Food Hydrocoll.* **2021**, *113*, 106530. [CrossRef]
52. Mohite, B.V.; Koli, S.H.; Patil, S.V. Bacterial Cellulose-Based Hydrogels: Synthesis, Properties, and Applications. In *Cellulose-Based Superabsorbent Hydrogels*; Polymers and Polymeric Composites: A Reference Series; Mondal, M., Ed.; Springer Nature: Cham, Switzerland, 2019; pp. 1255–1276.
53. Walker, K.T.; Keane, J.; Goosens, V.J.; Song, W.; Lee, K.-Y.; Ellis, T. Self-dyeing textiles grown from cellulose-producing bacteria with engineered tyrosinase expression. *bioRxiv* **2023**. [CrossRef]
54. Fernandes, M.; Souto, A.P.; Dourado, F.; Gama, M. Application of Bacterial Cellulose in the Textile and Shoe Industry: Development of Biocomposites. *Polysaccharides* **2021**, *2*, 566–581. [CrossRef]
55. Norhasri, M.S.M.; Hamidah, M.S.; Fadzil, A.M. Applications of using nano material in concrete: A review. *Constr. Build. Mater.* **2017**, *133*, 91–97. [CrossRef]
56. Sanchez, F.; Sobolev, K. Nanotechnology in concrete—A review. *Constr. Build. Mater.* **2010**, *24*, 2060–2071. [CrossRef]
57. Silvestre, J.; Silvestre, N.; De Brito, J. Review on concrete nanotechnology. *Eur. J. Environ. Civ. Eng.* **2016**, *20*, 455–485. [CrossRef]
58. Li, D.; Tian, X.; Wang, Z.; Guan, Z.; Li, X.; Qiao, H.; Ke, H.; Luo, L.; Wei, Q. Multifunctional adsorbent based on metal-organic framework modified bacterial cellulose/chitosan composite aerogel for high efficient removal of heavy metal ion and organic pollutant. *Chem. Eng. J.* **2020**, *383*, 123127. [CrossRef]
59. Galdino, C.J.S.; Maia, A.D.; Meira, H.M.; Souza, T.C.; Amorim, J.D.P.; Almeida, F.C.G.; Costa, A.F.S.; Sarubbo, L.A. Use of a bacterial cellulose filter for the removal of oil from wastewater. *Process Biochem.* **2020**, *91*, 288–296. [CrossRef]
60. Shen, H.; Liao, S.; Jiang, C.; Zhang, J.; Wei, Q.; Ghiladi, R.A.; Wang, Q. In situ grown bacterial cellulose/MoS_2 composites for multi-contaminant wastewater treatment and bacteria inactivation. *Carbohydr. Polym.* **2022**, *277*, 118853. [CrossRef]
61. Prilepskii, A.; Nikolaev, V.; Klaving, A. Conductive bacterial cellulose: From drug delivery to flexible electronics. *Carbohydr. Polym.* **2023**, *313*, 120850. [CrossRef] [PubMed]
62. Anjan, A.; Bharti, V.K.; Sharma, C.S.; Khandelwal, M. Carbonized Bacterial Cellulose-Derived Binder-Free, Flexible, and Free-Standing Cathode Host for High-Performance Stable Potassium-Sulfur Batteries. *ACS Appl. Energy Mater.* **2023**, *6*, 3042–3051. [CrossRef]
63. Gilbert, C.; Tang, T.-C.; Ott, W.; Dorr, B.A.; Shaw, W.M.; Sun, G.L.; Lu, T.K.; Ellis, T. Living materials with programmable functionalities grown from engineered microbial co-cultures. *Nat. Mater.* **2021**, *20*, 691–700. [CrossRef]
64. Gilbert, C.; Ellis, T. Biological Engineered Living Materials: Growing Functional Materials with Genetically Programmable Properties. *ACS Synth. Biol.* **2019**, *8*, 1–15. [CrossRef] [PubMed]
65. Liu, X.; Wu, M.; Wang, M.; Hu, Q.; Liu, J.; Duan, Y.; Liu, B. Direct Synthesis of Photosensitizable Bacterial Cellulose as Engineered Living Material for Skin Wound Repair. *Adv. Mater.* **2022**, *34*, 2109010. [CrossRef]
66. Lin, S.P.; Loira Calvar, I.; Catchmark, J.M.; Liu, J.R.; Demirci, A.; Cheng, K.C. Biosynthesis, production and applications of bacterial cellulose. *Cellulose* **2013**, *20*, 2191–2219. [CrossRef]
67. Ostadhossein, F.; Mahmoudi, N.; Morales-Cid, G.; Tamjid, E.; Navas-Martos, F.J.; Soriano-Cuadrado, B.; Paniza, J.M.L.; Simchi, A. Development of chitosan/bacterial cellulose composite films containing nanodiamonds as a potential flexible platform for wound dressing. *Materials* **2015**, *8*, 6401–6418. [CrossRef] [PubMed]
68. Cherng, J.H.; Chou, S.C.; Chen, C.L.; Wang, Y.W.; Chang, S.J.; Fan, G.Y.; Leung, F.S.; Meng, E. Bacterial cellulose as a potential bio-scaffold for effective re-epithelialization therapy. *Pharmaceutics* **2021**, *13*, 1592. [CrossRef] [PubMed]
69. Zheng, L.; Li, S.; Luo, J.; Wang, X. Latest Advances on Bacterial Cellulose-Based Antibacterial Materials as Wound Dressings. *Front. Bioeng. Biotechnol.* **2020**, *8*, 593768. [CrossRef]
70. Urbina, L.; Eceiza, A.; Gabilondo, N.; Corcuera, M.Á.; Retegi, A. Tailoring the in situ conformation of bacterial cellulose-graphene oxide spherical nanocarriers. *Int. J. Biol. Macromol.* **2020**, *163*, 1249–1260. [CrossRef]
71. Cacicedo, M.L.; Islan, G.A.; León, I.E.; Álvarez, V.A.; Chourpa, I.; Allard-Vannier, E.; García-Aranda, N.; Díaz-Riascos, Z.V.; Fernández, Y.; Schwartz, S.; et al. Bacterial cellulose hydrogel loaded with lipid nanoparticles for localized cancer treatment. *Colloids Surf. B Biointerfaces* **2018**, *170*, 596–608. [CrossRef]
72. Islam, S.U.; Ul-Islam, M.; Ahsan, H.; Ahmed, M.B.; Shehzad, A.; Fatima, A.; Sonn, J.K.; Lee, Y.S. Potential applications of bacterial cellulose and its composites for cancer treatment. *Int. J. Biol. Macromol.* **2021**, *168*, 301–309. [CrossRef]

73. Autier, L.; Clavreul, A.; Cacicedo, M.L.; Franconi, F.; Sindji, L.; Rousseau, A.; Perrot, R.; Montero-Menei, C.N.; Castro, G.R.; Menei, P. A new glioblastoma cell trap for implantation after surgical resection. *Acta Biomater.* **2019**, *84*, 268–279. [CrossRef]
74. Zhang, W.; Wang, X.C.; Li, X.; Zhang, L.; Jiang, F. A 3D porous microsphere with multistage structure and component based on bacterial cellulose and collagen for bone tissue engineering. *Carbohydr. Polym.* **2020**, *236*, 116043. [CrossRef] [PubMed]
75. Niamsap, T.; Lam, N.T.; Sukyai, P. Production of hydroxyapatite-bacterial nanocellulose scaffold with assist of cellulose nanocrystals. *Carbohydr. Polym.* **2019**, *205*, 159–166. [CrossRef]
76. Klinthoopthamrong, N.; Chaikiawkeaw, D.; Phoolcharoen, W.; Rattanapisit, K.; Kaewpungsup, P.; Pavasant, P.; Hoven, V.P. Bacterial cellulose membrane conjugated with plant-derived osteopontin: Preparation and its potential for bone tissue regeneration. *Int. J. Biol. Macromol.* **2020**, *149*, 51–59. [CrossRef] [PubMed]
77. Gorgieva, S.; Hribernik, S. Microstructured and degradable bacterial cellulose–gelatin composite membranes: Mineralization aspects and biomedical relevance. *Nanomaterials* **2019**, *9*, 303. [CrossRef] [PubMed]
78. Klemm, D.; Schumann, D.; Udhardt, U.; Marsch, S. Bacterial synthesized cellulose—Artificial blood vessels for microsurgery. *Prog. Polym. Sci.* **2001**, *26*, 1561–1603. [CrossRef]
79. Bae, S.; Shoda, M. Statistical Optimization of Culture Conditions for Bacterial Cellulose Production Using Box-Behnken Design. *Biotechnol. Bioeng.* **2005**, *90*, 20–28. [CrossRef]
80. Ruka, D.R.; Simon, G.P.; Dean, K.M. Altering the growth conditions of *Gluconacetobacter xylinus* to maximize the yield of bacterial cellulose. *Carbohydr. Polym.* **2012**, *89*, 613–622. [CrossRef]
81. Son, H.-J.; Heo, M.-S.; Kim, Y.-G.; Lee, S.-J. Optimization of fermentation conditions for the production of bacterial cellulose by a newly isolated *Acetobacter* sp. A9 in shaking cultures. *Biotechnol. Appl. Biochem.* **2001**, *33*, 1–5. [CrossRef]
82. Cheng, K.C.; Catchmark, J.M.; Demirci, A. Effect of different additives on bacterial cellulose production by *Acetobacter xylinum* and analysis of material property. *Cellulose* **2009**, *16*, 1033–1045. [CrossRef]
83. Jagannath, A.; Kalaiselvan, A.; Manjunatha, S.S.; Raju, P.S.; Bawa, A.S. The effect of pH, sucrose and ammonium sulphate concentrations on the production of bacterial cellulose (Nata-de-coco) by *Acetobacter xylinum*. *World J. Microbiol. Biotechnol.* **2008**, *24*, 2593–2599. [CrossRef]
84. Wang, J.; Tavakoli, J.; Tang, Y. Bacterial cellulose production, properties and applications with different culture methods—A review. *Carbohydr. Polym.* **2019**, *219*, 63–76. [CrossRef] [PubMed]
85. De Amorim, J.D.P.; da Silva Junior, C.J.G.; de Medeiros, A.D.M.; do Nascimento, H.A.; Sarubbo, M.; de Medeiros, T.P.M.; Costa, A.F.d.S.; Sarubbo, L.A. Bacterial Cellulose as a Versatile Biomaterial for Wound Dressing Application. *Molecules* **2022**, *27*, 5580. [CrossRef] [PubMed]
86. Son, H.J.; Kim, H.G.; Kim, K.K.; Kim, H.S.; Kim, Y.G.; Lee, S.J. Increased production of bacterial cellulose by *Acetobacter* sp. V6 in synthetic media under shaking culture conditions. *Bioresour. Technol.* **2003**, *86*, 215–219. [CrossRef]
87. Zhou, L.L.; Sun, D.P.; Hu, L.Y.; Li, Y.W.; Yang, J.Z. Effect of addition of sodium alginate on bacterial cellulose production by *Acetobacter xylinum*. *J. Ind. Microbiol. Biotechnol.* **2007**, *34*, 483–489. [CrossRef] [PubMed]
88. Nguyen, V.T.; Flanagan, B.; Gidley, M.J.; Dykes, G.A. Characterization of cellulose production by a *Gluconacetobacter xylinus* strain from Kombucha. *Curr. Microbiol.* **2008**, *57*, 449–453. [CrossRef] [PubMed]
89. Bae, S.; Shoda, M. Bacterial cellulose production by fed-batch fermentation in molasses medium. *Biotechnol. Prog.* **2004**, *20*, 1366–1371. [CrossRef] [PubMed]
90. Krystynowicz, A.; Czaja, W.; Wiktorowska-Jezierska, A.; Gonçalves-Miśkiewicz, M.; Turkiewicz, M.; Bielecki, S. Factors affecting the yield and properties of bacterial cellulose. *J. Ind. Microbiol. Biotechnol.* **2002**, *29*, 189–195. [CrossRef]
91. Ishihara, M.; Matsunaga, M.; Hayashi, N.; Tišler, V. Utilization of D-xylose as carbon source for production of bacterial cellulose. *Enzyme Microb. Technol.* **2002**, *31*, 986–991. [CrossRef]
92. Keshk, S.; Sameshima, K. The utilization of sugar cane molasses with/without the presence of lignosulfonate for the production of bacterial cellulose. *Appl. Microbiol. Biotechnol.* **2006**, *72*, 291–296. [CrossRef]
93. Pourramezan, G.Z.; Roayaei, A.M.; Qezelbash, Q.R. Optimization of Culture Conditions for Bacterial Cellulose Production by *Acetobacter* sp. 4B-2. *Biotechnology* **2009**, *8*, 150–154. [CrossRef]
94. Fang, L.; Catchmark, J.M. Characterization of cellulose and other exopolysaccharides produced from *Gluconacetobacter* strains. *Carbohydr. Polym.* **2015**, *115*, 663–669. [CrossRef]
95. Basu, A.; Vadanan, S.V.; Lim, S. Rational design of a scalable bioprocess platform for bacterial cellulose production. *Carbohydr. Polym.* **2019**, *207*, 684–693. [CrossRef]
96. Toyosaki, H.; Naritomi, T.; Seto, A.; Matsuoka, M.; Tsuchida, T.; Yoshinaga, F. Screening of Bacterial Cellulose-producing *Acetobacter* Strains Suitable for Agitated Culture. *Biosci. Biotechnol. Biochem.* **1995**, *59*, 1498–1502. [CrossRef]
97. Seto, A.; Kojima, Y.; Tonouchi, N.; Tsuchida, T.; Yoshinaga, F. Screening of Bacterial Cellulose-producing *Acetobacter* Strains Suitable for Sucrose as a Carbon Source. *Biosci. Biotechnol. Biochem.* **1997**, *61*, 735–736. [CrossRef]
98. Xie, H.; Du, H.; Yang, X.; Si, C. Recent Strategies in Preparation of Cellulose Nanocrystals and Cellulose Nanofibrils Derived from Raw Cellulose Materials. *Int. J. Polym. Sci.* **2018**, *2018*, 7923068. [CrossRef]
99. Lindman, B.; Karlström, G.; Stigsson, L. On the mechanism of dissolution of cellulose. *J. Mol. Liq.* **2010**, *156*, 76–81. [CrossRef]
100. Xiong, B.; Zhao, P.; Hu, K.; Zhang, L.; Cheng, G. Dissolution of cellulose in aqueous NaOH/urea solution: Role of urea. *Cellulose* **2014**, *21*, 1183–1192. [CrossRef]

101. Shanshan, G.; Jianqing, W.; Zhengwei, J. Preparation of cellulose films from solution of bacterial cellulose in NMMO. *Carbohydr. Polym.* **2012**, *87*, 1020–1025. [CrossRef]
102. Jin, H.; Zha, C.; Gu, L. Direct dissolution of cellulose in NaOH/thiourea/urea aqueous solution. *Carbohydr. Res.* **2007**, *342*, 851–858. [CrossRef]
103. Pham, T.T.H.; Vadanan, S.V.; Lim, S. Enhanced rheological properties and conductivity of bacterial cellulose hydrogels and aerogels through complexation with metal ions and PEDOT/PSS. *Cellulose* **2020**, *27*, 8075–8086. [CrossRef]
104. Abe, K.; Iwamoto, S.; Yano, H. Obtaining Cellulose Nanofibers with a Uniform Width of 15 nm from Wood. *Biomacromolecules* **2007**, *8*, 3276–3278. [CrossRef] [PubMed]
105. Wang, S.; Cheng, Q. A Novel Process to Isolate Fibrils from Cellulose Fibers by High-Intensity Ultrasonication, Part 1: Process Optimization. *J. Appl. Polym. Sci.* **2009**, *113*, 1270–1275. [CrossRef]
106. Saibuatong, O.; Phisalaphong, M. Novo aloe vera-bacterial cellulose composite film from biosynthesis. *Carbohydr. Polym.* **2010**, *79*, 455–460. [CrossRef]
107. De Lima Fontes, M.; Meneguin, A.B.; Tercjak, A.; Gutierrez, J.; Cury, B.S.F.; dos Santos, A.M.; Ribeiro, S.J.L.; Barud, H.S. Effect of *in situ* modification of bacterial cellulose with carboxymethylcellulose on its nano/microstructure and methotrexate release properties. *Carbohydr. Polym.* **2018**, *179*, 126–134. [CrossRef] [PubMed]
108. Müller, D.; Mandelli, J.S.; Marins, J.A.; Soares, B.G.; Porto, L.M.; Rambo, C.R.; Barra, G.M.O. Electrically conducting nanocomposites: Preparation and properties of polyaniline (PAni)-coated bacterial cellulose nanofibers (BC). *Cellulose* **2012**, *19*, 1645–1654. [CrossRef]
109. Zhu, W.; Li, W.; He, Y.; Duan, T. In-situ biopreparation of biocompatible bacterial cellulose/graphene oxide composites pellets. *Appl. Surf. Sci.* **2015**, *338*, 22–26. [CrossRef]
110. Arias, S.L.; Shetty, A.R.; Senpan, A.; Echeverry-Rendón, M.; Reece, L.M.; Allain, J.P. Fabrication of a functionalized magnetic bacterial nanocellulose with iron oxide nanoparticles. *J. Vis. Exp.* **2016**, *2016*, e52951. [CrossRef]
111. Yan, Z.; Chen, S.; Wang, H.; Wang, B.; Jiang, J. Biosynthesis of bacterial cellulose/multi-walled carbon nanotubes in agitated culture. *Carbohydr. Polym.* **2008**, *74*, 659–665. [CrossRef]
112. Ruka, D.R.; Simon, G.P.; Dean, K.M. *In situ* modifications to bacterial cellulose with the water insoluble polymer poly-3-hydroxybutyrate. *Carbohydr. Polym.* **2013**, *92*, 1717–1723. [CrossRef]
113. Jiang, Y.; Yu, G.; Zhou, Y.; Liu, Y.; Feng, Y.; Li, J. Effects of Sodium Alginate on Microstructural and Properties of Bacterial Cellulose Nanocrystal Stabilized Emulsions. *Colloids Surf. A Physicochem. Eng. Asp.* **2020**, *607*, 125474. [CrossRef]
114. Ul-Islam, M.; Shah, N.; Ha, J.H.; Park, J.K. Effect of chitosan penetration on physico-chemical and mechanical properties of bacterial cellulose. *Korean J. Chem. Eng.* **2011**, *28*, 1736–1743. [CrossRef]
115. Zhijiang, C.; Guang, Y. Bacterial cellulose/collagen composite: Characterization and first evaluation of cytocompatibility. *J. Appl. Polym. Sci.* **2011**, *120*, 2938–2944. [CrossRef]
116. Wang, F.; Kim, H.J.; Park, S.; Kee, C.D.; Kim, S.J.; Oh, I.K. Bendable and flexible supercapacitor based on polypyrrole-coated bacterial cellulose core-shell composite network. *Compos. Sci. Technol.* **2016**, *128*, 33–40. [CrossRef]
117. Lopes, T.D.; Riegel-Vidotti, I.C.; Grein, A.; Tischer, C.A.; Faria-Tischer, P.C. de S. Bacterial cellulose and hyaluronic acid hybrid membranes: Production and characterization. *Int. J. Biol. Macromol.* **2014**, *67*, 401–408. [CrossRef]
118. Hutchens, S.A.; Benson, R.S.; Evans, B.R.; O'Neill, H.M.; Rawn, C.J. Biomimetic synthesis of calcium-deficient hydroxyapatite in a natural hydrogel. *Biomaterials* **2006**, *27*, 4661–4670. [CrossRef] [PubMed]
119. Pourreza, N.; Golmohammadi, H.; Naghdi, T.; Yousefi, H. Green in-situ synthesized silver nanoparticles embedded in bacterial cellulose nanopaper as a bionanocomposite plasmonic sensor. *Biosens. Bioelectron.* **2015**, *74*, 353–359. [CrossRef] [PubMed]
120. Barud, H.S.; Barrios, C.; Regiani, T.; Marques, R.F.C.; Verelst, M.; Dexpert-Ghys, J.; Messaddeq, Y.; Ribeiro, S.J.L. Self-supported silver nanoparticles containing bacterial cellulose membranes. *Mater. Sci. Eng. C* **2008**, *28*, 515–518. [CrossRef]
121. Ul-Islam, M.; Khan, T.; Park, J.K. Nanoreinforced bacterial cellulose-montmorillonite composites for biomedical applications. *Carbohydr. Polym.* **2012**, *89*, 1189–1197. [CrossRef]
122. Gao, M.; Li, J.; Bao, Z.; Hu, M.; Nian, R.; Feng, D.; An, D.; Li, X.; Xian, M.; Zhang, H. A natural in situ fabrication method of functional bacterial cellulose using a microorganism. *Nat. Commun.* **2019**, *10*, 437. [CrossRef]
123. Seto, A.; Saito, Y.; Matsushige, M.; Kobayashi, H.; Sasaki, Y.; Tonouchi, N.; Tsuchida, T.; Yoshinaga, F.; Ueda, K.; Beppu, T. Effective cellulose production by a coculture of *Gluconacetobacter xylinus* and *Lactobacillus mali*. *Appl. Microbiol. Biotechnol.* **2006**, *73*, 915–921. [CrossRef]
124. Liu, K.; Catchmark, J.M. Enhanced mechanical properties of bacterial cellulose nanocomposites produced by co-culturing *Gluconacetobacter hansenii* and *Escherichia coli* under static conditions. *Carbohydr. Polym.* **2019**, *219*, 12–20. [CrossRef] [PubMed]
125. Liu, K.; Catchmark, J.M. Bacterial cellulose/hyaluronic acid nanocomposites production through co-culturing *Gluconacetobacter hansenii* and *Lactococcus lactis* in a two-vessel circulating system. *Bioresour. Technol.* **2019**, *290*, 121715. [CrossRef] [PubMed]
126. Ding, R.; Hu, S.; Xu, M.; Hu, Q.; Jiang, S.; Xu, K.; Tremblay, P.L.; Zhang, T. The facile and controllable synthesis of a bacterial cellulose/polyhydroxybutyrate composite by co-culturing *Gluconacetobacter xylinus* and *Ralstonia eutropha*. *Carbohydr. Polym.* **2021**, *252*, 117137. [CrossRef]
127. Gunduz, G.; Erbas Kiziltas, E.; Kiziltas, A.; Gencer, A.; Aydemir, D.; Asik, N. Production of bacterial cellulose fibers in the presence of effective microorganism. *J. Nat. Fibers* **2019**, *16*, 567–575. [CrossRef]
128. Brugnoli, M.; Mazzini, I.; La China, S.; De Vero, L.; Gullo, M. A Microbial Co-Culturing System for Producing Cellulose-Hyaluronic Acid Composites. *Microorganisms* **2023**, *11*, 1504. [CrossRef]

129. Nakai, T.; Tonouchi, N.; Konishi, T.; Kojima, Y.; Tsuchida, T.; Yoshinaga, F.; Sakai, F.; Hayashi, T. Enhancement of cellulose production by expression of sucrose synthase in *Acetobacter xylinum*. *Proc. Natl. Acad. Sci. USA* **1999**, *96*, 14–18. [CrossRef] [PubMed]
130. Battad-Bernardo, E.; McCrindle, S.L.; Couperwhite, I.; Neilan, B.A. Insertion of an *E. coli lacZ* gene in *Acetobacter xylinus* for the production of cellulose in whey. *FEMS Microbiol. Lett.* **2004**, *231*, 253–260. [CrossRef]
131. Shigematsu, T.; Takamine, K.; Kitazato, M.; Morita, T.; Naritomi, T.; Morimura, S.; Kida, K. Cellulose production from glucose using a glucose dehydrogenase gene (*gdh*)-deficient mutant of *Gluconacetobacter xylinus* and its use for bioconversion of sweet potato pulp. *J. Biosci. Bioeng.* **2005**, *99*, 415–422. [CrossRef]
132. Chien, L.J.; Chen, H.T.; Yang, P.F.; Lee, C.K. Enhancement of cellulose pellicle production by constitutively expressing *Vitreoscilla* hemoglobin in *Acetobacter xylinum*. *Biotechnol. Prog.* **2006**, *22*, 1598–1603. [CrossRef]
133. Yadav, V.; Paniliatis, B.J.; Shi, H.; Lee, K.; Cebe, P.; Kaplan, D.L. Novel in vivo-degradable cellulose-chitin copolymer from metabolically engineered *Gluconacetobacter xylinus*. *Appl. Environ. Microbiol.* **2010**, *76*, 6257–6265. [CrossRef]
134. Imai, T.; Sun, S.J.; Horikawa, Y.; Wada, M.; Sugiyama, J. Functional reconstitution of cellulose synthase in *Escherichia coli*. *Biomacromolecules* **2014**, *15*, 4206–4213. [CrossRef] [PubMed]
135. Fang, J.; Kawano, S.; Tajima, K.; Kondo, T. In Vivo Curdlan/Cellulose Bionanocomposite Synthesis by Genetically Modified *Gluconacetobacter xylinus*. *Biomacromolecules* **2015**, *16*, 3154–3160. [CrossRef]
136. Florea, M.; Hagemann, H.; Santosa, G.; Abbott, J.; Micklem, C.N.; Spencer-Milnes, X.; De Arroyo Garcia, L.; Paschou, D.; Lazenbatt, C.; Kong, D.; et al. Engineering control of bacterial cellulose production using a genetic toolkit and a new cellulose-prod ucing strain. *Proc. Natl. Acad. Sci. USA* **2016**, *113*, E3431–E3440. [CrossRef] [PubMed]
137. Buldum, G.; Bismarck, A.; Mantalaris, A. Recombinant biosynthesis of bacterial cellulose in genetically modified *Escherichia coli*. *Bioprocess Biosyst. Eng.* **2018**, *41*, 265–279. [CrossRef] [PubMed]
138. Jang, W.D.; Kim, T.Y.; Kim, H.U.; Shim, W.Y.; Ryu, J.Y.; Park, J.H.; Lee, S.Y. Genomic and metabolic analysis of *Komagataeibacter xylinus* DSM 2325 producing bacterial cellulose nanofiber. *Biotechnol. Bioeng.* **2019**, *116*, 3372–3381. [CrossRef]
139. Gwon, H.; Park, K.; Chung, S.C.; Kim, R.H.; Kang, J.K.; Ji, S.M.; Kim, N.J.; Lee, S.; Ku, J.H.; Do, E.C.; et al. A safe and sustainable bacterial cellulose nanofiber separator for lithium rechargeable batteries. *Proc. Natl. Acad. Sci. USA* **2019**, *116*, 19288–19293. [CrossRef]
140. Walker, K.T.; Goosens, V.J.; Das, A.; Graham, A.E.; Ellis, T. Engineered cell-to-cell signalling within growing bacterial cellulose pellicles. *Microb. Biotechnol.* **2019**, *12*, 611–619. [CrossRef]
141. Teh, M.Y.; Ooi, K.H.; Danny Teo, S.X.; Bin Mansoor, M.E.; Shaun Lim, W.Z.; Tan, M.H. An Expanded Synthetic Biology Toolkit for Gene Expression Control in *Acetobacteraceae*. *ACS Synth. Biol.* **2019**, *8*, 708–723. [CrossRef]
142. Jacek, P.; Ryngajłło, M.; Bielecki, S. Structural changes of bacterial nanocellulose pellicles induced by genetic modification of *Komagataeibacter hansenii* ATCC 23769. *Appl. Microbiol. Biotechnol.* **2019**, *103*, 5339–5353. [CrossRef]
143. Liu, D.; Cao, Y.; Qu, R.; Gao, G.; Chen, S.; Zhang, Y.; Wu, M.; Ma, T.; Li, G. Production of bacterial cellulose hydrogels with tailored crystallinity from *Enterobacter* sp. FY-07 by the controlled expression of colanic acid synthetic genes. *Carbohydr. Polym.* **2019**, *207*, 563–570. [CrossRef]
144. Huang, L.H.; Liu, Q.J.; Sun, X.W.; Li, X.J.; Liu, M.; Jia, S.R.; Xie, Y.Y.; Zhong, C. Tailoring bacterial cellulose structure through CRISPR interference-mediated downregulation of *galU* in *Komagataeibacter xylinus* CGMCC 2955. *Biotechnol. Bioeng.* **2020**, *117*, 2165–2176. [CrossRef] [PubMed]

MDPI AG
Grosspeteranlage 5
4052 Basel
Switzerland
Tel.: +41 61 683 77 34

Polymers Editorial Office
E-mail: polymers@mdpi.com
www.mdpi.com/journal/polymers

Academic Open
Access Publishing

mdpi.com

ISBN 978-3-7258-7311-1